Airborne in situ measurements of ice particles in the tropical tropopause layer

DISSERTATION

zur Erlangung des Grades
Doktor der Naturwissenschaften
(Dr. rer. nat.)

Wiebke Frey

am Fachbereich 08 für Physik, Mathematik und Informatik
(Institut für Physik der Atmosphäre)
der Johannes Gutenberg-Universität Mainz

vorgelegt von
Wiebke Frey
geboren in Celle / Niedersachsen
Mainz, 2011

Tag der mündlichen Prüfung: 18.10.2011

1. Gutachter: [redacted]
2. Gutachter: [redacted]
3. Gutachter: [redacted]

D77 - Mainzer Dissertationen

Abstract

Ice clouds have a strong effect on the Earth-atmosphere radiative energy balance, on the distribution of condensable gases in the atmosphere, as well as on the chemical composition of the air. The ice particles in these clouds can take on a variety of shapes which makes the description of the cloud microphysical properties more difficult. In the tropical upper troposphere/lower stratosphere (UTLS), a region where ice cloud abundance is relatively high, different types of ice clouds can be observed. However, in situ measurements are rare due to the high altitude of these clouds and the few available research aircraft, only three worldwide, that can fly at such altitudes. This work focuses on in situ measurements of the tropical UTLS clouds performed with a Cloud Imaging Probe (CIP) and a Forward Scattering Spectrometer Probe (FSSP-100), whereof the CIP is the key instrument of this thesis. The CIP is an airborne in situ instrument that obtains two-dimensional shadow images of cloud particles. Several cloud microphysical parameters can be derived from these measurements, e.g. number concentrations and size distributions. In order to obtain a high quality data set, a careful image analysis and several corrections need to be applied to the CIP observations. These methods are described in detail.

Measurements within the tropical UTLS have been performed during two campaigns: SCOUT-O3, 2005 in Northern Australia and SCOUT-AMMA, 2006 in West Africa. The obtained data set includes first observations of subvisible cirrus clouds over a continental area and observations of the anvils of deep convective clouds. The latter can be further divided into clouds in mesoscale convective system outflows of different ages and clouds in overshooting cloud turrets that even penetrated the stratosphere. The microphysical properties of these three cloud types are discussed in detail. Furthermore, the vertical structure of the ice clouds in the UTLS is investigated. The values of the microphysical parameters were found to decrease with increasing altitude in the upper troposphere. Particle numbers and maximum sizes were also decreasing with increasing age of the outflow clouds. Further differences between the deep convective clouds and subvisible cirrus were found in the particle morphology as well as in the ratio of the observed aerosol particles to cloud particles which indicates that the different freezing processes (deposition, contact, immersion freezing) play different roles in the formation of the respective clouds. For the achievement of a better microphysical characterisation and description numerical fits have been adjusted onto the cloud particle size distributions of the subvisible cirrus as well as on the size distributions of the clouds at different altitudes in the UTLS.

Zusammenfassung

Eiswolken haben einen starken Einfluss auf die Strahlungsbilanz des Energiesystems Erde - Atmosphäre, auf die Spurengasverteilung in der Atmosphäre, sowie auf die chemische Zusammensetzung der Atmosphäre. Die Eispartikel in diesen Wolken können einen Vielzahl von Formen annehmen, was die Beschreibung der mikrophysikalischen Eigenschaften erschwert. In der tropischen oberen Troposphäre/unteren Stratosphäre (UTLS, vom Englischen upper troposphere/lower stratosphere), einer Region mit relativ hohem Vorkommen von Eiswolken, können verschiedene Typen von Eiswolken beobachtet werden. Bisher gibt es nur wenige in situ Messungen von diesen in großer Höhe vorkommenden Wolken, da weltweit nur drei Forschungsflugzeuge diese Höhen erreichen können.

Diese Arbeit beschäftigt sich mit in situ Messungen von tropischen UTLS Wolken, die mit einem Cloud Imaging Probe (CIP) und einem Forward Scattering Spectrometer Probe (FSSP-100) durchgeführt wurde, wobei das CIP das Hauptinstrument dieser Arbeit ist. Das CIP ist ein flugzeuggetragenes in situ Instrument, das zweidimensionale Schattenbilder von Wolkenpartikeln aufzeichnet. Verschiedene wolkenmikrophysikalische Parameter können aus den Messungen gewonnen werden wie z.B. Anzahlkonzentrationen und Größenverteilungen. Um einen hochwertigen Datensatz zu erhalten, müssen mehrere Auswertealgorithmen und Korrekturen auf die CIP-Beobachtungen angewendet werden. Diese Methoden werden im Detail beschrieben.

Messungen innerhalb der tropischen UTLS wurden im Verlauf von zwei Messkampagnen durchgeführt: SCOUT-O3, 2005, in Nordaustralien und SCOUT-AMMA, 2006, in Westafrika. Der gewonnene Datensatz enthält erste Beobachtungen von nichtsichtbaren Cirren über einer kontinentalen Region sowie Beobachtungen von Ambossen hochreichender konvektiver Wolken. Die Letzteren können weiter unterteilt werden in Wolken in der Ausströmregion von mesoskaligen konvektiven Systemen und Wolken in überschießenden Wolkentürmen, die sogar bis in die Stratosphäre hineinreichen. Die mikrophysikalischen Eigenschaften dieser drei Wolkentypen werden genau beschrieben. Weiterhin wird die vertikale Struktur der Eiswolken in der UTLS untersucht.

Eine Abnahme der Eispartikelanzahlkonzentration, des Eiswassergehalts und des mittleren Partikeldurchmessers mit zunehmender Höhe in der oberen Troposphäre wurde beobachtet. Die Partikelanzahlen und die maximalen Größen der Partikel zeigten ebenfalls eine Abnahme mit zunehmendem Alter der Wolken in der Ausströmregion. Weitere Unterschiede zwischen den Wolken in hochreichender Konvektion und den nichtsichtbaren Cirren werden in der Eispartikelmorphologie als auch im Verhältnis zwischen den beobachteten Aerosolpartikeln zu Wolkenpartikeln gezeigt. Dies ist ein Hinweis dafür, dass die verschiedenen Gefrierprozesse (Depositions-, Kontakt-, Immersionsgefrieren) eine unterschiedliche Gewichtung in der Wolkenbildung der verschiedenen Wolken haben. Um eine bessere mikrophysikalische Charakterisierung und Beschreibung zu erreichen wurden mathematische Fits an die Wolkenpartikelgrößenverteilungen der nichtsichtbaren Cirren und der Wolken in verschiedenen Höhen in der UTLS erstellt.

Contents

List of figures **v**

List of tables **viii**

1 Introduction **1**
1.1 Cloud formation . . . 3
1.1.1 Deep convection . . . 3
1.1.2 Cloud ice particles . . . 4
1.2 Tropical ice clouds . . . 6
1.2.1 Vertical structure of the tropical atmosphere . . . 8
1.2.2 Cloud particles within the UTLS . . . 9
1.3 Motivation and outline . . . 10

I Methodology **13**

2 Description of the in situ cloud particle instrument and data processing **15**
2.1 Cloud Imaging Probe . . . 15
2.2 Calculation of Sample Volume . . . 17
2.3 Cloud particle parameters . . . 18
2.3.1 Sizing methods . . . 18
2.3.2 Single particle parameters . . . 20
2.3.3 Combined particle parameters . . . 20
2.4 Data evaluation and correction mechanisms . . . 23
2.4.1 Reconstruction of first slice . . . 23
2.4.2 Probe TAS related deformation of particles . . . 24
2.4.3 Area ratio . . . 25
2.4.4 Out-of-focus images . . . 26
2.4.5 Empty images . . . 29
2.4.6 Partial images . . . 30
2.4.7 Shattering . . . 30
2.4.8 More instrumental issues . . . 32
2.4.9 Summary of quality assessment . . . 34
2.5 Particle data reduction and evaluation . . . 34
2.6 Instrument uncertainty . . . 37
2.7 Size calibration . . . 39
2.8 Placement among airborne in situ cloud particle instrumentation . . . 40
2.8.1 Holographic instruments . . . 41

2.8.2 Imaging instruments . . . 41
2.8.3 Scattering instruments . . . 42
2.9 Application on other platforms . . . 44

3 Experimental setup: Aircraft and tropical field campaigns 47
3.1 Aircraft: the M-55 Geophysica . . . 47
3.1.1 Instruments on board . . . 48
3.1.2 Further measurements . . . 51
3.2 Campaigns . . . 51
3.2.1 Tropical Australia: SCOUT-O3 . . . 51
3.2.2 Tropical West Africa: AMMA . . . 52

II Clouds in the TTL - observations of microphysical properties 55

4 Mesoscale Convective System outflow over West Africa 57
4.1 Meteorological background - Mesoscale Convective Systems . . . 57
4.1.1 MCSs in the West African Monsoon environment . . . 60
4.1.2 Outflow identification . . . 63
4.2 Measurements of MCS outflow . . . 65
4.2.1 Satellite observations . . . 65
4.2.2 Tracer observations . . . 68
4.2.3 Young outflow case on 7 August 2006 . . . 71
4.2.4 Recent outflow case on 16 August 2006 . . . 74
4.2.5 Aged outflow on 11 August 2006 . . . 76
4.2.6 Precursor state for MCS formation on 8 August 2006 . . . 78
4.3 Discussion and summary . . . 81

5 Overshooting convection over tropical Australia 87
5.1 Meteorological background . . . 87
5.1.1 Hector storm system . . . 88
5.1.2 The role of convective overshoots for stratospheric dryness . . . 90
5.2 Measurements of convective overshooting . . . 92
5.2.1 Cloud observations . . . 93
5.2.2 Observations of tropospheric tracers . . . 97
5.2.3 Particle composition . . . 98
5.2.4 Effect on stratospheric water budget . . . 98
5.3 Discussion and summary . . . 102

6 Subvisible Cirrus at the West African Tropical Tropopause 105
6.1 Meteorological background . . . 105
6.1.1 Formation of SVC . . . 108
6.1.2 Dehydration potential . . . 110
6.2 Observations of SVC during SCOUT-AMMA . . . 111
6.2.1 Parameterisation of SVCs . . . 116
6.3 Discussion and summary . . . 117

7 Comparison of general observations from West African and Australian tropical clouds 121
7.1 Background . . . 121
7.1.1 Vertical cloud profiles . . . 121
7.2 Observations of the vertical cloud structure . . . 123
7.2.1 Microphysical parameters . . . 123
7.2.2 Profiles of the radiative properties . . . 125
7.2.3 Size distribution profiles . . . 126
7.3 Activation of aerosol to cloud ice particles . . . 130
7.3.1 Concurrent observations of aerosol and cloud particles . . . 131
7.4 Discussion and summary . . . 133

8 Overall summary and conclusions 137
8.1 Instrumental implementation . . . 137
8.2 Observations of TTL clouds . . . 137
8.3 Future work . . . 142

III Appendix 145

Particle Gallery 147

List of abbreviations 151

List of chemical species 155

List of symbols 156

List of constants 158

A Cloud particle data quality assessment 159
A.1 Applied corrections . . . 159
A.2 Statistics of CIP image corrections . . . 160
A.3 Combined size distributions of FSSP-100 and CIP . . . 160
A.4 Instrument performance and the removal of shattering artefacts . . . 161
A.4.1 General arguments . . . 161
A.4.2 CIP performance and shattering artefacts . . . 164
A.4.3 General treatment of FSSP-100 data: Application of the T-matrix method . . . 165
A.4.4 Removal of shattering artefacts . . . 166

B Experimental setup 169
B.1 Campaign flight overview . . . 171

C Database 173
C.1 MCS outflow . . . 174
C.2 Convective overshoots . . . 181

List of Publications 183

Conference Contributions **185**

Bibliography **187**

List of Figures

1.1 The Earth's energy budget . . . 2
1.2 Schematic of deep convection . . . 4
1.3 Freezing mechanisms of atmospheric ice particles . . . 5
1.4 Ice crystal habit diagram . . . 7
1.5 Tropospheric and stratospheric properties of the TTL . . . 9
1.6 Sketch of tropical cloud types . . . 10

2.1 Shadowing principle of OAPs . . . 16
2.2 Influence of effective array width on sample volume . . . 18
2.3 Influence of sizing method on particle size determination . . . 20
2.4 Examples of faulty CIP images . . . 23
2.5 Erosion function . . . 24
2.6 Multiple images . . . 26
2.7 Modelled diffraction images . . . 27
2.8 Poisson spot . . . 28
2.9 Symbol calibration particles in and out of focus . . . 28
2.10 Partial images . . . 30
2.11 Frequency distribution of interarrival times . . . 31
2.12 Shattered particles appear in one image . . . 32
2.13 Observation of Double Particles . . . 33
2.14 Data reduction scheme . . . 36
2.15 Spinning disc calibrator . . . 40
2.16 FSSP operating principle . . . 43
2.17 CIP and FSSP-100 on the Jungfraujoch mountain station . . . 45
2.18 The tandem measurement platform AIRTOSS . . . 46

3.1 The high altitude research aircraft M-55 Geophysica . . . 47
3.2 CIP and FSSP-100 mounted on the M-55 Geophysica . . . 49

4.1 Satellite image of two MCSs . . . 58
4.2 Schematic of a mature MCS squall line . . . 58
4.3 MCS lifetime . . . 60
4.4 Schematic of general flow configuration over West Africa in the monsoon season . . . 61
4.5 Schematic of MCSs in relation to AEW . . . 62
4.6 MSG IR satellite images during SCOUT-AMMA . . . 66
4.7 SCOUT-AMMA tracer profiles . . . 69
4.8 Section of time series of 7 Aug 2006 . . . 72

4.9 Size distributions from 7 Aug 2006 . . . 73
4.10 CIP images from MCS outflow on 7 Aug 2006 . . . 73
4.11 Section of time series on 16 Aug 2006 . . . 74
4.12 Size distributions from 16 Aug 2006 . . . 75
4.13 CIP images from 16 Aug 2006 . . . 76
4.14 Sections of time series of 11 Aug 2006 . . . 77
4.15 Size distributions from 11 Aug 2006 . . . 79
4.16 Section of time series on 8 Aug 2006 . . . 80
4.17 Size distributions from 8 Aug 2006 . . . 81
4.18 SCOUT-AMMA profiles of microphysical parameters . . . 82
4.19 Comparison of SCOUT-AMMA outflow size distributions . . . 83
4.20 Comparison of CIP outflow images . . . 84

5.1 Typical altitude profiles of tropospheric tracers . . . 88
5.2 Tiwi Islands . . . 89
5.3 Schematic of Hector Type B evolution . . . 90
5.4 Stratospheric water vapour observations as hint for hydration . . . 92
5.5 Golden Hector Day, the 30 Nov 2005 . . . 94
5.6 Stratospheric part of time series on 30 Nov 2005 . . . 95
5.7 Size distributions of overshoot events on 30 Nov 2005 . . . 99
5.8 Stratospheric residence times . . . 100

6.1 SVC occurrence frequency . . . 107
6.2 SVC size distributions from SCOUT-AMMA . . . 113
6.3 Frequency of number concentrations . . . 113
6.4 Time series of size distributions of the SVC encounters . . . 115
6.5 Summary of all SVC size distributions . . . 116
6.6 Exponential fit on SVC size distributions . . . 117

7.1 . . . 123
7.2 Potential temperature profiles of microphysical parameters . . . 124
7.3 Temperature profiles of microphysical parameters . . . 125
7.4 Profiles of MAS data . . . 126
7.5 Profiles of normalised size distributions . . . 128
7.6 Fitted size distributions and CEPEX parameterisations . . . 130
7.7 Activation ratio . . . 132

8.1 Comparison of the different cloud types . . . 140

A.1 Example of error bars for size distribution . . . 161
A.2 Influence of shattering on size distributions . . . 165
A.3 Small crystal concentration, large crystal mass correlations . . . 167
A.4 Spurious FSSP concentration . . . 168

C.1 SCOUT-AMMA MCS outflow ages . . . 174
C.2 Profiles through MCS outflow on 7 Aug 2006 . . . 175
C.3 Profiles through MCS outflow precursor on 8 Aug 2006 . . . 175
C.4 Profiles through MCS outflows on 11 Aug 2006 . . . 176
C.5 Profiles through MCS outflow on 16 Aug 2006 . . . 176

C.6 Time series of the measurement flight on 7 Aug 2006. 177
C.7 Time series of the measurement flight on 8 Aug 2006. 178
C.8 Time series of the measurement flight on 11 Aug 2006. 179
C.9 Time series of the measurement flight on 16 Aug 2006. 180
C.10 Time series of measurement flight on 29 Nov 2005 181
C.11 Time series of Golden Hector flight on 30 Nov 2005 182

List of Tables

2.1 Sizing methods for CIP particle images 19

3.1 Specifications of the M-55 Geophysica. 48

4.1 Trace gas lifetimes 64
4.2 Trace gas deviations in outflow 69
4.3 Summary of cloud parameters on 7 Aug 2006 73
4.4 Summary of cloud parameters on 16 Aug 2006 76
4.5 Summary of cloud parameters on 11 Aug 2006 78
4.6 Summary of cloud parameters on 8 Aug 2006 81
4.7 Summary of cloud parameters of the MCS outflow encounters 83

5.1 Meteorological and microphysical parameters of the overshoot events 96
5.2 IWC release in the stratosphere 101

6.1 Overview of former SVC in situ measurements 108
6.2 Summary of the SCOUT-AMMA SVC measurements 112

7.1 Parameters of fitted size distributions 129
7.2 Activation ratio fit parameters 132

8.1 Summary of the meteorological and mean microphysical parameters for the different TTL cloud types. 139

A.1 Applied corrections 159
A.2 Faulty image statistics 160

B.1 Geophysica instrumentation 169
B.2 CIP flights during SCOUT-O3 171
B.3 CIP flights during SCOUT-AMMA 171

Chapter 1

Introduction

Although only $0.001\,\%$ of the global abundance of water on our planet is present in the atmosphere, this portion of the global water cycle has a particular significance (Quante and Matthias, 2006). Water vapour is not only the most important greenhouse gas (Kiehl and Trenberth, 1997; Trenberth et al., 2005; Sussmann et al., 2009) but is also a key player in cloud formation. Clouds are by definition according to the World Meteorological Organisation (WMO) International Cloud Atlas a suspension of particles in the atmosphere consisting of minute water droplets and/or ice particles usually not touching the ground. Clouds may also include larger water or ice particles as well as non-aqueous liquid or solid particles (World Meteorological Organization, 1975). In the Earth's atmosphere clouds act as a reflecting shield for radiation. The effect of clouds on the Earth's energy budget can be comprehended from Figure 1.1: On the one hand clouds reflect solar radiation back to space and are thus cooling the atmosphere (see left hand side in Figure 1.1). On the other hand they also absorb and re-emit longwave radiation back to the earth surface and are thus warming the atmosphere (c.f. right hand side of Figure 1.1). By regulating incoming and outgoing radiation and releasing latent heat during their formation (depicted in the middle of Figure 1.1), clouds play a central role in the general circulation of the atmosphere (Dessler et al., 2006). Furthermore, the figure shows that the atmosphere itself absorbs (and emits) energy, i.e. by clouds, water vapour, oxygen, and other greenhouse gases as carbon dioxide and ozone (Kiehl and Trenberth, 1997). Whether the heating or cooling effect of clouds dominates is strongly dependent on the microphysical properties of the cloud. Different cloud particle states (liquid water or ice), shapes and sizes of the ice crystals or water droplets, and number concentrations influence the clouds' reflective behaviour. These microphysical variabilities and the variability in the cloud amount lead to high uncertainties in the determination of the radiative forcing of clouds, especially of ice clouds (cirrus[1], *Latin* for curl). In fact, clouds and their feedbacks are regarded as the biggest source of uncertainty in the prediction of future climate in reports by the Intergovernmental Panel on Climate Change (IPCC; Forster et al., 2007).

Clouds do not only have an impact on the Earth radiation budget but also on the atmospheric chemistry. Cloud particles, especially ice particles, provide a surface on which chemical substances can react. For example, heterogeneous reactions on the surfaces of polar stratospheric clouds (PSCs) activate chemical species leading to

[1] For a comprehensive overview of cirrus, see Lynch (2002).

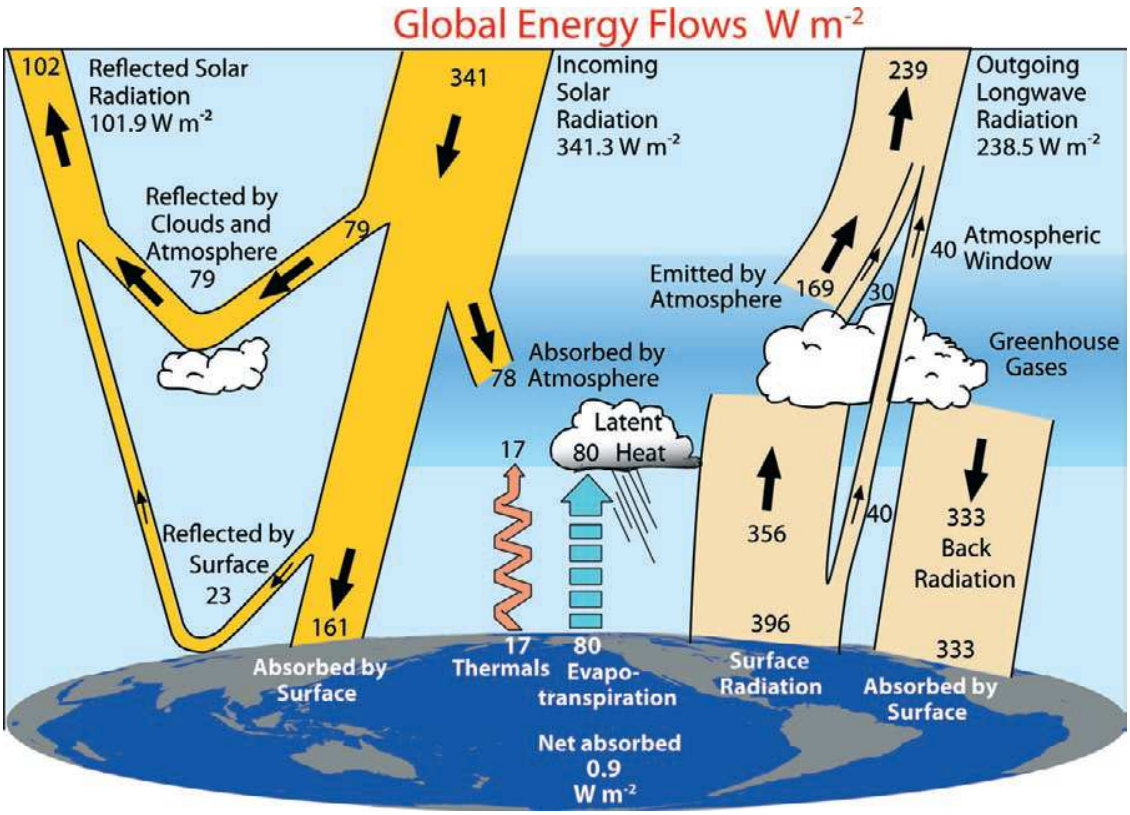

Figure 1.1: The global annual mean energy budget for the period between March 2000 to May 2004 in $\mathrm{W\,m^{-2}}$. The broad arrows indicate the schematic flow of energy in proportion to their importance. Taken from Trenberth et al. (2009).

ozone destruction (e.g. Peter, 1997; Schreiner et al., 2003; Voigt et al., 2005; Lowe and MacKenzie, 2008). Evidence for chlorine activation, which leads to ozone destruction, has also been found on cirrus in the midlatitudes and tropical tropopause regions (Borrmann et al., 1996; Solomon et al., 1997; von Hobe et al., 2011). For estimates of effectiveness of several chemical reactions in the atmosphere it is thus important to know the magnitude of surface provided by cloud particles. Furthermore, chemical substances and aerosol particles may deposit onto cloud particles such that they are removed from the atmosphere by washout and rainout. Thus, the water cycle and clouds contribute crucially to the selfcleansing of the atmosphere (Quante and Matthias, 2006).

Weather does not only affect the private life but has also a strong impact on industry and agriculture. Thus, an accurate prediction of clouds and their microphysical properties, as well as the amount of cloud coverage and precipitation, is important. However, in numerical weather prediction (NWP) as well as in global climate models (GCM), clouds are most often parameterised instead of being explicitly resolved. That means, that the effects of small-scale processes in clouds in all their variety are not represented directly by means of physical equations, but are represented by admittedly oversimplified parameters. As Randall et al. (2003) states, the cloud parameterisation problem is overwhelmingly complicated. Cloud parameterisation developers are struggling to identify the most important processes on the basis of woefully incomplete observations. Nevertheless, improved parameterisations will lead to a more accurate prediction of the clouds, as long as not enough computing power and speed are available.

1.1 Cloud formation

Many types of clouds exist, differing in appearance, altitude, extension, and microphysical properties. In addition, there are different ways of cloud formation (for a complete survey of cloud formation, refer to e.g. Rogers and Yau, 1989). For a cloud to form a large volume of air needs to be cooled below its dew point. This is the temperature at which saturation occurs when the air parcel is cooled at constant pressure and constant water vapour content. In the atmosphere the chilling is mostly achieved by lifting of air masses that expand approximately adiabatically. Other ways of chilling below the dew point can be caused by radiative cooling or isobaric mixing of two air masses with different temperatures and humidities. When the dew point is reached, i.e. the air mass is saturated, condensation becomes possible. In case of lifted air masses, the height where saturation is reached is called lifting condensation level (LCL). The lifting of air masses can be forced by orography (e.g. mountains) or by frontal zones. Furthermore, the lifting can be induced by surface heating that leads to convection, i.e. a thermally driven turbulent vertical mixing of the atmosphere. Convection may be confined to the boundary layer (lowest one or two kilometres of the atmosphere) which is referred to *shallow convection*. When the convection breaks through the temperature inversion that caps the boundary layer it often develops clouds that extend all the way to the tropopause. This type of *deep convection* is described in the following since measurements of deep convective clouds are presented in this thesis.

1.1.1 Deep convection

Due to the strong insolation in the tropics, surface heating is vigorous. Therefore, the surface temperature may increase to the convective temperature (CT) which is the temperature that an air parcel at the surface must reach in order to become unstable and start to rise on its dry adiabatic lapse rate. When reaching its convective condensation level (CCL) saturation occurs and cumuliform clouds form. Under well mixed boundary layer conditions CCL and LCL often agree closely with another (Rogers and Yau, 1989). In a thermodynamic diagram the CCL is the point of intersection of the sounding curve (temperature) and the saturation mixing ratio line which corresponds to the average mixing ratio in the surface layer. This is depicted in the schematic in Figure 1.2 with the temperature sounding in red and the saturation mixing ratio line in green. Dry and moist adiabat are shown in orange and brown, respectively. Above the CCL the air parcel will further ascend on its moist-adiabat. As long as the air parcel is warmer than its surrounding it will have a positive buoyancy and thus will keep ascending until it reaches its level of neutral buoyancy (LNB, also called equilibrium level EL) above which the air parcel will no longer be warmer than its environment. The strength of the buoyancy depends on the temperature difference between the air mass and its environment.

In the general picture, updraughts in deep convection cease at the LNB. However, depending on the strength of the updraughts air parcels may overshoot their LNB because of their mass inertia, forming convective overshoots, as depicted in Figure 1.2. Due to their colder temperature and higher density these air parcels are heavier than their surroundings above the LNB and thus they will sink back. Therefore, the LNB is an approximation of convective cloud top height, if overshooting is neglected.

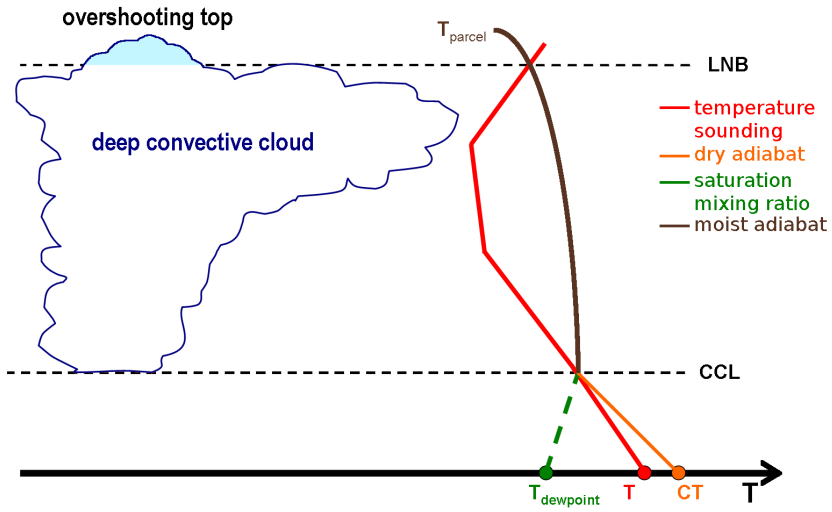

Figure 1.2: Schematic of overshooting deep convection. A hypothetical sounding is shown on the right hand side where convective condensation level (CCL) and level of neutral buoyancy (LNB) are indicated.

1.1.2 Cloud ice particles

Condensation of water vapour is the basic cloud formation process. However, to form cloud droplets not only sufficient water vapour is needed but also aerosol particles that act as condensation nuclei (CN). Without CN supersaturations of several hundred percent would be needed to form a cloud droplet (Rogers and Yau, 1989). Such conditions, however, are not reached in the atmosphere. In regions where temperatures are below the freezing point cloud droplets may remain liquid as supercooled droplets. Droplets smaller than $5\,\mu\mathrm{m}$ will freeze spontaneously at temperatures of about $-40\,^{\circ}\mathrm{C}$, larger droplets at slightly warmer temperatures (up to a few degrees). This spontaneous freezing is called homogeneous nucleation (see e.g. Rogers and Yau, 1989; Kärcher and Lohmann, 2002). Ice particle formation at higher temperatures can only be triggered by the presence of aerosol particles acting as ice nuclei (IN). This process is called heterogeneous ice nucleation and can happen in different ways, as depicted in Figure 1.3. In an environment supersaturated with respect to ice water vapour directly deposits onto an IN and, given sufficiently low temperatures, the vapour is deposited as ice in its lattice structure. This process is called *heterogeneous deposition* or *deposition nucleation*. Other heterogeneous freezing mechanisms involve water droplets. Condensation followed by freezing or *condensation freezing nucleation* requires an CN to first form a droplet. At sufficiently low temperatures the incorporated aerosol particle (the CN) acts as IN and initiates freezing. The process in which aerosol particles cause freezing after becoming embedded in a water droplet is named *immersion freezing*. When an IN collides with a supercooled droplet, the droplet freezes instantaneously, a process called *contact freezing nucleation*. Rosinski and Morgan (1991) have shown that after evaporation of a droplet the residual aerosol particle can become an IN. Under conditions, when the relative

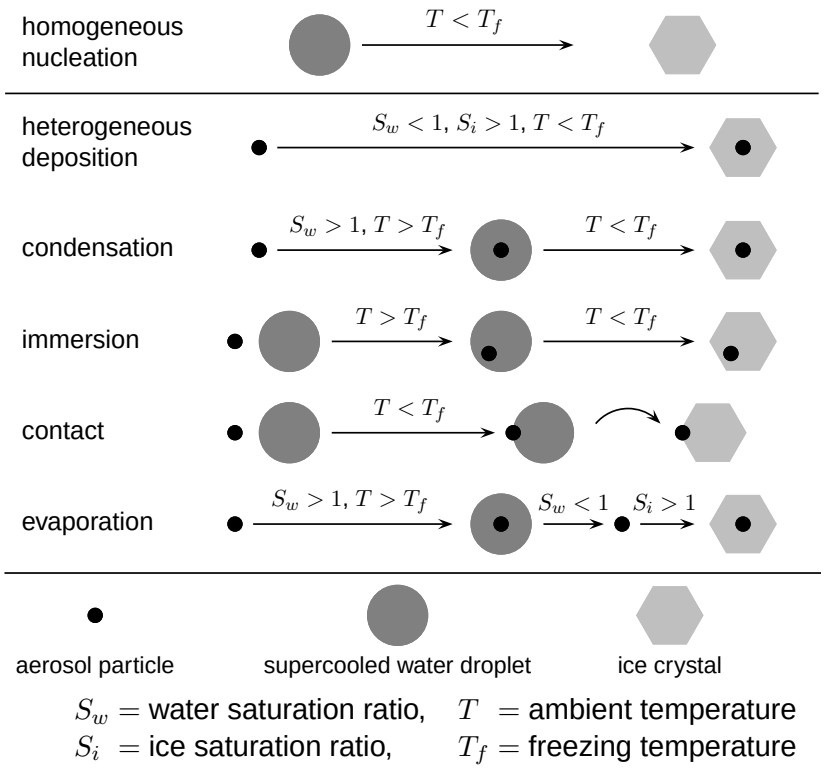

Figure 1.3: Freezing mechanisms of atmospheric ice particles. Processes which include an aerosol particle are called heterogeneous processes. See text for further information.

humidity with respect to water is below $100\,\%$ and with respect to ice still above $100\,\%$, ice crystals are formed instantaneously via deposition nucleation. The whole process is then named *evaporation freezing nucleation*. The freezing temperature depends on the aerosol particle's substance (e.g. type of mineral, organic material) and nucleation mode (Pitter and Pruppacher, 1973; von Blohn et al., 2005).
Once formed the ice particles may grow by diffusion and deposition of water vapour. In cloud conditions with concurrent subsaturation over water and saturation over ice supercooled liquid droplets evaporate and the water vapour deposits onto the ice crystals. This process is known as Wegener-Bergeron-Findeisen process (Wegener, 1911; Bergeron, 1935; Findeisen, 1938). However, the growth of ice crystals by diffusion of water vapour cannot explain the variety of crystal shapes. Further growth processes are the riming and aggregation of ice particles. The former is the growth process of ice particles by collision with supercooled droplets which subsequently freeze. Ice particles may also grow by collision with each other, referred to aggregation. Riming and aggregating particles may also grow simultaneously by deposition of water vapour. The effectiveness of the single growth mechanisms is dependent on the ambient conditions (e.g. temperature and relative humidity). More detailed descriptions of freezing mechanisms and cloud particle growth mechanisms can be found in e.g. Rogers and Yau (1989), Lynch (2002), and Pruppacher and Klett (2010). Due to the differing freezing and growth conditions of the ice particles a wide variety of ice particle habits can form, as can be seen in the Particle Gallery (see page 147 ff.) and Figure 1.4. The figure shows the ice particle shape as a function of temperature and supersaturation with respect to ice.

Surprisingly, vast discrepancies have sometimes been found between the observed ice crystal concentrations and the measured concentrations of IN, amounting up to a factor of 10^4 more ice particles (Mossop, 1985; Hobbs and Rangno, 1985). Processes leading to this discrepancy are called ice multiplication or secondary processes. One mechanism, which is thought to be very effective under certain conditions, is the Hallett-Mossop process (also called rime splintering; Hallett and Mossop, 1974). In the temperature range of $-3\,^{\circ}\mathrm{C}$ to $-8\,^{\circ}\mathrm{C}$ small ice splinters are produced as graupel grows by accretion (riming) of supercooled droplets. Further requirements are the availability of supercooled droplets larger than $24\,\mu\mathrm{m}$ and droplet impact velocities between $1.4\,\mathrm{m\,s^{-1}}$ and $3\,\mathrm{m\,s^{-1}}$ (see e.g. Pruppacher and Klett, 2010, for further information). The mechanical break up of ice crystals when two particles collide within clouds is a further mechanism for ice multiplication (Vardiman, 1978). The highest rate of secondary particle generation was found if heavily rimed plane dendrites and graupel collide. The relative velocity between the two colliding particles was found to be another important factor of secondary particle enhancement. When the Hallett-Mossop process is active, it dominates overall ice multiplication. However, if the process is inactive and large graupel is abundant, then the break up process dominates as shown recently by Yano and Phillips (2011). They state that the effectiveness of the break up mechanisms has been underestimated so far. A third process has been indicated by laboratory and theoretical studies (cf. Rangno and Hobbs, 2001, and references therein): a momentary burst of high supersaturation ($>10\,\%$) in the air surrounding a supercooled droplet in the moment of freezing may lead to enhanced primary ice nucleation. Rangno and Hobbs (2001) also discuss the possibility of shattering of isolated droplets when they are freezing, which is favoured by droplets larger than $50\,\mu\mathrm{m}$. However, Johnson and Hallett (1968) indicate that this mechanism appears unlikely under atmospheric conditions.
Depending on the shape the single-scattering properties of non-spherical ice crystals may differ substantially from those of spheres (e.g. Kinne and Liou, 1989; Takano and Liou, 1989; Kalesse, 2009). Thus, the particle shape is an important factor influencing the radiative behaviour of clouds (e.g. Macke and Francis, 1998; Wendisch et al., 2007). Nevertheless, in NWP models and GCMs cirrus clouds are often represented by a fixed shape (mostly hexagonal prisms or even as sphericals; Garrett et al., 2003; Edwards et al., 2007). Furthermore, vertical position (temperature), ice water content, and ice crystal size are important factors that influence the radiative properties of cirrus (Macke and Francis, 1998; Wendisch et al., 2007). In order to reduce the uncertainty in predicting climate change it is important to accurately represent the single-scattering properties of ice crystals in models as well as microphysical properties such as the size distribution (Baran, 2009). Thus, it is important to know the microphysical properties of the cirrus clouds and the shape of the ice crystals.

1.2 Tropical ice clouds

In the tropics, clouds are predominantly of convective nature and occur in a wide range of sizes, extending from small isolated cumuli to large cloud ensembles, so-called Mesoscale Convective Systems (MCS). Although the smaller cumuli and cumulonimbi greatly outnumber the cloud clusters, the MCS dominate the total cloud

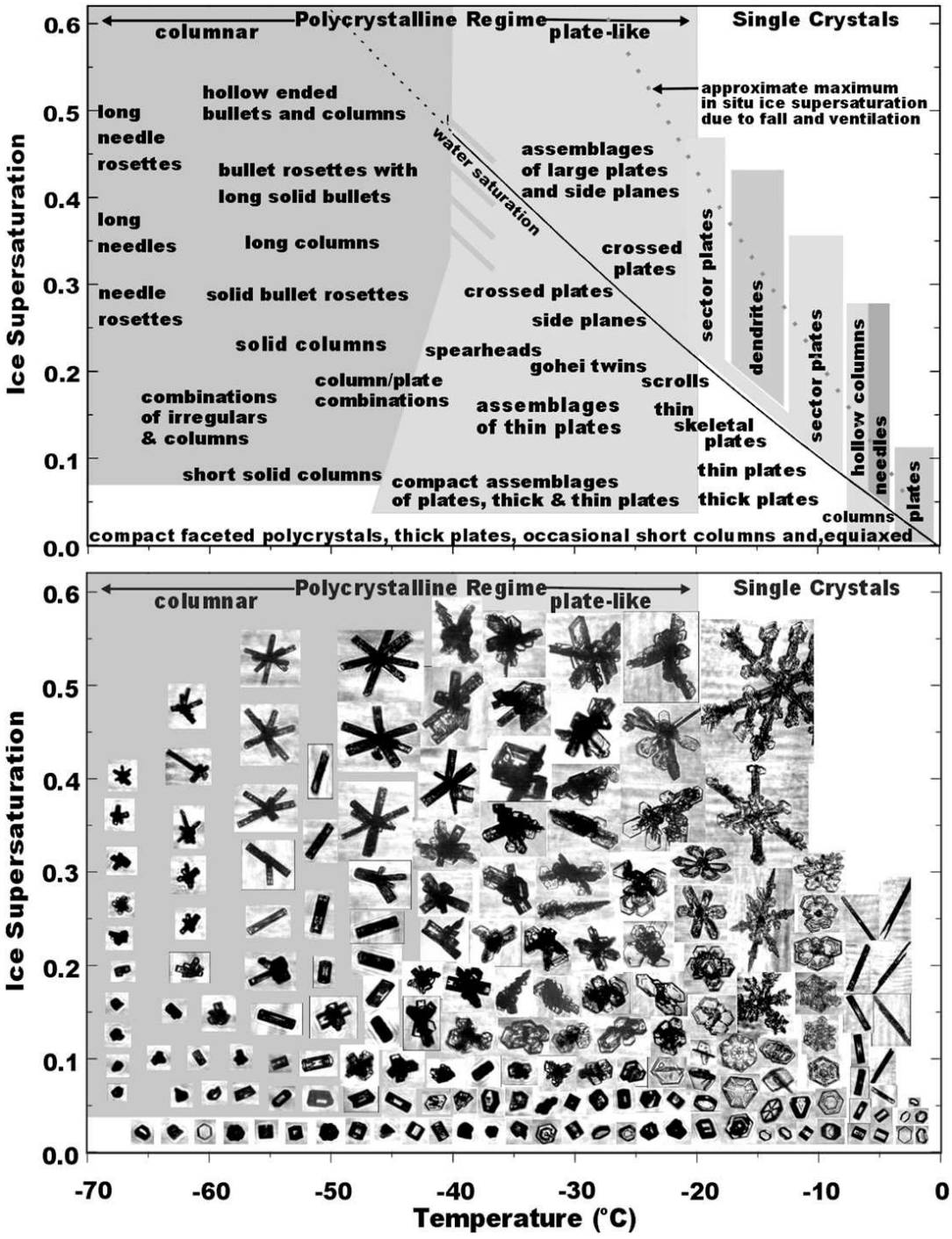

Figure 1.4: Habit diagram in text and pictorial format for atmospheric ice crystals derived from laboratory results by Bailey and Hallett (2004) and in situ images gathered in field studies. Diagonal bars near the middle of the upper diagram are drawn to suggest the possibility of the extension of the bullet rosette habit to temperatures slightly higher than $-40\,^{\circ}\mathrm{C}$. Taken from Bailey and Hallett (2009).

coverage and rainfall of the tropics (Hastenrath, 1991b). Tropical clouds are of particular interest since they may reach the high altitudes of the upper troposphere and lower stratosphere (UTLS) with consequently cold temperatures and are thus mostly ice clouds. Furthermore, the tropical cirrus have a high relative abundance covering $45\,\%$ of the Tropics (Stubenrauch et al., 2006). This large cirrus coverage is to a large part a result of anvils produced by deep convection in the intertropical convergence zone (ITCZ) and in tropical regions associated with monsoon convection (Mace et al., 2006). The tropical cirrus impose a substantial radiative effect on the Earth's climate system (Hartmann, 1993; Mace et al., 2006). As discussed above, the microphysical properties, e.g. ice crystal shapes and size distributions, are therefore important to know and sufficiently detailed knowledge can ultimately be gained by in situ measurements only.

1.2.1 Vertical structure of the tropical atmosphere

In order to assess the vertical extension of the tropical clouds, a brief description of the vertical structure of the atmosphere in the tropics is given in the following. The troposphere, the part of the atmosphere which contains almost all of the atmospheric water vapour (more than $99\,\%$; Quante and Matthias, 2006) and where most of the weather takes place, extends in the tropics from ground to about $17\,\mathrm{km}$, whereas in the midlatitudes it extends to about $10\,\mathrm{km}$ (Wallace and Hobbs, 2006). Generally, the temperature decreases with altitude within the troposphere at an average lapse rate (Γ) of $6.5\,\mathrm{K\,km^{-1}}$. The troposphere is topped by the tropopause which is characterised by a temperature inversion (i.e. increasing temperature with altitude). However, the tropopause can be defined in several ways, e.g. by temperature profile or lapse rate, ozone profile (sharp increase in ozone mixing ratios) or dynamically by the potential vorticity. Above the tropopause the stratosphere extends to about $50\,\mathrm{km}$. The different definitions of the tropopause may lead to different tropopause heights, indicating that the transition from troposphere to stratosphere occurs in a layer rather than at a sharp tropopause (Highwood and Hoskins, 1998; Folkins et al., 1999; Fueglistaler et al., 2009). In the tropics this "tropopause layer" may extend over several kilometres vertically. It combines tropospheric and stratospheric characteristics, as depicted in Figure 1.5, and is called the Tropical Tropopause Layer (TTL, or also Tropical Transition Layer). Furthermore, it is the dominant source region of air entering the stratosphere (Park et al., 2007). Slightly varying altitude definitions of the TTL exist, e.g. Fueglistaler et al. (2009) give a synthesis definition of the TTL integrating the radiative, dynamical, and chemical processes that lead to the three-dimensional structure of the TTL. With this they define the TTL above the level of main convective outflow from $14\,\mathrm{km}$ to $18.5\,\mathrm{km}$, corresponding to $355\,\mathrm{K}$ to $425\,\mathrm{K}$ potential temperature and a pressure altitude of $\sim$$150\,\mathrm{hPa}$ to $\sim$$70\,\mathrm{hPa}$, while Park et al. (2007) divides the TTL in the lower TTL and upper TTL. These are bound to $350\,\mathrm{K}$ to $360\,\mathrm{K}$ potential temperature or approximately $12\,\mathrm{km}$ to $14\,\mathrm{km}$, which is influenced by convective outflow as seen in CO_2 tracer data, and $360\,\mathrm{K}$ to $390\,\mathrm{K}$ potential temperature ($14\,\mathrm{km}$ to $18\,\mathrm{km}$), where CO_2 linearly declines. In both definitions, the level of zero radiative heating (LZRH) under clear-sky conditions is located within the lower part of the TTL. This is of importance since above this level air is subject to slow ascent due to radiative heating while below the air is descending, if not lifted convectively. The upwelling air

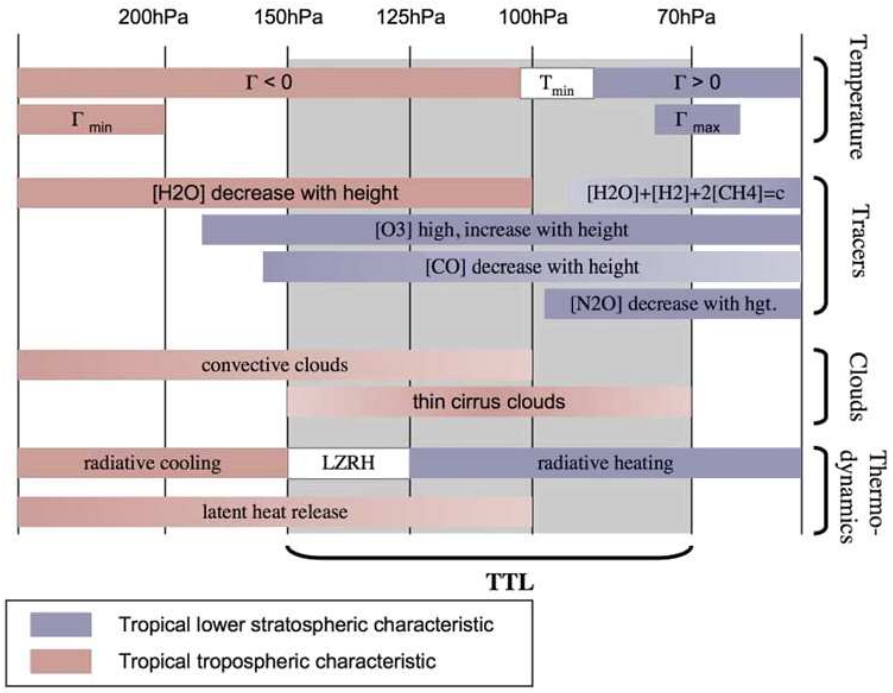

Figure 1.5: Summary of tropospheric and stratospheric properties as can be found in the TTL, figure adapted from Fueglistaler et al. (2009). The cold point tropopause is indicated by T_{min} and located at roughly $100\,\mathrm{hPa}$ ($\approx 17\,\mathrm{km}$). Further properties related to temperature and circulation are not shown.

may also transport fine and ultrafine aerosol particles (Brock et al., 1995) and by this, the aerosols in the upper troposphere and TTL most likely contribute significantly to the global stratospheric aerosol layer, or Junge layer. Furthermore, the cold point tropopause is located in the upper part of the TTL. Laterally, the TTL is bounded by the position of the underlying subtropical jets (i.e., equatorward of approximately $30°$ latitude). Due to its definition the TTL can be considered as a sub-volume of the UTLS region and as interface between the free troposphere and the stratospheric overworld. The dynamical and radiative characteristics of the TTL, which implicate roughly two month of residence time for the air parcels (Krüger et al., 2009; Ploeger et al., 2010), allow microphysical and chemical processes to affect tropospheric air entering the stratosphere to a great extent. A detailed review on the TTL is given by Fueglistaler et al. (2009).

1.2.2 Cloud particles within the UTLS

Deep convection provides a fast pathway to transport air between the boundary layer and the free troposphere, sometimes reaching into the TTL or even above. This is depicted in Figure 1.6. The solar insolation triggers convection and the formation of convective clouds over land. Over ocean the moisture fluxes (e.g. due to evaporation from the ocean's surface) and surface wind speeds, which enhance the ocean evaporation, play a more important role in excitation of convection than the sensible heat. The deep convective clouds produce large shields of anvil cirrus in their outflows in the lower TTL region. Very strong updraughts may produce convective overshoots into the TTL which sometimes even reach the stratosphere (e.g. Adler and Mack,

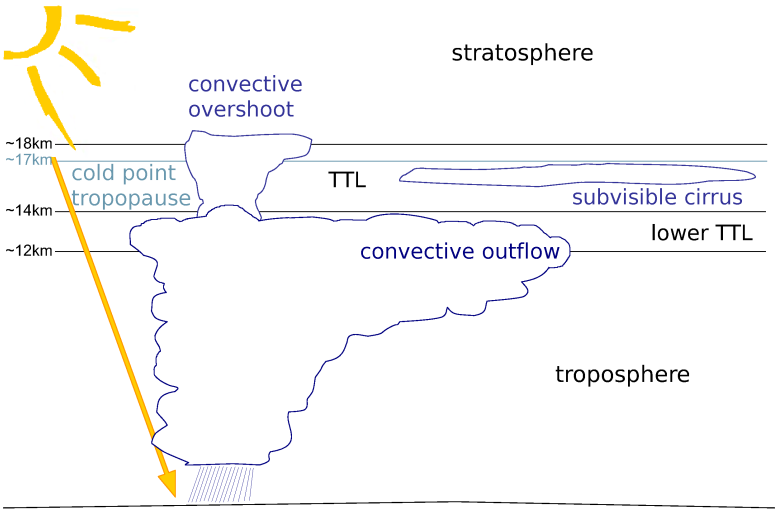

Figure 1.6: Sketch of tropical clouds: Deep convective clouds with a large vertical extension building convective outflows and overshooting convection, widespread layers of thin subvisible cirrus in the TTL.

1986; de Reus et al., 2009). In addition to the convectively formed (visible) cirrus, also large sheets of subvisible cirrus close to the tropopause are present, which either are formed in situ or as remnants of deep convection (e.g. Pfister et al., 2001). The microphysical properties of these cloud types differ substantially, as shown in this work, and thus have a different impact on the radiative budget of the atmosphere (Comstock et al., 2002). The clouds in the TTL have in common that they may affect the troposphere to stratosphere exchange, especially having an impact on the water vapour budget (Rosenfield et al., 1998). Due to freeze drying in the TTL cirrus water vapour is removed effectively from the upwelling air before entering the stratosphere.

1.3 Motivation and outline

The introduction outlined the important role of tropical (high altitude) ice clouds for the Earth's climate. The scientific understanding of ice clouds, as introduced by the IPCC, is low. For example, the cloud albedo effect on radiative forcing has large uncertainties (Forster et al., 2007). Several studies using vastly different methodologies (modelling, theoretical, and observational studies) point out that there is a lack of experimental data (e.g. Hartmann, 1993). Mace et al. (2006) emphasise

> Because they exert such a significant control on the energy budget of the atmosphere, tropical cirrus clouds represent an important yet poorly documented component of the global climate system.

Measurements shall give a description of the atmospheric conditions, help validating remote sensing measurements (such as radar and lidar) and models. Furthermore, measurements shall provide the basis for more accurate parameterisations for models because the representation of tropical ice clouds in numerical models is poor (Randall et al., 2003). In situ measurements in TTL clouds are rare because of the high altitude of these clouds, which can only be reached by specialised high altitude

research aircraft. Therefore, this work aims at filling the gap of experimental data and therewith at contributing important information about the microphysical properties of the clouds within the tropical UTLS. Additionally, shape information are obtained from two dimensional shadow images of the ice particles. Furthermore, mathematical fits are established which may help to improve numerical models, leading to a better predictability of clouds and their impact on our climate. In the first part of this thesis the cloud particle instrumentation and data treatment (Chapter 2), as well as the aircraft, further instrumentation, and the campaigns during which measurements have been performed (Chapter 3) are described. In the second part measurements of the tropical UTLS clouds are presented. Chapter 4 discusses the clouds in outflows of mesoscale deep convective systems, while Chapter 5 deals with convective overshooting clouds, even penetrating the stratosphere. In Chapter 6 measurements of subvisible cirrus clouds are presented. Since those cloud types show different microphysical characteristics, all measurements are compared in Chapter 7 before the conclusions and an outlook are given in Chapter 8.

Part I

Methodology

Chapter 2

Description of the in situ cloud particle instrument and data processing

Several instruments exist for airborne in situ measurements of cloud particles and their microphysical properties. Generally, more than one airborne cloud particle probe is needed in order to be capable of obtaining in situ measurements over the full range of cloud particle sizes due to the limited size ranges of the probes. Thus, combinations of those instruments are often used, also combining different measurement techniques. Nevertheless, the focus of this chapter is laid on the description of the Cloud Imaging Probe (CIP) which is the basic instrument of this thesis. Furthermore, the data processing of CIP data including derivation of the cloud microphysical parameters, sources of errors and subsequent correction mechanisms are be described in detail. The measurements of the CIP which are discussed in Part II of this thesis present the first deployment of a CIP in the TTL.

2.1 Cloud Imaging Probe

Optical Array Probes (OAPs) as introduced by Knollenberg (1970) have been used in the past decades to measure cloud and precipitation particles in situ. In the course of this time the probes have been refined in their electronics and optics. For example, the first probes were able to only capture one-dimensional (1D) shadow cast particle images, whereas now two-dimensional (2D) images can be obtained. One of the recent refinements, provided with faster electronics, is the Cloud Imaging Probe (CIP), manufactured by Droplet Measurement Technologies (DMT), Boulder, USA. Figure 2.1 shows the operating principle of OAPs/CIP. A collimated laser beam is focused on a linear diode array. Anytime a particle crosses the laser beam a shadow is cast on the diode array which will trigger the recording of the particle image. The shadowing response of the diodes is set to $50\,\%$ of the full laser illumination, i.e. when the intensity of the laser light is decreased to $50\,\%$ or less a diode will report to be shadowed. Any diode that is shadowed will initiate the recording of the whole diode array which reports for every diode whether it is shadowed or not. Such a record is called a slice. Up to 128 slices compose a particle image. Consecutive slices will be

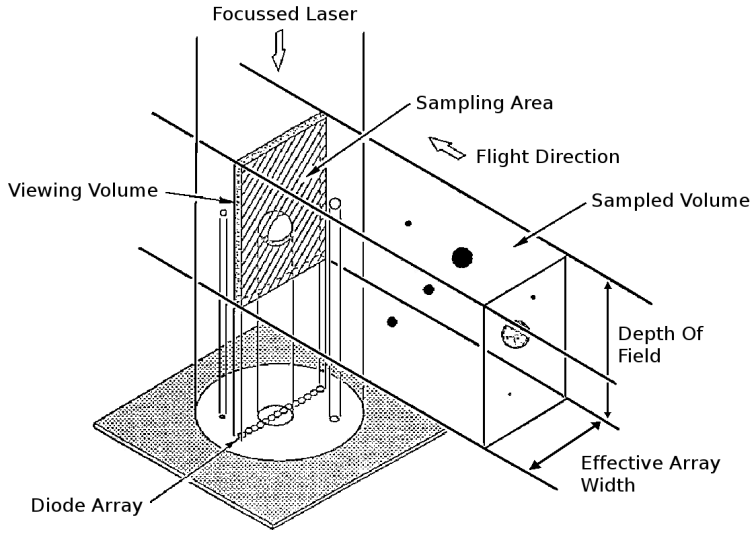

Figure 2.1: The shadowing principle of OAPs and some important dimensions (see Section 2.2 for explanation) for the cloud particle measurements are indicated, adapted from Baumgardner and Korolev (1997).

captured either at a clock rate that is associated with the true air speed (TAS) or at a fixed TAS, set in the data acquisition program. The TAS is measured by a pitot tube which is included in the instrumental package of the CIP, an improvement to older OAP versions. Thus, the TAS measured by the pitot tube will be referred to as probe TAS to avoid confusion with the aircraft TAS. It is important to note that the probe TAS differs from the TAS of the aircraft, due to a deceleration of the air at the instrument body by $13\,\%$ (D. Baumgardner, personal communication, 2010). Therefore, it is important to use the probe TAS for achieving the correct slice rate. The sampling frequency f can now be calculated with

$$f = v/res \tag{2.1}$$

with v the velocity of particles that cross the laser beam (which in the horizontal is equal to the probe TAS), and res the resolution of the diodes. The maximum slice rate is achieved at a probe TAS of $200\,\mathrm{m\,s^{-1}}$ and is $8\,\mathrm{MHz}$. The resolution of the CIP diodes is $25\,\mu\mathrm{m}$, i.e. any diode will create a pixel in the particle image that corresponds to $25\,\mu\mathrm{m}\times25\,\mu\mathrm{m}$. The recording stops when no diode is occulted for two TAS time periods. Every particle image will be assigned with a header and the data will be stored in a compressed format by the DAQFactory software[2]. The header yields e.g. encoding information but also information about the exact time when the particle was measured. Whenever the compressed data fills a 4096-byte buffer the image data is transmitted to the host computer where the information is stored to disc. For image display the Image Playback uncompresses the data and displays the particle images. Image stripes that show a set of consecutive images are then displayed by the Image Playback with a discontinuous timeline, i.e. times at which no particles are recorded are not displayed.

[2]The DAQFactory software has been delivered from DMT. In 2007 the software has been exchanged with the Particle Analysis and Display System (PADS) software package which provides an improved user interface and also a particle Image Playback program.

Besides the pitot tube for airspeed measurements the CIP also holds a King probe, i.e. a hotwire Liquid Water Content (LWC) sensor, and a temperature sensor for the ambient temperature.

2.2 Calculation of Sample Volume

Some cloud particle parameters are specified per volume of air, e.g. number or mass concentrations. In order to derive these parameters it is necessary to know the exact sample volume (SV) of the probe, i.e. the volume of air that travels through the sensitive area, called sample area (SA), of the laser beam during the sample time (t_s):

$$SV = SA \cdot TAS \cdot t_s \ , \tag{2.2}$$

with the sample area in mm^2, TAS in $\mathrm{m\,s}^{-1}$, and sample time in s resulting in a sample volume in cm^3. The sample area in turn is defined through the effective array width w_{eff} and the depth of field (DOF)

$$SA = DOF \cdot w_{eff} \ , \tag{2.3}$$

The effective array width varies with particle diameter as will be discussed below and is located perpendicular to the laser beam, along the diode array, as depicted in Figure 2.1. The depth of field is the sampling interval along the laser beam, stretching from the centre of focus to the probe arm tips on both sides. The object plane (= point of true focus) is usually located in the middle between the probe tips. Any particle passing the laser beam through the object plane casts a sharp, in-focus shadow on the diode array. Particles passing through the laser beam a further distance from this point cast a somewhat blurred shadow on the diode array. Diffraction effects cause the particle shadow to decrease in intensity and increase in size. This phenomenon is described in more detail in Section 2.4.4. Knollenberg (1970) first described the DOF of OAPs as the distance from the object plane that would result in a certain loss of shadow intensity. For a threshold level of $50\,\%$ the accuracy of the size measurements was found to be within $\pm 10\,\%$. Thus, Knollenberg (1970) defined the DOF as

$$DOF = \pm\, 7.5 \times 10^{-5} D_p^2 \,/\, \lambda \ < \ 10\, cm \ , \tag{2.4}$$

with DOF in cm, and particle diameter D_p and laser wavelength λ in $\mu\mathrm{m}$, where λ = $0.68\,\mu\mathrm{m}$ for the CIP. Note that if not specified explicitly, all particle sizes in this thesis are given in terms of their diameter. The distance between the probe arms imposes a mechanical limitation so that a maximum DOF of $10\,\mathrm{cm}$ can be obtained. This DOF is achieved by any particle with a diameter larger than roughly $213\,\mu\mathrm{m}$.
The effective array width can be determined in different ways depending on which data processing technique is used. When only particles are considered, that are entirely within the sampling volume, i.e. not touching either of the end diodes, this technique is referred to the all-in method. Here, the effective array width varies as

$$w_{eff} = [res(num - 1) - D_p] = (25\,\mu m \cdot 63 - D_p) \tag{2.5}$$

with the effective array width in $\mu\mathrm{m}$ and res the probe resolution, num the number of diodes.

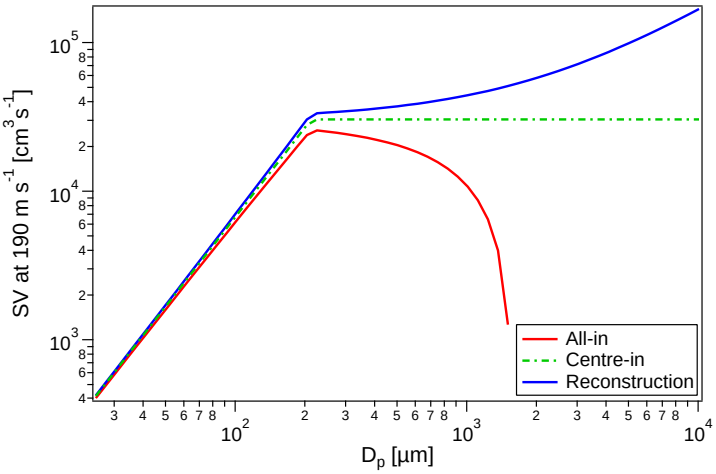

Figure 2.2: Sample volume calculated using the different methods for deriving the effective array width for a TAS of $190\,\mathrm{m\,s^{-1}}$ (which is typical for the aircraft used in the following data analysis).

If the centre of quasi-spherical particles that obscure one or both end diodes is located within the array, the centre-in technique can be used. Here, the effective array width varies as

$$w_{eff} = res \cdot num = 25\,\mu m \cdot 64\ . \tag{2.6}$$

However, particles that obscure one or both end diodes can be reconstructed in size, as discussed in Section 2.4.6. The reconstruction procedure is described in Heymsfield and Parrish (1978). When reconstruction is used, the effective array width ($w_{eff}^{'}$), computed as the maximum distance between the centres of equal-diameter particles that are reconstructed according to Heymsfield and Parrish (1978), increases and is found to be:

$$w_{eff}^{'} = w_{eff} + 2\left(\frac{D_p}{2} - \frac{4\,D_p}{29}\right) = w_{eff} + 0.724\,D_p\ . \tag{2.7}$$

The effect of the different calculation methods for the effective array width is shown in Figure 2.2. There are just slight differences for particles smaller than about $220\,\mu\mathrm{m}$ (roughly $10\,\%$ difference for $100\,\mu\mathrm{m}$ particles). For larger particles the sample volume is clearly affected by the method of determining the effective array width.

2.3 Cloud particle parameters

2.3.1 Sizing methods

Determining the size of a particle measured by the CIP is not always definite. As Table 2.1 shows even a two pixel image can be sized differently depending on the method used. A simple sizing approach is to take the x dimension (maximum number of occulted pixels in a slice) or y dimension (number of slices) of the particle as the diameter. The area equivalent diameter, the so-called minimum dimension, is determined by fitting the pixel area into a circle and calculate the diameter of this circle. The approach that leads to the biggest size is the maximum dimension (also called projected length, see Heymsfield et al., 2002) which can be sketched as the

Table 2.1: Sizing methods for CIP particle images. The application on a two pixel image is demonstrated.

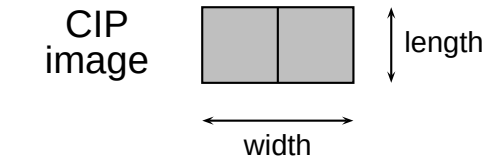

width = $50\,\mu\mathrm{m}$
length = $25\,\mu\mathrm{m}$
area = $50\,\mu\mathrm{m} \cdot 25\,\mu\mathrm{m} = 1250\,\mu\mathrm{m}^2$

	Sizing method	Diameter
	x dimension	$D_p = 50\,\mu\mathrm{m}$
	y dimension	$D_p = 25\,\mu\mathrm{m}$
	maximum dimension	$D_p = \sqrt{\mathrm{length}^2 + \mathrm{width}^2} = 55.9\,\mu\mathrm{m}$
	minimum dimension	$D_p = 2 \cdot \sqrt{\mathrm{area}/\pi} = 39.9\,\mu\mathrm{m}$

minimum circle that includes the whole image (= maximum chord length). The effect of the different sizing methods on e.g. the size distributions is shown in Figure 2.3. Here, data of a flight through summertime stratocumulus clouds on the 21 July 2007 is displayed[3]. For this example three periods with different cloud particle habits were chosen. For particles with spherical shapes, like water droplets, the different sizing methods yield similar results. For a perfectly spherical particle the x and y dimension yield the same diameter and the minimum dimension yields a diameter close to that value. Only the maximum dimension will yield a larger diameter. Also for graupel, which still have quasi-spherical shapes, the results of the sizing methods, except for the maximum dimension, agree reasonably well. For irregular shapes like needles, the differences are striking. In all cases, the maximum dimension leads to smaller values in the small particle size bins, while values are higher for particles sizes larger than a few hundreds $\mu\mathrm{m}$ compared to the other sizing methods.

[3]This flight was part of the Observation Methodologies of the first indirect Aerosol effect in water Clouds (OMAC) campaign (2007, Southern Germany) where the CIP was mounted to the wing of a Partenavia aircraft.

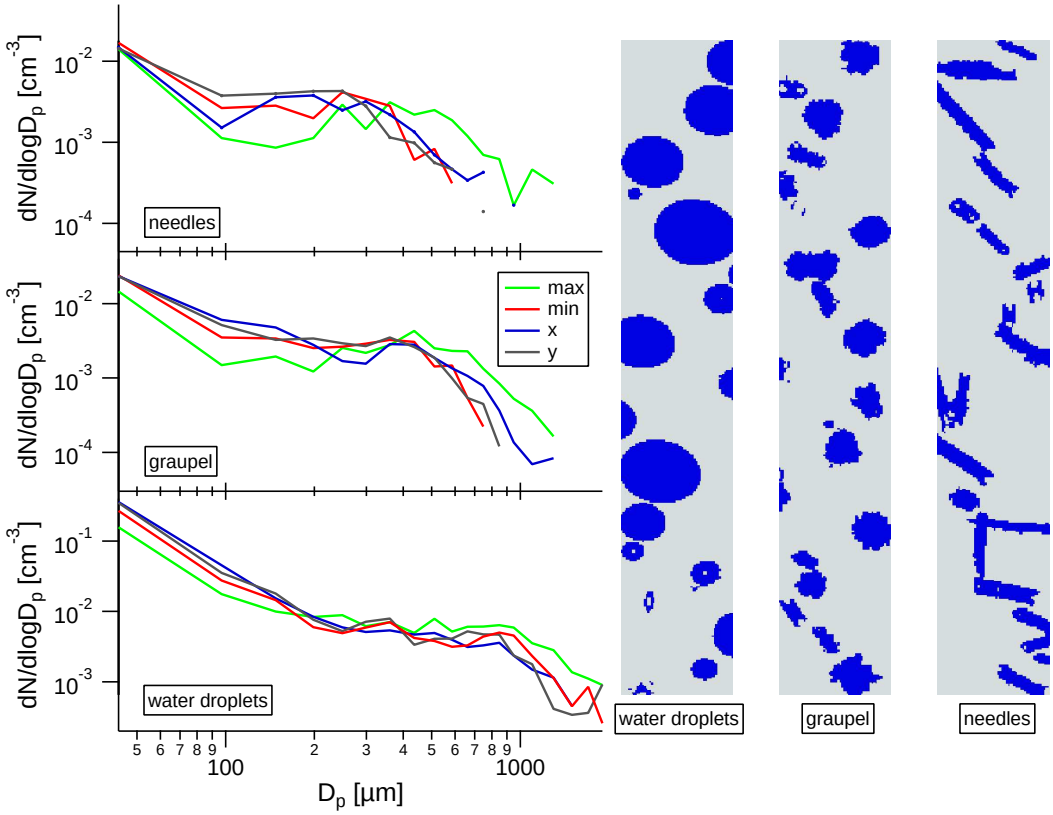

Figure 2.3: Size distributions for different particle shapes (examples of CIP image stripes shown on the right hand side) calculated with the four different sizing methods: maximum dimension (max), minimum dimension (min), x dimension (x), and y dimension (y). Note, the slight deformation of the water droplets is a result of wrong probe TAS measurement (c.f. Section 2.4.2). A correction for the sizing has been performed.

2.3.2 Single particle parameters

By assuming that all particles are spherical, surface area A, volume V, and mass m of the particles can be easily calculated:

$$A = 4\pi r_p^2 = \pi D_p^2 \tag{2.8}$$

$$V = \frac{4}{3}\pi r_p^3 = \frac{1}{6}\pi D_p^3 \tag{2.9}$$

$$m = \rho V = \frac{1}{6}\pi \rho D_p^3 \tag{2.10}$$

with r_p the particle radius and ρ the density of water or ice, respectively.

2.3.3 Combined particle parameters

Mean particle diameters

The mean diameter of the particles can be calculated in different ways depending on which parameter was chosen for weighting. The number weighted mean diameter is

calculated as follows:

$$\overline{D_{pN}} = \frac{1}{n}\sum_{i=1}^{n} D_{p_i}, \tag{2.11}$$

with n the number of cloud particles with the respective diameter D_{p_i}. Even if the number of larger particles is small their contribution to the total mass can be high. Thus, the mass weighted mean diameter $\overline{D_{pM}}$ is calculated:

$$\overline{D_{pM}} = \frac{\sum_{i=1}^{n} m_i\, D_{p_i}}{\sum_{i=1}^{n} m_i} = \frac{\sum_{i=1}^{n} \frac{1}{6}\pi\rho D_{p_i}^3\, D_{p_i}}{\sum_{i=1}^{n} \frac{1}{6}\pi\rho D_{p_i}^3} = \frac{\sum_{i=1}^{n} D_{p_i}^4}{\sum_{i=1}^{n} D_{p_i}^3}, \tag{2.12}$$

with m_i the mass of D_{p_i}.

Number concentration

The number concentration N is the number of particles per unit volume of air. For calculation of concentrations the sample volume is needed. Since the sample volume changes with size, concentrations are determined for several size bins before added to a total concentration:

$$N = \sum_{j=1}^{k} \frac{n_j}{SV_j} = \sum_{j=1}^{k} N_j, \tag{2.13}$$

with k the number of size bins, n_j the number of particles in size bin j, SV_j the sample volume in size bin j, and N_j the number concentration in size bin j. Further concentrations can be calculated similar to (2.13) by replacing the number of particles per size bin with the respective parameter, e.g. surface or volume per size bin for surface or volume concentration.

Size Distribution

Cloud particle sizes may cover a wide range of sizes (over three orders of magnitude). In order to see how the particles are distributed among these sizes, size distributions are employed and particles are grouped into bins according to their size. That means, the number concentrations for every size bin divided by the width of the size bin are plotted as histograms. The normalisation for the bin width is done because the height of any bin is dependent on the width of the bin. Thus, the distortion of the size distribution is removed. Since particles exist in a wide size range, the particle diameters are displayed on a logarithmic scale and therefore, the size bin width is normalised with the logarithm of the bin width.

$$(dN/d\log D_p)_j = \frac{n_j}{SV_j\left(\log\frac{D_{p_{j\_up}}}{D_0} - \log\frac{D_{p_{j\_low}}}{D_0}\right)} = N_j\left(\log\frac{D_{p_{j\_up}}}{D_{p_{j\_low}}}\right)^{-1} \tag{2.14}$$

with $D_{p_{j\_up}}$ and $D_{p_{j\_low}}$ being the upper and lower size limit of size bin j and $D_0 = 1\mu m$ is needed to eliminate the unit. In order to avoid large errors due to counting statistics it is necessary to average the size distribution over an adequate time period. The size bins for the CIP, as chosen in this thesis, have the following limits: 25, 75, 125, 175, 225, 275, 325, 400, 475, 550, 625, 700, 800, 900, 1000, 1200, 1400, 1600, 1800, and $2000\,\mu$m.

Liquid Water Content

The Liquid Water Content (LWC) or Ice Water Content (IWC) for spherical particles can also be calculated in the same manner as (2.13) by taking the particle masses instead of numbers. However, for non-spherical ice particles this equation is not valid since for mass calculation the assumption of spherical particles has been made. Several studies have been performed to derive a relationship between particle mass and some other particle parameters, mostly the (maximum dimension) diameter (e.g. Mitchell et al., 1990; Brown and Francis, 1995; Heymsfield et al., 2002; Baker and Lawson, 2006). These relationships have the form of

$$m = \alpha X^{\beta} \tag{2.15}$$

with X the chosen particle parameter (e.g. diameter), and the constants α and β which are determined from linear regression on particle image and mass pairs. Baker and Lawson (2006) found that when using one single parameter, the projected area $X = A_{proj}$ yielded the best results and reduced the root mean square (rms) error in the mass by nearly $50\,\%$. They determined the constants $\alpha = 0.115$ and $\beta = 1.218$ from linear regression on a population of particle image and mass pairs. Lawson and Baker (2006) applied this relationship to a data set and compared the results to former power law relationships. They showed major improvements. One additional main advantage is that their relationship is independent of particle habit.

Effective radius

The radiative properties of clouds are governed by the cloud particle properties and can be described with the effective radius r_{eff} of the cloud. The effective radius represents the mean radius for scattering of a cloud. It is proportional to the ratio of Condensed Water Content (CWC=IWC+LWC) to the extinction coefficient β_{ext} (Heymsfield et al., 2006), which describes the attenuation of light. Several definitions are available, depending on particle phase (liquid or solid) or crystal shape. A bunch of these are summarised and compared in McFarquhar and Heymsfield (1998). Most definitions rely on the ratio of the third to the second moment of a size distribution. In this work the definition by McFarquhar and Heymsfield (1996) is used in terms of spheres of equivalent cross-sectional area for any cloud particle shape:

$$r_{eff} = \frac{\int_0^{\infty} N(r_a) r_a^3 \, dr_a}{\int_0^{\infty} N(r_a) r_a^2 \, dr_a}, \tag{2.16}$$

where N is the number concentration and r_a the radius of a sphere of equivalent cross-sectional area. For liquid water clouds, r_{eff} can also be written in terms of LWC and the geometric cross-sectional area of water drops per unit volume G (which is the projected area) as

$$r_{eff} = \frac{3LWC}{4G\rho_w}, \tag{2.17}$$

with ρ_w the density of water.
A thick cloud that contains large particles will have a much larger effective radius than a thin cloud, consisting of small particles.

2.4 Data evaluation and correction mechanisms

Careful treatment is required during data analysis of the CIP images. Data has to be checked for several sources of faulty images. After identification of those images these can either be corrected or need to be rejected depending on the nature of the fault. An automated evaluation of the particle images is necessary since during a typical flight through clouds several thousands of particle images are recorded. For example, roughly $160\,000$ particles were detected within ten minutes during ascent through an MCS anvil[4]. Thus, evaluation software (see Section 2.5) needs to be capable of identifying and correcting or rejecting faulty images. However, to ensure the best setting of correction and rejection mechanisms the images of a flight need to be inspected closely. First of all, a visual inspection of the particle images should be performed in order to assess the nature of the particle habits. Significant community efforts are put into the algorithm development and software implementation of those algorithms to enhance data quality. In this section the different correction and rejection mechanisms for faulty images are described. Figure 2.4 shows image stripes that contain such faulty images.

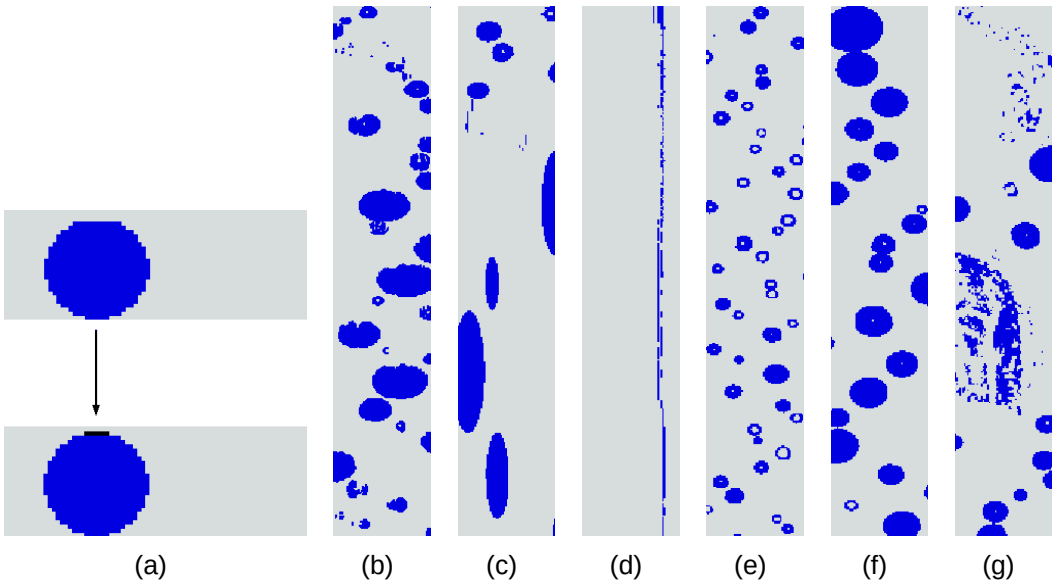

Figure 2.4: Examples of images that need correction: (a) Reconstruction of the first slice; (b) Deformed particles due to systematic wrong probe TAS; (c) Stretched particles due to momentary faulty probe TAS measurement; (d) Streaker caused by electronics; (e) Poisson spots of out-of-focus particles; (f) Partial images touching end diodes; (g) Shattering obvious in splashed like images.

2.4.1 Reconstruction of first slice

The recording of image data starts when at least one diode reports to be shadowed. This discontinuous recording of data leads to a loss of the first slice of an image in the older processor board versions of the CIP. In case of the CIP of Mainz University this means, any data acquired before the year 2010 consist of images that lose the first

[4]Data and analysis of this cloud crossing are presented in Chapter 4, Section 4.2.4.

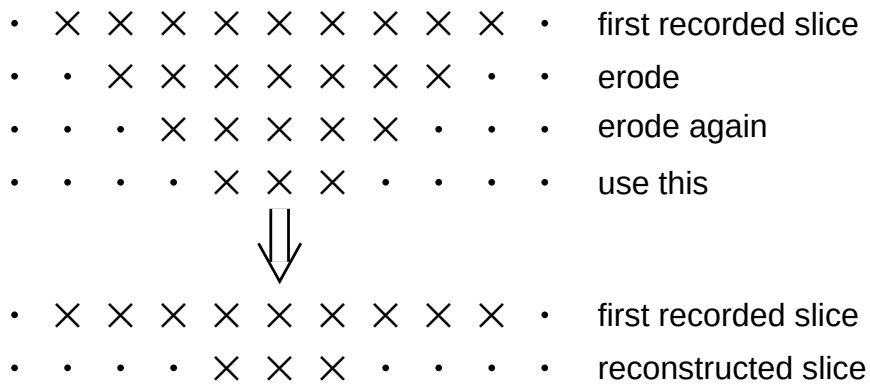

Figure 2.5: Schematical explanation of the erosion function which reconstructs the lost first slice. Shaded pixels are denoted with an X, unshaded pixels with a dot. For further explanation see the text.

slice. Thus, this first slice needs to be reconstructed. An example for such a reconstruction is shown in Figure 2.4(a). Depending on the number of shadowed pixels in the first recorded slice, the number of pixels for the reconstructed slice is calculated. For this an erosion function is used. It duplicates the first recorded slice, removes one pixel from each edge of the slice and repeats this until at least half of the pixels are gone, as illustrated in Figure 2.5. The resulting slice is then added to the particle image. This way of eroding at least half of the pixels leads to the most realistic reconstruction of spherical or quasi-spherical particle images. For non-spherical particles, e.g. needles, this reconstruction would probably not rebuild the real particle image realistically. In this case a blind repeat can be used as reconstruction of the first slice, i.e. the first recorded slice is added to the particle image instead of the eroded slice. The image width is increased by one pixel when using the reconstruction. In case of spherical or quasi-spherical particles the length of the particle image is not determined by the lost first slice. Thus, the reconstruction does not imply a source of error for the calculation of the maximum dimension diameter. For some irregularly shaped ice crystals the length of the particle image might be increased by the first lost slice. In such cases, the calculated maximum dimension undersizes the particle. Presumably, this would mostly affect needle images. The resulting sizing error is larger for smaller particles. For example, if a three times one pixel image is recorded and the lost slice is reconstructed as one pixel slice while the original slice would add a fourth pixel to the image length, the resulting diameters are $90\,\mu\mathrm{m}$ and $112\,\mu\mathrm{m}$, respectively. This leads to an error of roughly $20\,\%$. In case of a three times twenty pixel image, where a ten pixel slice is added instead of a slice which would increase the length to 21 pixels, the error is roughly $5\,\%$. It becomes clear that the knowledge of the particle habit is important in order to estimate the sizing errors. However, as long as the lost first slice would not increase the particle image length no sizing error is added to the maximum dimension.

2.4.2 Probe TAS related deformation of particles

In case of a miscalibrated pitot tube the probe TAS and the real probe TAS differ systematically. This affects the CIP sample rate which will be either too low or too high,

resulting in compressed or stretched images. That means the sizing of the image pixels in y direction is wrong, the real dimension would be greater or less than $25\,\mu\mathrm{m}$, respectively. To check the correct y dimension of the image pixels the aircraft TAS and the probe TAS can be compared. However, the deceleration of the air by about $13\,\%$ at the measurement point needs to be considered. Thus, the y dimension of the image pixels can simply be corrected by multiplying with the quotient of (aircraft TAS – $13\,\%$)/(probe TAS). Since a wrong calibration of the pitot tube affects all particle measurements the correction has to be applied to all images. Compressed particle images due to underestimated probe TAS are illustrated in Figure 2.4(b). Another source of error for the probe TAS measurement can be found in an erroneous temperature measurement because the ambient temperature is needed for TAS calculation as the following equation shows:

$$TAS_{probe} = Ma\sqrt{T_a\,\gamma\,R}, \tag{2.18}$$

with Ma the Mach number, T_a the ambient temperature, $\gamma = 1.403\,509$, the ratio of specific heat capacity for dry air at a constant pressure ($c_p = 1005.6\,\mathrm{J\,kg^{-1}K^{-1}}$) to specific heat for dry air at constant volume ($c_v = 716.49\,\mathrm{J\,kg^{-1}K^{-1}}$), and the gas constant for dry air $R = 287.058\,\mathrm{J\,kg^{-1}\,K^{-1}}$. Especially measuring in regions with temperatures below $-50\,^{\circ}\mathrm{C}$ leads to wrong probe TAS measurements, since the CIP temperature sensor is specified down to $-50\,^{\circ}\mathrm{C}$ only.
It is possible to force the CIP to use a fixed sample frequency by setting a fixed probe TAS. Consequently, a correction for the missizing in y direction has to be performed. Setting a fixed probe TAS can be helpful when the probe TAS measurements are expected to be erroneous, e.g. due to miscalibration or flying at too cold temperatures. In order to keep the corrections small, the fixed probe TAS should be set to the estimated aircraft TAS. A slight overestimation of TAS is of advantage over a slight underestimation since more details of the particle habit is captured. In case that the probe TAS is used but the measurements fail during a flight, the value for the fixed probe TAS will then be taken for deriving the sample rate. Thus, the fixed probe TAS value should always be set close to the expected aircraft TAS.

2.4.3 Area ratio

There are two kinds of faulty images that can be recognised by the area ratio ar. The area ratio is simply the area of the shadowed pixels divided by the particle area calculated using the maximum dimension diameter. If the area ratio is smaller than a certain threshold, 0.4 and 0.1 for water and ice, respectively, the particle is rejected. The differences in the area ratio thresholds result from the different particle shapes. Water droplets are in a good approximation spherical, thus, a higher area ratio threshold can be used to identify stretched particle images (see below). Ice particles on the other hand can be of elongated shape. Thus, a too high area ratio threshold would lead to incorrect rejection.
Electronic disturbances can lead to stripes in the images, so-called streakers, as shown in Figure 2.4(d). These can easily be identified by a very small area ratio. Figure 2.4(c) shows stretched particle images. Such images result from a wrong probe TAS measurement by the pitot tube. Possibly the pitot tube has been choked by water and thus, the measurement has been mistaken as too high TAS. This leads to a

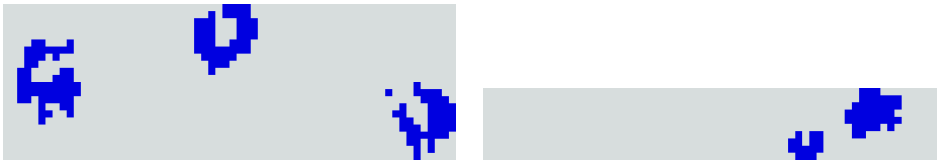

(a) (b)

Figure 2.6: Examples of multiple images. a) Even three particles captured in one image frame, resulting in an area ratio of 0.05, and b) two closely spaced particles imaged in one frame with a corresponding area ratio of 0.13.

higher sample rate, resulting in too many sampled slices. Those stretched particle images can also be identified by the area ratio. The chance of ice particles choking the pitot tube is rare and so is the chance of stretched particle images in ice conditions due to sporadic wrong probe TAS measurements.
In very few cases two or more particles cross the laser beam at the same time (coincidence). That would mean that there are multiple images stored as one image. Two examples for such images are displayed in Figure 2.6. The area ratio that has been calculated for these images results in 0.05 and 0.13, respectively. In case of water clouds both cases would be rejected due to the area ratio criterion. Since both occasions were observed in ice clouds only the first example (Figure 2.6(a)) is rejected while the second example shows that multiple images in ice clouds may not be detected if the two particles cross the laser beam in close vicinity to each other. However, the probability of multiple images is a function of number concentration and increases with increasing number concentration (Baumgardner et al., 1985) and also increases with increasing particle size of the first imaged particle. For example, assuming a particle concentration of $1\,\mathrm{cm}^{-3}$ and the first imaged particle of $100\,\mu\mathrm{m}$ size then the probability of multiple images is only $0.3\,\%$. If the concentration is $100\,\mathrm{cm}^{-3}$ the probability increases to $30\,\%$. Thus, in ice clouds with typical concentrations (below $1\,\mathrm{cm}^{-3}$) the error of not-detected multiple images is rather low and lies well within the measurement uncertainty.

2.4.4 Out-of-focus images

So far images have been treated as if they are sharp, in-focus images. This is not always the case. The diffraction of the laser light can lead to blurred images. Particle shadow images are not only formed of the absorbed light component but also of the diffracted and refracted components of the light. The Mie theory gives the exact solution of the electromagnetic field scattering by a spherical particle. Since Mie calculations are rather laborious (and not possible for aspherical particles), Korolev et al. (1991) simplified the theory and demonstrated that it is possible to use the Fresnel diffraction theory. They showed in laboratory and theoretical studies that Fresnel diffraction by an opaque disc accurately represents the shadow images of spheres as water droplets. A particle within the DOF will produce a sharp image. When a particle moves towards the edge of the DOF the diffraction will cause a distinct feature: a bright spot in the middle of the image, the so-called Poisson spot. Measured examples are given in Figure 2.4(e), modelled diffraction images are shown in Figure 2.7. The size of the Poisson spot depends on the dimensionless distance

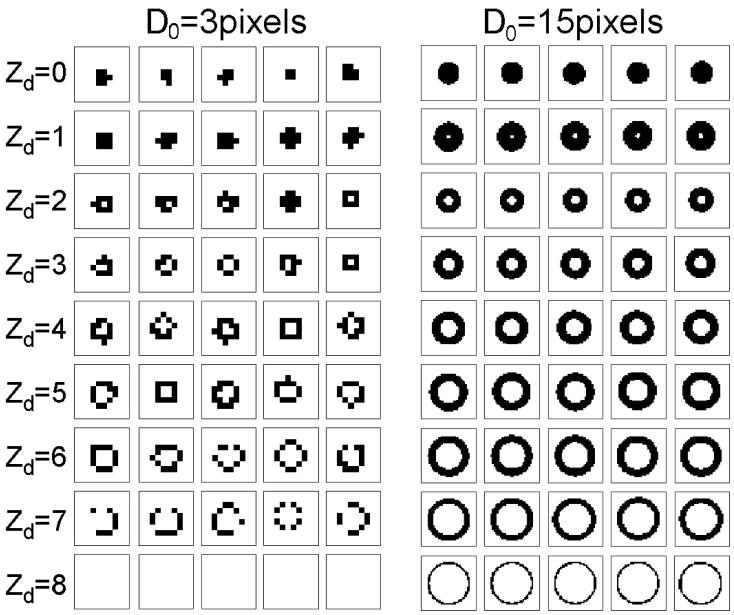

Figure 2.7: Modelled diffraction images with different distances Z_d from the object plane of an original image size of 3 and 15 pixels, taken from Korolev (2007). Note that $Z_d = 8$ corresponds to a real distance (Z) of $16.5\,\mathrm{mm}$ from the centre of focus for three pixel images while $Z_d = 1$ of the 15 pixel images corresponds to $51.7\,\mathrm{mm}$. This is already located behind the CIP probe tips assuming that the centre of focus is located in the middle between the probe tips (which are $100\,\mathrm{mm}$ apart).

$Z_d = 4\lambda Z/D_0^2$ with Z the particle distance from the object plane (= true focus), λ the laser wavelength, and D_0 the actual diameter of the particle. Thus, the Poisson spot yields information about the particle's position within the laser beam. Together with another geometrical dimension of the particle shadow (e.g. the outer diameter of the particle image, D_{edge}) it is possible to reconstruct the original particle size. Figure 2.8(a) shows the diameter of the Poisson spot, D_{spot}, and the outer diameter, D_{edge}, which are taken for calculation of the correction factor in this analysis, according to the correction mechanisms suggested by Korolev et al. (1998) and Korolev (2007). The ratio of D_{spot}/D_{edge} is a continuous function of Z_d as shown in Figure 2.8(b). Thus, Z_d and with this the missizing of D_{edge} can be determined. However, this correction can so far only be applied if the cloud particles are spheres like water droplets or round shaped ice crystals. Nevertheless, also ice crystals of different shape can cause a different appearance if these particles are not in focus. Examples for this are shown in Figure 2.9. A calibration device is used (spinning disc, see Section 2.7) that simulates different crystal shapes. The symbols are in-focus on the left hand side, moving further away from the focus until the calibration device is placed directly next to the probe arm (the farthest away from focus) on the right hand side of Figure 2.9(a). Needle shaped particles that move out of focus start to grow in their cross direction, showing holes in the middle, until they almost appear as two parallel lines when far away from focus. Diagonal orientated needles show this behaviour closer to focus than horizontal or vertical orientated needles. The diagonal orientated needles even disappear when the symbol calibration devise is situated next to the probe arm. The simple stars and stellar dendrites change their structure by moving away from the object plane. The bullet rosette type symbol gains holes resembling Poisson spots and increases slightly in size by about $8\,\%$ from the left to the right image stripe.

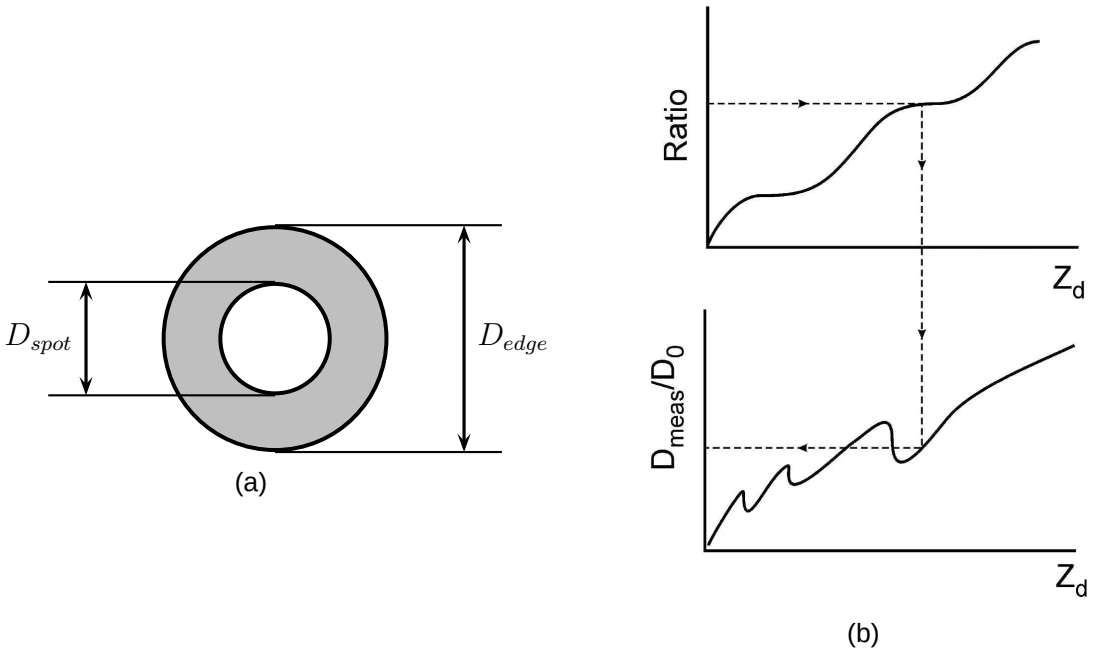

Figure 2.8: (a) Schematic of particle image with Poisson spot. Diameters used for calculation of correction are shown. (b) Conceptual diagram of the size retrieval of the sizes and distances of the diffraction images. Ratio applies here to the ratio D_{spot}/D_{edge}. Both figures adapted/taken from Korolev (2007).

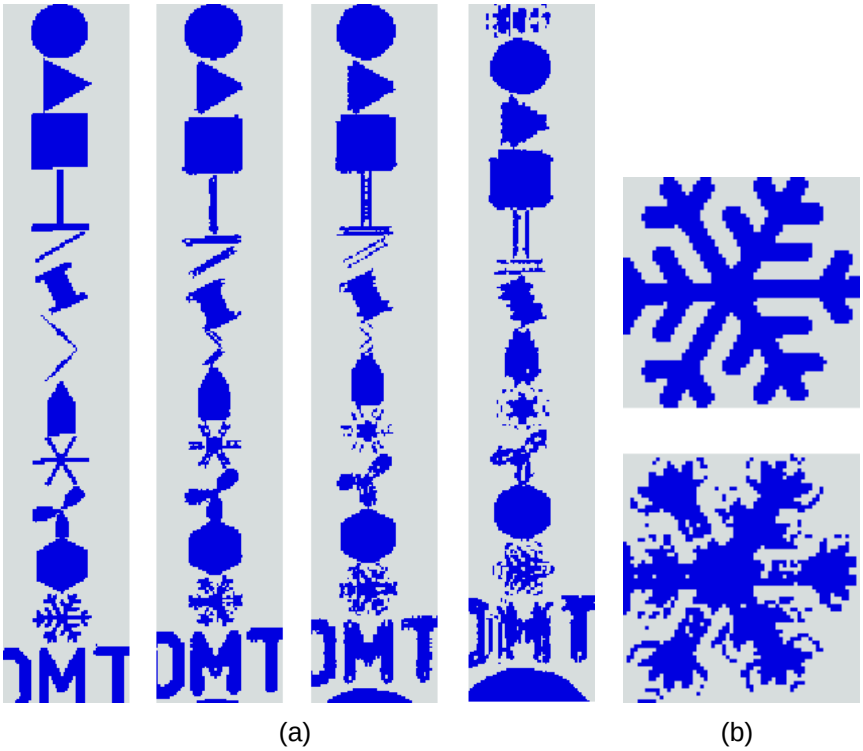

Figure 2.9: Symbol calibration particles in and out-of-focus. a) Different symbols are imaged in-focus in the leftmost image stripe, the calibration device is moved further towards the probe arm to simulate out-of-focus images. The rightmost image stripe shows the shadow images taken from the closest to the probe arm as possible. b) In and out-of-focus image of a large stellar dendrite. Even for such large non-spherical particles an out-of-focus effect is obvious.

While the stellar dendrite also increases in size by about $5\,\%$, all needle type images, including the simple star, decrease in size by $5\,\%$ to $10\,\%$, the diagonal oriented needles even disappear. The solid symbols are most likely to conserve their shape habit. However, the diagonal oriented capped column appears graupel-like in the rightmost image stripe. Figure 2.9(b) makes clear that also large particles of non-solid habit, in this case a large stellar dendrite, change their structure when moving out of focus. However, the size change is most dramatic for diagonal orientated needle shapes that diminish even to their entire disappearance and needles of all orientations that grow in their cross direction while their maximum dimension decreases. Since the out-of-focus correction has been established for spherical particles, the particle images need to be inspected carefully before applying this correction. Furthermore, for ice particles $<60\,\mu\mathrm{m}$ and ice particles of quasi-spherical shape Korolev (2007) state that this correction may give reasonably adequate results. Some ice particles have transparent parts and consequently the images of such particles have transparent areas inside their circumference (c.f. plates in the Particle Gallery, page 148). Application of the correction algorithm thus may lead to large sizing errors. In addition, for particles with elongated shapes, especially needles, this correction should not be applied. So far, however, no correction mechanisms have been established for non-spherical out-of-focus images. Thus, the development of such a correction would most probably result in a fruitful contribution to the CIP data analysis.

2.4.5 Empty images

Sporadically particle image frames show no shaded pixels. This can happen in two ways. Either particles have triggered the data acquisition program, but only left a signal in the first, non recorded, slice. Or small particles moved so far towards the edge of the DOF that they stopped triggering pixels. This effect is described in Korolev (2007) and can be seen in Figure 2.7 in the three pixel images for $Z_d = 8$. Since the processing software does not determine which of these effects leads to the empty image, these images are assumed to have been triggered by a particle that would shadow one pixel. Therefore, these empty images are reconstructed as one pixel images. Due to the mechanical limitation of the DOF (c.f. probe arm distance), only small particles with diameters up to four or five pixels can create empty images (see Korolev, 2007, for a complete illustration of Figure 2.7). The reconstruction as one pixel image can thus lead to an overcount of one pixel images and simultaneously to an undercount of few pixel images. In the size distribution these reconstructed particles will appear in the first size bin, while few of them should have been allocated to the second size bin which comprises particles of $75\,\mu\mathrm{m}$ to $125\,\mu\mathrm{m}$ size, i.e. three to five pixel images in diameter. One possibility to overcome this missizing would be to combine the first two size bins. It has to be reminded that in case the original particle is larger than $25\,\mu\mathrm{m}$ also the sample volume is larger. Thus, the number concentration of particles in this combined size bin would be overestimated (c.f. Equation 2.13). The size distributions shown in this work are a combination of measurements from the CIP and an FSSP[5]. Since the latter detects particles in a size range from $2.7\,\mu\mathrm{m}$ to $31\,\mu\mathrm{m}$, which is partly overlapping with the CIP size range, the first two CIP size bins are not

[5]Forward Scattering Spectrometer Probe, see Section 2.8.3

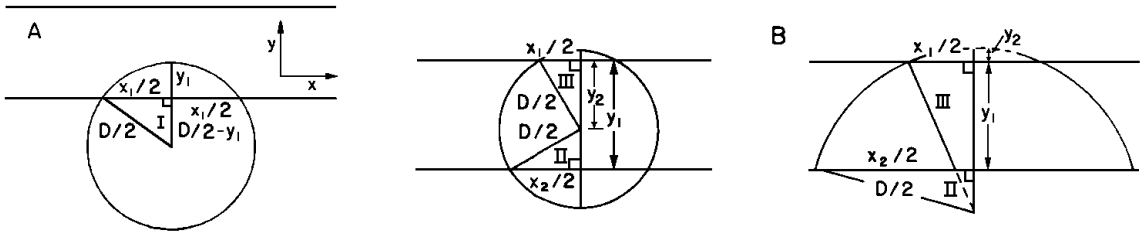

Figure 2.10: Geometry of partial images used for reconstruction for particles that touch on end diode (A) or both end diodes (B) either with the center inside or outside of the sensing area, taken from Heymsfield and Parrish (1978).

combined here. Around five percent of the CIP images from the data sets used in this thesis are empty images. However, it is not possible to identify how many of these images result from particles that should have been allocated in the second CIP size bin.

2.4.6 Partial images

During the measurement particles may not always be fully within the sampling volume but protrude out of it. In these cases particle images will be partial, the image touches one of the end diodes or both end diodes of the diode array as can be seen in Figure 2.4(f). Thus, they are easy to identify and can either be rejected (this analysis method is called the all-in method) or reconstructed. Rejection of these particles can lead to a high number of lost particles. Larger particles have a higher possibility to touch an end diode and are thus more likely to be rejected. A reconstruction of the partial images is possible using the method described in Heymsfield and Parrish (1978). The x and y dimensions of the partial image, as indicated in Figure 2.10, are used to calculate the particles' diameter due to the following equation:

$$D_p = \sqrt{\left(y_1 + \frac{x_2^2 - x_1^2}{4y_1}\right)^2 + x_1^2}. \tag{2.19}$$

Note that the x and y dimension as introduced by Heymsfield and Parrish (1978) here, are opposite of x and y dimension in sizing. When only one enddiode is shadowed x_2 turns 0 and with this Equation 2.19 reduces to

$$D_p = \frac{1}{y_1}\left(y_1^2 + \left(\frac{x_1}{2}\right)^2\right). \tag{2.20}$$

When reconstructing partial images a change in the sample volume has to be considered due to the change in effective array width, as indicated in Equation 2.7 and Figure 2.2.

2.4.7 Shattering

A widely discussed phenomenon that occurs during in situ measurements of cloud particles is the shattering (e.g., in Korolev and Isaac, 2005; Field et al., 2006; Heymsfield, 2007; McFarquhar et al., 2007; Jensen et al., 2009; Korolev et al., 2011; Lawson,

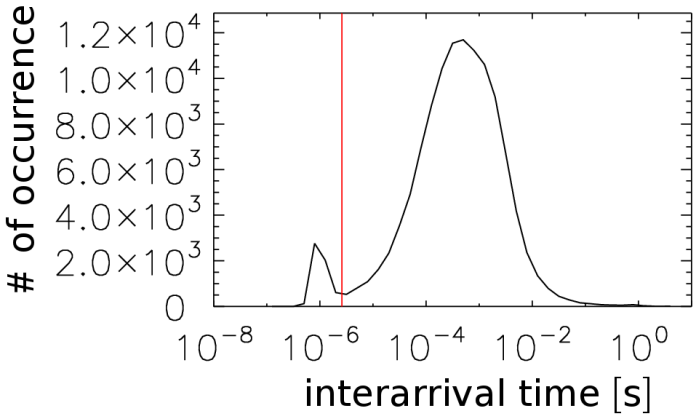

Figure 2.11: Frequency distribution of interarrival times measured by the CIP on board the M-55 Geophysica at airspeeds around $130\,\mathrm{m\,s^{-1}}$ on 7 Aug 2006.

2011). It happens when large particles hit the probe tips and break up into a burst of small particles. Water as well as ice particles can potentially shatter. High frame rate camera images of shattering ice particles are shown in Emery et al. (2004). Shattering is obvious in the particle images as Figure 2.4(g) shows. Since shattering leads to an overcount of small particles and introduces artefacts in the size distributions it needs to be identified in order to remove shattered particles from the data set. It can also occur that shattered particles appear as one big image (as in Figure 2.4(g) in the middle). Such big images consist either of a burst of small particles with so short interarrival times that these particles are recognised as one particle or, in case of water droplets, of the original shattered particle in a fragmented shape. A common identification method for shattering is the usage of particle interarrival times, as described in Field et al. (2006). For each particle the time when the particle arrives and triggers the recording is measured with an accuracy of $10^{-9}\,\mathrm{s}$. The interarrival time of two particles is simply the difference of their arrival times. Shattering will cause the particle fragments to cross the sample volume in very short times compared to non-shattered particles. This can lead to a bimodal distribution of interarrival times of the measured particles. For a flight on 7 August 2006[6] this bimodal frequency distribution of measured interarrival times is shown in Figure 2.11. The short interarrival time mode results from fragments of shattered particles, while the peak around $5 \times 10^{-4}\,\mathrm{s}$ results from unshattered particles, representing real cloud structure. Therefore, all particles with interarrival times shorter than a chosen threshold that lies between the two modes are labelled as shattered and can then be rejected. The threshold, here indicated by the red line, is often found at times around $10^{-5}\,\mathrm{s}$. Even cases of one big particle image (as mentioned above) are removed since these are usually followed by one or more shattered fragments and such fulfill the interarrival time criterion. Furthermore, these big splashed or clustered particle images are mostly rejected due to the area ratio criterion, see Section 2.4.3. An example for such a particle image is shown in Figure 2.12. The dimensions of this image (i.e. length, width, D_p) that are used for the calculation of the area ratio are given at the right hand side. This example has been recorded in an ice cloud and the resulting area ratio of 0.063 fulfils the criterion of area ratio rejection for ice clouds, i.e. $ar < 0.1$.

[6]Data and analysis of cloud data from this flight are presented in Chapter 4, Section 4.2.3.

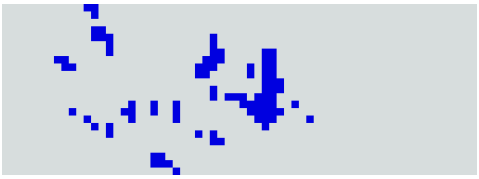

length = $875\,\mu\mathrm{m}$, width = $600\,\mu\mathrm{m}$
D_p = $1061\,\mu\mathrm{m}$
area$_{D_p}$ = $884\,064\,\mu\mathrm{m}^2$
num$_{pixel}$ = 89, area$_{pixel}$ = $55\,625\,\mu\mathrm{m}^2$
ar = 0.063

Figure 2.12: Example of shattering artefacts that appear in one image frame. The calculations on the right show that this particle image is rejected due to the area ratio criterion (additionally to the interarrival time threshold).

If not corrected shattering could lead to substantial overestimations of particle concentration and IWC. McFarquhar et al. (2007) found these overestimations to reach up to $300\,\%$ for concentration and $49\,\%$ for IWC. Several attempts have been made to change the probe tip design (and/or probe inlet design) of different cloud particle probes to minimise shattering or to avoid shattered particles crossing the sample volume (Korolev et al., 2011). Shattering is regarded to be absent or to have at most a minor effect if no large particles (roughly $150\,\mu\mathrm{m}$) are present (Lawson et al., 2008; Jensen et al., 2009). For example Gayet et al. (2006) concluded that the effect of shattering on their concentration measurements is not larger than the uncertainty of the measurement in conditions were particles were smaller than $100\,\mu\mathrm{m}$. Since relatively low ice crystal number concentrations of relatively large ice crystals have been observed and since the size of the largest ice crystal did not exceed $500\,\mu\mathrm{m}$ de Reus et al. (2009) concluded that it is not likely that shattering had significantly influenced their measurements.
When using the interarrival time criterion for removal of shattering artefacts it is important to carefully determine the interarrival time threshold specifically for each flight or even flight segments if clouds of different nature have been probed (e.g. low level water clouds and high level cirrus). If the interarrival time threshold is set to too high values, a significant fraction of legitimate particles may be removed. If it is set to too low values, a significant part of shattered particles may not be removed. (Specific considerations on the removal of shattering artefacts related to the observations discussed in Part II of this thesis can be found in Appendix Section A.4 and more specifically in Section A.4.4.)

2.4.8 More instrumental issues

Double Particles
At the time of the measurements which are discussed in Part II of this thesis, i.e. before 2007, the DAQFactory data acquisition software was used on the CIP computer. During one of the campaigns, using this software, a feature occured hereafter called Double Particles. Occasionally, sets of observed particles have been stored to disc several times. The reason for this is presumably a software bug. As reported in Section 2.1, particles are stored consecutively to disc in a buffer. In case Double Particles occurred, buffers would contain information of particles that are repeatedly stored to disc. For example, if two clouds have been encountered in one flight, cloud *A* and cloud *B*, images of particles from cloud *A* would be stored to disc as Double Particles during times when also images of particles from cloud *B* are stored. There is a consecutive time line in the buffer times and in the particle times of correctly re-

ported images. However, images of Double Particles are reported with their original time (during cloud encounter *A*) and thus, particle times jump backwards from the correct reported particles of cloud *B*. This makes the Double Particles easy to identify by searching for double particle times and remove the so-found Double Particles from the data stream. Double Particles are always stored at the end of a buffer but do not necessarily fill the whole buffer.
Figure 2.13(a) shows a time period during a measurement flight on 7 August 2006 where Double Particles are found. The red dots indicate correctly measured particles while blue dots mark the Double Particles. The green lines show the buffer times of the Double Particles. Two times close to each other, one with and one

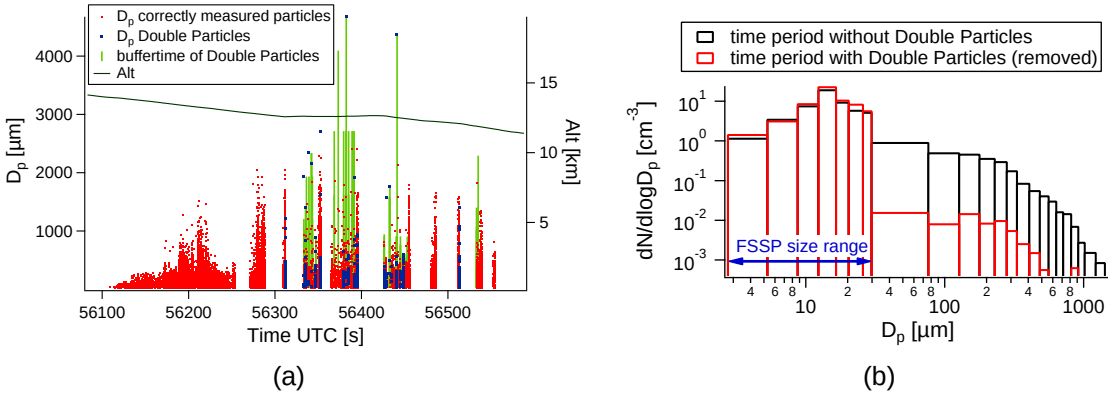

Figure 2.13: Measurements made during times when Double Particles occured. a) Time series of a flight on 7 Aug 2006 and b) size distributions of a time period with Double Particles compared to a time period without Double Particles ten seconds later.

without the Double Particle feature, have been picked for comparison of the respective size distributions, and Double Particles are excluded from the measurements. This comparison is shown in Figure 2.13(b). The size distributions also include the measurements of the FSSP-100 which show similar concentrations for both times. It has to be noted that possible shattering effects in the FSSP data have not been removed. Nevertheless, for the time without Double Particles the overlap of FSSP and CIP is quite reasonable, concluding that shattering has no high influence on these data. Since the times are just 10 seconds apart and measurement conditions were similar it can be assumed that there is no high shattering effect on the time period with Double Particles, either. But here, a big gap of over two orders of magnitude between CIP and FSSP measurements is obvious. Additionally, the total number concentration changes when comparing consecutive time periods with and without Double Particles. During the former time periods the concentrations decrease by roughly an order of magnitude. This leads to the conclusion that buffers that contain Double particles overwrite good particles which are thus lost from the measurements. Therefore, time periods with Double Particles should be treated with special care during data analysis, times where buffers contain Double Particles should presumably be removed from detailed analysis. The Double Particles that have been observed originated mostly from the same flight. In one case, however, calibration particles have been reported by the probe. That means that even after switching the instrument off and on again, particles were still stored somewhere in the instruments memory. The total time affected by this issue is about $300\,\mathrm{s}$. More details on which particular flights

are affected by Double Particles can be found in the Appendix Section A.2.
The Double Particles appeared as subtlety in the original data stream. Due to the backward jumping particle times the affected data were easily identified by an additional data filter in the analysis software and removed subsequently. After the campaign during which these Double Particles were observed the data acquisition software has been exchanged in 2007. With the new software this problem has not been observed again.

2.4.9 Summary of quality assessment

This section has shown a variety of correction and rejection mechanisms which can be applied to any data measured by the CIP. Most of these mechanisms should always be used in the data analysis, however, the way these are applied depends on the nature of the data:

- the reconstruction of the first slice is just appropriate for specific processor board versions, the newer processor boards do not miss the first slice (in case of the Mainz CIP the newer processor board has been installed in 2010)
- the probe and aircraft TAS need to be compared in order to identify whether a correction factor for the y-sizing has to be considered
- the threshold of the area ratio rejection criterion should be chosen depending on whether measurements are performed in water or ice clouds
- if no spherical particles are present the out-of-focus correction should be handled with care since it is developed for spherical particles only
- if only a small amount of large particles are present one might consider to reject partial images instead of reconstructing them
- unexpected instrumental issues might always occur. In these cases corrections have to be applied accordingly (e.g. rejection of Double Particles)

A reconstruction of empty images and rejection of shattered particles should always be done. The former confines the loss of small particles. The latter confines a burst of particles which are generated by impaction of particles on the probe tips and do not represent the real nature. However, the interarrival time threshold for the shattering rejection has to be determined carefully for every flight or even flight section. The specific corrections which have been applied to the data analysis presented in Part II are summarised in Table A.1 (Appendix Section A.1). In addition, Table A.2 shows the numbers of detected particles and states how many of them are corrected or rejected according to the different mechanisms.

2.5 Particle data reduction and evaluation

As mentioned in Section 2.1 the DAQFactory program is used for data acquisition. The program stores the image data in a compressed format. Auxiliary data, e.g. ambient temperature or TAS, are stored uncompressed in a separate file. Image data

can be decompressed and displayed with the Image Playback program. In 2007 the Particle Analysis and Display System (PADS) software package has been installed on the CIP computer. PADS accomplishes the image playback and the data acquisition and thus replaces the DAQFactory software. However, for further data reduction and analysis a software is needed that decompresses the image data. Figure 2.14 displays the data reduction process starting with the encoded data at the top. Two programs are used for decoding the image data, the Image Playback to the left delivering particle images and image stripes, and the SODA to the right. SODA is an Interactive Data Language (IDL) based evaluation program which was initially developed at the National Center for Atmospheric Research/University Corporation for Atmospheric Research (NCAR/UCAR) by Aaron Bansemer. This program decompresses the particle image files and applies the correction and rejection mechanisms as discussed in Section 2.4. In the beginning (before adopting SODA for data analysis) it was necessary to refine SODA to improve the data analysis and further subroutines have been implemented, most important the out-of-focus correction, see Section 2.4.4. The user of SODA can choose between the different sizing mechanisms (Section 2.3.1) for the derivation of the particle size. It is possible to pass the probe TAS measurements for calculation of concentrations to the SODA program by an additional routine or to set a fixed TAS in the SODA interface. A correction factor for the missizing due to wrong probe TAS and an interarrival time threshold for the identification of shattering artefacts can be set. The empty images are reconstructed by default as well as the lost first slice. The out-of-focus correction is usually performed but can be turned off if desired. Furthermore, the area ratio threshold can be selected and whether partial images are reconstructed. The start and end times for the data reduction can be chosen. This is specifically useful if one wants to apply different correction mechanisms for different time periods of one data set. For example if the flight was performed at two altitude levels such that during one time period a cloud containing only water droplets has been encountered whereas during a later time period an ice cloud has been sampled. Accordingly one wants to set the area ratio differently for the respective clouds. Two types of output files are created by the SODA. One file is an IDL SAVE file containing processing options, statistical data (e.g. number of processed buffers, count of particles), and particle concentrations. The SAVE file can be loaded by a subprogram of the SODA called SODA browse (lower left of Figure 2.14) which displays the images side by side with particle size distributions. A colour code indicates if particle images are rejected and for what reason. Additionally, a second SAVE file can be loaded by SODA browse and the concurrent size distributions can be compared, e.g. if the settings for one file included all correction options and the second included no correction options. The second SODA output file is optional and is delivered in a text format called *particle by particle* (.pbp). The pbp file contains one row for each particle, the columns provide the following information: 1) buffertime, 2) particle time, 3) interarrival time, 4) TAS, 5) particle size, 6) area ratio, 7) indicator whether particle touches one of the end diodes, 8) rejection code, 9) out-of-focus correction factor, and 10) the dimensionless distance Z_d. The rejection code indicates if a particle should be rejected and for what reason (area ratio, interarrival time, partial image, bad time line, i.e. a software bug). The codes are additive, i.e. the code can identify if a particle should be rejected for several reasons. The pbp file is used for the calculation of the different particle parameters as introduced in Section 2.3.

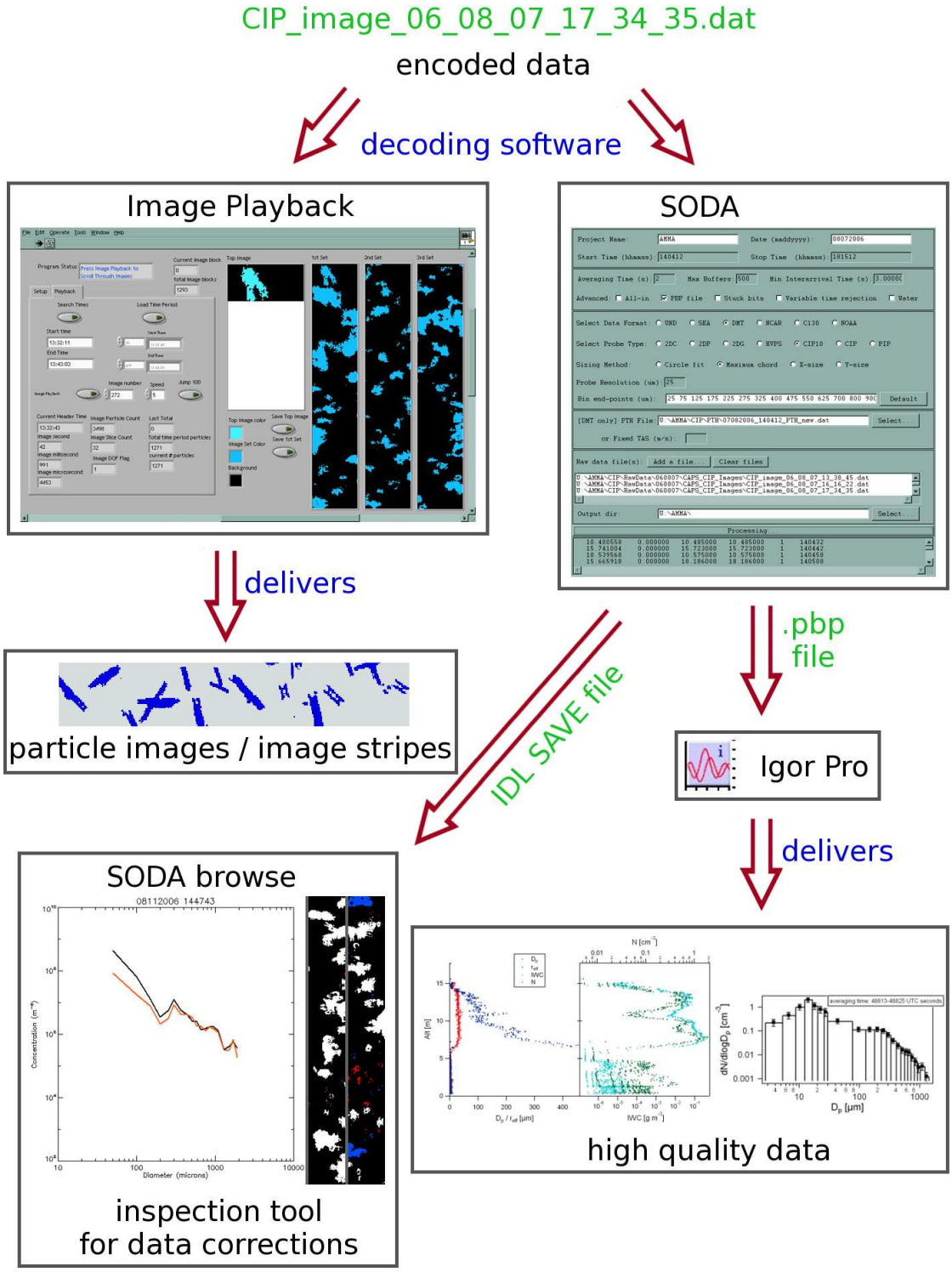

Figure 2.14: Data reduction scheme for CIP image data. The different programs and their deliverables are displayed.

These calculations are performed with user-written Igor Pro[7] routines. Furthermore, the routines are used to display the calculated data. Examples for those deliverables are shown in the lower right of Figure 2.14.

2.6 Instrument uncertainty

Instruments of OAP type have been used extensively since their introduction by Knollenberg (1970). Nevertheless, very little has been published on the performance characteristics and limitations of OAPs in the first 20 years. Knowing the uncertainties of a measurement on the other hand is crucial. While first publications reported on sizing problems in the lower size ranges (Curry and Schemenauer, 1979; Gordon and Marwitz, 1984), they did not identify the physical causes of the missizing. Progress in that regard has been made in the early 1990's. To date several studies (of which some are discussed below) have investigated the uncertainties of 1D and 2D OAPs, as well as 2D greyscale OAPs by addressing different issues. This section focuses on the uncertainties of 2D probes even though not all analyses are strictly transferable to other probes due to slightly different geometries and technical and electrical specifications of the probes. Nevertheless, the methods described in these studies, if applied to other instruments of OAP type, should lead to similar results. Thus, the general/qualitative statements made in all these studies are valid also for the CIP.
There are two main issues that concern the instrument accuracy. This is the exact sizing of particles and the correct determination of the sample volume, mainly governed by the correct determination of the DOF. Both affect the calculation of size distributions. The latter also affects the calculation of concentrations.

Important factors that control the size uncertainty are the probe resolution of $25\,\mu\mathrm{m}$ and the $50\,\%$ shadowing threshold that has to be met to trigger particle recording. The particle size uncertainty decreases considerably with particle size and is $\pm 25\,\mu\mathrm{m}$ for particles larger than $50\,\mu\mathrm{m}$. A $25\,\mu\mathrm{m}$ particle can be imaged as $50\,\mu\mathrm{m}$ particle if it casts its shadow exactly over the middle of two diodes. On the other hand, a particle of $74.9\,\mu\mathrm{m}$ size could also be recorded as $50\,\mu\mathrm{m}$ particle if it shadows two diodes completely and two diodes by just $49.8\,\%$. A one pixel image that has a nominal size of $25\,\mu\mathrm{m}$ in diameter can be triggered by particles with sizes between $12.5\,\mu\mathrm{m}$ and $49.9\,\mu\mathrm{m}$.

A stable laser performance is crucial for maintaining the $50\,\%$ shadowing threshold. Laser variations, e.g. due to significant altitude or temperature changes, that lead to slight changes in the alignment, or laser deterioration, can cause uncertainties as reported by Strapp et al. (2001). For example, a declining laser power will lead to a decrease of observed laser intensity at the photodiodes which means that the full particle shadow needs to cover less than $50\,\%$ of a diode to trigger the image recognition. Thus, particles will possibly be oversized. However, laser variations are less crucial for the CIP since the voltage levels of the diodes, as a result of laser power, are monitored with the sample frequency. The single voltage levels are then compared to a running average of the voltage levels in order to identify a decrease by

[7] analysis software Igor Pro from Wavemetrics

$50\,\%$ in laser light intensity (D. Baumgardner, personal communication, 2010). Times at which particles cross the laser beam are included in this running mean and thus, times where not the full laser intensity impact on the respective diodes. However, it will hardly impact the threshold level, with the exception of periods of extremely high particle concentration ($>1\,\mathrm{cm}^{-3}$).

Another source of missizing is given by the particle's distance from the object plane. This out-of-focus effect has been reported by several laboratory and theoretical studies (e.g., in Joe and List, 1987; Hovenac and Hirleman, 1991; Korolev et al., 1998; Korolev, 2007). A particle that is out-of-focus will appear increased in size with increasing distance from the centre of focus. Particularly particles with diameters smaller than $200\,\mu\mathrm{m}$ are strongly affected since they only need a small offset from the focus to cast a shadow with an increased size. This missizing can be removed by the out-of-focus correction, as described in Section 2.4.4.

The reconstruction of empty images (see Section 2.4.5) is a further source of particle missizing. This will affect the first two size bins of a size distribution since particles up to a size of about $125\,\mu\mathrm{m}$ might be identified as one pixel image, leading to an undersizing of those particles. Hence, more particles will appear in the first size bin of the size distributions and fewer particles in the second size bin.

Calibrations and laboratory studies often have to deal with unrealistic low airspeeds. As reported by Strapp et al. (2001) the average droplet diameter has been found to decrease with increasing airspeed. Their observations indicate a net undersizing for small particles ($D_p < 100\,\mu\mathrm{m}$) and a net oversizing for larger particles. Furthermore, the TAS has an effect on the DOF. One has to bear in mind that for particles larger than $213\,\mu\mathrm{m}$ the theoretical DOF will always be larger than the mechanical limit which is given by the distance between the probe arms ($10\,\mathrm{cm}$). That means effects which govern the DOF have to be taken into account mainly for small particles. For particles smaller than $100\,\mu\mathrm{m}$ the DOF decreases rapidly with increasing TAS (Baumgardner and Korolev, 1997; Strapp et al., 2001) which was found to be an effect of the non-zero response time of the probe. This leads to an underestimation of particle concentrations of small particles. Nevertheless, these studies allude to response times of $0.4\,\mu\mathrm{s}$ and $0.44\,\mu\mathrm{s} - 0.9\,\mu\mathrm{s}$, respectively, for their instruments, while the CIP diode array board response shows a delay of $0.12\,\mu\mathrm{s}$ at the worst (B. Dawson, DMT, personal communication, 2010). Consequently, as also stated by Baumgardner et al. (2001), the dependency of the DOF on airspeed is eliminated. Recent measurements have shown that the CIP is capable of imaging $50\,\mu\mathrm{m}$-particles at airspeeds of $150\,\mathrm{m\,s}^{-1}$ (Lawson, 2011). Furthermore, an excellent agreement between the CIP and the 2D-S[8], a probe which has demonstrated to detect and count small particles at airspeeds up to $\approx 230\,\mathrm{m\,s}^{-1}$ (Lawson et al., 2006), was found during measurements at altitudes of $11\,\mathrm{km}$ to $12\,\mathrm{km}$ (Jensen et al., 2009). The often-observed poor overlap between the scattering instruments (e.g. Forward Scattering Spectrometer Probe) and OAPs was found to be an effect of the response time issue (Baumgardner and Korolev, 1997; Strapp et al., 2001). However, as shown in Part II of this thesis, the CIP and FSSP show mostly a reasonably good agreement in their overlapping size ranges. Korolev et al. (1998) point out that even with a zero response time small

[8]two-dimensional stereo probe, see Section 2.8.2

particles will be undercounted because of particle losses due to the discrete nature of the particle image recording. These losses can reach $70\,\%$ for $25\,\mu\mathrm{m}$ particles. A non zero response time will even increase the counting losses. It has to be noted that the response time mainly affects the measurements of small particles (when just a few diodes are shadowed).

Including the discussed effects the sample volume uncertainty (as a result from DOF uncertainty) is estimated to be $20\,\%$ (de Reus et al., 2009). For low number concentrations the counting statistics have to be considered as a further source of uncertainty. This counting statistics uncertainty is defined as the square root of the number of particles measured. Thus, the error bars for any size distribution display the combined uncertainty derived from counting statistics and sample volume.
The calculation of the IWC is affected by both, uncertainty in number concentration and sizing. An estimate for the IWC uncertainty using combined measurements of an FSSP and and a 2D OAP is given by Heymsfield (2007). Small particles ($\lesssim 50\,\mu\mathrm{m}$) as detected by the FSSP are usually assumed to be spheres, while deriving the volume of ice particle structures from the 2D images adds further uncertainty to the IWC which is estimated to be within a factor of 2.

As discussed in Section 2.4.7 shattering of cloud particles can lead to a severe overestimation of small particle numbers and consequently an overestimation of IWC. Therefore, shattering artefacts need to be removed from the analysed data set to ensure a high-quality analysis. Specific considerations about shattering affecting the measurements presented in Part II of this thesis are given in Appendix A.4.4.

The discussion shows that especially for small particles corrections are important, since those particles are more affected by uncertainties than larger particles. Furthermore, small ice particles have a more important contribution to the radiative effects of clouds. In case of combination with other instruments that measure in the smaller size ranges than the CIP, as e.g. in this work the FSSP-100, the correct derivation of the number concentrations of small particles is a concern for the respective overlap regions of the size distributions.
Besides adding all known correction mechanisms to available data, further approaches for improvement are suggested. Smedley et al. (2003) discovered that sampling with a higher slice rate than that which will produce images with an aspect ratio of $1{:}1$ will reduce the sizing errors for small particles. They suggest an oversampling factor of 10. The process of oversampling is also found to significantly increase the sample area for the smallest particles. However, the typical aircraft speeds and maximum sample frequencies of the probes will restrict the oversampling, plus large particles might get lost if the probe's image acquisition stops at a certain slice number for a single image. Thus, oversampling might be applicable to newer probes with higher maximum sampling frequencies and more buffer storage capacities for images.

2.7 Size calibration

In order to achieve good quality data it is necessary to verify the correct particle sizing of the CIP. Therefore, a spinning disc calibrator, similar to the rotating reticle

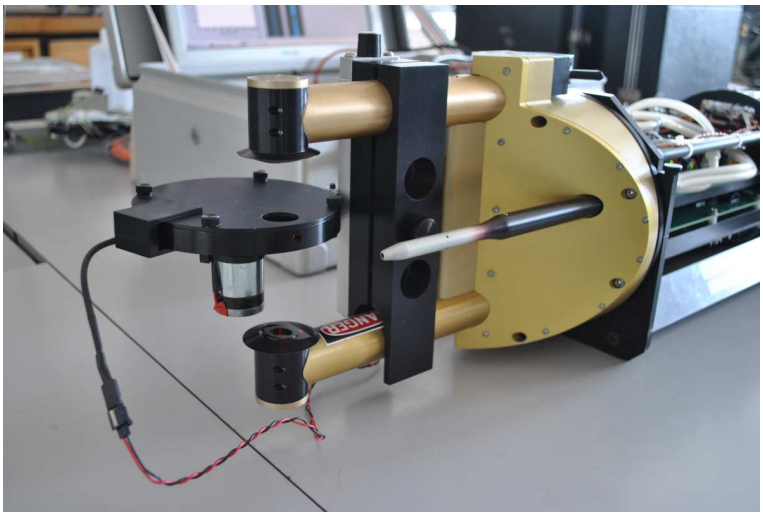

Figure 2.15: CIP front section with spinning disc calibrator mounted to the probe arms. The glass disc is sheltered by a housing below which the motor can be seen.

described by Hovenac and Hirleman (1991), is used. Spots of known size (here, 50, 125, 250, 500, 1000, and $2000\,\mu\mathrm{m}$, repeated 12 times) are placed on a glass disc which is mounted between the probe arms. The disc is rotated with 5000 rotations per minute so that the spots pass the laser beam with a speed of $25\,\mathrm{ms}^{-1}$. Thus, 6000 particles per second should be imaged by the probe. Figure 2.15 shows the spinning disc calibrator mounted to the probe arms. The rotating device provides a steady source of particles that stresses the probe with extreme high concentrations of particles, resembling a worst case scenario for the UTLS. Note, the CIP is specified for concentrations up to $100\,\mathrm{cm}^{-3}$. The spinning disc cannot only be used to check the correct sizing but also to indicate whether failures in the electronic system of the probe or failures in the communication between probe and data acquisition computer occur. Furthermore, it is possible to move the spinning disc along the laser beam in order to perfectly position the disc in the centre of focus. By moving the disc out of focus diffraction images as described in Section 2.4.4 can be observed. However, with the spinning disc it is not possible to simulate realistic air speeds which occur when the probe is operated on board an aircraft. In case a missizing is detected by the use of the spinning disc, the probes' optics can be adjusted to gain correct sizing.

2.8 Placement among airborne in situ cloud particle instrumentation

As mentioned above several different in situ cloud particle probes exist. In order to give a comprehensive picture of the state of the art airborne in situ cloud particle instrumentation, the different probes and their operation principles are introduced in the following. Furthermore, the placement of the CIP among these probes is exposed. A particular focus is placed on the Forward Scattering Spectrometer Probe (FSSP), since this instrument has been operated together with the CIP during the measurements that are presented in Part II of this thesis.

2.8.1 Holographic instruments

Holographic instruments obtain the most realistic images of cloud particles. The earlier analogue holographic cloud probes (e.g. Conway et al., 1982; Brown, 1989; Borrmann and Jaenicke, 1993) had to suffer from the mechanical and chemical requirements for exposure and development of the photographic emulsion. Furthermore, expensive, rather large laser systems were needed, and in the first place the analysis of the obtained holograms was laborious and time consuming. With the arrival of digital imaging devices and increasing computer power, digital holography became feasible, where digital cameras replaced photo-chemical films. First tests with digital holographic instruments were performed by Lawson and Cormack (1995). Holography has the benefit of providing a well-defined sample volume, a uniform and well-defined resolution, and three-dimensional spatial information that can assist in identifying bursts of shattered ice particles.

Cloud Particle Imager (CPI)
High resolution, 256 grey level images are obtained by the Cloud Particle Imager (CPI). By freezing the motion of cloud particles using a $40\,\mathrm{ns}$ pulsed, high-power laser diode, the CPI registers particle images on a solid state, one-million-pixel digital charge-coupled device (CCD) camera (Lawson et al., 2001; Shcherbakov et al., 2006; Gayet et al., 2009). The pixels of the camera have an equivalent size in the sample area of $2.3\,\mu\mathrm{m}$, so particles with sizes of approximately $10\,\mu\mathrm{m}$ to $2\,\mathrm{mm}$ are imaged while the camera flashes up to 75 frames per second (fps) with the potential of imaging more than 25 particles per frame. Internal structures of the ice particles can be imaged with the CPI and these images allow a judgment about the three-dimensional structure of the particles.

Holographic Detector for Clouds (HOLODEC)
With a 8-bit greyscale camera that has 1024×768, $4.65\,\mu\mathrm{m}$ pixels and a frame rate of $15\,\mathrm{Hz}$ the Holographic Detector for Clouds (HOLODEC) detects particles (Fugal and Shaw, 2009). The potential sample volume is $4.8\,\mathrm{mm}\times3.6\,\mathrm{mm}\times50\,\mathrm{mm}$, while in practice just an inner volume of $0.52\,\mathrm{cm}^3$ per hologram is used. Determined by the diffraction limit, minimum size of reliably measured particles is $15\,\mu\mathrm{m}$ and the size range extend to $1000\,\mu\mathrm{m}$.

2.8.2 Imaging instruments

OAPs similar to the CIP exist like the parent versions of 2DC probes (= 2dimensional cloud probes) and their one dimensional parent version (1DC). Furthermore, OAPs covering other size ranges are available, but also some newer developments of OAPs.

Greyscale OAP
In a further development of the OAP the diode array now has a shadowing threshold detection of three different shadow thresholds, the so-called greyscale OAP (Joe and List, 1987; Reuter and Bakan, 1998). With this, some more structure in the ice crystals can be observed and also sizing uncertainty can be reduced.

Two-dimensional stereo probe (2D-S)
The two-dimensional stereo probe (2D-S: Lawson et al., 2006) relies on the OAP principle but it uses two orthogonal laser beams that cross in the middle of the sam-

ple volume and thus consists of two OAPs. It only captures two-dimensional images of particles passing through the sample volume where the laser beams overlap. The diode arrays consist of 128 photodiodes and the resolution of the pixels is $10\,\mu\mathrm{m}$. The overlap region of the laser beams defines the DOF and thus the sample volume as well as the sizing of particles smaller than $100\,\mu\mathrm{m}$ is improved. The stereo views of particles in the overlap region can also improve determination of three-dimensional properties of some particles.

2.8.3 Scattering instruments

Mainly for the measurement of smaller cloud particles, i.e. particles with sizes reaching down to around the wavelength dimension, scattering instruments are used. Particles scatter light following the Mie theory (c.f. Bohren and Huffman, 1983) and the intensity of the scattered light is proportional to the particle size. Thus, by measuring the intensity of the scattered light particle sizes can be derived if particle shape and refractive index as well as the wavelength of the incident light are known. Some instruments detect the forward scattered light, others additionally detect the backward scattering.

Forward Scattering Spectrometer Probe (FSSP)
The Forward Scattering Spectrometer Probe (FSSP) measures the forward scattering of light within a scattering angle of $4°$–$12°$. A laser, focusing on the object plane, is projected across the probe's sampling aperture on a dump spot. This is located on a prism such that it avoids direct illumination of the detectors. Light scattered by particles, however, will pass beneath the dump spot, pass the optical system, and fall on a beam splitting prism in front of the detectors. One detector is partially masked in order to identify whether particles pass in the DOF by comparing the signal of the masked and unmasked detector. A schematic of the laser pathway and the optical components is shown in Figure 2.16 (taken from Dye and Baumgardner, 1984). A detailed description of the operating principle and the electronics can be found in Dye and Baumgardner (1984). Newer electronic packages (Signal Processing Package - SPP) for the FSSPs are provided by DMT, the SPP-100 and SPP-300 for the FSSP-100 and FSSP-300, respectively. These are two slightly different constructions of FSSPs. The difference consists in the gain stages of the detectors, in the mask, and the FSSP-300 has a more powerful laser. Therefore, the particle size detection range varies as well and is roughly $2\,\mu\mathrm{m}$ to $47\,\mu\mathrm{m}$ for the FSSP-100 and $0.5\,\mu\mathrm{m}$ to $40\,\mu\mathrm{m}$ for the FSSP-300, depending on particle phase and instrument settings. One major issue for FSSP measurements is that for the size determination from the scattered light signal all particles are assumed to be spherical. This, however, is not always the case in ice clouds and will result in missizing of the ice particles. Borrmann et al. (2000a) have shown that for particles smaller than $16\,\mu\mathrm{m}$ the FSSP forward scattering geometry is insensitive towards asphericities for axis length ratios larger than 0.5 allowing for reliable sizing of particles.
The standard FSSPs have a sample frequency of maximum $1\,\mathrm{Hz}$. Thus, particles are sized and counted and subsequently the condensed data without single particle information is written to disc in time steps of minimum $1\,\mathrm{s}$. Newer versions of FSSPs have been developed which also store single particle information such as pulse duration and arrival times. These versions are called Fast-FSSP (Brenguier et al., 1998;

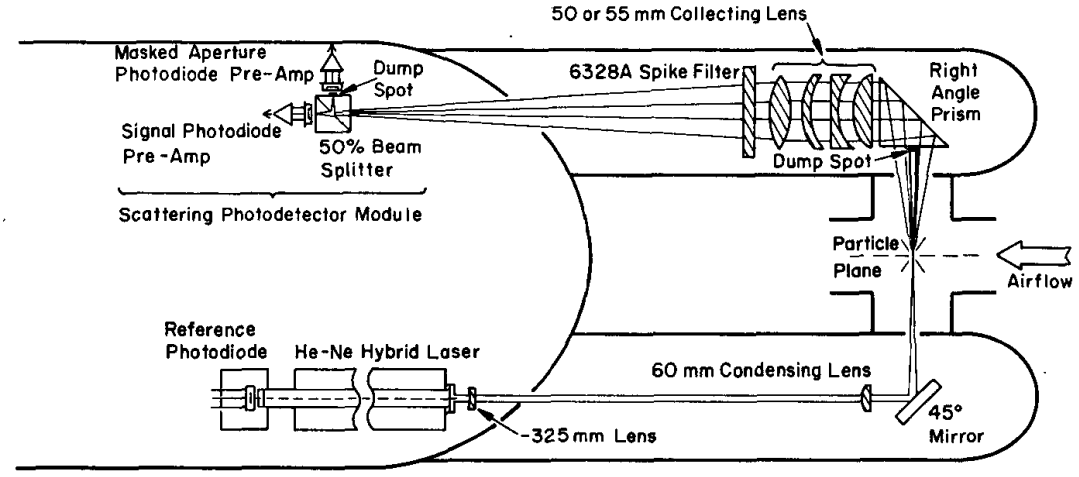

Figure 2.16: Schematic showing the optical components and the laser pathway of the FSSP (taken from Dye and Baumgardner, 1984).

Schmidt et al., 2004) and Cloud Droplet Probe (CDP).

Cloud and Aerosol Spectrometer (CAS)
In order to be able to differentiate between spherical and aspherical particles, the Cloud and Aerosol Spectrometer (CAS: for more details see Baumgardner et al., 2001) makes use of the forward and backward scattered light. The forward to backscatter ratio is a function of refractive index and can be used to determine the asphericity of cloud particles. The forward scattered light is detected within a scattering angle of $4°$–$13°$ and the backward scattered light in an angle of $5°$–$14°$. The size range reaches from aerosol sizes of $0.35\,\mu\mathrm{m}$ to $50\,\mu\mathrm{m}$.

Small Ice Detector (SID)
Cloud probes like the FSSP can indeed measure rather small cloud particles but are unable to discriminate between supercooled liquid drops and small ice particles. Therefore, the Small Ice Detector (SID; Hirst et al., 2001) has been developed. It takes advantage of the fact that any discrete particle will scatter incident light spatially in a pattern which is dependent on the particle's size, shape, and internal structure (and on the wavelength and polarisation of the incident radiation). Therefore, when looking at the azimuthal distribution of the scattered light, information about the particle shape can be obtained. The now operational SID-2 (Cotton et al., 2010) uses a hybrid photodiode that contains 27 independently sensed photodiode elements with three central and 24 outer ones arranged azimuthally. The latter covering a forward scattering angle of $9°$–$20°$. The SID-2 observes particles in the size range of $3\,\mu\mathrm{m}$ to $140\,\mu\mathrm{m}$. The arrival times of the single particles can be recorded, too.

Polar Nephelometer
The Polar Nephelometer (Gayet et al., 1998, 2009) is designed to measure the optical and microphysical parameters of clouds of any phase (water, ice, or mixed phase) over a size range from a few micrometers to about $1\,\mathrm{mm}$ diameter. The probe measures directly the scattering phase function of an ensemble of cloud particles intersecting a collimated laser beam near the focal point of a paraboloidal mirror. The light scattered from polar angles from $\pm 3.5°$ to $\pm 169°$ is reflected onto a circular array of 54

photodiodes. The measurement of the scattering phase function allows the discrimination of particle type (water or ice), and optical parameters as extinction coefficient and asymmetry parameter can be calculated.

Scattering instruments are useful to expand the size range of measured cloud particles to smaller sizes when operated together with the CIP. However, particle shapes can only be determined by the SID. Holographic instruments show much finer crystal structures compared to the CIP shadow images. For measurements of concentrations the holographic instruments need a continuously measuring instrument to scale the concentrations. Thus, all instruments have their advantages and disadvantages. As a stand-alone instrument, the CIP has the ability to detect particles in a relatively wide size range and it does provide direct measurements of concentrations.

2.9 Application on other platforms

Even though the CIP was designed for airborne use, e.g. mounted to an aircraft wing, it has been operated on other platforms. In order to give an overview and to show the benefits of the CIP operated on other platforms these are described in the following without specifying the scientific outcome. (For this the reader may be referred to the cited publications.)

Cloud chamber
A place for studying the initial ice particle nucleation mechanism under controlled conditions is a cloud chamber. It is possible to control meteorological parameters but also parameters like aerosol load. In March 2007 the CIP has been deployed in the aerosol and cloud chamber AIDA (Aerosol Interactions and Dynamics in the Atmosphere; Möhler et al., 2003) during an intercomparison experiment (HALO-01) for in situ cloud particle instruments, which are intended to fly on the High Altitude and LOngrange research aircraft (HALO). Such instrument intercomparisons have the advantage to yield a better comparability between the instruments and their measurements, e.g. from former field measurements reported in the literature or future campaigns. Furthermore, due to the controlled conditions studies about ice forming mechanisms can be performed.

Ground/mountain based
In flat country clouds hardly reach down to the ground level (apart from fog). In contrast, contact between clouds and the ground surface occurs frequently in the mountains. Here, clouds sometimes obscure single mountains and therefore those sites can be used for cloud studies. Such a site is the Jungfraujoch mountain station in the Swiss Alps where the CLACE5 (Cloud and Aerosol Characterisation Experiment; Winterhalter et al., 2009) was held. As Figure 2.17 shows, CIP and FSSP-100 have been operated side by side. The instruments were oriented to the mean wind direction by the vane which can be seen above the instruments.

Sensor shuttle
In order to investigate the cloud radiation interactions it is necessary to obtain the cloud microphysical and radiative properties, preferably simultaneously. Since the cloud particles are measured in situ and the radiative properties remotely this was either done by taking two aircraft, one flying above, one inside the cloud, or by flying

Figure 2.17: CIP and FSSP-100 (behind CIP) operated on the Jungfraujoch mountain station during the CLACE5 experiment in February/March 2006.)

fourth and back, above and inside the cloud. A new platform for combining those measurements with only need to use one single aircraft has been developed: the AIRcraft TOwed Sensor Shuttle (AIRTOSS; Frey et al., 2009). The aircraft is mainly instrumented with radiation sensors and the AIRTOSS with the CIP for measuring cloud particle properties (see Figure 2.18). With this tandem platform truly collocated measurements of cloud microphysical and radiative properties can be performed. A large part of the second PhD year focused on the investigation of the suitability of this tandem platform for detailed cloud microphysics and radiation interaction studies.

UAV

In the future the deployment of instruments on Unmanned Aerial Vehicles (UAVs) may become important. UAVs may be navigated into cloud regions where aircraft can not fly due to flight safety regulations (e.g. heavy convective clouds) or several UAVs can be deployed in stack to obtain simultaneous cloud radiative and microphysical measurements.

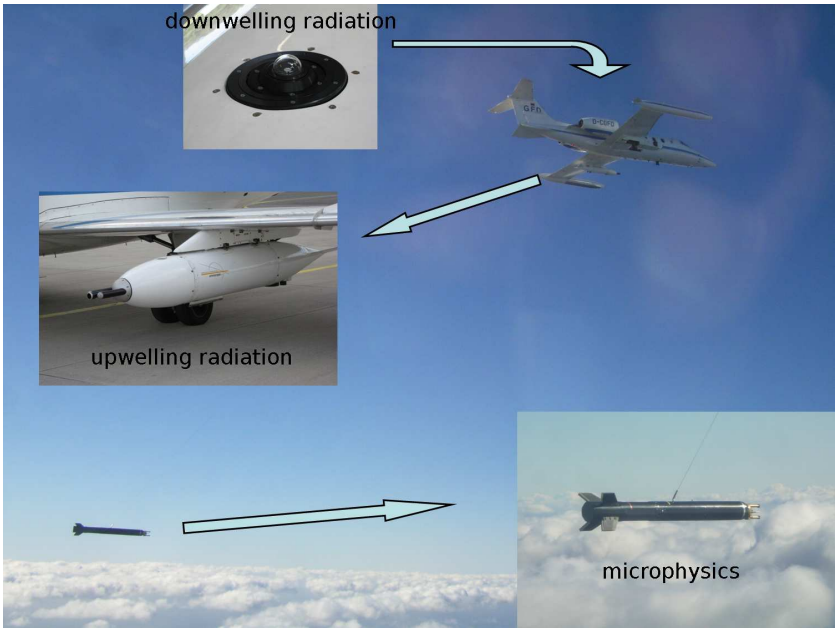

Figure 2.18: The tandem measurement platform AIRTOSS, picture from the first AIRTOSS flight on 4 Sep 2007 taken by enviscope GmbH. Locations of microphysics and radiation measurements are indicated.

Chapter 3

Experimental setup: Aircraft and tropical field campaigns

In situ measurements within the tropical UTLS (roughly $10\,\mathrm{km}$ to $22\,\mathrm{km}$ or $345\,\mathrm{K}$ to $550\,\mathrm{K}$ potential temperature) are hard to obtain due to the high altitude of this region. Looking at the European Facility For Airborne Research fleet (EUFAR; `http://www.eufar.net/`) it becomes clear that most research aircraft are not able to reach such altitudes. From this fleet only eight out of 40 aircraft can reach $12\,\mathrm{km}$ which is still too low to probe the tropical UTLS. Stratospheric balloons may be used to reach those altitudes. However, flying in the vicinity of deep convective systems with a balloon is problematic, e.g. due to strong turbulences. Therefore, specialised high altitude aircraft are required for field experiments that aim to obtain in situ measurements within the UTLS. Data and analyses from two of these campaigns are presented in the following chapters. This chapter provides information on the employed aircraft, the instrumentation, and the field experiments.

3.1 Aircraft: the M-55 Geophysica

Currently, only three research aircraft worldwide are able to reach the altitude of the tropical lower stratosphere. These are the National Aeronautics and Space Administration's (NASA) ER-2 and WB-57, and the Russian M-55 Geophysica. Only the latter is available to the European community through the Geophysica-European Economic Interest Grouping (EEIG) which was formed in January 2002 in order to plan all sci-

Figure 3.1: The high altitude research aircraft M-55 Geophysica, picture taken in Kiruna, Sweden, 2010.

Table 3.1: Geometrical and technical specifications of the M-55 Geophysica.

Wingspan	$37.5\,\mathrm{m}$	Takeoff weight	$24\,000\,\mathrm{kg}$
Overall length	$22.9\,\mathrm{m}$	Payload weight	$2155\,\mathrm{kg}$
Overall height	$4.83\,\mathrm{m}$	Cruising speed	$(640-720)\,\mathrm{km/h}$
Flight ceiling	up to $21\,\mathrm{km}$	Fuel capacity	$7600\,\mathrm{kg}$
Takeoff / landing distance	$1500\,\mathrm{m}$	Maximum endurance	$6.5\,\mathrm{h}$
Instrument bays	12	Power (AC)	$60\,\mathrm{kVA}$ / $115\,\mathrm{V}$
Crew	1	Power (DC)	$3\,\mathrm{kW}$ / $27.5\,\mathrm{V}$

entific operations of the M-55 Geophysica.
The M-55 Geophysica has been developed by the Soviet Union's Myasishchev Design Bureau (MDB) and built by Smolensky Aircraft Plant as a single-seated high altitude reconnaissance aircraft. It is a dual turbofan aircraft with a maximum ceiling of $21\,\mathrm{km}$. The aircraft speed ranges between $170\,\mathrm{m\,s^{-1}} - 200\,\mathrm{m\,s^{-1}}$ and the maximum flight time is 6.5 hours. The ceiling and flight time decrease when the M-55 Geophysica is carrying heavy payload, as is usually the case during field experiments. Details about geometry and other specifications are summarised in Table 3.1.
The first flight of the M-55 Geophysica took place on 16 August 1988. The M-55 Geophysica holds 16 world records, e.g. for altitude and climb rates, all set in 1993. While only five aircraft of this type were built, one of them has been modified and became one of the few operational stratospheric research aircraft. The M-55 Geophysica has a shorter radius of action compared to the other high altitude aircraft but it is more flexible during manoeuvres (e.g. dives) and less susceptible to bad weather conditions (e.g. side winds). It is an all weather aircraft and can thus fly in visual and instrumental meteorological conditions. Furthermore, it can operate in a wide range of ground weather conditions. The scientific instrumentation is installed in the various bays and in the wing carriers. The first scientific measurement campaign of the M-55 Geophysica was the Airborne Polar Experiment (APE 1) in winter 1996/1997 (Stefanutti et al., 1999; Borrmann et al., 2000b). More information about the Geophysica-EEIG and the aircraft itself can be found at `http://www.geophysica-eeig.eu/index.php`.

3.1.1 Instruments on board

During a campaign several instruments are deployed on the M-55 Geophysica, covering in situ and remote measurements of different parameters from chemical species, meteorological parameters to aerosol and cloud particle parameters. Figure 3.2 shows the cloud particle instruments (CIP and FSSP-100) located under the left wing of the aircraft. An overview of the complete instrumentation for the campaigns discussed below can be found in the Appendix, Table B.1. In the following, a brief description is given of those instruments from which data is used for this thesis. If not specified otherwise, sampling rates for all instruments are $1\,\mathrm{Hz}$, i.e. the data of the respective measured properties are acquired in time intervals of $1\,\mathrm{s}$. However, for the data reduction to higher order deliverables the sampled data often needed to be averaged over longer time periods. The accuracies, i.e. the degree of nearness of measurements of a quantity to its actual (true) value, and precisions, i.e. the degree to which repeated measurements under the same conditions show the same results

Figure 3.2: The two cloud particle probes (CIP and FSSP-100) mounted under the left wing of the M-55 Geophysica. This instrumental setup was used during the SCOUT-O3 and the SCOUT-AMMA campaigns.

and thus an indicator of the scatter of the measurements, are specified if stated in the publications related to the particular instruments.

Particles and water

CIP Cloud particles are detected by the CIP (as described in detail in Chapter 2) and microphysical parameters have been calculated in $2\,\mathrm{s}$ time intervals in order to combine with the FSSP-100 measurements.

COPAS For measurements of ultrafine aerosol particles the COndensation PArticle counting System (COPAS; Weigel et al., 2009) has been developed. COPAS operates with two Condensation Particle Counters (CPCs) and detects particles up to sizes of $1\,\mu\mathrm{m}$. The lower size limit is $6\,\mathrm{nm}$ and $15\,\mathrm{nm}$ for the two CPCs, respectively. A second COPAS has been deployed and the lower size limit was set to $10\,\mathrm{nm}$, whereby one additional channel was heated to $250\,^{\circ}\mathrm{C}$ in order to differentiate between volatile and non-volatile particles. The total accuracy is $\pm 10\,\%$ for each channel.

FISH A Lyman-α hygrometer named Fast In situ Stratospheric Hygrometer (FISH) detects the total water content in a range from $0.5\,\mu\mathrm{mol/mol}$ to $1000\,\mu\mathrm{mol/mol}$ (Schiller et al., 2008). This is accomplished by using the photofragment fluorescence technique and yields a precision of $0.2\,\mu\mathrm{mol/mol}$ and an accuracy of $6\,\%$ (Zöger et al., 1999). The FISH uses a forward facing inlet and thus samples total water, i.e. the sum of both gas-phase molecules and ice particles.

FLASH A second Lyman-α hygrometer for the measurement of gas phase water has been deployed: The FLuorescent Airborne Stratospheric Hygrometer (FLASH). Its measurement range is $0.5\,\mu\mathrm{mol/mol} - 300\,\mu\mathrm{mol/mol}$ at altitudes between $8\,\mathrm{km}$ and $21\,\mathrm{km}$. The precision is $0.2\,\mu\mathrm{mol/mol}$ and the accuracy is $8\,\%$ (Sitnikov et al., 2007). FLASH uses a backward facing inlet and thus samples gas-phase water only.

FSSP-100 The FSSP-100, as described in Section 2.8.3, was configured to measure cloud particles in the size range of $2.7\,\mu\mathrm{m} - 31\,\mu\mathrm{m}$. The sample rate was set to

$0.5\,\mathrm{Hz}$. No anti-shattering tips were mounted on the probe since those tips were first introduced in 2009.

MAL A Miniature Aerosol Lidar (MAL; Mitev et al., 2002) measures the backscatter and depolarisation ratio profiles in the vertical direction from $200\,\mathrm{m}$ to a few kilometers above and below the aircraft at a wavelength of $532\,\mathrm{nm}$. The vertical resolution of the profiles is $40\,\mathrm{m}$ and one profile is obtained in $15\,\mathrm{s}$.

MAS In order to give an in situ characterisation of the optical properties of the air masses in the atmosphere in close proximity to the aircraft (within $3\,\mathrm{m}$ to $30\,\mathrm{m}$), the Multiwavelength Aerosol Scatterometer (MAS) was designed (Adriani et al., 1999; Buontempo et al., 2006). This is a backscatter sonde which measures the volume backscatter ratio and the depolarisation ratio at $532\,\mathrm{nm}$ and $1064\,\mathrm{nm}$ wavelength. Under average measurement conditions in daylight, random errors are of the order of $2\,\%$ for the $532\,\mathrm{nm}$ backscatter ratio, and $5\,\%$ for the depolarisation (Cairo et al., 2004). The time resolution is $10\,\mathrm{s}$ and allows a resolution of horizontal spatial structures of a few hundred meters.

Chemical species

COLD In situ carbon monoxide measurements are performed by the Cryogenically Operated Laser Diode (COLD; Viciani et al., 2008) instrument which has a lower detection limit of a few $\mathrm{nmol/mol}$, an accuracy of $6\,\%$ to $9\,\%$ and a precision of $1\,\%$ at a time resolution of $4\,\mathrm{s}$.

FOZAN Ozone mixing ratios of $10\,\mathrm{nmol/mol} - 1000\,\mathrm{nmol/mol}$ are detected by the Fast OZone ANalyser (FOZAN; Yushkov et al., 1999; Ulanovsky et al., 2001) using chemiluminescence. FOZAN is a fast response ozonometre with an accuracy of $8\,\%$ and a precision of $0.01\,\mu\mathrm{mol/mol}$.

HAGAR A gas chromatograph for the detection of long-lived tracers (N_2O, H_2, CH_4, SF_6, CFC-11, CFC-12, Halon-1211) is the High Altitude Gas AnalyseR (HAGAR; Riediger, 2000). The time resolution is 90 seconds with accuracies of $(2-4)\,\%$, depending on the species. An additional non-dispersive infrared (IR) absorption sensor is used for CO_2 measurements. This sensor has a time resolution of 5 seconds, an accuracy of $0.1\,\%$, and a precision of about $0.3\,\mu\mathrm{mol/mol}$.

SIOUX Measurements of nitric oxides (NO), total reactive nitrogen (NO_y), and NO_y which is contained in particles larger than $107\,\mu\mathrm{m}$ are performed by the StratospherIc Observation Unit for nitrogen oXides (SIOUX; Voigt et al., 2005). The detection of NO of this two channel instrument relies on NO/O_3 chemiluminescence. Using a heated gold-converter and CO gas as a catalyst higher oxidised NO_y species are reduced to NO prior to detection. With a forward facing inlet gaseous and enhanced particulate NO_y can be sampled. The accuracy of the NO_y data is $\pm 18\,\%$ for total NO_y, $\pm 12\,\%$ for gas phase NO_y, and $\pm 5\,\%$ for NO. The detection limits for NO and NO_y are better than $1\,\mathrm{pmol/mol}$ and $5\,\mathrm{pmol/mol}$.

Meteorological parameters

TDC An autonomous Thermo Dynamic Complex (TDC) has been developed for the inflight measurements of ambient pressure, temperature, and wind speed. High precision sensors made by Rosemount as well as a unit for collecting, processing, and storing the measured data are part of this complex (Shur et al., 2007). The temperature accuracy is $0.5\,\mathrm{K}$.

UCSE Flight parameters, such as position, aircraft attitude, and true airspeed, are reported by the on board navigational system Unified Communications for System Engineer (UCSE) of the M-55 Geophysica (Sokolov and Lepuchov, 1998).

3.1.2 Further measurements

Besides the in situ measurements performed aboard the aircraft further data and tools are available for examining the meteorological situation. Satellite images provide an overview of the larger scale atmospheric situation. Images of e.g. cloud coverage are delivered by the European Organisation for the Exploitation of Meteorological Satellites (EUMETSAT)/European Space Agency (ESA) Meteosat Second Generation (MSG) satellites, Environmental Satellite (ENVISAT), and Cloud-Aerosol Lidar and Infrared Pathfinder Satellite Observations (CALIPSO), a joint NASA and Centre National d'Études Spatiales (CNES, French space agency) environmental satellite.
Numerical weather forecasts are an important tool for flight planning, not only for predicting weather conditions but also for the prediction of the chemical composition of the atmosphere. Furthermore, re-analysis data is used in order to relate the measurements to the meteorological context. Forward and backward trajectories are calculated based on European Centre of Medium Range Weather Forecast (ECMWF) data.

3.2 Campaigns

3.2.1 Tropical Australia: Stratospheric-Climate Links with Emphasis on the Upper Troposphere and Lower Stratosphere (SCOUT-O3)

In order to provide data and knowledge for the global assessments on ozone depletion and climate change for the Montreal and Kyoto Protocols the European Commission Integrated Project SCOUT-O3 has been initiated. 59 partner institutions and over 100 scientists from 19 countries are involved in the project that started on 1 May 2004 and expired on 31 April 2009. The SCOUT-O3 framework includes modelling studies with coupled chemistry-climate models (CCMs), tropical field campaigns during which data are collected aboard aircraft and balloons, laboratory studies, and satellite observations (from ENVISAT and CALIPSO). The project aims at an improved understanding of (a) processes in the UTLS, (b) past, present, and future status of the ozone layer and variability of ultraviolet (UV) radiation, (c) how clouds and aerosols modify the atmospheric radiation, and (d) how these processes contribute to climate change. Further general information on the SCOUT-O3 project are available under

http://www.ozone-sec.ch.cam.ac.uk/scout_o3/.
Part of the SCOUT-O3 project was an aircraft campaign in Darwin, Australia, in November and December 2005. The main objectives of this campaign were to gain a better understanding of

- the transport of trace gases through the TTL,
- the dehydration processes close to the tropical tropopause,
- the role of deep convection for these processes.

Darwin was chosen as campaign base not only for the good infrastructure but also because of the so-called Hector storm system. This is a mesoscale deep convective system that develops during the pre-monsoon period and during monsoon breaks almost every day over the Tiwi Islands, about $100\,\mathrm{km}$ north of Darwin (Crook, 2001). An extended description about the large scale meteorological context and about every single flight is given in Brunner et al. (2009) and Vaughan et al. (2008) who also report on the transfer flights. A total of nine local flights were performed of which the CIP delivered data during five flights successfully. The Mainz CIP was deployed the first time during this campaign. The flights were either dedicated to measurements of Hector or to the survey of the TTL (including transfer flights). Table B.2 in Appendix B summarises the flight objectives and the CIP data status for the single flights. During Hector flights the anvil tops and overshoot regions were probed in order to investigate the role of the convective overshoots in hydration (Kley et al., 1982; Corti et al., 2008) or dehydration (Danielsen, 1982; Sherwood and Dessler, 2001) of the UTLS. The CIP and FSSP-100 were deployed in order to provide cloud particle measurements within the Hector anvils and overshooting cloud tops. These measurements are presented in Chapter 5.

3.2.2 Tropical West Africa: African Monsoon Multidisciplinary Analysis (AMMA)

The African Monsoon Multidisciplinary Analysis (AMMA) is an international, long-term project to improve the understanding of fundamental scientific issues related to the West African Monsoon (WAM), its prediction, and the prediction of the impacts of WAM on the local society (Giles, 2006). Thus, one main objective was to gain a better understanding of the WAM and its influence on the physical, chemical, and biological environment on a regional to global scale. The project, which started in 2001, includes a dense observational network of routine and campaign-based measurements. Detailed information about the project can be found in Redelsperger et al. (2006) and on the AMMA homepage (http://www.amma-international.org). AMMA is funded by a large number of agencies, especially from France, UK, USA, and Africa with a major contribution from the European Community's 6th Framework Research Programme. During 2006 Special Observing Periods (SOP) took place within the AMMA framework during dry season, monsoon onset, peak monsoon, and late monsoon. A meteorological large-scale overview of the 2006 monsoon is given in Janicot et al. (2008). As part of the AMMA and SCOUT-O3 framework and within the SOP2 (peak monsoon) the SCOUT-AMMA campaign was conducted from

July 31 to August 18, 2006 based in Ouagadougou, Burkina Faso. The aim was to study effects of deep convection on aerosols, trace gases, and water vapour distributions, and to characterise the chemical composition and the transport mechanisms in the UTLS over West Africa. An overview of all SCOUT-AMMA activities, including balloon and sonde launches, is given by Cairo et al. (2010). The M-55 Geophysica performed nine flights in total during the SCOUT-AMMA campaign. Four of the flights were transfer flights (Verona - Marrakesh - Ouagadougou, and reverse) and five flights were local starting from Ouagadougou. The CIP was deployed during six of these flights (four local and two transfer flights), which are summarised in Table B.3. Different flight strategies have been set up for the different scientific goals, i.e. the investigation of the long-range transport or the probing of air that is linked to Mesoscale Convective Systems (MCS). In order to obtain measurements of cloud particles and microphysical properties of the MCSs the CIP and FSSP-100 were operated on board the Geophysica. The cloud observations of the MCSs are presented in Chapter 4. Additionally, encounters of subvisible cirrus were observed and those measurements are presented in Chapter 6.

Part II

Clouds in the TTL - observations of microphysical properties

Chapter 4

Mesoscale Convective System outflow over West Africa

This chapter presents in situ cloud particle measurements within Mesoscale Convective System outflows over West Africa during the West African Monsoon (WAM). The measurements have been performed by the CIP and FSSP-100 aboard the M-55 Geophysica during the SCOUT-AMMA campaign in 2006. In order to provide an overview of the meteorological background the properties of Mesoscale Convective Systems and their outflows as well as special aspects of these systems with respect to West Africa are outlined in Section 4.1. The measurements and case studies of the cloud microphysical parameters are presented in Section 4.2 and summarised in Section 4.3.

4.1 Meteorological background - Mesoscale Convective Systems

The structure of tropical deep convection is governed by complexes of thunderstorms which become organised and produce contiguous precipitation on scales that are larger than $100\,\mathrm{km}$ (Houze, 2004). These systems are called Mesoscale Convective Systems (MCS) and can take on a variety of forms. The two main forms are a) the Mesoscale Convective Complex (MCC), a circular-shaped structure, as defined by Maddox (1980), which lasts for at least six hours and has an interior cold cloud region (temperature $-52\,^{\circ}\mathrm{C}$) that has an area of $\geq 50\,000\,\mathrm{km}^2$, or b) squall lines that can extend up to $1000\,\mathrm{km}$. An example for both types is given by the MSG IR satellite image in Figure 4.1. MCSs often develop a large stratiform precipitation region and they account for most of the precipitation and latent heating in the tropics (Cetrone and Houze, 2009). The precipitation region of a mature MCS can be distinctly separated into a convective and a stratiform region (Houze, 2004), as can be seen in Figure 4.2 which shows a schematic of a mature MCS squall line (Houze, 1989, 2004). The general pattern of upward and downward motion in and around the clouds is indicated by the arrows. Near the gust front (bottom right) in the boundary layer the air starts to move upward. This motion propagates through the convective region and declines more gently into the trailing stratiform cloud in mid to upper levels. During the genesis and early development phases of such a squall line the stratiform precipitation

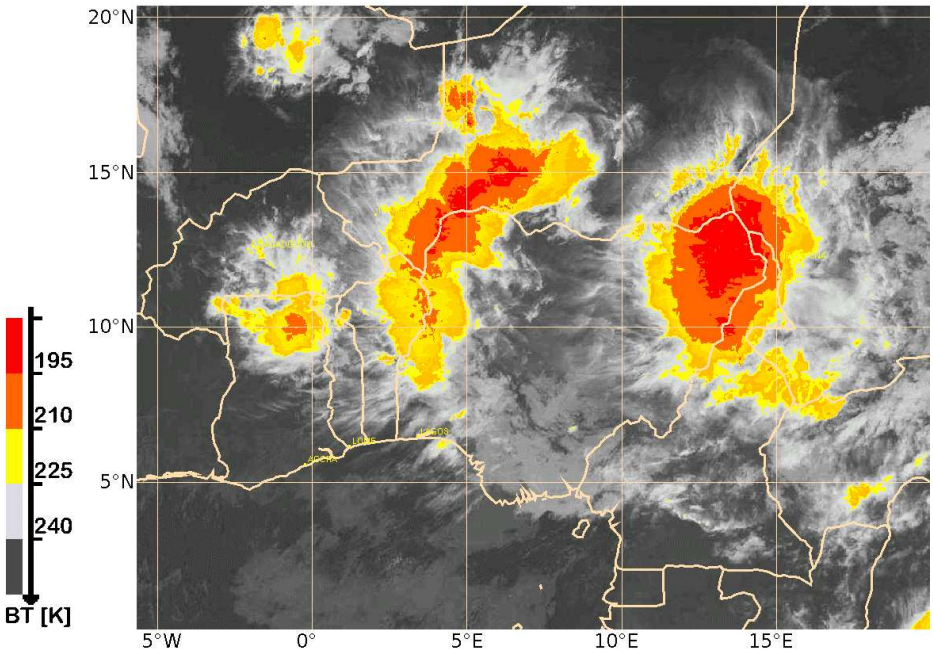

Figure 4.1: MSG IR satellite image of 10 Aug 2006, 23:45 UTC showing two MCSs over West Africa. An MCC on the right hand side extending in the yellow colours over roughly $500\,\mathrm{km}$ and a squall line on the left. The red colour indicates a cloud top temperature below $195\,\mathrm{K}$.

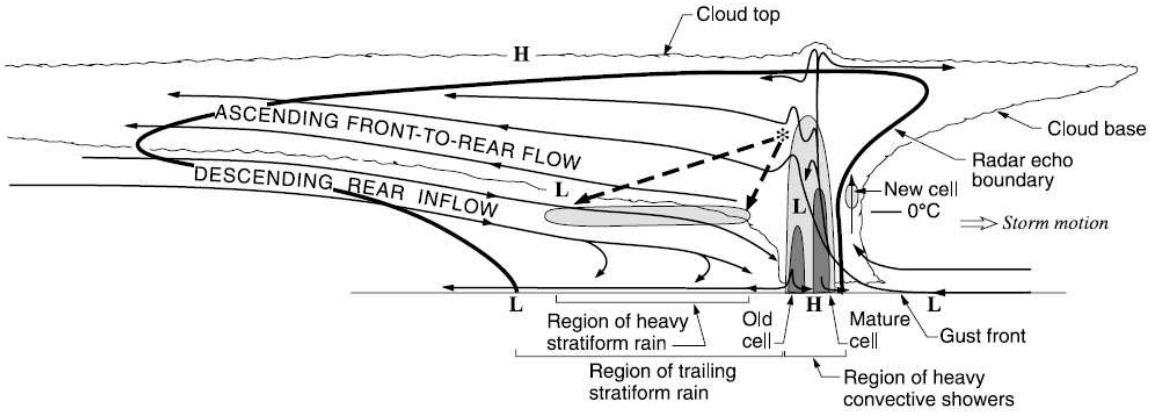

Figure 4.2: Schematic of a mature MCS squall line with trailing-stratiform precipitation, taken from Houze (2004). The thick black line shows the cloud boundary as seen by a weather radar. The shading indicates radar reflectivity and H and L mark centres of positive and negative pressure perturbations, respectively. Trajectories of falling ice particles passing through the melting layer are indicated by the dashed arrows. See text for further explanations.

regions are not present. At these early stages the convective cells are even more intense. In the area of the leading edge of the heavy convective shower region, or just ahead, new convective cells tend to form. These are followed by the mature cell which is associated with heavy precipitation. Weakening older cells follow the mature cell successively farther behind (just one older cell is indicated in Figure 4.2). Older cells are advected rearward above the layer of descending rear inflow and are thus located at increasingly higher altitudes. In this stage the structure as given in Figure 4.2 evolves and persists for $5\,\mathrm{h}$ to $10\,\mathrm{h}$. During this time the trailing stratiform region is associated with large amounts of rainfall. The presence of the forward overhang of cloud and precipitation is dependent on wind shear normal to the leading convective line. No such upper-level overhang exists if there is a strong relative flow towards the squall line at those levels (Houze, 1993b).
However, not all MCS are of such a leading-line/trailing-stratiform squall line structure as described above and depicted in Figure 4.2. A non-squall MCS may have no well-defined front or rear side. Apparently, the flow in the large-scale environment determines to a large extent the direction from which the middle level inflow enters the MCS (Houze, 2004). Nevertheless, any well-defined MCS is likely to have a stratiform rain area made up of cloud particles which were produced earlier in active convective cells and were then either left behind or advected from those cells (Houze, 1993a, 2004).
The region into which air from the convective cells is advected - the convective outflow region - has been the focus of the SCOUT-AMMA campaign. The level of main convective outflow is located at a pressure level of $200\,\mathrm{hPa}$ (Fueglistaler et al., 2009; Law et al., 2010) or in terms of potential temperature in altitudes of $345\,\mathrm{K}$ to $356\,\mathrm{K}$ (Folkins, 2002). Due to the intense convection in the mature cell the strong updraughts can penetrate a region above the cirriform cloud shield and produce overshooting cloud tops (which is subject of Chapter 5).
The lifetimes of MCSs can differ quite considerably depending on the system's spatial extent. From satellite IR data obtained during TOGA COARE[9] over the western Pacific warm pool Chen and Houze (1997) deduced maximum areal extents and lifetimes for the MCSs. The maximum size is defined as the square root of the net area of IR temperatures $< 208\,\mathrm{K}$ at the time of the maximum extent of the MCS. They found that the vast majority of smaller systems ($<150\,\mathrm{km}$) have a lifetime of only $1\,\mathrm{h}$ to $3\,\mathrm{h}$ while most of the systems larger than $300\,\mathrm{km}$ last for $8\,\mathrm{h}$ – $20\,\mathrm{h}$. Thus, MCSs with greater horizontal extension tend to have longer lifetimes as is obvious in Figure 4.3 which shows a frequency distribution of the MCSs observed during TOGA COARE in dependence of maximum size and lifetime. The time that large systems ($> 300\,\mathrm{km}$) needed to reach their mature stage (maximum area extent) was mostly between $6\,\mathrm{h}$ and $12\,\mathrm{h}$ but could be as long as a day. However, Chen and Houze (1997) note that these lifetimes for the large MCSs are an underestimation since the systems are tracked as long as their cloud top temperatures are below $208\,\mathrm{K}$ only, but they may not have been totally dissipated when the tracking algorithm dropped the particular MCS. Based on observations in 1986 and 1987 the West African MCS were found to have an average lifetime of 11.5 hours (Barnes, 2001).

[9] Tropical Ocean Global Atmosphere Coupled Ocean-Atmosphere Response Experiment, western tropical Pacific Ocean, November 1992 - February 1993 (Webster and Lukas, 1992; Yuter et al., 1995)

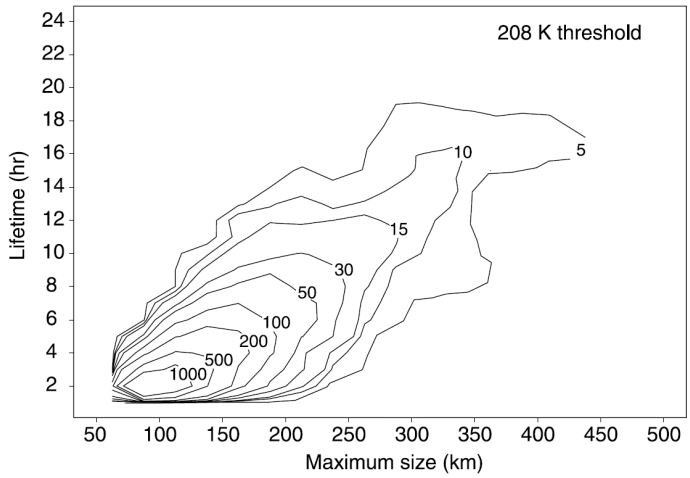

Figure 4.3: Occurrence frequency distribution of MCSs over the warm pool during TOGA COARE. The isolines show the number of occurrence (per 25-km-size interval per hour) of MCSs as a function of the maximum size reached by a convective system during its lifetime (from start to end of its life cycle). Adapted from Chen and Houze (1997) and Houze (2004).

4.1.1 MCSs in the West African Monsoon environment

In West Africa MCSs develop frequently during the monsoon and their occurrence was found to be correlated to African Easterly Waves (AEW; e.g. Fink and Reiner, 2003; Kiladis et al., 2006; Mekonnen et al., 2006). The AEWs are westward-propagating synoptic-scale waves, as e.g. described by Burpee (1972, 1974). Also, the African Easterly Jet (AEJ) plays a crucial role in organising moist convection and the generation of squall lines (Thorncroft and Blackburn, 1999). Therefore, a brief introduction to the West African flow conditions is given below, following to the description given by Hall and Peyrille (2006).

During spring and summer intense surface heating leads to a heat low and an ascending region with surface convergence and mid-tropospheric divergence over the Sahara. The air in this ascending region is well mixed by dry convection and is called the Saharan Air Layer (SAL). Potential and equivalent potential temperature are uniformly distributed within the SAL. The levels above the SAL are characterised by subsidence. In conjunction with the dry conditions this descent from above inhibits deep moist convection in the SAL. The Harmattan winds transport the hot, dry air of the SAL southwards. Contrary to the Harmattan, the monsoon flow carries oceanic air, i.e. colder moist air, from the south onto the continent. The confluence zone of these two currents is the intertropical discontinuity (ITD) or intertropical front (ITF). These flows are depicted in the meridional sketch in Figure 4.4 together with the SAL and further elements of the general flow configuration. When the heat low deepens the monsoon flow penetrates further north and the monsoon onset progresses. The northernmost extension that the ITF reaches in summer is at $20°$N and the ITCZ, also migrating north behind the ITF, is located at about $10°$N (Sultan and Janicot, 2003).

The Saharan heat low induces a meridional circulation that transports Saharan air south. As the SAL extends southwards it lifts above the cooler and moister monsoon flow at the front of the monsoon flow which is coming from the south. Here, between the ITCZ and ITF, the SAL limits convection such that deep moist convection oc-

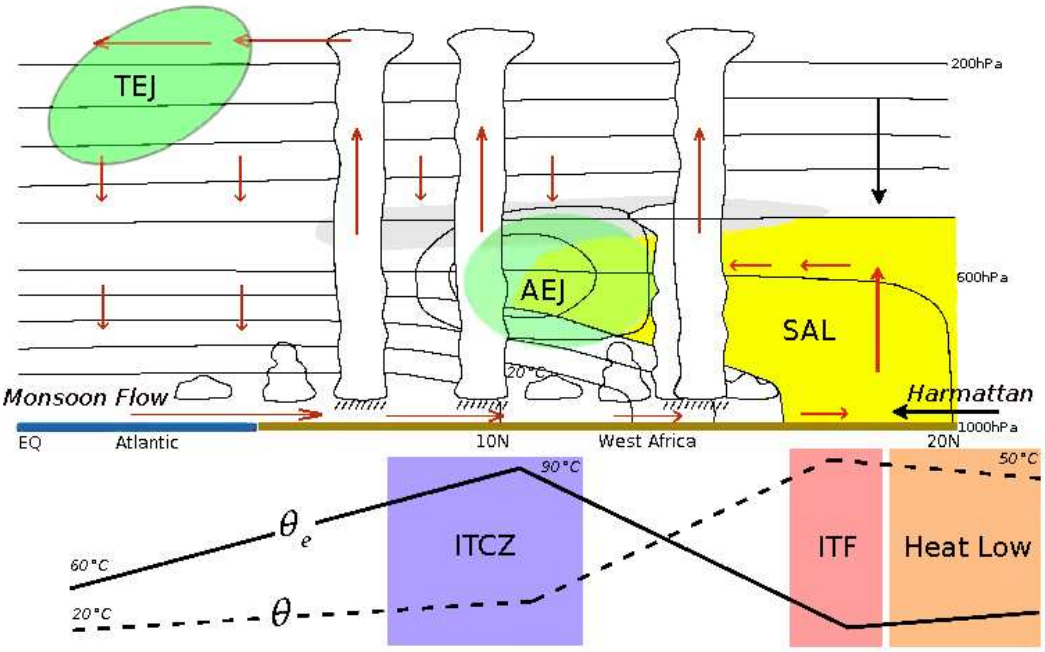

Figure 4.4: Schematical meridional cross-section showing the general flow configuration over West Africa in the monsoon season, with the typical meridional profiles of potential and equivalent potential temperature (θ and θ_e). A description of the single elements is given in the text. The figure is taken from Hall and Peyrille (2006).

curs in energetic organised large scale systems only, the MCSs (Parker et al., 2005). North of the equator the ascending branch of the Hadley circulation can be found. In the upper levels the air of the southern Hadley branch flows south and is deflected westwards by the Coriolis force. As a consequence the Tropical Easterly Jet (TEJ) evolves with its core at about $16\,\mathrm{km}$ altitude (Koteswaram, 1958; Hastenrath, 1991a). Another easterly jet that evolves seasonally over West Africa is the African Easterly Jet (AEJ) which is essentially geostrophic (Cook, 1999) and extends from the Red Sea to the Atlantic (Tompkins et al., 2005). The jet is in thermal balance with the temperature meridional gradient which develops due to the soil moisture gradient. Between the Gulf of Guinea and the Sahara there is a positive surface temperature gradient which, according to the thermal wind relation, induces an easterly shear over the surface monsoon westerlies. The vertical temperature lapse rate over the Sahara is steep whereas the temperature in the moister air further south decreases more slowly with height. Thus, the level at which the surface-induced positive temperature gradient reverses and becomes negative in the free atmosphere determines the height of the AEJ. The AEJ has a maximum speed of around $12.5\,\mathrm{m\,s^{-1}}$ at a pressure altitude of $600\,\mathrm{hPa}$ to $700\,\mathrm{hPa}$ and at $15°$N (Thorncroft and Blackburn, 1999). African Easterly Waves (AEW) develop along the AEJ which are barotropically and baroclinically unstable (Burpee, 1972). The AEWs feed on this combined instability and thus draw energy from the AEJ. Therefore, the AEWs are weakening the AEJs (Gu and Adler, 2004). Detailed investigations of the relationship between AEJ and AEW were presented by Leroux and Hall (2009). Convective cloud and precipitation amounts have been found to be definitely related to AEWs (e.g. Reed et al., 1977) and further analyses of this relationship indicate that MCSs tend to occur in preferred regions in

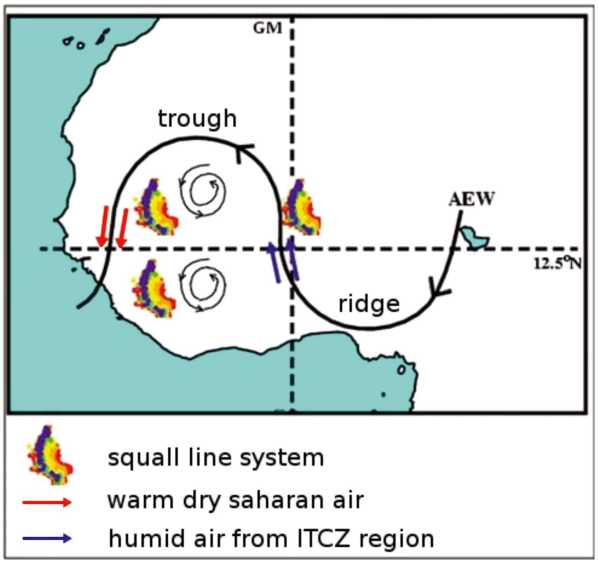

Figure 4.5: Schematic of AEW at $850\,\mathrm{hPa}$ to $700\,\mathrm{hPa}$ taken from Fink (2006). The stylised rain rates indicate the preferred locations of MCS.

the AEWs (Mekonnen et al., 2006, and references therein): Over land and in vicinity of the ITCZ MCSs occur at or ahead of the AEW trough, north of the ITCZ convection is enhanced ahead of the AEW ridge; and over the ocean MCSs are collocated with the trough. The positions of the MCSs in relation to the AEW is depicted in Figure 4.5. This brief overview shows that the manifestation of the WAM is associated with seasonal reversals in the upper tropospheric circulation. When the summertime heating over the land surfaces weakens (due to the seasonal migration of the sun) the circulation patterns over West Africa change. The WAM ends with the appearance of upper tropospheric westerlies from October onwards (Hastenrath, 1991a).
After the discussion of the meteorological context of the West African MCSs, the following gives an overview of the microphysical properties of the MCSs. Cetrone and Houze (2009) allude to the difference between the anvils of MCSs in West Africa, the Maritime Continent (i.e. the islands of Indonesia, Philippines, and parts of Southeast Asia), and the bay of Bengal. Due to the greater buoyancy over the West African continent, stronger updraughts are prevalent and would be more likely to produce larger graupel particles compared to the ice particles within maritime MCSs. The extremely high lightning frequency (Cecil et al., 2005; Houze, 2004) is a further indication for graupel existence in the African MCSs. Chain aggregates were observed in the outflow of continental storm systems over Florida, USA, and Northern Australia (Connolly et al., 2005). The aggregation was explained by the electrification of the clouds due to lightning and has not been observed in maritime convective systems near Kwajalein Atoll, Marshall Islands, where there is less lightning activity. During in situ measurements described by Bouniol et al. (2010) rimed aggregates have been detected in West African MCS anvils. Their observations were performed at ambient temperatures between $228\,\mathrm{K}$ and $257\,\mathrm{K}$. The particle densities and diameters were found to decrease when moving further rearward from the stratiform towards the cirriform anvil region. These were the first reported in situ measurements of ice particles in the West African MCS anvils. However, no distinction between the detrained cloud parts and the direct outflow from the convective core has been performed. Further-

more, the clouds in the MCSs may reach much higher altitudes and corresponding colder temperatures. Thus, a detailed description of the microphysical properties within West African MCS outflow clouds is lacking. Filling this gap is subject to the analysis presented in Section 4.2 including measurements reaching into the TTL.

4.1.2 Outflow identification

In order to differentiate between air masses in an outflow, i.e. air masses that have directly been advected from the convective core region, and the surrounding air masses in an MCS it is important albeit not easy to identify air masses that have been influenced by convection. Convection is a fast transport process and becomes increasingly dominant below the level of zero net radiative heating (Vaughan et al., 2008). Generally, vertical updraught speeds in deep convective systems range in the order of several tens of $\mathrm{m\,s^{-1}}$ (Quante, 2004). Thus, air masses are transported from the lower troposphere to the upper troposphere in about $30\,\mathrm{min}$ (Thompson et al., 1997; Houze, 2004). Due to different chemical compositions of air masses in the boundary layer and in the UT/TTL region air masses that have been transported by convection have specific signatures. Mixing, chemical loss and deposition appear negligible during vertical transport for major species like CO and NO_x (Bechara et al., 2010) whereas HNO_3 is reduced efficiently due to wet scavenging (Bertram et al., 2007; Monks et al., 2009). Satellite images can be used to estimate whether clouds are connected to deep convection. In order to identify if clouds or cloud-free air masses have been influenced by deep convection trace gas measurements are taken into account, e.g. of NO_x, NO_y, CO_2, CO, and O_3. In order to identify outflow clouds it is important to consider that not all MCS anvil clouds are necessarily part of an outflow. Cloud particles may sediment out of the outflow air stream, extending the anvil downwards to regions without outflow current. Furthermore, as reported by e.g. Garrett et al. (2006), pileus clouds may form directly above the anvil. Thus, clouds may be present just above or below the outflow without belonging to the direct convective outflow. In both cases an outflow identification is only possible by the detection of trace gases. Trace gas mixing ratios within convectively lifted air masses and air masses in the unaffected atmosphere may differ due to production of the tracers in convection or uplift from boundary layer air that contains other mixing ratios. Due to the different lifetimes (c.f. Table 4.1) of the tracers the outflow age, i.e. the time since the air mass has been advected from the updraught into the outflow, can be estimated. In the measurement section of this chapter (Section 4.2) the terms young, recent, and aged outflow are used. In the first instance these terms do not define a specific age but shall rather indicate that there are outflows of different ages which are arranged in the order young, recent, aged. The particular contribution of the tracers that have been measured on board of the M55 Geophysica (i.e. NO, NO_y, CO_2, CO, and O_3) to the outflow identification is explained below.
Lightning is the dominating source of NO_x (= NO + NO_2, NO_x produced by lightning is also called lightning NO_x (LNO_x)) in the upper troposphere (Schumann and Huntrieser, 2007; Höller et al., 2009; Huntrieser et al., 2009) and lightning is (mostly) present in the deep convective parts of MCSs. There is a rapid interconversion between NO and NO_2 (Levine et al., 1984). NO_x are short-lived species and are chemically transferred to NO_y, which is the sum of all oxidised nitrogen compounds

Table 4.1: Lifetimes of trace gases in the upper troposphere used for outflow identification.

Tracer	Lifetime	Reference
CO	20 to 30 days/ ≈ 50 days	Real et al. (2008)/Avery et al. (2010)
CO_2	several hundred years	Archer (2005)
O_3	≈ 50 days	Avery et al. (2010)
NO_x	2 to 5 days	Huntrieser et al. (2007)
HNO_3[a]	10 to 20 days	Schumann and Huntrieser (2007)
PAN[a]	weeks to months	Murphy et al. (1993)

[a]The lifetime of NO_y is constrained by the most long-lived species of NO_y. The lifetime of HNO_3 is given here since it is one major constituent of NO_y. Furthermore, PAN lifetime is presented since it is a rather long-lived NO_y constituent.

including NO_x, e.g. by

$$\mathrm{NO_2 + OH + M \longrightarrow HNO_3 + M} \qquad \text{(R 4.1)}$$

where M represents a molecule that absorbs the excess vibrational energy (Bertram et al., 2007). Due to the short lifetime of NO_x high NO_x concentrations can be taken as indicator for recent convective influence. Several studies corroborate the use of the ratio between NO_x and NO_y or single species of these two groups, e.g. NO_x/NO_y (Jaegle et al., 1998), NO_x/HNO_3 (Bertram et al., 2007), NO/NO_y (Ziereis et al., 2000; Hamburger, 2007), as an age indicator for outflow. A high ratio indicates a recent production of NO or NO_x by lightning and thus a deep convective influence. For example, Jaegle et al. (1998) observed a NO_x/NO_y ratio of 0.1 to 0.8 with an average of 0.2 above $8\,\mathrm{km}$ over the Central USA. Over West Africa NO/NO_y ratios of up to 0.47 were found in an altitude of $10\,\mathrm{km}$ (Hamburger, 2007), while the maximum flight altitude for their experiment was $12\,\mathrm{km}$. Furthermore, Hamburger (2007) established an index (I_{NONO_y}) ranging from 1 to 10 in order to differentiate between air masses that have not been influenced by convection ($I_{NONO_y} = 1$) and air masses that have recently detrained from the convective cell ($I_{NONO_y} = 10$). It has to be noted that enhanced NO mixing ratios can also result from uplift of soil emissions. For example, Stewart et al. (2008) found mixing ratios of $1\,\mathrm{nmol/mol}$ for soil emissions. On the other hand soluble NO_y species might be removed by wet deposition and thus reduce the NO_y mixing ratios (Tuck, 1976) in the convective cells. In model simulations by Grewe (2009) highest LNO_x emissions were found in the main convective outflow level.
CO_2 can be used as tracer over continental regions. Plants remove CO_2 from the air in the boundary layer which is transported upwards through the convective updraughts. Thus, air with reduced CO_2 concentrations, i.e. a deviation with respect to the average value, found in the upper troposphere is an indicator for convective influence (Fierli et al., 2011). However, Homan et al. (2010) state that CO_2 cannot be used to distinguish between recent and older convection due to the relatively long lifetime of CO_2.
Furthermore, ozone (O_3) poor air can be transported upwards into the TTL region in deep convection (Bertram et al., 2007). Here, the mixing ratio, if not affected by other processes, steadily increase by photochemical production until the steady state is reached (Homan et al., 2010). Therefore, ozone could be used as indicator for the age of the possible outflow air masses. Besides the photochemical production there are other sources for an ozone increase: the ozone mixing ratio can be affected by

mixing with stratospheric ozone-rich air or may increase due to photolytic production of ozone by LNO_x (Thompson et al., 2000).
However, not only local convection influences the tracer composition over West Africa but also transport of air masses from remote areas: In the Asian summer monsoon air masses are uplifted to the UT and trapped in the Asian Monsoon Anticyclone (AMA). In the south the AMA is flanked by the TEJ which is responsible for the transport of air masses from India and Southeast Asia over Africa (Barret et al., 2008). Domain filling trajectory analyses indicate that roughly $39\,\%$ of the air masses at about $355\,\mathrm{K}$ potential temperature in the West African TTL during August 2006 were influenced by mid to lower tropospheric air from Asia, India, and oceanic regions (Law et al., 2010). That means there was import of clean oceanic (e.g. O_3-poor) or polluted air masses from Asia (high O_3, CO, CO_2) into West Africa. Furthermore, Law et al. (2010) estimated an impact of about $52\,\%$ from local convection on the lower TTL during the SCOUT-AMMA period. Biomass burning plumes from central Africa are transported to the north-east where they are uplifted by deep convection and further transported to West Africa by the TEJ (Real et al., 2010). Furthermore, mixing of air masses from the lower stratosphere into the TTL region can affect the tracer composition (Marcy et al., 2007). Thus, it is important to consider possible sources and sinks of the trace gases when using these as indicator for convection.

4.2 Measurements of MCS outflow

In the course of the 2006 West African Monsoon several MCSs were encountered by the M-55 Geophysica during the SCOUT-AMMA campaign. Thus, during three local flights and one transfer flight observations in the vicinity of MCSs were obtained. Whether the cloud encounters were within an outflow region has been identified by tracer measurements (NO, NO_y, CO_2, CO, and O_3), analysis of backtrajectories, and by inspection of satellite images. Cloud particle data are examined carefully, the specific corrections that have been applied to the data measured by the CIP can be found in Appendix A as well as further considerations about shattering. The main results of the following analysis are subject of a publication by Frey et al. (2011).

4.2.1 Satellite observations

Figure 4.6 shows the MSG IR satellite images of the cloud configurations for the flights which are discussed in the following subsections. The image for the most interesting part of the respective flight has been chosen in each case. The cloud observations which are discussed below have been performed during those time periods. The red lines in the satellite images display the complete flight tracks of the individual flights while the blue section of each line highlights that part of the flight track which was executed in the $30\,\mathrm{min}$ around the time as the satellite image was taken. One degree latitude and longitude in these images correspond to roughly $100\,\mathrm{km}$ distance. The general flow direction is from East to West (easterly trade winds). The satellite image of 7 August (Figure 4.6(a)) shows that the air in the wake of a large MCS has been probed. On the eastern part of the highlighted flight track the aircraft encountered a smaller, developing MCS which had an horizontal extent of roughly

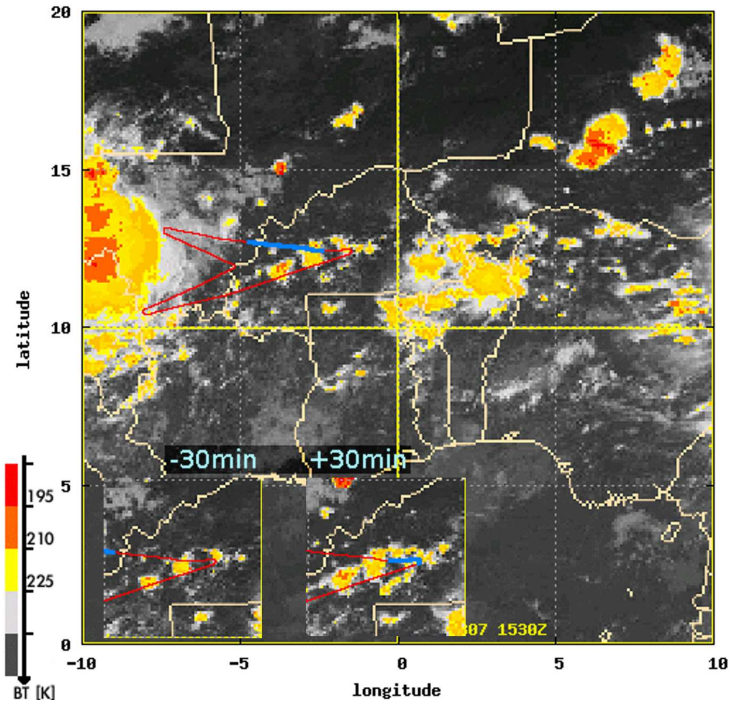

(a) 7 Aug 2006, 15:30 UTC

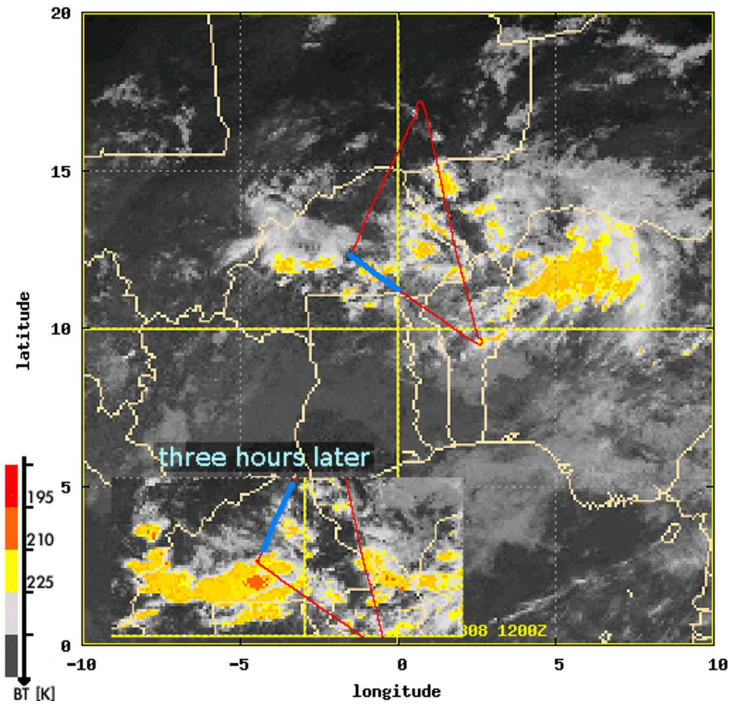

(b) 8 Aug 2006, 12:00 UTC

Figure 4.6: MSG IR satellite images showing the cloud top temperatures indicative of the atmospheric cloud arrangements which were prevalent during the individual flights. The tropical colour threshold has been used for the IR images, i.e. $-65\,^{\circ}\mathrm{C}$ is displayed in orange (MCS tracking orange), other colours are indicated in the colour scale in the lower left of each satellite image. In (a) and (b) sections of particular interest are superimposed on the satellite images (see text for details).

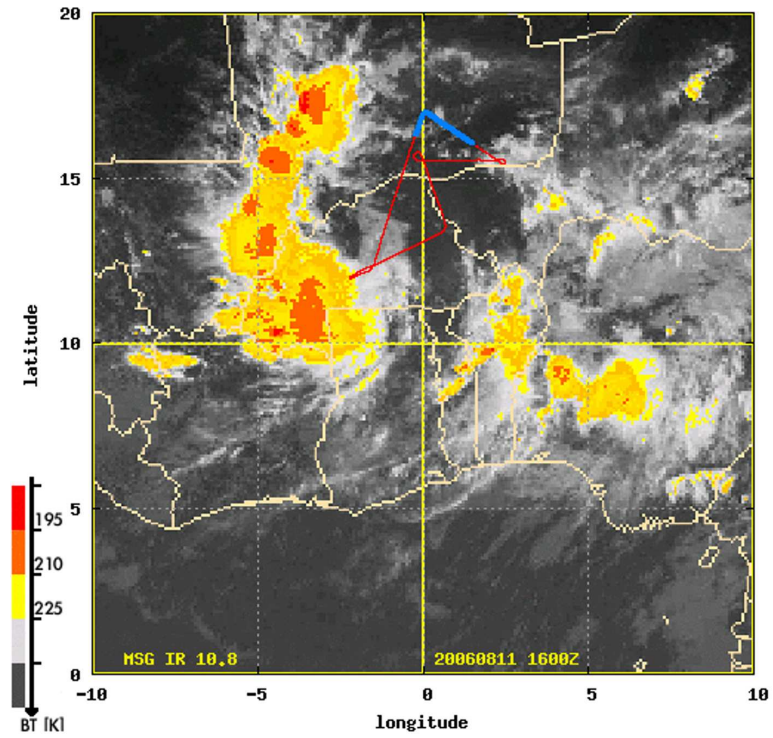

(c) 11 Aug 2006, 16:00 UTC

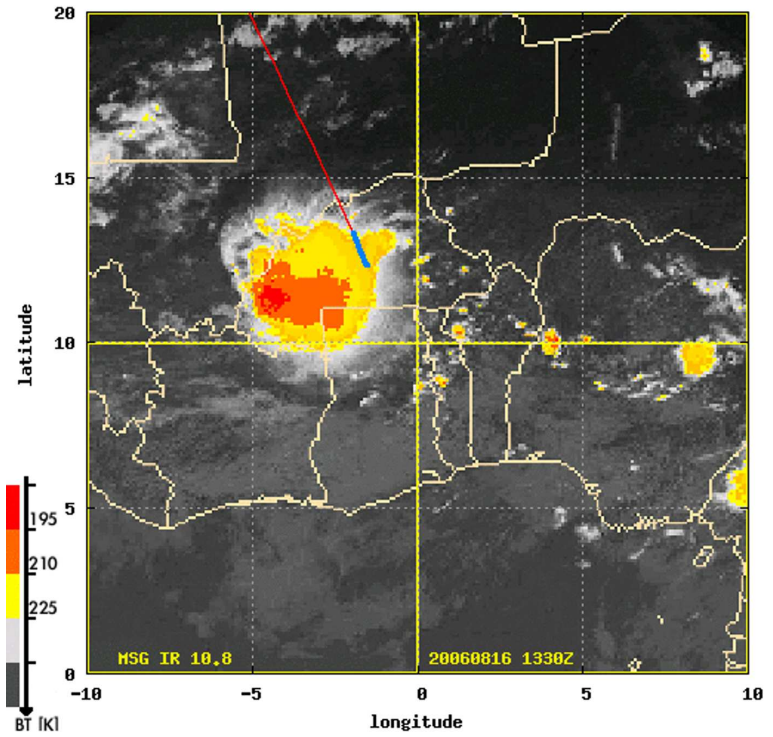

(d) 16 Aug 2006, 13:30 UTC

Figure 4.6: *continued*

$70\,\mathrm{km} \times 90\,\mathrm{km}$. Superimposed on this satellite image are the two sections of the satellite images (between $5°\mathrm{W}$ and $0°\mathrm{W}$ and $10°\mathrm{N}$ and $15°\mathrm{N}$) 30 minutes before and after the current image in order to show the development of this particular MCS. The cloud system was not visible in the satellite image taken two and a half hours before. Thus, the clouds observed during this flight segment have probably formed just a few hours before and are possibly located in a young outflow.
The flight of 8 August aimed at the validation of the CALIPSO satellite measurements. The cloud field is less intense and in a developing stage. No mesoscale clouds have been probed at this time. However, the yellow/orange colours of the small clouds indicate cloud top temperatures of around $210\,\mathrm{K}$. It can be assumed that these cloud tops belong to small convective cells. The section of the satellite image between $5°\mathrm{W}$ and $5°\mathrm{E}$ and $10°\mathrm{N}$ and $15°\mathrm{N}$ taken three hours later shows that the cloud field became denser in the measurement region (especially in the western part of the flight region) and that an MCS had developed. Thus, the sparse cloud field at the beginning of the flight might have been a precursor of a developing MCS.
The flight of 11 August was performed in the wake of a huge squall line with a meridional extent of approximately $1000\,\mathrm{km}$. The broadest extent in longitudinal direction was about $500\,\mathrm{km}$. At the time of the cloud encounters the distance of the aircraft to the MCS squall line was about $300\,\mathrm{km}$ to $400\,\mathrm{km}$. About seven hours earlier the core MCS had crossed the flight track at that point. Any outflow air probed by the aircraft had thus time to undergo considerable chemical processing and is presumably a result of an aged outflow.
The flight on 13 August focused on measurements of long range transport and did only encounter low-level clouds. This day was exceptionally cloud free and therefore no satellite image is provided here.
On the transfer flight from Ouagadougou to Marrakech on 16 August a vertical profile through an MCS of roughly $400\,\mathrm{km}$ in diameter was obtained. The horizontal distance to the core region of the MCS was estimated from the satellite image to be about $300\,\mathrm{km}$. Still, the probed clouds are connected to the system (in contrast to the cloud events on 11 August) and thus it can be concluded that possible outflow observations result from a more recent outflow.
In order to further gain an estimate about possible outflow ages, synoptic backtrajectories have been calculated from ECMWF data and matched with the MSG satellite observations (Fierli et al., 2011). The analyses indicate ages of less than three hours on 7 August, around five hours on 16 August, and about ten hours on 11 August (c.f. Figure C.1 in Appendix C.1).

4.2.2 Tracer observations

In the following trace gas measurements are examined in order to corroborate the indication of outflow encounters by satellite and trajectory analysis. Furthermore, the exact times of the outflow encounters can be identified by tracer measurements. In Figure 4.7 vertical profiles of tracer mixing ratios are displayed. The profiles comprise tracer data from time periods close to and during outflow events that contain cloud encounters. Vertical profiles for each single flight including meteorological and cloud particle parameters can be found in the Appendix C.1, Figures C.2 – C.5. The tracer data in Figure 4.7 are colour coded for each flight. The potential temperature (θ)

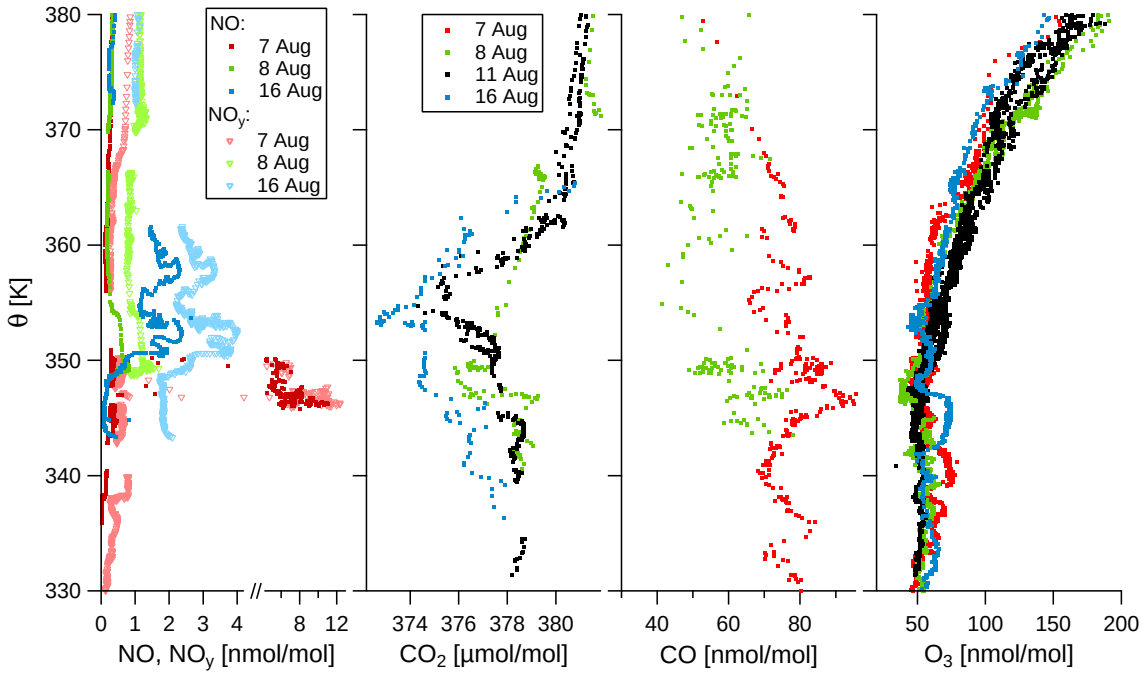

Figure 4.7: Tracer profiles for extracted time periods that contain cloud encounters concurrently to an outflow event from the flights on 7 (red), 8 (green), 11 (black), and 16 (blue) Aug 2006. The uncertainties of the measurements are stated in Table 4.2, except for ozone which is measured with an accuracy of $8\,\%$.

Table 4.2: Differences of trace gas mixing ratios between the outflow regions and the UTLS background. The last column gives the measurement accuracies of the respective species.

	Date	7 Aug	8 Aug	11 Aug	16 Aug	accuracy
ΔNO	[nmol/mol]	10.5	0.6	n.a.	2.3	$\pm 5\,\%$
ΔNO_y	[nmol/mol]	11.7	0.8	n.a.	3.2	$\pm 12\,\%$
ΔCO	[nmol/mol]	26.9	22.0	n.a.	n.a.	$\pm(6$ to $9)\,\%$
ΔCO_2	[μmol/mol]	n.a.	-2.7	-4.2	-4.7	$\pm 0.1\,\%$

has been chosen as vertical coordinate since thermodynamics determine the height of the outflow and the potential temperature yields a better comparability between the flights. In the leftmost panel, the vertical profiles of NO and NO_y are displayed. Remarkably high mixing ratios of $11\,\mathrm{nmol/mol}$ and $12.4\,\mathrm{nmol/mol}$, respectively, were measured on 7 August in an altitude range between $345\,\mathrm{K}$ and $350\,\mathrm{K}$ which indicates a very recent outflow event. This is supported by the very high ratio of NO to NO_y of around 0.82. The age index I_{NONO_y} of Hamburger (2007) sets a threshold of 0.4571 for indication of most recent outflow at this altitude which is much lower than the observed ratio. An enhancement in these tracers can also be seen on 16 August above $350\,\mathrm{K}$. However, the mixing ratios were not as high as on 7 August which can be indicative either for less lightning (weaker source) or for removal of the tracers by chemical processing or washout. The difference in the two mixing ratios indicates that the air had some time to be processed and NO was transformed to higher oxidised species. Still, the high NO values indicate a recent outflow but not as young as the event on 7 August. Slightly enhanced mixing ratios of NO were found below $350\,\mathrm{K}$ on 8 August while no data are available on 11 August. The particular maximum

deviations from the UT background mixing ratios for NO, NO_y, and the other trace gases are summarised in Table 4.2 for the respective flights.
A closer look on the CO_2 distributions reveals more evidence for convective activity. On 8 August only slightly decreased mixing ratios were observed. Either the convection has not been as strong and did not carry much of CO_2 poor air upwards or the air masses have not recently been influenced by convection. Since CO_2 is a longer lived tracer and the region is heavily convectively influenced during the monsoon somewhat decreased CO_2 mixing ratios may have survived (Homan et al., 2010). Clear evidence for convective influence can be seen on 11 and 16 August. A distinct minimum is obvious between $352\,\mathrm{K}$ and $358\,\mathrm{K}$ on 11 August and an extended minimum between roughly $347\,\mathrm{K}$ and $360\,\mathrm{K}$ on 16 August. The latter confirms the enhanced NO and NO_y mixing ratios as observed on 16 August. However, decreased NO and NO_y mixing ratios can be found between $353\,\mathrm{K}$ and $356\,\mathrm{K}$ concurrently to a distinct minimum in CO_2. Possibly this filament resulted from more recent uplift of NO, NO_y, and CO_2 poor air masses from the boundary layer compared to the probed air masses slightly above and below this layer. This observation indicates that air masses within this MCS have not mixed significantly and thus different air masses have been probed.
CO measurements are available from two flights only. The CO mixing ratios on 7 August are enhanced in the same altitude band as were the NO and NO_y mixing ratios during this flight ($345\,\mathrm{K}$ to $350\,\mathrm{K}$). Thus, it gives a further indication of convective influence. The measurements on 8 August show a slight enhancement in this altitude region as well.
The ozone profiles of all flights look similar, although some deviations are to be mentioned. The profiles of 7 and 16 August show clear increases in ozone in the altitude range of $340\,\mathrm{K}$ to $348\,\mathrm{K}$. Since no correlation to NO or NO_y can be found, the enhanced ozone mixing ratios do probably not result from the recent outflow events and concurrent photochemical production, but could rather be due to downwind production of ozone from lightning NO_x emissions produced by an MCS upwind or due to uplift of soil NO_x emissions which are more elevated over the Northern Sahel region (Barret et al., 2010). Above $350\,\mathrm{K}$ and up to about $370\,\mathrm{K}$ the ozone profiles diverge. The profile of the 11 August shows the highest ozone mixing ratios. Following Avery et al. (2010) low ozone mixing ratios in the upper troposphere indicate convective transport. Lowest ozone concentrations are found for the flight on 7 August between $355\,\mathrm{K}$ and $364\,\mathrm{K}$ and on 16 August around $353\,\mathrm{K}$, where also a distinct minimum in CO_2 is apparent. Since ozone is a less long-lived species, it can more conveniently be used as age indicator for outflows. Thus, the higher ozone mixing ratios support that the outflow cases on 11 August are the most aged events.

The inspection of the satellite images, trajectory analysis, and tracer data indicates that the outflow case on 7 August is the most recent ($<3\,\mathrm{h}$), followed by the case on 16 August ($\approx 5\,\mathrm{h}$), and 11 August as most aged outflow case ($\approx 10\,\mathrm{h}$). Therefore, the cases will be described in this order. The measurements of 8 August did not clearly identify an outflow, although they show slight convective signatures. Nevertheless, the region has been in an MCS precursor state and thus, this cloud event will also be discussed.

4.2.3 Young outflow case on 7 August 2006

On the descent of the flight on 7 August the aircraft encountered a developing MCS which had an extent of roughly $70\,\mathrm{km} \times 90\,\mathrm{km}$. By definition, this is not yet an MCS (not larger than $100\,\mathrm{km}$ in at least one horizontal direction). Since the system was, however, in a growing state this cloud is defined here as pre-mature MCS with concurrent young outflow. A close-up of the time series[10] for this MCS crossing is displayed in Figure 4.8. A time series for the whole flight can be found in the Appendix, Figure C.6. The cloud extended from $13.2\,\mathrm{km}$ to $11\,\mathrm{km}$ altitude in the vertical and three parts can be discerned (as indicated on top of Figure 4.8). The upper $1\,\mathrm{km}$ is characterised by lower cloud particle concentrations and very high ultrafine aerosol particle concentrations (N_{6-15} denoting the number concentration for particles with diameters between $6\,\mathrm{nm}$ and $15\,\mathrm{nm}$). These high values reveal a new particle formation event which is described in further detail in Weigel et al. (2011). Furthermore, the tracer measurements give no indication for outflow air masses in this cloud part, e.g. the NO mixing ratio is low. The NO mixing ratio stays low during the second cloud part, while ozone is decreasing. Also the ultrafine aerosol number concentration decreases until the new particle formation ceased. The cloud particle number concentration increases by almost a factor of ten. In the lowest part of the cloud the NO and NO_y increase significantly to remarkably high values of up to $11\,\mathrm{nmol/mol}$ and $12.4\,\mathrm{nmol/mol}$, respectively. Such high values indicate a very recent or high production of NO in lightning. Furthermore, the NO had not or just to small amounts been further processed and oxidised to NO_y as can be deduced from the NO to NO_y ratio. CO peaks at the same time with a maximum of $96\,\mathrm{nmol/mol}$ while ozone remains reduced at around $50\,\mathrm{nmol/mol}$ compared to roughly $60\,\mathrm{nmol/mol}$ in the layers above and below. The cloud particle number concentration remains high throughout this cloud part. Several time periods from above and inside the outflow have been selected for calculating the cloud particle size distributions. These time periods are shaded in blue in Figure 4.8 and labelled with *A1 – A3* (*A* denoting cases above the outflow) and *O1 – O3* (denoting outflow cases). The size distributions are displayed in Figure 4.9, the *A* cases in the upper panel in green and the outflow cases in black in the middle panel. For better comparison all given size distributions are summarised in the lower panel and some more information on the single events are given in Table 4.3. Details on how the size distributions from the CIP and FSSP-100 measurements are combined and information about the error bars are given in Appendix A, Section A.3. An enhancement of particle concentrations in the FSSP-100 size bins due to shattering cannot be ruled out, especially for those size distributions where CIP and FSSP-100 have a little jump in the overlapping size range (here, *A2*, *O2*, and *O3*). In case the CIP observations indicate a higher fraction of shattered particles the FSSP-100 part of the size distributions is underlayed with a shading (for further explanations see Appendix Section A.4.2). Additionally, a slight decrease in CIP particle concentrations might be possible due to the Double Particles which partly occurred before and after the outflow events, although time periods with Double Particles were examined carefully and consequently excluded from the size distribution analysis. When descending to the outflow level, the size distributions show that the maximum particle sizes steadily increase. The largest particles in the highest cloud level (*A1*) were smaller than $400\,\mu\mathrm{m}$

[10] The time here and in the following is given in seconds from midnight UTC

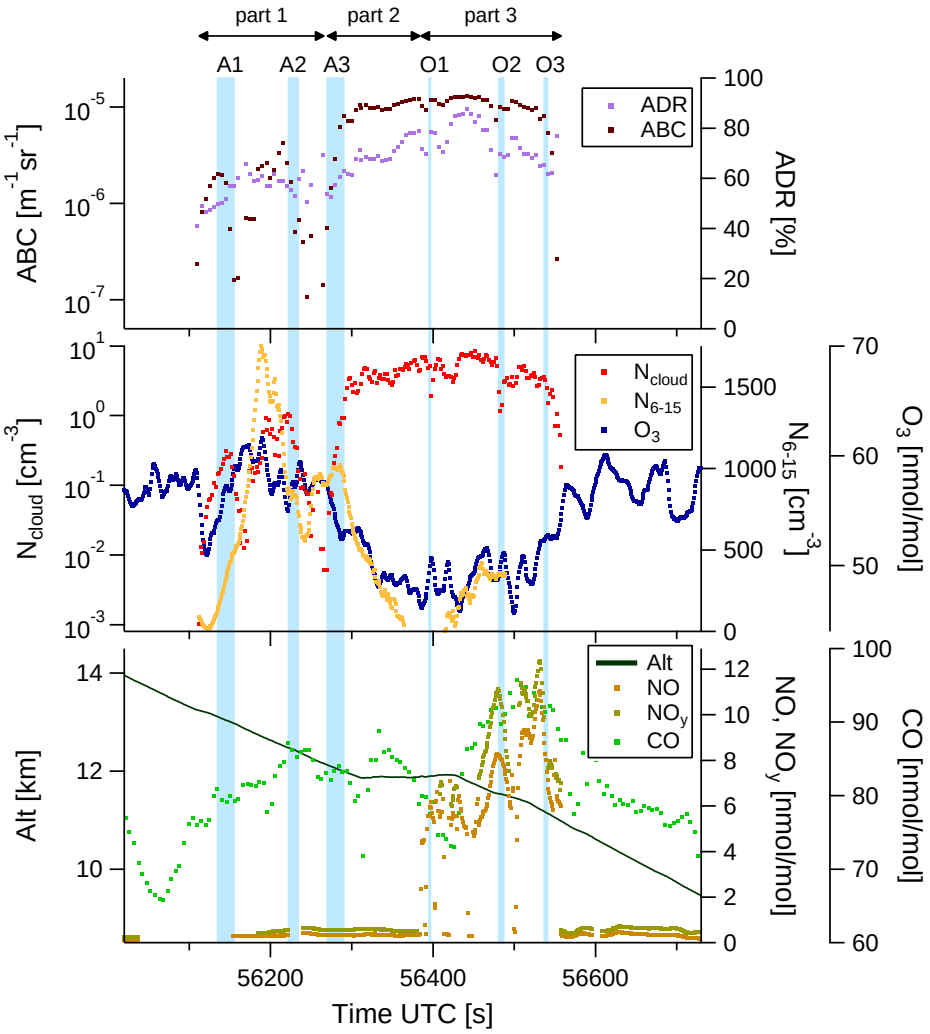

Figure 4.8: Time series of the MCS crossing during descent on 7 Aug 2006. Tracer mixing ratios and particle concentrations are displayed in the lower two panels, the upper panel presents the aerosol backscatter coefficient (ABC) and aerosol depolarisation ratio (ADR), both measured by the MAS. The blue shading indicates time periods which were selected for compiling size distributions displayed in Figure 4.9.

while a kilometre below (in *A3*) particle sizes reached the maximum size that can be imaged by the CIP diode array, i.e. $1600\,\mu\mathrm{m}$. Furthermore, the numbers of the larger particles (in the CIP size range) increase. This can be seen from the three *A* cases, coloured in green, in the upper panel of Figure 4.9. Most probably the maximum sizes of particles in the event *A3* and especially in *O1* conspicuously exceeded the CIP imaging limit. Some examples of individual CIP shadow images are presented in Figure 4.10. The images have the appearance of mostly heavily rimed ice particles, rimed aggregates, or chain aggregates (c.f. also Particle Gallery, page 147 ff.). The number concentrations of the ice particles in the outflow are higher compared to the cases from above and range about a few particles per cm^3. In addition, the IWC increases in the outflow by about one order of magnitude. The effective radii decrease successively with increasing altitude above the outflow.

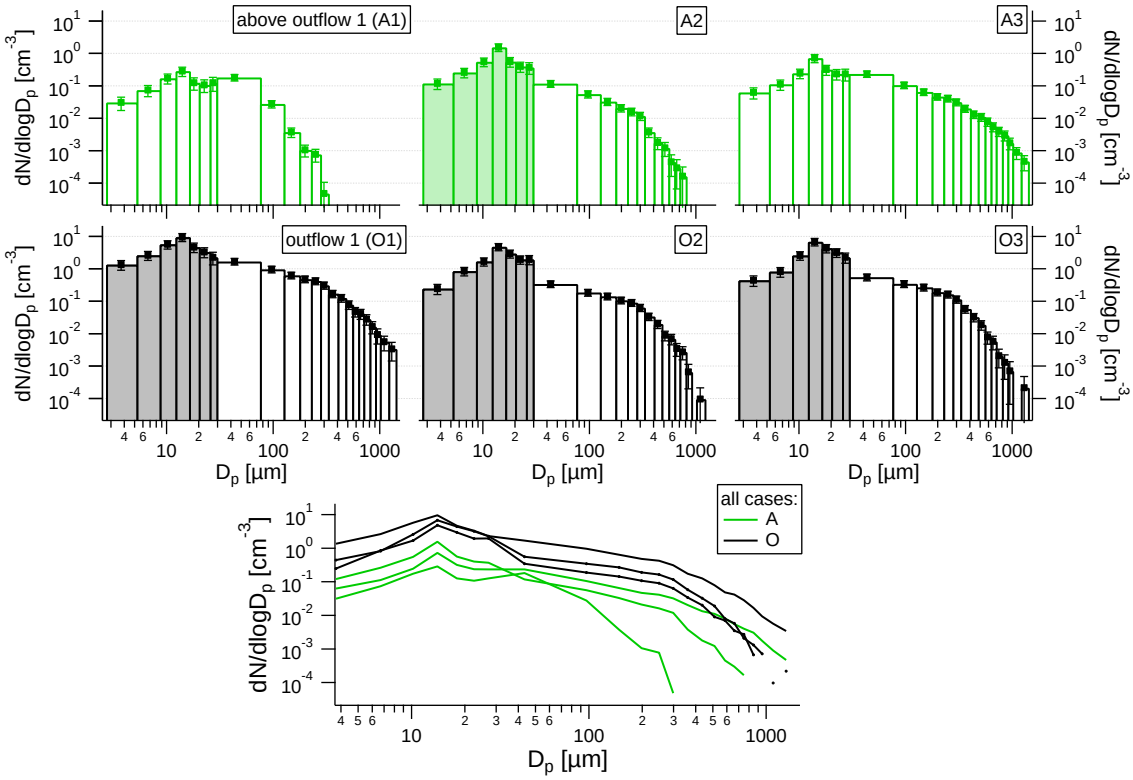

Figure 4.9: Ice particle size distributions from the selected time periods as indicated in Figure 4.8 on 7 Aug 2006. The upper panel shows the size distributions that were observed above the outflow, the middle panel those from within the outflow. All distributions are summarised in the lower panel.

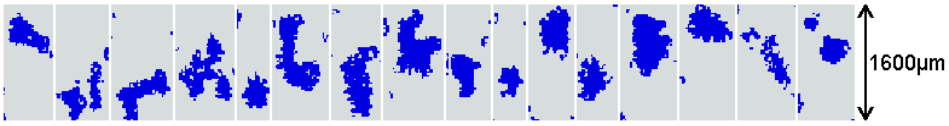

Figure 4.10: Selected examples of CIP shadow images as observed within the MCS outflow on 7 Aug 2006. Mostly heavily rimed ice particles or rimed aggregates are identifiable.

Table 4.3: Summary of meteorological and microphysical parameters for the cloud events as defined in Figure 4.8 above and inside the outflow on 7 Aug 2006.

Case	Alt [km]	θ [K]	$T_{ambient}$ [K]	RHi [%]	N [cm^{-3}]	IWC [g m^{-3}]	r_{eff} [μm]
A1	13.0 – 13.1	351	209.5	71	0.21 ± 0.05	3.7×10^{-3}	30.9
A2	12.4 – 12.5	349	214.1	76	0.57 ± 0.12	3.6×10^{-3}	75.7
A3	12.0 – 12.1	348	217.2	103	0.40 ± 0.08	7.6×10^{-3}	144.1
O1	11.9	350	219.8	69	5.19 ± 1.10	60.2×10^{-3}	180.9
O2	11.5	347	221.9	96	1.96 ± 0.42	13.7×10^{-3}	93.7
O3	11.1	346	225.0	32	2.85 ± 0.61	21.9×10^{-3}	124.7
errors*			± 0.5	± 15		$\times / \div 2$	$\pm 10\,\%$

*The errors for N are derived from $20\,\%$ uncertainty in the sample volume plus the error determined by counting statistics. The uncertainty of the IWC is estimated to be within a factor of two, i.e. in a range of half to double the value. The uncertainty of the effective radius is strongly dependent on the fraction of smaller particles ($\lesssim 50\,\mu$m) since the sizing uncertainty is higher for those particles. However, $10\,\%$ seems to be a good estimate for r_{eff} uncertainty which is mostly smaller for larger r_{eff} ($\gtrsim 100\,\mu$m). Due to the counting statistics the errors of N cannot be expressed as a fraction of the total value of N and are thus provided in the following tables.

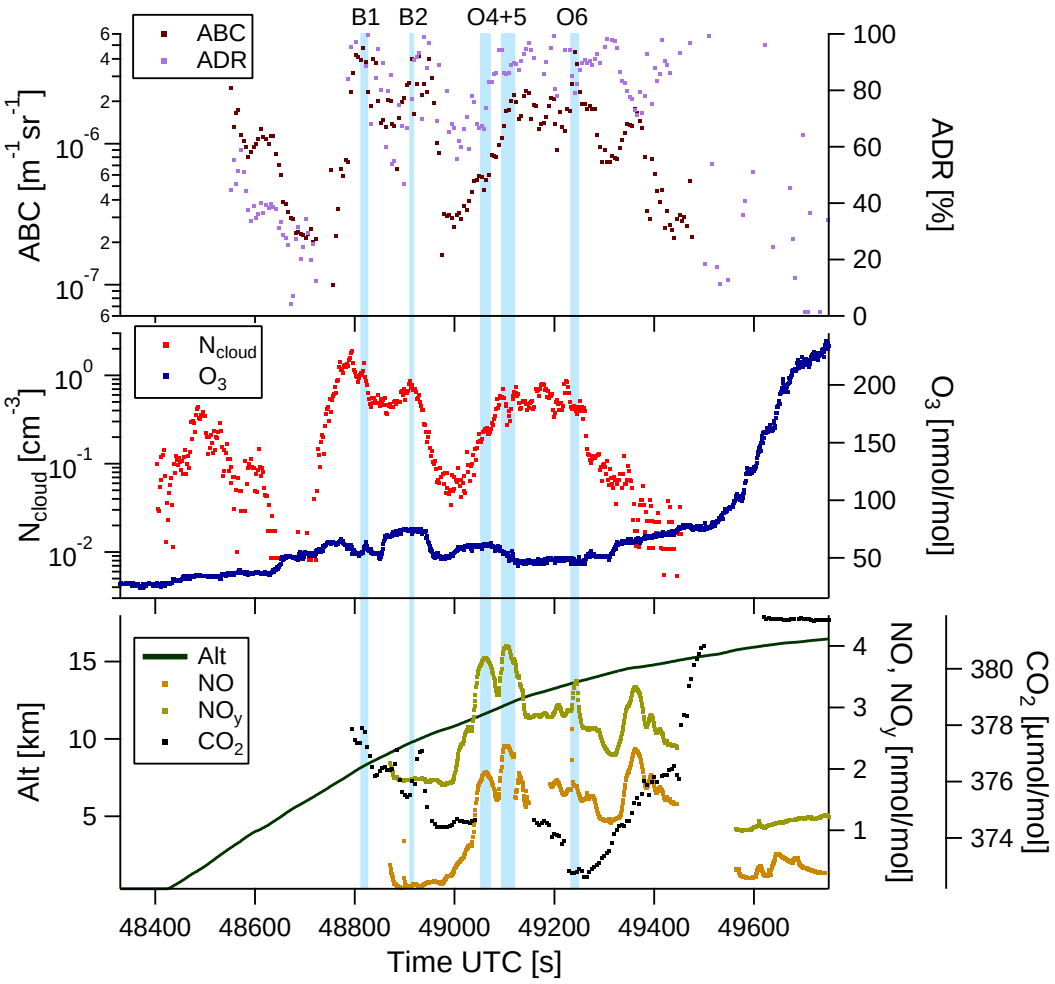

Figure 4.11: Time series showing the ascent through the MCC anvil on 16 Aug 2006. The blue shading indicates time periods which were selected for compiling size distributions displayed in Figure 4.12.

4.2.4 Recent outflow case on 16 August 2006

The satellite image of 16 August (Figure 4.6(d)) shows a Mesoscale Convective Complex of roughly $400\,\mathrm{km}$ in diameter with the coldest cloud top temperatures at a distance of about $300\,\mathrm{km}$ from the flight track. The flight at this day ascended through this MCS and a vertical cloud profile up to an altitude of $15.1\,\mathrm{km}$, corresponding to $363\,\mathrm{K}$ potential temperature, was obtained. Figure 4.11 shows the time series of the ascent, the size distributions of selected time periods are presented in Figure 4.12 and the meteorological and microphysical parameters of these events are summarised in Table 4.4. Since most instruments on board of the Geophysica were designed for measurements at very high altitudes no tracer data have been obtained during the first part of the ascent up to an altitude of about $7.8\,\mathrm{km}$. Cloud particle data measured by CIP and FSSP-100 are present for the whole ascent, MAS measurements commence at an altitude of $3\,\mathrm{km}$.

The observed cloud can be divided in three parts when having a closer look on the cloud particle data. The first part or cloud layer extends from ground to an altitude of $4.8\,\mathrm{km}$ where an extended minimum in cloud particle number concentrations can be found. In this layer the CIP did not observe any particles, the FSSP-100 de-

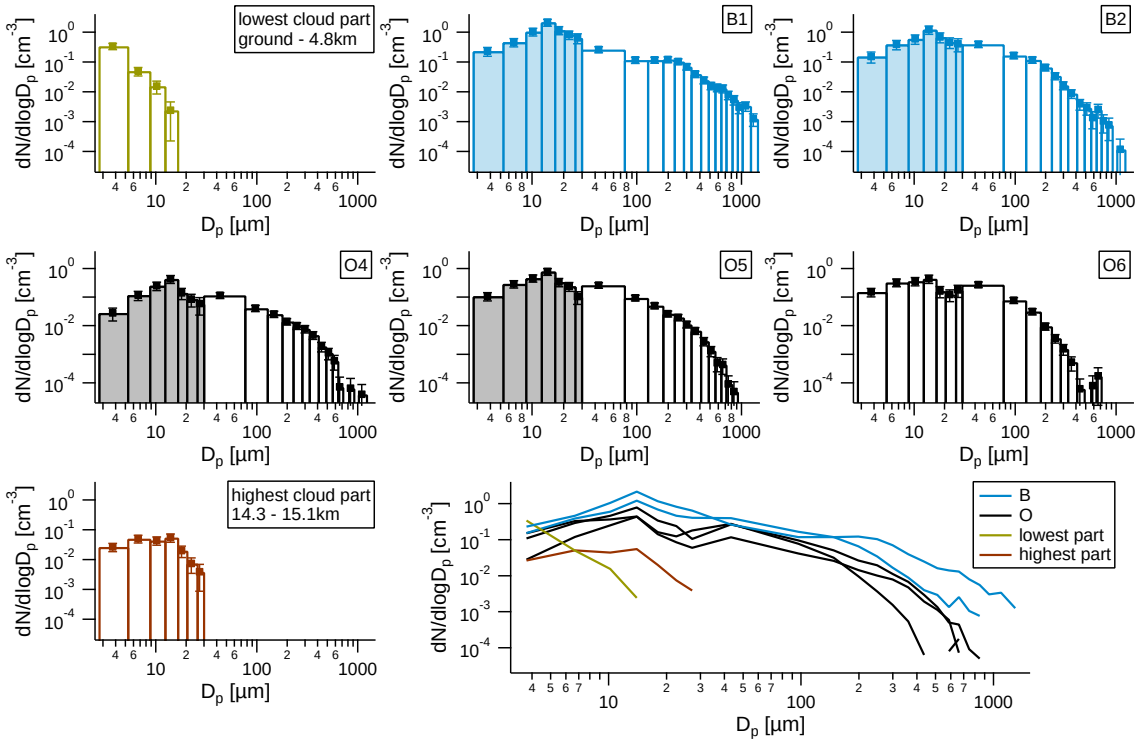

Figure 4.12: Size distributions as compiled for the blue shaded time periods in Figure 4.11 on 16 Aug 2006. Additional size distributions are given for the lowest and highest cloud part where only the FSSP-100 detected particles (upper left and lower left panel). All distributions are summarised in the lower right panel.

tected only particles that were smaller than $20\,\mu\mathrm{m}$ (as displayed in the size distribution in the upper left in Figure 4.12). With particles of this size no shattering has to be expected. These particles could be remnants of evaporating precipitation, haze droplets or large aerosol particles (either grown by water uptake or resuspended from the ground by the gust fronts). The second cloud layer extended from $5.8\,\mathrm{km}$ to $10.6\,\mathrm{km}$ (between the two local minima of the cloud particle number concentration and aerosol backscatter coefficient (ABC) in Figure 4.11, corresponding to roughly $48\,700\,\mathrm{s\,UTC}$ to $49\,000\,\mathrm{s\,UTC}$). Other tracer measurements than ozone have not commenced during the first part of this cloud layer crossing. CO_2 mixing ratios decline from $378\,\mu\mathrm{mol/mol}$ to $374.5\,\mu\mathrm{mol/mol}$ towards the end of the encounter and NO mixing ratios were low (around $0.1\,\mathrm{nmol/mol}$) which implies that there was no outflow. Enhanced ozone mixing ratios of up to $75\,\mathrm{nmol/mol}$ in this layer are possibly a result of biomass burning events. The cloud particles in the lower part of this layer often had sizes which exceeded the maximum CIP shadow image size ($1600\,\mu\mathrm{m}$). The images show very large ice crystals such as snow flakes or aggregates. Some examples of those images, recorded at an altitude of about $6\,\mathrm{km}$, are given in Figure 4.13. The third part of the cloud exhibits high values for NO and NO_y (up to $2.4\,\mathrm{nmol/mol}$ and $4\,\mathrm{nmol/mol}$, respectively) as well as low CO_2 (down to $372.6\,\mu\mathrm{mol/mol}$) and decreased ozone mixing ratios (minimum $43\,\mathrm{nmol/mol}$) which gives an indication for an outflow event. This layer extends from $10.6\,\mathrm{km}$ to $15.1\,\mathrm{km}$. The depolarisation ratio within the layer is high and indicates the presence of irregular shaped ice particles as can also be deduced from the CIP shadow images. At the highest part of this layer

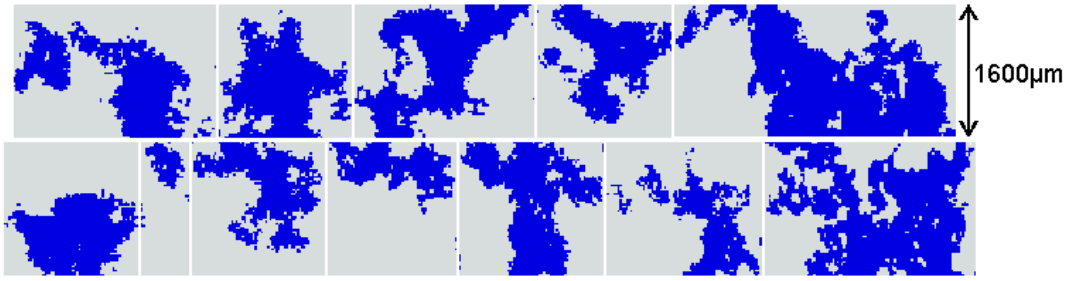

Figure 4.13: Examples of CIP shadow images as observed within the MCC at roughly $6\,\mathrm{km}$ altitude on 16 Aug 2006. The images show large ice particles such as snowflakes and aggregates, some of them even exceed the the maximum size of the CIP images across the diode array.

Table 4.4: Summary of meteorological and microphysical parameters for the cloud events, as shown in Figure 4.12, in and around outflows on 16 Aug 2006.

Case	Alt [km]	θ [K]	$T_{ambient}$ [K]	N [cm^{-3}]	IWC [$\mathrm{g\,m}^{-3}$]	r_{eff} [μm]
low	1.7 – 4.5	310 – 321	274.4 – 293.1	0.11 ± 0.03	5.6×10^{-6}	2.4
B1	8.2 – 8.4	339 – 340	249.6 – 250.7	1.02 ± 0.22	12.2×10^{-3}	219.1
B2	9.7 – 9.8	345	238.1 – 238.8	0.76 ± 0.17	9.8×10^{-3}	103.7
O4	11.5 – 11.8	350 – 351	221.8 – 224.0	0.22 ± 0.05	2.8×10^{-3}	103.7
O5	12.1 – 12.4	352 – 353	216.7 – 219.0	0.48 ± 0.10	6.1×10^{-3}	85.4
O6	13.6 – 13.7	353 – 354	204.6 – 205.8	0.42 ± 0.09	5.7×10^{-3}	50.5
high	14.3 – 15.1	355 – 363	196.8 – 200.1	0.04 ± 0.01	25.8×10^{-6}	6.2

again only the FSSP-100 detected cloud particles. The respective size distribution is provided in the lower left panel in Figure 4.12. Furthermore, the figure displays size distributions which are compiled for the blue shaded time periods in Figure 4.11. Two of these periods were measured below the outflow (*B1* and *B2*) and three inside the outflow (*O4* to *O6*). When comparing the size distributions from below and inside the outflow, a decrease of maximum particle size with increasing altitude can be found (see the lower right panel for comparison). The number concentrations are similar, though there is a slight decrease, as can be seen in Table 4.4. The IWCs below the outflow (in the second cloud layer) are higher compared to those within the outflow. The effective radius decreases for all ice cloud cases with increasing altitude.

4.2.5 Aged outflow on 11 August 2006

The flight on 11 August 2006 was performed in the wake of an MCS squall line (c.f. Figure 4.6(c)). Two dives were performed during that flight. Thus, together with the ascent and descent the aircraft crossed the outflow layer six times. The sections of the time series which show cloud crossings within this outflow layer are displayed in Figure 4.14, the respective size distributions in Figure 4.15, and a summary of important parameters is given in Table 4.5. The outflow level has been identified with the help of CO_2 observations which show a distinct minimum in an altitude band of roughly $353\,\mathrm{K}$ to $357\,\mathrm{K}$ potential temperature (Figure 4.7). In some cases clouds have been probed in this altitude but CO_2 data were occasionally not available (cases *O8* and *O10*). However, since the CO_2-profile shows a minimum at the altitude of these two cases they have also been regarded as outflow cases. Clouds have also been

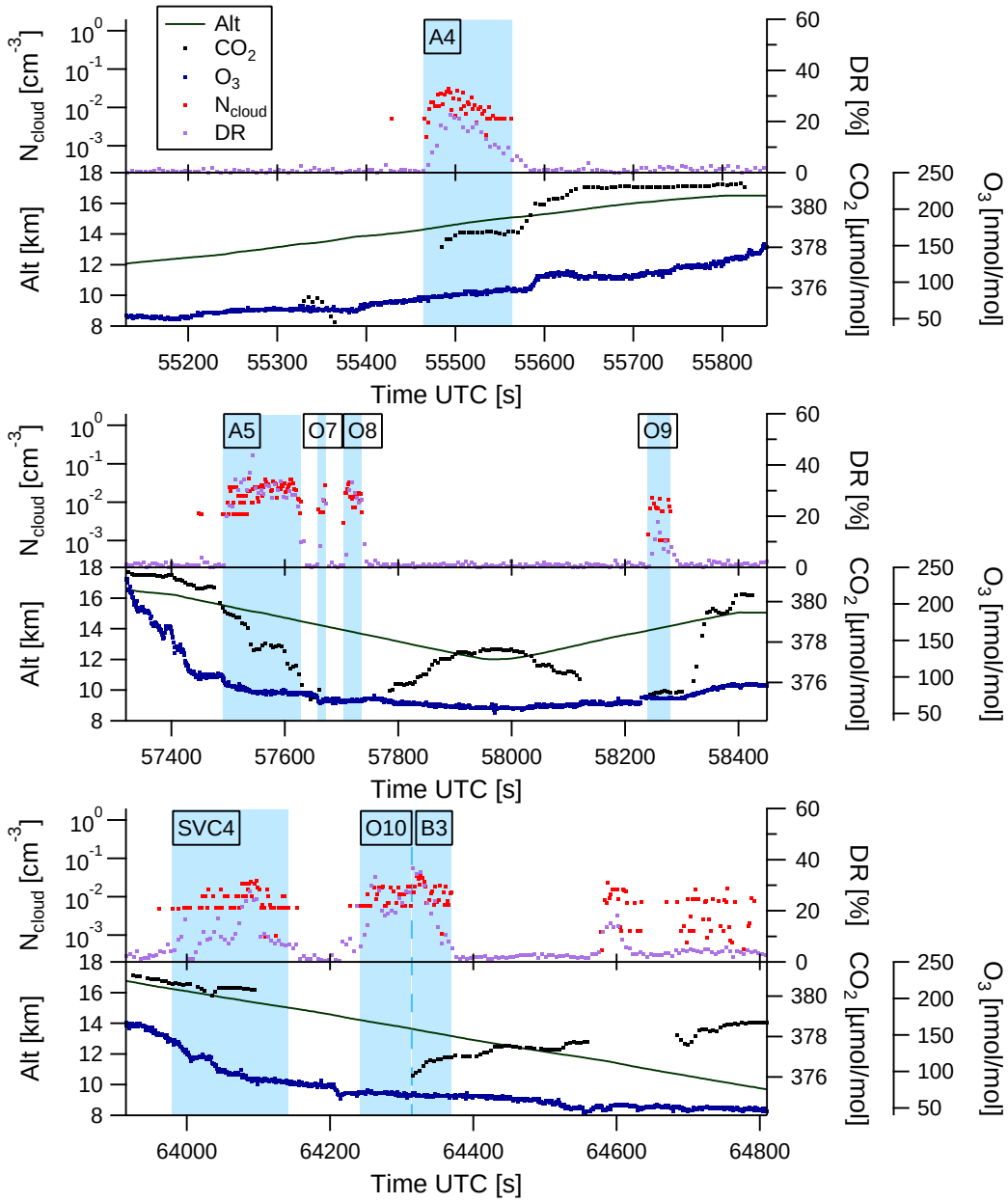

Figure 4.14: Close-ups of the time series of the flight on 11 Aug 2006. The following flight sections are displayed: ascent (upper panel), the first dive (middle panel), and descent (lower panel). Note that the depolarisation ratio (DR) is displayed here instead of the ADR since the latter was affected by noise during this flight.

observed above and below this altitude band. Figure 4.14 displays the sections of the time series during which clouds in and around an outflow were found. The upper panel shows the ascent, the middle panel the first dive, and the lower panel displays the descent of the flight. Right above the outflow layer a cloud layer has been crossed during ascent, which is denoted as *A4*. The first encountered cloud layer in the descent of the first dive, as shown in the middle panel, was also located above the outflow. The CO_2 mixing ratios decrease here from the stratospheric background value (roughly $381\,\mu\mathrm{mol/mol}$) to almost outflow values (roughly $376\,\mu\mathrm{mol/mol}$). Outflow values are reached shortly before the second cloud encounter in the dive which

Table 4.5: Summary of meteorological and microphysical parameters for the cloud events indicated in Figure 4.14 in and around outflows on 11 Aug 2006.

Case	Alt [km]	θ [K]	$T_{ambient}$ [K]	RHi [%]	N [cm^{-3}]	IWC [$\mathrm{g\,m}^{-3}$]	r_{eff} [μm]
A4	14.3 – 15.0	358 – 361	197.3 – 202.2	79	0.010 ± 0.003	15.0×10^{-5}	17.8
A5	14.5 – 15.5	357 – 362	193.4 – 199.8	64	0.020 ± 0.005	9.5×10^{-5}	12.3
B3	13.2 – 13.6	351 – 352	200.9 – 201.6	95	0.015 ± 0.005	5.7×10^{-5}	13.1
O7	14.2 – 14.3	355 – 356	203.4 – 205.4	41	0.007 ± 0.003	1.6×10^{-5}	6.7
O8	13.7 – 14.0	354 – 355	201.8 – 204.6	80	0.015 ± 0.005	11.9×10^{-5}	16.2
O9	13.8 – 14.1	355 – 356	199.7 – 204.1	78	0.005 ± 0.002	4.0×10^{-5}	12.4
O10	13.7 – 14.2	352 – 354	204.2 – 208.1	78	0.009 ± 0.003	3.1×10^{-5}	8.6

happened within the outflow altitude band. Thus, this encounter is labelled as *O7*. A second cloud in this altitude band is denoted as *O8*. In both outflow cases, *O7* and *O8*, the ozone mixing ratio is lower than during the *A5* encounter. At the reversal point of the dive the CO_2 has increased to its tropospheric background value of approximately $378\,\mu\mathrm{mol/mol}$. During the following ascent the CO_2 decreases again and the aircraft encountered one more cloud in the outflow altitude band (*O9*). At the time of this encounter CO_2 measurements were available and show a minimum, indicating an outflow air mass. During the final descent the Geophysica flew through a subvisible cirrus (*SVC4*). This cloud type and this particular cloud is described in detail in Chapter 6. CO_2 is at a high level during this encounter. When descending to the outflow altitude a jump in the ozone can be seen from about $80\,\mathrm{nmol/mol}$ to $70\,\mathrm{nmol/mol}$. CO_2 data at this time is not available. However, the first part of the cloud encountered here is still situated in the typical outflow altitude and is therefore denoted as *O10*, while the following cloud part, which is below the typical outflow level, exhibits background values for CO_2 and is thus labelled with *B3*. As Table 4.5 points out the outflow and no-outflow cases differ not only in altitude and potential temperature but also in the number concentrations of cloud particles. These are less for the outflow cases while the events above the outflow contain slightly more particles. The IWC above the outflow is about a factor of two higher than inside the outflow and the effective radii are slightly larger. Size distributions for the clouds were calculated and are presented in Figure 4.15. On the left hand side the size distributions for the cloud events above and below the outflow are displayed in green and blue, respectively. Black colour indicates the four outflow cases and all size distributions are summarised for comparison in the lower right panel. It has to be noted that the cases *A4* and *A5* contain larger particles than the outflow cases. Usually, one would expect smaller particles at higher altitudes and also lower number concentrations, as shown in Chapter 7.

4.2.6 Precursor state for MCS formation on 8 August 2006

The tracer profiles of the measurements on 8 August in Figure 4.7 have shown that there were slight enhancements in NO, NO_y, and CO, as well as slight decreases in CO_2 and ozone in the altitude band between $347\,\mathrm{K}$ and $355\,\mathrm{K}$, corresponding to $11\,\mathrm{km}$ to $13.6\,\mathrm{km}$. The tracer signatures are more pronounced right below $350\,\mathrm{K}$, though. In the satellite image (Figure 4.6(b)) no MCS was visible at the time of the ascent (for which the tracer profiles were presented) but a smaller scale cloud indicated by the yellow/orange colours in the satellite image was discernible. However, three hours later an MCS had developed at that location. Thus, these slight tracer

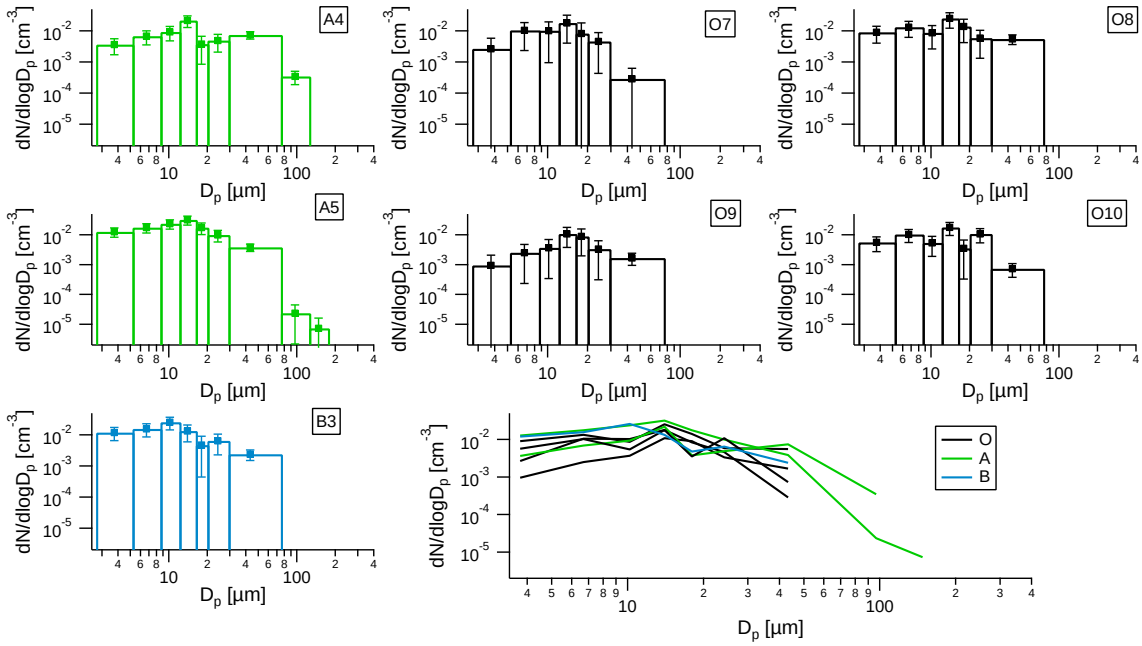

Figure 4.15: Cloud particle size distributions for the cloud events as indicated in Figure 4.14 on 11 Aug 2006. For comparison, all size distributions are summarised in the lower right panel.

indications for convective influence might be a result of incipient convection and MCS formation.

This can further be investigated by having a closer look on the ascent time series in Figure 4.16. Between $9\,\mathrm{km}$ and $10.3\,\mathrm{km}$ the CO_2 mixing ratios show a background value of about $378.3\,\mu\mathrm{mol/mol}$. The mixing ratios decrease below this level at altitudes above $11\,\mathrm{km}$. At that time cloud particle concentrations were at a maximum. A minimum in ozone mixing ratios (around $40\,\mathrm{nmol/mol}$) can be found concurrently with the cloud particle concentration maximum (about $20\,\mathrm{cm^{-3}}$). Ascending further, the number densities decrease. At an altitude of $12.1\,\mathrm{km}$ the NO and NO_y measurements start and show slightly enhanced mixing ratios of $0.83\,\mathrm{nmol/mol}$ and $1.55\,\mathrm{nmol/mol}$, respectively. At the time when NO, NO_y, and CO_2 mixing ratios return to their background levels, a small jump in the ozone from $52\,\mathrm{nmol/mol}$ to $67\,\mathrm{nmol/mol}$ is obvious. A major problem for the analysis of the cloud data on this particular ascent is that the CIP encountered the Double Particles problem (as described in Section 2.4.8), starting at the time indicated by the grey dashed line in Figure 4.16. In addition, after $43\,160\,\mathrm{s\,UTC}$ the CIP detected no more particles but the data file contained calibration particle images. These can not have been measured during the flight under any circumstances. Therefore, the CIP data are not reliable after that time, the first dependable data were again obtained at $51\,435\,\mathrm{s\,UTC}$. That means there are no CIP data from within the precursor outflow and it is not possible to say whether there were particles larger $30\,\mu\mathrm{m}$ at all. Nevertheless, FSSP-100 data obtained during this time period will still be provided here in order to give at least some information about the cloud encounters. The aerosol backscatter coefficient (ABC) and aerosol depolarisation ratio (ADR) are presented in the upper panel of Figure 4.16 in order to substantiate the presence of clouds. The blue shading indicates the time periods for which size distributions are compiled and presented in Figure 4.17. Even though there was

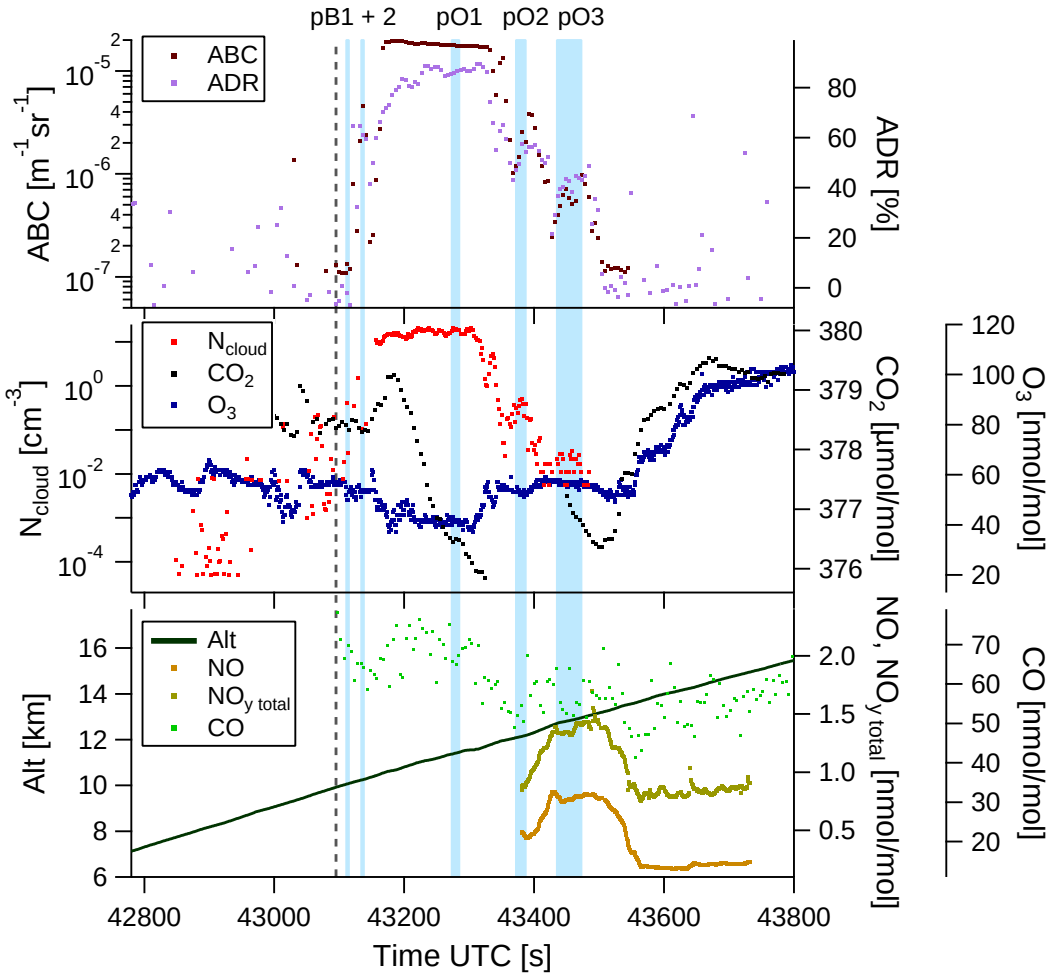

Figure 4.16: Zoom in on the time series during ascent of the flight on 8 Aug 2006. Blue shaded time periods were selected for compiling the size distributions in Figure 4.17.

the Double Particles problem in the CIP data, some seconds of measurements could be identified without this problem. For these time periods (denoted as *pB1* and *pB2* for “precursor state below outflow” in the blue shading of Figure 4.16) the first two size distributions are calculated and displayed in the upper panel. These were times when the tracer mixing ratios were at their background level. For times with slight outflow signatures three size distributions are compiled (*pO1*, *pO2*, and *pO3*) and presented in the lower panel of Figure 4.17. For these times no CIP data were available. The very high values of small particle number concentrations during *pO1* have to be noted. These high concentrations are confirmed by the rather high ABC which is indicative for a large amount of small particles. Possibly, the high concentrations of small particles are a result of homogeneous freezing of cloud drops. In contrast, the ADR shows that the particles have depolarising structures, i.e. that they are of non-spherical shape. This might be an indication of abundance of particles larger than $30\,\mu\mathrm{m}$. It has to be noted that the values of the microphysical parameters in Table 4.6 might be higher than shown here, due to the fact that only FSSP-100 data were available. However, possible shattering effects (if larger particles were available) can not be excluded.

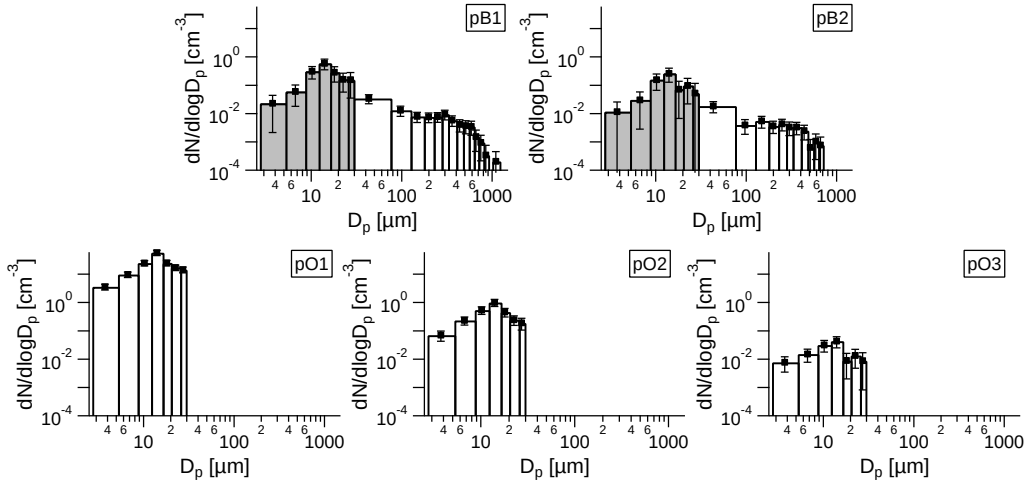

Figure 4.17: Size distributions compiled for the blue shaded time periods of Figure 4.16 on 8 Aug 2006. For the size distributions *pO1*, *pO2*, and *pO3* FSSP-100 data were available only.

Table 4.6: Summary of meteorological and microphysical parameters for the cloud encounters in the outflow precursor state on 8 Aug 2006. Note that the microphysical values for the cases *pO1 – pO3* contain FSSP-100 data only.

Case	Alt [km]	θ [K]	$T_{ambient}$ [K]	N [cm^{-3}]	IWC [g m^{-3}]	r_{eff} [μm]
pB1	10.1	344	234.8	0.22 ± 0.06	1.7×10^{-3}	196.2
pB2	10.2	344	233.1	0.10 ± 0.03	0.7×10^{-3}	151.7
pO1*	11.4 – 11.5	347	222.9	19.13 ± 3.95	36.5×10^{-3}	9.0
pO2*	12.1 – 12.2	349	216.9	0.36 ± 0.09	0.6×10^{-3}	8.5
pO3*	12.7 – 13.0	349	210.4	0.02 ± 0.01	0.02×10^{-3}	7.0

*Microphysical data contain FSSP-100 measurements only since CIP data are not reliable. Thus, especially values for IWC and effective radius may be significantly higher.

4.3 Discussion and summary

During four of the SCOUT-AMMA flights measurements in the areas of MCS outflows of different ages have been performed. The ages range from a precursory state (onset of convection), young outflow ($<$ three hours), recent outflow (approximately five hours) to aged outflow (approximately ten hours). It has to be reminded that within the AMMA framework the first in situ measurements were obtained in MCS anvils above continental West Africa (this study and Bouniol et al., 2010). Therefore, this chapter has a rather descriptive character since the microphysical properties of the MCS clouds in this region were unknown so far. The vertical profiles of the microphysical parameters observed in the vicinity of outflow events are displayed in Figure 4.18. The colours are identical to those in Figure 4.7 and indicate the particular flights. The shading gives an estimate of the outflow altitude band based on the altitudes of the selected outflow events discussed above (*O1 – O10 and pO1 – pO3*).The upper part of the shading reflects the outflow altitude for the flights on 11 and 16 August and the lower part the outflow altitude for the flights of 7 and 8 August. The number concentrations and IWCs show both a maximum in the respective outflow altitude except for the 11 August. At that day, the values for particle number concentrations and IWC

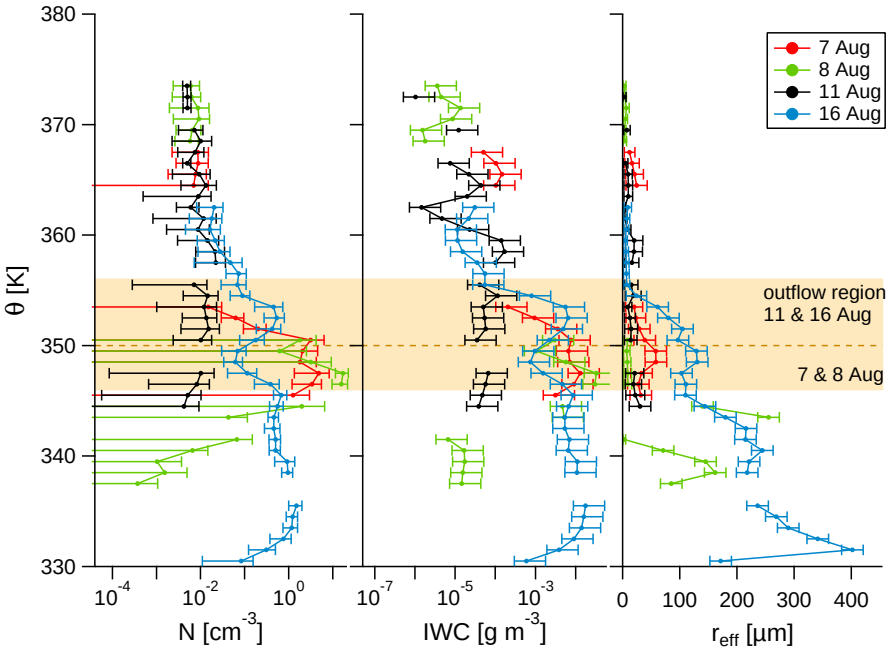

Figure 4.18: Mean profiles of number concentration (N), IWC, and effective radius (r_{eff}) for extracted time periods that contain cloud encounters concurrently to an outflow event observed on the discussed flights on 7 (red), 8 (green), 11 (black), and 16 (blue) Aug 2006. The error bars denote the instrumental measurement uncertainties. The outflow altitudes are indicated in the shading as identified from the trace gas measurements, the upper part corresponds to the outflow altitudes on 11 and 16 Aug, the lower for 7 an 8 Aug, respectively.

are slightly higher above the outflow. Usually one would expect a decrease in number concentration, IWC, and effective radius with increasing altitude (e.g. Garrett et al., 2003; Schiller et al., 2008; Krämer et al., 2009). This is discussed in detail in Chapter 7.

Size distributions have been presented for selected outflow cases of different age and are summarised in Figure 4.19. The younger the outflow is, the higher are the number concentrations and the larger are the maximum particle sizes. For the cases on 8 August only data for particles with sizes up to $31\,\mu\mathrm{m}$ are available, the CIP encountered instrumental failures during that time period . Thus, no statements about larger sized particles, which were most probably present, and maximum particle size can be made. Table 4.7 shows the ranges of altitudes and temperatures at which outflows were encountered and mean values for the microphysical parameters observed in the selected outflow events for each flight. Due to the high variability of the encounters on 8 August, these cases are itemised individually. The table also reflects the decreasing number concentrations and IWCs with age of the outflow. Furthermore, the effective radius decreases, indicating a decrease in the size of the average scatterer. A comparison of the outflow cases reveals that the outflows are located at increasing altitudes and potential temperatures with increasing age. This agrees with Houze (1989) who states that older convective cells in an MCS are advected rearward over the layer of descending rear inflow (compare Figure 4.2) and are thus located at increasingly higher altitudes. Former observations showed a decrease in particle numbers and sizes with increasing altitude (c.f. Chapter 7). Contrary, the size distributions derived from above the aged outflow on 11 August contain larger parti-

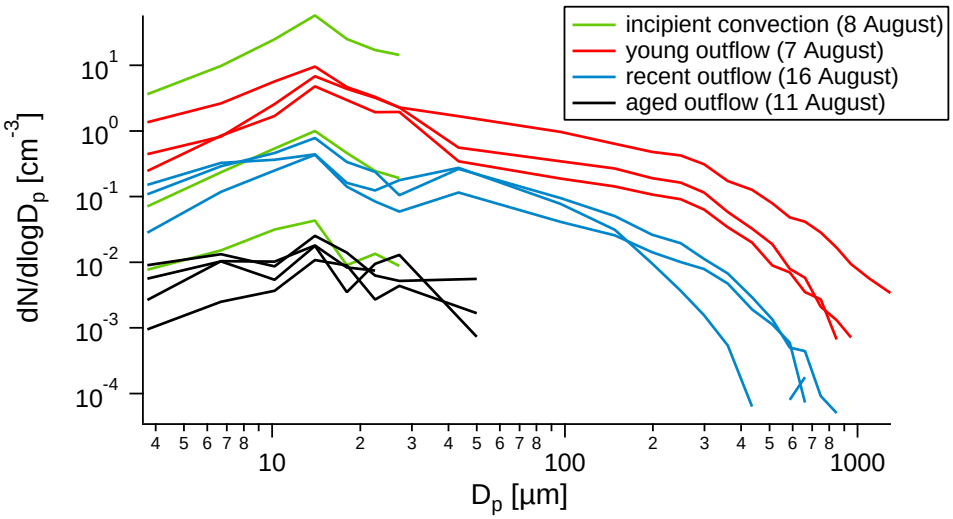

Figure 4.19: Comparison of all outflow size distributions of different ages from the flights during the SCOUT-AMMA campaign in Aug 2006.

Table 4.7: Summary of meteorological and microphysical parameters for the different outflow ages. Note, measurements performed in the precursor state on 8 Aug contain FSSP-100 data only.

Day	Alt [km]	θ [K]	$T_{ambient}$ [K]	N [cm^{-3}]	IWC [g m^{-3}]	r_{eff} [μm]
7	11.0 – 12.5	346 – 350	219.8 – 225.0	3.3	31.9×10^{-3}	133.1
16	11.5 – 13.7	350 – 354	204.6 – 224.0	0.37	4.9×10^{-3}	83.2
11	13.7 – 14.3	352 – 356	199.7 – 208.1	0.01	5.2×10^{-5}	11.0
8 (*pO1*)	11.4 – 11.5	347	222.9	19.13	36.5×10^{-3}	9.0
8 (*pO2*)	12.1 – 12.2	349	216.9	0.358	0.6×10^{-3}	8.5
8 (*pO3*)	12.7 – 13.0	349	210.4	0.018	2.5×10^{-5}	7.0

cles and partly higher number concentrations than those obtained within the outflow. This observation can not be explained. Even sedimentation of comparatively larger ice crystals from further above seems unlikely because the satellite image (Figure 4.6(c)) does not indicate higher cloud layers. Highest number concentrations have been found in an altitude of around $11.5\,\mathrm{km}$, the altitude of the youngest outflow. On the flight on 8 August the highest of all observed number concentrations has been detected in that altitude, even though these numbers are just obtained by FSSP-100 measurements since the CIP was not operational at that time. However, ABC is very high during that event (compare Figure 4.16), indicating a thick layer of particles. Since particles in the FSSP-100 size range contribute the most to the ABC, it can be assumed that a high amount of those small particles was present. This finding underpins the FSSP-100 observations. Possibly the cloud was in a developing state. Thus, these particles might be newly formed ice particles. Unfortunately, neither gas phase nor total water measurements were performed at the time of this cloud crossing. The number concentrations decrease significantly when ascending further up. That means, possibly just a thin layer of newly forming ice particles was present while at higher altitudes number concentrations are comparable to those observed during the other flights. Lawson et al. (2010) observed peak number concentrations

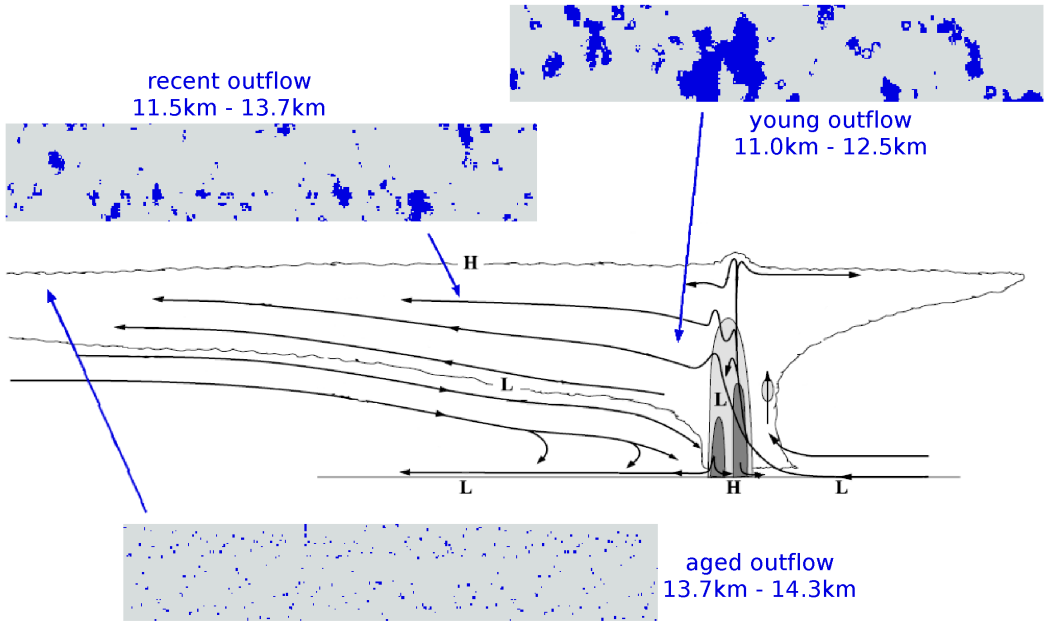

Figure 4.20: Snap-shots of consecutive CIP images as detected during outflow crossings on 7, 16, and 11 Aug 2006. The height of each image stripe corresponds to $1600\,\mu\mathrm{m}$. The location of the measurements within the MCS is indicated by the arrows.

of $32\,\mathrm{cm}^{-3}$ in a vigorous updraught in a convective turret during TC4[11]. In such updraughts they found mostly small frozen quasi-spherical particles, likely a result of homogeneous freezing, and milimetre-sized graupel particles. The satellite image of 8 August 4.6(b) indicates that also the cloud observations during the precursory state were performed in an updraught region which would further explain the high number concentrations of small particles. Furthermore, ADR is at a very high level (roughly $80\,\%$), indicating the abundance of non-spherical ice crystals. Since ADR has similar values compared to the young and recent outflow events, the particles are possibly also aggregates or rimed ice crystals. Several aggregates observed during the young outflow events on 7 August (c.f. Figure 4.10) look similar to the chain aggregates observed by Connolly et al. (2005) in continental MCS above the USA and Northern Australia. They explained the aggregation by the electrification of clouds due to lightning. In the young outflow event very high NO mixing ratios were encountered, indicating a strong lightning activity and thus corroborating the finding of enhanced aggregation by electric fields.
A comparison of snap-shots of consecutive CIP particle images is given in Figure 4.20, alongside with the schematic of an MCS (adapted from Figure 4.2) in order to give an estimate of where inside the MCS outflow the images were detected. One representative image stripe for each outflow age has been chosen. The decrease of maximum particle size is obvious. Probably the large particles have sedimented out due to gravitational settling while moving away from the convective core region. It has to be noted that the aged outflow was observed in a cloud layer that was detached from the MCS unlike in the schematic here. The outflows were encountered

[11] Tropical Composition, Clouds and Climate Coupling (TC4) experiment, Costa Rica, July and August 2007 (Toon et al., 2010)

in increasing distance to the MCS core with increasing age. During the young outflow event on 7 August the particle sizes partly exceeded the CIP imaging limit of $1600\,\mu\mathrm{m}$ across the diode array. That means ice particles of the size of a precipitation particle have been observed in an altitude of about $11.5\,\mathrm{km}$. This is in agreement with Cetrone and Houze (2009) who state that large particles should be found within the continental African MCS anvils. During September 2006 further in situ observations of cloud particles were performed over West Africa, as described by Bouniol et al. (2010). They also found rimed aggregates of large sizes inside the anvils. However, their measurements were mostly performed at lower altitudes and thus, it is unlikely that they were performed frequently within the outflow region. The influence of MCS outflows on the aerosol properties (up to an altitude of $12\,\mathrm{km}$) was subject of the study by Hamburger (2007). The first in situ measurements inside continental African MCS outflow clouds were performed during the SCOUT-AMMA campaign. A more comprehensive comparison of the current results with other in situ measurements is therefore not possible within the scope of this thesis. The same is true for modelling for which this data provides input.

Chapter 5

Overshooting convection over tropical Australia

5.1 Meteorological background

As described in Section 1.1.1 deep convection may produce overshooting cloud tops. Such overshoots possibly penetrate the TTL and sometimes even the lower stratosphere. Thus, it is important to characterise the overshooting convection in the context of troposphere to stratosphere transport (TST) of short- and long-lived chemical species, aerosols, and water vapour. Pommereau (2010) point out that observations over tropical land all suggest a significant, or even dominant, contribution of the fast updraughts in overshooting convection to TST compared to the slow diabatic heating which is usually considered. Several studies investigating overshooting convective cloud turrets can be found in the literature (e.g. Adler and Mack, 1986; Danielsen, 1993; de Reus et al., 2009). A 22-year (1983–2005) survey of tropical convection penetrating into the lower stratosphere, based on satellite data, by Rossow and Pearl (2007) revealed that such overshoots predominantly occur in larger, organised MCS. They found that $2\,\%$ of deep convective systems penetrate the TTL, and $1\,\%$ penetrate into the lower stratosphere. Another study based on satellite data by Romps and Kuang (2009), who used a slightly different definition of deep convection, showed that $3\,\%$ of the deep convective clouds overshoot the tropopause, while in tropical cyclones even $8\,\%$ of deep convection penetrates above the tropopause. However, not only different definitions of deep convection and TTL or tropopause affect the observed fraction of convective overshoots penetrating the TTL or above the tropopause, but also instrumental capabilities. For example Liu and Zipser (2005) stated that their radar only detects precipitating ice particles (several hundred $\mu\mathrm{m}$ in diameter; Alcala and Dessler, 2002) and does not see smaller sized particles. With this they found $0.1\,\%$ of the overshooting convection penetrating the $380\,\mathrm{K}$ potential temperature level.
Convective overshoots into the stratosphere carry tropospheric air masses aloft and can thus be identified by means of tracer measurements. In order to distinguish between tropospheric and stratospheric air masses ozone is a reliable tracer in the tropics because of its strong increase in the stratosphere, as can be seen in Figure 5.1, which shows an example for a typical vertical ozone profile in the left panel. The figure displays data from a SCOUT-AMMA measurement flight on 8 August 2006. These measurements have been chosen because this day was less convectively ac-

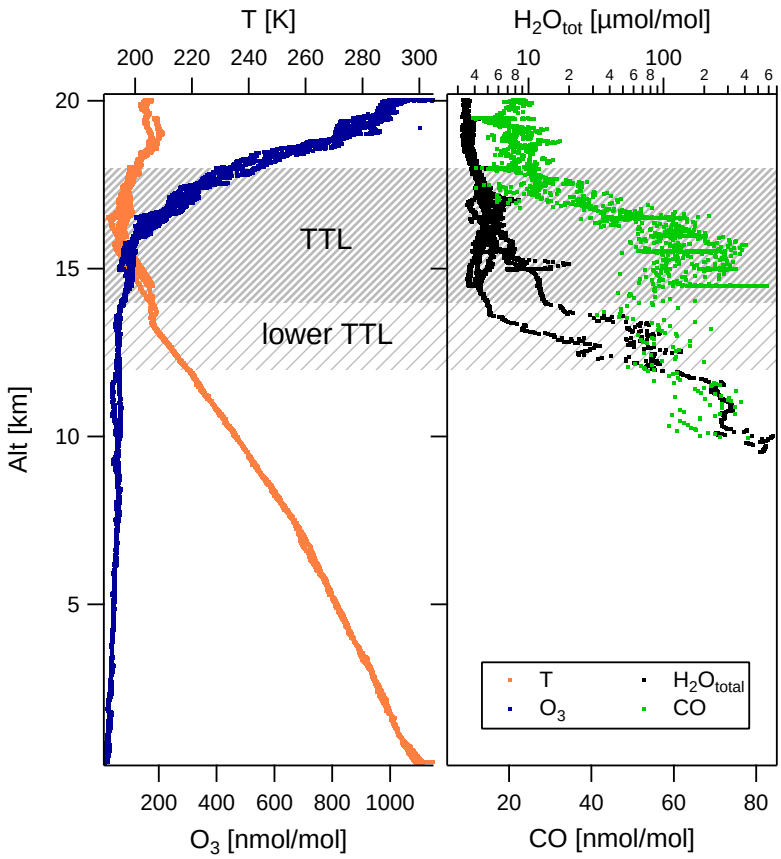

Figure 5.1: Typical atmospheric altitude profiles of ozone and temperature in the left panel, total water and CO in the right panel. A strong increase of the ozone mixing ratio can be seen in the stratosphere, as well as an increase in temperature. In contrast, water and CO decrease in the stratosphere. All data were measured on 8 Aug 2006.

tive and less influence of overshooting convection on the stratospheric composition was expected during SCOUT-AMMA compared to SCOUT-O3. In the stratosphere ozone is formed due to UV light absorption by molecular oxygen and the subsequent reactions (Chapman-cycle). Other indicators for stratospheric air masses are temperature, water content, CO, and potential vorticity (PV). However, the latter is not further discussed here since no PV data were acquired during the SCOUT-O3 measurement flights. The temperatures increase with altitude above the tropopause whereas the water content decreases with increasing altitude (c.f. Figure 5.1). A few spikes can be seen in the total water profile which result from measurements inside clouds. The spread is a result of different humidities during ascent and descent through the TTL. The CO has significantly lower mixing ratios in the stratosphere, as also obvious in Figure 5.1. For this reason ozone, CO, humidity, and temperature are used as tropospheric tracers for the analysis in this chapter.

5.1.1 Hector storm system

The so called Hector storm system (e.g. Keenan et al., 1994; Carbone et al., 2000; Crook, 2001; Connolly et al., 2006) is a very intense MCS that forms very frequently over the Tiwi Islands north of Darwin, Australia (see Figure 5.2). During the pre-

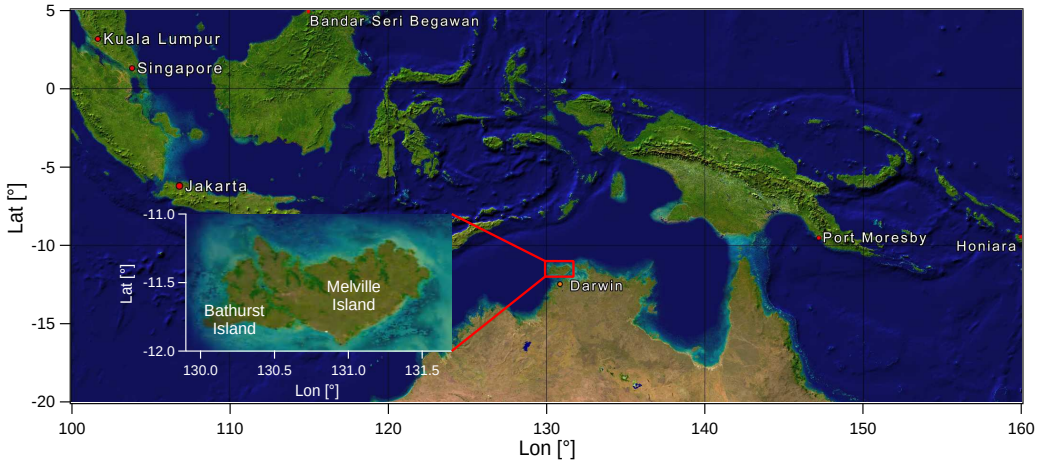

Figure 5.2: Maritime continent region with Australia in the South. The enlarged area shows the Tiwi Islands over which the Hector storm system develops.

monsoon period (November/December) and monsoon breaks (February/March) Hector develops on an almost diurnal basis in the afternoon or early evening (Vaughan et al., 2008). A general description on the monsoon flow around the Tiwi Islands is given by Brunner et al. (2009) and for the $2005/2006$ Australian monsoon cycle, during which SCOUT-O3 was conducted, by Shaik and Cleland (2006).

Carbone et al. (2000) identified direct (Type A) and indirect (Type B) forcing mechanisms that lead to Hector formation. Type A Hectors result from a collision of sea breeze fronts that advance on the islands from north and south. This Hector type occurs when prevailing convective development is delayed or otherwise suppressed and is responsible for about $20\,\%$ of Hector systems (Carbone et al., 2000). Therefore, it can be seen as a nature's backup mechanism when the Type B forcing mechanism fails. The more effective Hector development Type B is shown schematically in Figure 5.3. Type B Hectors are much stronger than Type A Hectors and are initiated by a multistage (4–5 stages) process including precipitating convection: 1) The sea-breeze front forces and maintains convection resulting in showers. Due to evaporation the showers produce cold pools which are depicted by the dark shading in Figure 5.3. 2) When the cold pools become cooler than the air in the marine boundary layer a transition from breeze-forced and breeze-maintained convection to self-organised and self-sustained travelling squall lines takes place. The transition allows the convection to travel inland and feed on the heated island boundary layer. 3) The merge or maturation of cold pools leads to westward propagating squalls with accompanying gust fronts in the easterly shear conditions which prevail in the Tiwi Islands during the pre-monsoon. 4) The gust front of the travelling squall line subsequently amplifies convection along a sea-breeze front that is oriented zonally near the north or south coast of the island complex. The interaction of these two fronts forces the most intense convection. The fifth stage is optional. Here, the gust fronts of coexistent MCSs collide, which tends to yield the most intense MCSs. Beringer et al. (2001) confirmed the initial development (stage 1) near a leeward coast.

Hector storm systems are known to belong to the most intense and deepest convective systems and to be among the world's tallest systems often developing overshooting tops that reach altitudes of $20\,\mathrm{km}$ (Simpson et al., 1993; Crook, 2001). Thus, they

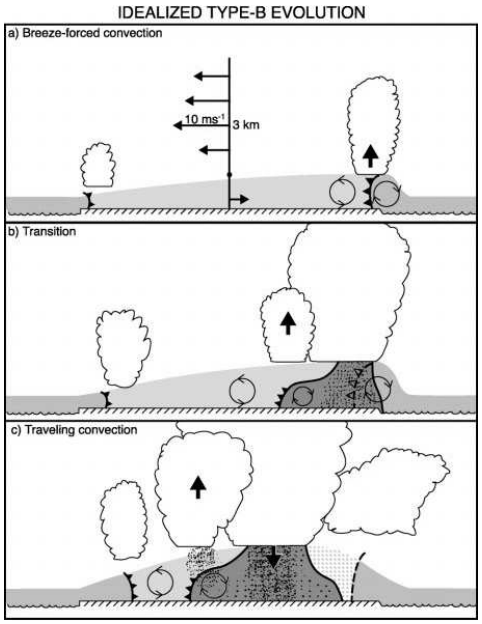

Figure 5.3: E-W cross section depicting optimal Hector Type B evolution. In the uppermost panel the westerly surface flow, easterly shear, and critical level are indicated. Boundary layers and cold pools are represented by shaded areas, where the darkness of the shading indicates the temperature of the layers: the darker the colder. The mottling shows precipitation. A recovering island boundary layer after convective disruption of original breeze front is indicated by the hatched area in the lowermost panel. Note that the diagrams are not according to scale. Taken from Carbone et al. (2000).

have been the natural laboratory for the investigation of the SCOUT-O3 campaign, in order to learn about the role of deep convection on the troposphere to stratosphere exchange and dehydration processes in the TTL.

5.1.2 The role of convective overshoots for stratospheric dryness

Generally, the stratosphere is very dry compared to the troposphere (Lelieveld et al., 2007). In order to understand and explain this dryness several hypotheses have been brought forward in the past. In this regard, overshooting convection is of particular interest since ice particles can possibly be injected into the dry stratosphere. Thus, the question arises whether the ice particles are evaporating and significantly hydrating the stratosphere and, if so, to what extent. In contrast, some hypotheses see convective overshoots as source of dryness. This section gives an overview of the main hypotheses for the mechanisms leading to the low stratospheric water vapour mixing ratios. Newell and Gould-Stewart (1981) proposed a “stratospheric fountain”, an area where air masses enter the stratosphere from the tropical troposphere over the tropical West Pacific. In this region, tropopause temperatures are coldest and the fountain occurs from November to March and moves over to the Bay of Bengal and India during the monsoon. Due to these very low temperatures in the tropopause, air is freeze-dried before entering the stratosphere, driven by the slow upwelling flow of the Hadley cell. That means, water vapour condenses on ice particles or forms ice particles that are not transported upwards with the airstream due to their gravitational settling. Thus, water vapour is removed irreversibly from the air masses before en-

tering the stratosphere. Holton and Gettelman (2001), however, point out that there is evidence for a mean downward motion in the fountain region and with this the stratospheric fountain theory is invalid for dehydration of stratospheric air masses. Therefore, they renamed this region to the 'cold trap' due to its cold tropopause temperatures. They established a hypothesis in which air is advected from upstream the cold trap, providing a moisture source. During passage through the cold trap TTL, which takes several days, the air undergoes cooling that leads to ice particle formation. The long time scales allow the ice particles to sediment and with this, irreversible dehydration of the air occurs. Having passed the cold trap region the newly dehydrated air masses will undergo diabatic heating and rise, radiatively driven, into the stratosphere.

Besides hypotheses containing large scale vertical and horizontal motions also convective scale motions are thought to explain the dry stratosphere. Overshooting convection possibly penetrates the lower stratosphere. Subsequently, cirrus anvils are formed with minimum temperatures much colder than the surrounding air. Ice crystals will rapidly form and grow, and be accelerated downward when large enough, leaving a dehydrated air mass. Thus, the overshoots build an environment favourable for dehydration (Danielsen, 1993, 1982). Sherwood and Dessler (2000, 2001) suggested that overshooting convective turrets penetrate the TTL, which they defined as the layer approximately between $150\,\mathrm{hPa}$ and $50\,\mathrm{hPa}$, corresponding to the LNB and Level of Maximum Overshoot (LMO). Following Danielsen (1982) the air is then dehydrated to moisture levels below the TTL average. The overshooted air parcels mix with ambient air and the resulting air parcel settles to its LNB. Then the air parcel will slowly be lifted through the TTL eventually into the stratosphere by radiatively balanced ascent.

However, in order to effectively dehydrate an air parcel, it needs to be exposed to the very cold temperatures over a sufficient long time period (Holton and Gettelman, 2001). If this is the case in convective overshoots remains questionable. In fact, Corti et al. (2008) point out that in contrast convective overshoots rather hydrate the stratosphere by evaporation of ice particles. Data from TROCCINOX[12] and SCOUT-O3 build the basis for Figure 5.4. An example of a stratospheric water vapour profile (from the SCOUT-O3 flight on 25 November 2005) in cloud free air is displayed. In general, the profile is compact, however, it shows some positive deviations. Prominent positive deviations can be found in the profiles of most flights but contrary no prominent negative deviations as panel (b) illustrates. Since those measurements have been performed in the vicinity of deep convective overshoots this is a clear indication of the hydrating effect of such overshoots. Furthermore, simulations by Chaboureau et al. (2007) yield an upward mass transport of water vapour by convection across the tropopause.
Thus, there are different hypotheses on how convective overshoots affect the stratospheric water vapour content. Dessler (1998) estimated the mixing ratio of water vapour entering the stratosphere and found a value of $(3.8 \pm 0.3)\,\mu\mathrm{mol/mol}$. Nevertheless, it should be noted that the question remains whether overshoots would have a significant contribution to water vapour exchange from the troposphere to the

[12] TROpical Convection, CIrrus, and Nitrogen OXides experiment, Brazil, February-March 2004 (Huntrieser et al., 2007)

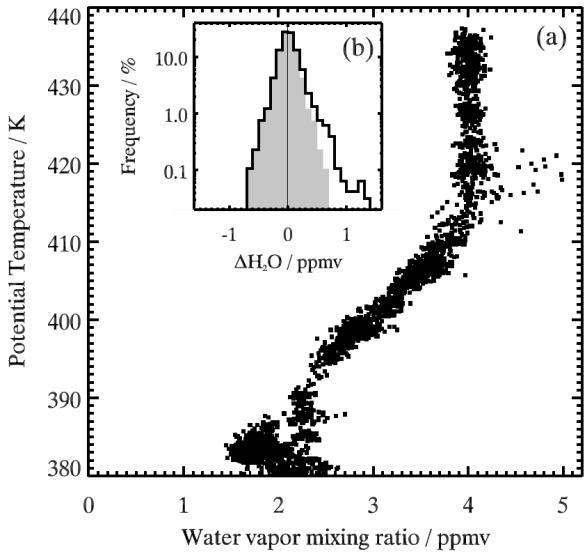

Figure 5.4: Observations of stratospheric water vapour in air free of particles during SCOUT-O3 and TROCCINOX. (a) Vertical profile of water vapour mixing ratio as observed on 25 Nov 2005. (b) Probability distribution of water vapour mixing ratio deviations from the respective mean profiles. The symmetric grey shading illustrates the skewness of the distribution and highlights the positive deviations which indicate hydrating events. Taken from Corti et al. (2008).

stratosphere at all. Addressing this question of tropical troposphere to stratosphere transport, Pommereau (2010) concluded that the contribution of fast convective overshooting updraughts is significant compared to the slow rising by diabatic heating. However, the latter process is usually considered while overshooting convection is often ignored or neither parameterised nor resolved in numerical models. The purpose of the measurements presented in this chapter is to provide further detailed evidence of the hydrating effect of overshooting convection, beyond the publication by de Reus et al. (2009).

5.2 Measurements of convective overshooting

During the SCOUT-O3 campaign (described in Section 3.2.1) turrets of overshooting convection have been probed. Most notably, on 30 November 2005, the “golden Hector day” (Brunner et al., 2009), several encounters of covective overshoots which even penetrated the stratosphere have occurred. This section presents the analysis of these events, whereof the main results have been published by de Reus et al. (2009). The major contribution of this thesis to the publication was the supply and application of image evaluation methods in order to be able to analyse the specific data of Hector observations. Additionally, an event of overshooting convection reaching the stratosphere that occured on 29 November 2005 is discussed. The correction and rejection mechanisms that were used for the SCOUT-O3 CIP data set are listed in Appendix Section A.1.

5.2.1 Cloud observations

Figure 5.5(a) shows the flight track of 30 November 2005 besides the UTLS section of the temperature altitude profile (Figure 5.5(b)). A large part of that flight was conducted above the Hector storm system in the stratosphere and several times cloud encounters have been observed. Those overshooting cloud events are indicated with circles and triangles in both figures. Six major events could be identified which exceeded a duration of $30\,\mathrm{s}$ of flight time. These events are marked with circles, the colour in the altitude profile indicates whether these events consisted mainly of large particles (red) or small particles (black). The amount of large and small particles is deduced by comparing the number of particles measured by the CIP and FSSP-100, respectively. Three shorter encounters occurred which had durations between $16\,\mathrm{s}$ and $28\,\mathrm{s}$, indicated by orange triangles. With an aircraft speed of approximately $190\,\mathrm{m\,s^{-1}}$ this corresponds to a horizontal extension of the clouds of $6.3\,\mathrm{km}$ to $16.8\,\mathrm{km}$ for the major and $3.4\,\mathrm{km}$ to $5.0\,\mathrm{km}$ for the minor events. Most events were concentrated over the southern part of the south-west coast of Melville Island. A set of images as measured with the CIP is shown in Figure 5.5(c). The presence of these CIP images unequivocally demonstrates the real existence of cloud particles in the stratosphere. Measurements by cloud particle probes that use scattering (as the FSSP-100) might be prone to misalignment or affected by noise e.g. due to sunlight. The shapes of the ice crystals cannot be assessed by the CIP from smaller particles ($<100\,\mu\mathrm{m}$) because too few pixels are shaded. However, the shapes of the larger particles were found to be mainly aggregates and columns. Spherical objects were not observed, which indicates that large frozen droplets from the main updraught were not carried into the stratosphere in significant numbers. This is the first time that images of stratospheric particles were large enough to discern particle shapes. A more detailed view on the encounters is given in Figure 5.6 (extending figure 6 of de Reus et al., 2009). Here, the section of the time series which includes the stratospheric cloud encounters is displayed. Ten second averages of meteorological and microphysical parameters are shown, including the aircraft altitude. The occurrences of overshooting cloud tops in the stratosphere can clearly be discerned by the spikes in the ice particle number concentration (N, middle panel), aerosol depolarisation ratio (ADR), and colour index (CI[13], both second panel from bottom) measurements. The encounters are numbered and shaded in grey, solid shadings indicate major events which are numbered 1 through 6, dashed shadings indicate minor events with the labels a, b, and c. The complete time series of the basic meteorological parameters for this flight can be found in Appendix C.2, Figure C.11. Table 5.1 summarises the meteorological and cloud microphysical parameters of those overshooting cloud events. The ice crystals were observed at altitudes between $18.0\,\mathrm{km}$ and $18.7\,\mathrm{km}$, i.e. $0.7\,\mathrm{km}$ to $1.4\,\mathrm{km}$ above the cold point tropopause which was situated at $17.3\,\mathrm{km}$. Pressures ranged between $68.3\,\mathrm{hPa}$ and $78.3\,\mathrm{hPa}$ and temperatures from $192.3\,\mathrm{K}$ to $186.1\,\mathrm{K}$. This corresponds to potential temperature levels between $414\,\mathrm{K}$ and $386\,\mathrm{K}$. The relative humidity with respect to ice (not available for one of the events) shows subsaturated air masses during five events, ranging here

[13] The CI is defined from MAS backscatter measurements at $1064\,\mathrm{nm}$ and $532\,\mathrm{nm}$ (as in Liu and Mishchenko, 2001) and gives an indication for the size of the scattering particles. A CI of 4 indicates presence of particles in the size range of the used wavelength, decreasing CI to 0 shows a prevalence of particle much larger than the wavelength.

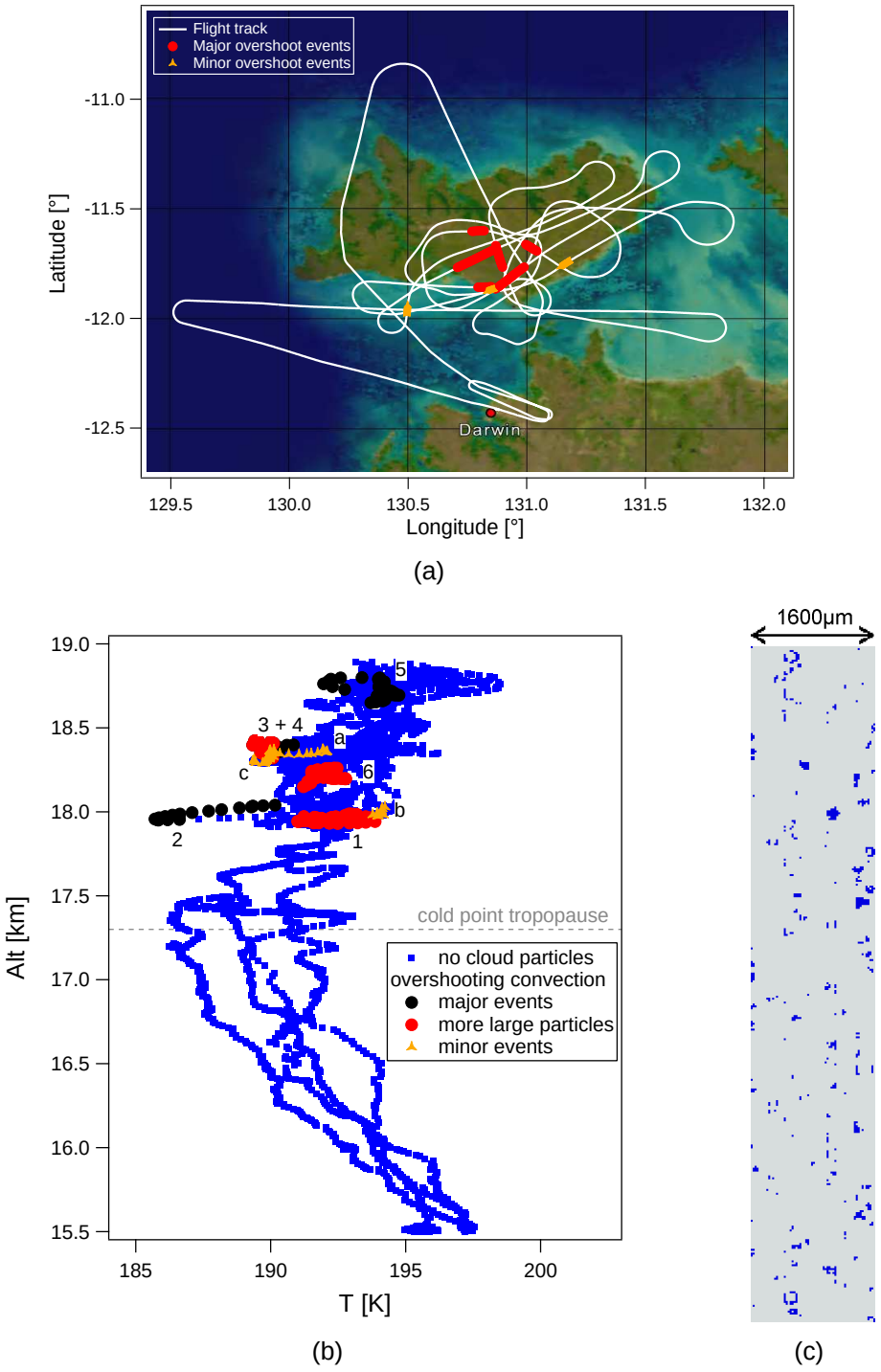

Figure 5.5: Overview over the flight of 30 Nov 2005, the golden Hector day. a) Flight track showing the cloud encounters of overshooting convection indicated in red circles (major events) and orange triangles (minor events). b) Altitude profile of the same flight, again triangles and circles depict minor and major events, respectively. The colour-code of the major events indicates whether the overshoots contain more large than small ice crystals. c) Set of consecutive images as measured by the CIP during event 1 (c.f. Figure 5.6).

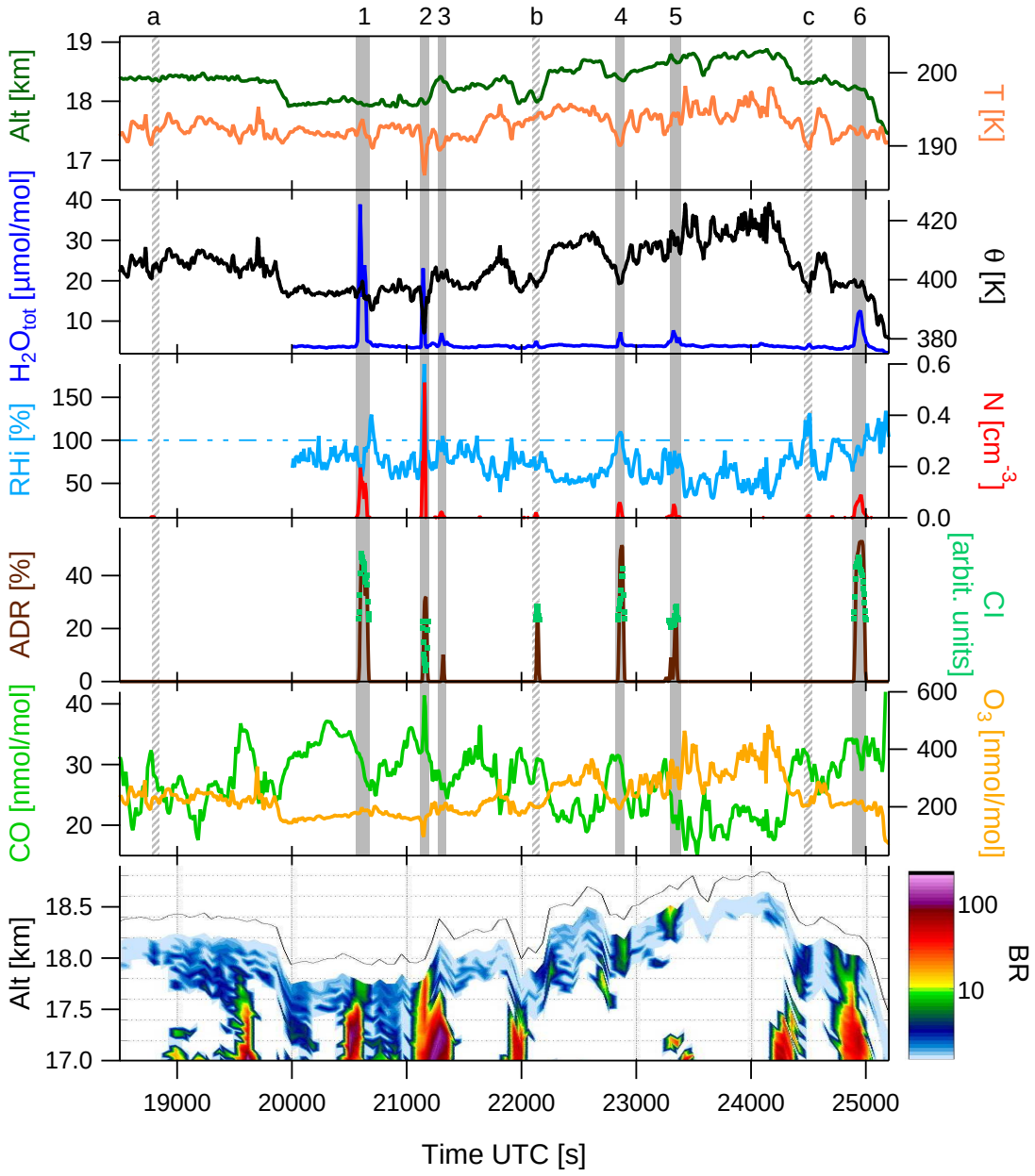

Figure 5.6: Zoom in on the stratospheric part of the time series of the flight on 30 Nov 2005. Displayed are the altitude, temperature, θ, total water content (H_2O_{tot}), relative humidity with respect to ice (RHi), ice crystal number concentrations (N), aerosol depolarisation ratio (ADR), colour index (CI), and ozone and CO mixing ratios. The shading indicates the overshooting cloud events, solid grey for the major, dashed for minor events. The bottom panel shows the backscatter ratio as observed by the downward looking lidar MAL. The numbering of the overshoot events is shown on top of the figure.

Table 5.1: Average values of meteorological and microphysical parameters for the selected overshoot events. The lower panel gives the tropospheric tracer tendencies with up and down pointing arrows indicating whether the tracer increase or decrease, respectively, slantwise pointing if they increase or decrease just slightly. In case no clear trend is visible a rightward pointing arrow is shown.

Event	1	2	3	4	5[c]	6	a	b[c]	c[c]	Part 1[d]	Part 2[d]
Alt [km]	18.0	18.0	18.4	18.4	18.7	18.2	18.4	18.0	18.3	17.4	17.4
p [hPa]	78.3	77.6	72.1	72.8	68.3	74.8	72.8	77.7	73.5	82.6	82.5
$T_{ambient}$ [K]	191.4	186.1	189.2	189.1	192.3	190.0	190.6	192.0	188.4	190	189
θ [K]	396	386	401	399	414	398	403	398	397	387	383
RHi [%]	76	157	95	107	75	89	n.a.	68	116	77	90
N [cm^{-3}]	0.12	0.31	0.015	0.048	0.02	0.05	0.005	0.014	0.006	1.5×10^{-3}	3×10^{-3}
ΔN [cm^{-3}]	± 0.03	± 0.07	± 0.004	± 0.013	± 0.005	± 0.01	± 0.002	± 0.005	± 0.003	$\pm 0.5 \times 10^{-3}$	$\pm 1 \times 10^{-3}$
IWC^a [$10^{-3}\,\mathrm{g\,m}^{-3}$]	1.3	1.1	0.17	0.1	0.008	0.34	0.05	0.007	0.005	8.6×10^{-3}	8.5×10^{-3}
IWC^b [$10^{-3}\,\mathrm{g\,m}^{-3}$]	1.4	1.1	0.18	0.2	0.08	0.44	n.a.	0.07	0.006	n.a.	n.a.
r_{eff} [μm]	40.3	23.1	38.0	12.9	4.1	24.4	27.6	4.8	3.4	8.7	8.1
D_{pN} [μm]	21.1	13.9	19.1	10.8	6.3	15.9	34.9	8.1	5.5	14.2	12.2
D_{pM} [μm]	126.2	72.6	110.4	36.2	8.8	72.2	66.2	10.2	7.0	18.4	17.5
D_{pmax} [μm]	504.9	351.7	369.1	165.5		331.3	230.5			224.1	163.2
ADR [%]	43.5	34.2	5.4	47.6	11.4	36	n.a.	21.7	n.a.	n.a.	n.a.
CI	-0.72	0.72	0	-0.45	-0.01	-0.48	n.a.	-0.14	n.a.	n.a.	n.a.
Tendences											
ΔT	$\uparrow$	$\downarrow$	$\downarrow$	$\downarrow$	$\uparrow$	$\rightarrow$	$\downarrow$	$\rightarrow$	$\downarrow$	$\rightarrow$	$\downarrow$
ΔRHi	$\downarrow$	$\uparrow$	$\uparrow$	$\uparrow$	$\rightarrow$	$\rightarrow$	n.a.	$\rightarrow$	$\uparrow$	$\rightarrow$	$\uparrow$
ΔO_3	$\rightarrow$	$\downarrow$	$\searrow$	$\downarrow$	$\uparrow$	$\rightarrow$	$\searrow$	$\downarrow$	$\downarrow$	n.a.	n.a.
ΔCO	$\rightarrow$	$\uparrow$	$\downarrow$	$\uparrow$	$\downarrow$	$\downarrow$	$\uparrow$	$\uparrow$	$\rightarrow$	$\rightarrow$	$\uparrow$

[a] IWC derived from particle probe measurements (CIP and FSSP), errors within a factor of 2
[b] IWC derived from hygrometer measurements (FISH and FLASH) with an uncertainty of 20 %
[c] no particle observations by the CIP, thus, size parameters affected and D_{pmax} omitted
[d] measurement of 29 Nov 2005

between $68\,\%$ and $95\,\%$. This indicates that the clouds were in a decaying state and ice particles were evaporating. The other three cases show a supersaturation with relative humidities between $107\,\%$ and $157\,\%$ and thus, an indication for ice crystal formation or very recent overshoots from the troposphere. The IWC deduced from the size distribution measurements ranged from $1.3 \times 10^{-3}\,\mathrm{g\,m^{-3}}$ to $4.5 \times 10^{-5}\,\mathrm{g\,m^{-3}}$, for the periods were the CIP detected particles, which agreed within a factor of 2 with the IWC deduced from the FISH and FLASH instruments. The effective radii varied between $12.9\,\mu\mathrm{m}$ and $40.3\,\mu\mathrm{m}$ while the number weighted mean diameter ranged from $10.8\,\mu\mathrm{m}$ to $34.9\,\mu\mathrm{m}$. The largest particle has been observed in event 1 with a diameter of $505\,\mu\mathrm{m}$. Table 5.1 also includes the values for the event of the 29 November 2005. This event was measured on level flight at an altitude of $17.4\,\mathrm{km}$ and $189.3\,\mathrm{K}$, the cold point tropopause was located at $17\,\mathrm{km}$ that day. The time series for this flight can be found in the Appendix C.2, Figure C.10. Over a time period of roughly $20\,\mathrm{min}$ patchy clouds (i.e. clouds that yield data points only for a few seconds with breaks of a few seconds in between) have been observed, whereof the CIP detected particles during roughly $12\,\mathrm{min}$. The largest particle observed had a diameter of $225\,\mu\mathrm{m}$. However, number concentrations are much lower compared to the events of the 30 November, also the IWC is much lower compared to those events where particles are detected by the CIP. Owing to this and the fact that the cloud was patchy, the effective radius and mean diameters are smaller than those of the events measured the next day.

5.2.2 Observations of tropospheric tracers

Besides the meteorological and microphysical parameters, also ozone and CO are displayed in ten second averages in Figure 5.6 as further tropospheric tracers (complementary to temperature and relative humidity). The events 2 and 4 show tropospheric signatures in all four tracers, that is, decreasing temperature and ozone mixing ratio and an increase in relative humidity and CO mixing ratios compared to the surrounding air masses. Furthermore, the events 3, a, and c show a decrease in temperature, (slightly) decreasing ozone mixing ratios, and increasing relative humidity (measurement not available for event a). The CO mixing ratios increase during the encounters of events a and c. This indicates that the air masses in these events resulted from an updraught of tropospheric air into the stratosphere. Event 3 exhibits decreasing CO in contrast. The minor encounter b shows a slight decrease in ozone and an increase in CO mixing ratios but does not reveal a clear trend in relative humidity or temperature, while the potential temperature decreases. The other events show no clear trend (event 6), or even an increase in temperature (event 1 and 5) and ozone mixing ratio (event 5). The latter events exhibit reduced CO mixing ratios also. Thus, the encounters 1, 5, and 6 show no indication for a tropospheric origin. All trends of temperature, relative humidity, and ozone and CO mixing ratios are summarised in Table 5.1. For the case of the 29 November 2005 the whole time period of patchy cloud measurement is shortened to the latter part of it because the cloud was a little less patchy during that time and it is split into two parts: Part 1 denotes the section without tropospheric indication while Part 2 shows tendencies that indicate tropospheric origin. Here, temperature decreases and relative humidity increases as well as the CO mixing ratio. Ozone measurements were not available at that time. It has to be noted that the decrease in temperature in the cases 2, 3, 4, a, and c (up to

$6\,\mathrm{K}$) cannot be a result of cooling due to evaporation. In a rough estimate evaporation of about $1 \times 10^{-3}\,\mathrm{g\,m^{-3}}$ would lead to a temperature decrease of a few hundredth to tenth K while the peaks here show a decrease of a few degree each (P. Spichtinger, personal communication, 2011).
The backscatter ratio, as measured by the downward looking lidar MAL on 30 November 2005, is shown in the bottom panel of Figure 5.6. The aircraft altitude is indicated by the black line. It can clearly be seen that ice crystals were detected down to the local tropopause with increasing backscatter ratios when descending further down, indicating that the crystals were of tropospheric origin and were transported into the stratosphere by overshooting convection. Possible explanations for the non-present tropospheric signature are either mixing of the surrounding stratospheric air with the overshot air parcels leading to a decay of tropospheric signatures or in situ formation of the ice crystals. The altitude profile in Figure 5.5(b) shows that the events with tropospheric signatures (2, 3, 4, a, and c) can be found at the colder temperature ranges to the left. These events comprise also the higher relative humidities of $95\,\%$ and more. On the other hand, the events without clear tropospheric tracer signatures (1, 5, and 6) occurred at warmer temperatures and lower RHi (below $89\,\%$), indicating that the clouds were in a decaying state. Event 5, for example, is situated the highest up in the stratosphere. Thus, this air mass most likely had sufficient time to mix with surrounding air and diminish its tropospheric tracer mixing ratios.

5.2.3 Particle composition

Size distributions for all stratospheric cloud encounters are compiled and displayed in Figure 5.7. It shows that relatively large ice crystals, even reaching sizes of $500\,\mu\mathrm{m}$ in encounter 1, were present in the stratosphere. It might be speculated whether the observed clouds exist of ice or e.g. NAT particles. The presence of NAT clouds in the tropical UTLS has been proven by Hervig and McHugh (2002) using satellite data and by Voigt et al. (2005) with in situ measurements. The measurements of total NO_y on 29 November however showed no peaks during the stratospheric cloud encounters as would have been expected if NO_y containing particles were present. Unfortunately, no NO_y measurements were available on 30 November. Instead, the IWCs derived from the two hygrometers FISH and FLASH give a clear evidence for the presence of ice during the respective cloud encounters. Only during event a neither water nor NO_y measurements are available. However, particles with sizes up to $230\,\mu\mathrm{m}$ have been detected during this event, much larger than the NAT particles observed by Voigt et al. (2008) which had sizes below $6\,\mu\mathrm{m}$.

5.2.4 Effect on stratospheric water budget

In the light of stratospheric dryness the question arises whether the observed ice crystals were formed in situ in the stratosphere, or if they were transported upwards in updraughts from the troposphere. The former would lead to dehydration of the stratosphere when the in situ formed ice particles become large enough to sediment out. The latter could lead to dehydration in case more water vapour deposits onto the ice crystals and consequent sedimentation, or to hydration of the stratosphere in case the ice particles sublimate. Furthermore, humid tropospheric air may mix with

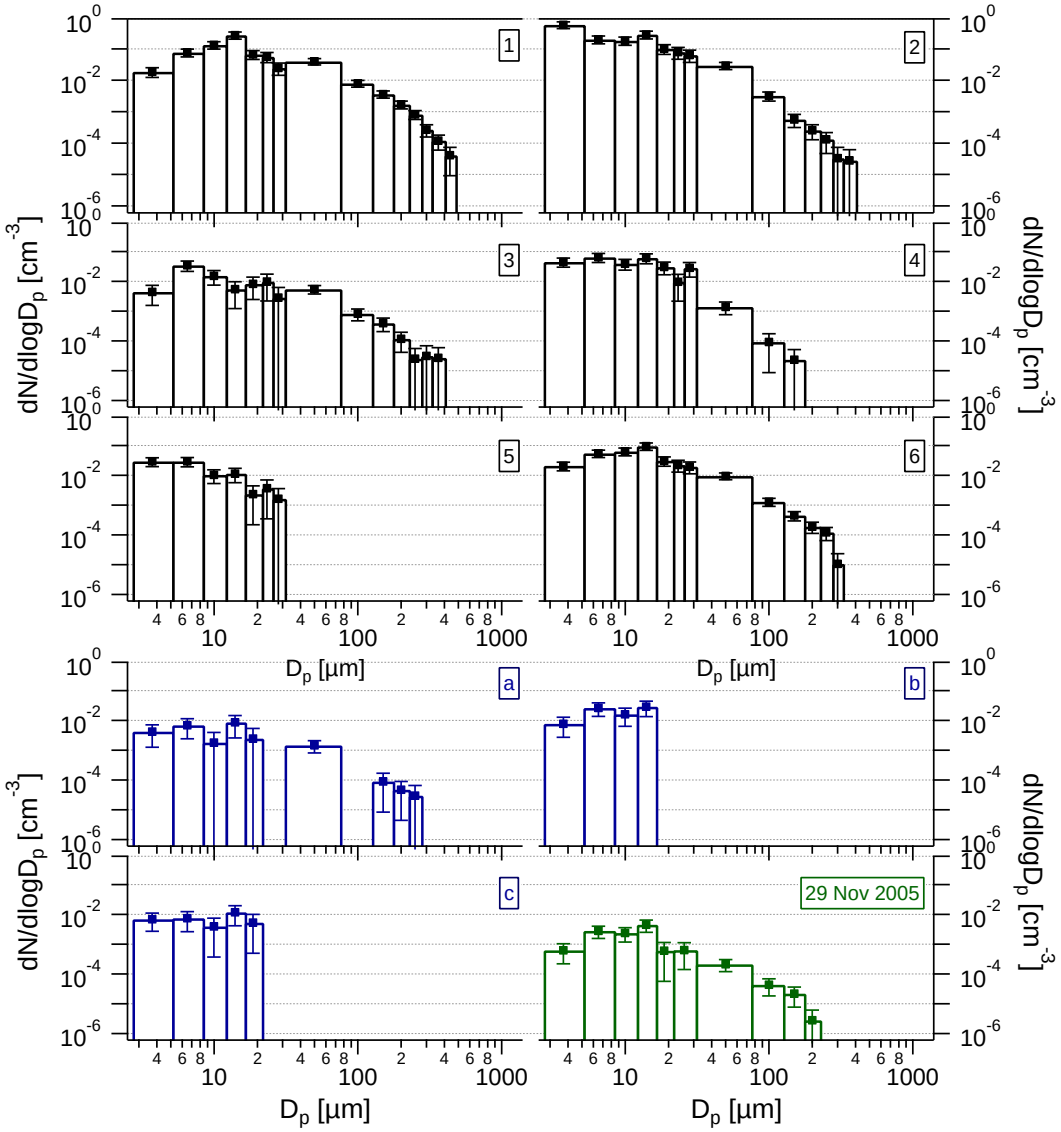

Figure 5.7: Size distributions of the overshooting convection cloud events on 30 Nov 2005. The major events (1 to 6) are displayed in black histograms, while the minor events are shown in dark blue in the lower panels. The size distribution of the 29 Nov 2005 event is displayed in the lower right edge in dark green.

dry stratospheric air, leading to an increase of the water vapour mixing ratio.
In order to gain an estimate of ice particle residence times in the stratosphere the terminal settling velocities have been calculated using the particle sizes given by the first major event since the largest particles have been observed here. According to Heymsfield et al. (2002) and Mitchell and Heymsfield (2005) the relation of terminal velocity V_t and Reynolds Number Re is used for deriving the terminal velocity

$$V_t = Re\frac{\nu}{D_p}, \tag{5.1}$$

with ν the kinematic viscosity of air. Since Re is a function of particle diameter and area, the terminal velocity increases with increasing particle diameter. Even though these particles were observed in a subsaturated air mass which leads to sublimation

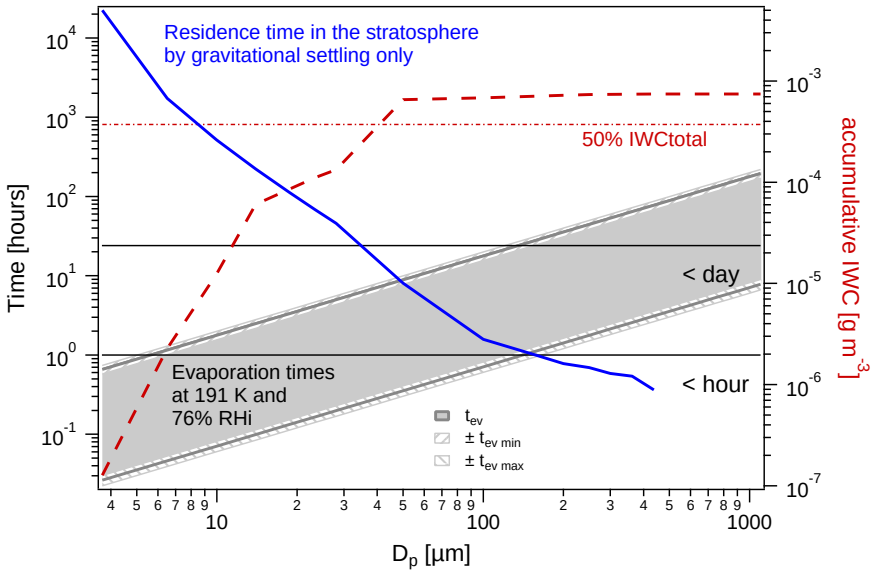

Figure 5.8: Stratospheric residence times based on gravitational settling and evaporation times for the ice particles observed in event 1. The accumulated ice water content derived from the size distribution is displayed as red dashed line on the right axis. The grey striped areas indicate the uncertainty in the evaporation rates. Adapted from de Reus et al. (2009).

of the ice crystals, the particle sizes for these calculations are kept constant. Thus, residence times given here are a lower limit, since the particles would decrease in size and thus, fall slower. Additionally, possible updraughts that could further decrease the fall speed are not taken into account. The terminal settling velocities for the mean ice particle sizes given by the size distribution range between $0.001\,\mathrm{cm\,s^{-1}}$ for the smallest and $54\,\mathrm{cm\,s^{-1}}$ for the largest particles. Using the local distance of $0.7\,\mathrm{km}$ to the tropopause in event 1, the residence times based on gravitational settling are illustrated in Figure 5.8 and range from half an hour for the largest to several days for the smallest particles. The events 6 and c have been investigated in detail by Corti et al. (2008), who conclude that the ice particles in those events were transported upwards from the troposphere by overshooting convection since they were able to exclude unintended contrail sampling as well as in situ formation, as explained in the following. Corti et al. (2008) performed box model simulations for the growth and sedimentation of ice particles using RHi of $130\,\%$. In order to explain the presence of an ice particle with a diameter of about $80\,\mu\mathrm{m}$ at $17\,\mathrm{km}$ altitude several hours of growth and a nucleation at $19\,\mathrm{km}$ altitude are needed. Particles of about $200\,\mu\mathrm{m}$, as observed in several events by the CIP, would have to have formed above $20\,\mathrm{km}$ requiring several hours of growth, even at RHi of $160\,\%$. Since radar observations revealed that, in several cases, the convective systems formed only half an hour prior to the observation of ice particles above $380\,\mathrm{K}$, the ice particles cannot have formed in situ.

Figure 5.8 also shows the evaporation times of the ice particles under the conditions of event 1. Using the observed temperatures and relative humidities the times that particles would need to evaporate completely have been calculated according to Pratte et al. (2006). They studied the condensation and evaporation fluxes at low temperatures such as those that can be found in the tropical tropopause region. In

Table 5.2: Released IWC by the convective overshooting cloud tops given in mass (IWC_{rel}) and fraction of total IWC at the slowest and fastest evaporation rates.

	slowest evaporation rate		fastest evaporation rate	
Event	IWC_{rel} [$\mathrm{g\,m^{-3}}$]	fraction [%]	IWC_{rel} [$\mathrm{g\,m^{-3}}$]	fraction [%]
1	$(5.6 \pm 0.5) \times 10^{-4}$	75 ± 7	$(7.10 \pm 0.10) \times 10^{-4}$	94 ± 1
3	$(4.5 \pm 0.6) \times 10^{-5}$	23 ± 3	$(1.76 \pm 0.01) \times 10^{-4}$	90 ± 0.2
5	7.8×10^{-6}	100	7.8×10^{-6}	100
6	$(2.1 \pm 0.2) \times 10^{-4}$	57 ± 5	$(3.47 \pm 0.02) \times 10^{-4}$	94 ± 0.5
b	7.1×10^{-6}	100	7.1×10^{-6}	100
Part1	$(5.7 \pm 0.4) \times 10^{-6}$	64 ± 4	$(8.52 \pm 0.05) \times 10^{-6}$	96 ± 0.5
Part2	$(3.7 \pm 0.2) \times 10^{-6}$	41 ± 1	$(8.60 \pm 0.10) \times 10^{-6}$	93 ± 0.3

a Knudsen flow reactor they determined evaporation rates for different types of ice (condensed, bulk, single crystal, snow, and cubic ice), finding lower values than previously had been given in the literature. At atmospheric pressures the evaporation rate is slowed down by a factor of 3.4 compared to the molecular flow conditions that have been used in their experiment. Thus, a maximum and minimum evaporation rate is given by Pratte et al. (2006) which are used in this thesis accordingly. The evaporation times of the ice particles have been calculated following the equation given below:

$$t_{ev} = \frac{\left(\frac{\rho_i N_A}{M}\right)^{2/3} \left(\frac{r_p}{a}\right)}{J_{ev}\,(1 - RH)}, \tag{5.2}$$

with ρ_i the density of ice, N_A the Avogadro constant, M =18 $\mathrm{g\,mol^{-1}}$ for H_2O, r_p the ice particle radius, a the distance between two layers of H_2O(ice) in the ice structure, J_{ev} the evaporation rate, and RH the relative humidity. Figure 5.8 shows that the calculations yield a large range of evaporation times, indicated in the grey shading. Taking the slow evaporation rate a $150\,\mu\mathrm{m}$ ice crystal, for example, would evaporate within a day, but the evaporation only takes one hour when using the fast evaporation rate instead. The cross-section of residence times and the evaporation times show that all ice crystals smaller than $50\,\mu\mathrm{m}$ will evaporate in the stratosphere, before they have left the stratosphere due to their gravitational settling, even when using the slowest evaporation rate. The mass of these ice crystals corresponds to $75\,\%$ of the total measured IWC during this event, with an amount of $5.6 \times 10^{-4}\,\mathrm{g\,m^{-3}}$. When looking at the fastest evaporation rate, $94\,\%$ of the ice will evaporate in the stratosphere, releasing $7.1 \times 10^{-4}\,\mathrm{g\,m^{-3}}$ water vapour. The same calculations have been performed for the other overshoot events with relative humidities below $100\,\%$ and the results are shown in Table 5.2. The calculations show that the mass that will be released by the evaporating ice particles accounts for more than the half of the total IWC on the 30 November, except for event 3 with only $23\,\%$. The overshoot event on 29 November did not reach as high above the tropopause (about $400\,\mathrm{m}$) and thus a smaller fraction of the ice particles will evaporate at the slowest evaporation rate compared to most events on 30 November. Since for the calculations in-mixing of surrounding air is not taken into account, which would lead to a decreasing humidity due to the dryness of the stratosphere, the evaporation times given here constitute an upper limit. The ice particles will thus decrease in size faster and with this have a lower fall speed and in turn a longer stratospheric residence time. Considering that also the residence times

constitute a lower limit most probably a larger part of the ice particles will evaporate in the stratosphere, possibly all ice crystals. This would mean that in these cases the overshooting convection contributes to the hydration of the stratosphere. The cases 2, 4, and *c* exhibit RHi above $100\,\%$ and thus the ice particles will not evaporate. However, these events show the strongest tropospheric signatures indicating that mixing with surrounding air masses has not proceeded significantly. With the help of water measurements and back trajectory calculations Schiller et al. (2009) showed, for cases over West Africa, that convective overshoots do not occur temporarily without mixing with surrounding air. Furthermore, they were able to refute a complete sedimentation of the ice particles back to the troposphere. That means that detrainment of air from the overshoot events here and subsequent mixing will lead to an increase of humidity in the surrounding dry stratospheric air. In case the RHi drops below $100\,\%$ ice particles will evaporate and lead to a further hydration of the stratospheric air. These considerations confirm the results of Corti et al. (2008, c.f. Figure 5.4).

5.3 Discussion and summary

During the SCOUT-O3 campaign events of overshooting convection have been measured over the Tiwi Islands. Several cloud encounters in the tropical stratosphere, up to $1.4\,\mathrm{km}$ above the local tropopause, directly above the Hector storm system have been observed. Unexpected large ice crystals of up to $505\,\mu\mathrm{m}$ in diameter maximum dimension have been imaged by the CIP, the first in situ images of such large particles in the stratosphere. At ambient RHi of $68\,\%$ to $157\,\%$ the IWC of the stratospheric cloud encounters ranged between $5 \times 10^{-6}\,\mathrm{g\,m^{-3}}$ and $1.3 \times 10^{-3}\,\mathrm{g\,m^{-3}}$. Ice particle number concentrations between $0.005\,\mathrm{cm^{-3}}$ and $0.31\,\mathrm{cm^{-3}}$ were found and effective radii varied from $3.4\,\mu\mathrm{m}$ to $40.3\,\mu\mathrm{m}$. Due to the difficulty to perform in situ measurements in the tropical stratosphere because of its high altitude and the lack of high altitude research aircraft, observations of such overshoots are rare. Knollenberg et al. (1982) found ice crystals with sizes up to $150\,\mu\mathrm{m}$ in the stratosphere over Panama, and even particles with sizes up to $1\,\mathrm{mm}$ in the cirrus deck below. Observational evidence, including other types of instruments as backscatter sondes and radar, of overshooting convection was found during the European HIBISCUS[14] (Pommereau et al., 2011), TROCCINOX (Chaboureau et al., 2007), SCOUT-AMMA (Cairo et al., 2010), and SCOUT-O3 (Brunner et al., 2009) campaigns. The in situ measurements of the latter are shown in this chapter.

The observed ice particles are remnants of recently overshooting cumulonimbus cloud tops and have thus been transported into the stratosphere by convective overshoots. Some of the cloud encounters show clear indication of their tropospheric origin in the air masses while others have resided long enough in the stratosphere to be mixed with surrounding air. Stratospheric origin of the ice particles by in situ formation can be excluded. On the one hand before growing to those (large) sizes the observed particles would have sedimented out (Corti et al., 2008), on the other hand, if the ice crystals would have formed in situ they would probably be much smaller. For example, Garrett et al. (2006) measured a pileus cloud with in situ formed ice crys-

[14] HIBISCUS is a title referring to the tropics, not an acronym and is a project consisting of a series of field campaigns that tool place during the summers of 2001, 2003 and 2004 in Brazil.

tals near the tropopause that have effective radii of about $2\,\mu\mathrm{m}$ to $4\,\mu\mathrm{m}$, compared to the $13\,\mu\mathrm{m}$ to $40\,\mu\mathrm{m}$ observed here. The calculation of stratospheric residence times of the observed cloud ice particles and their evaporation rate resulted in the estimate that a large part of these ice crystals evaporates in the stratosphere due to the prevalent dryness. Thus, it is a clear indication of the humidifying effect of these convective overshoots on the stratosphere, corroborating the findings of Corti et al. (2008, as highlighted in Figure 5.4). Furthermore, this is in agreement with Nielsen et al. (2007) who found remnants of an overshooting top in the stratosphere with the help of backscatter sondes and radars. They estimated the stratospheric age of those particles to be $5.5\,\mathrm{h}$ and argued that the originating thunderstorm must also have carried a considerable amount of ice-water into the stratosphere. The authors state that the particles were most likely composed of ice and that the particles could not be much larger than $20\,\mu\mathrm{m}$. In a rough estimate, they found the particle diameters to be in the range of $0.4\,\mu\mathrm{m}$ to $3\,\mu\mathrm{m}$, i.e. much smaller than the particles observed during SCOUT-O3. However, the question remains how effectively overshoots contribute to the water content of the stratosphere. A discussion about this can be found in Pommereau (2010) who points out that overshooting convection plays a major, if not dominant, role on the troposphere to stratosphere transport. He states that the European campaigns (mentioned above) over land indicate that those overshoots penetrating the stratosphere occur frequently. This is contrasting the generally assumed scarcity of those events (e.g. Folkins et al., 1999). Another indication for frequent overshoot events is given by Liu and Zipser (2005), who identified overshooting convection events from Tropical Rainfall Measuring Mission (TRMM) satellite measurements of the precipitation radar (PR). They found overshooting convection to be more frequent over land than over ocean, especially over central Africa, Indonesia, and South America and also to be more frequently reaching higher (above $17\,\mathrm{km}$). The question whether these events are dehydrating or moistening the stratosphere is not answered in their study, owing to the fact that the TRMM PR does detect particles which are probably large enough to sediment out in a short time, but it does not detect smaller particles that might be able to stay a longer time in the stratosphere and thus, may evaporate. However, they found a semiannual cycle of the deep convection overshooting area while the water vapour in the lower stratosphere has a well known annual cycle (McCormick et al., 1993; Dessler, 1998), suggesting that the convective overshooting cannot explain dehydration of air that enters the stratosphere. Also Khaykin et al. (2009) found evidence for hydration of the stratospheric air as a result of convective overshooting. There are also a few model studies supporting the hydrating effect of overshooting convection (Grosvenor et al., 2007; Chaboureau et al., 2007). These studies were carried out with small scale Cloud Resolving Models (CRM) and in 3D configuration. This is important since overshooting cloud tops are limited in space and time and are thus not correctly reproduced by models using a larger scale, which might have lead to the impression that overshooting convection does not humidify the stratosphere. The measurements shown here indicate that encounters of overshooting convection penetrating the stratosphere may contain only small number concentrations of ice particles. Some of the satellite based studies might thus not have detected all events of overshooting convection and thus underestimate the true occurrence frequency of such events. Therefore, as Nielsen et al. (2007) state, it would be premature, at this stage, to quantify the impact of such con-

vective overshoot events on the stratospheric water budget, without more information about their frequency and their microphysics. In this regard more remote sensing studies for deriving a climatology of overshooting convection events with instruments sensitive also to thin clouds and small ice particles, as well as more in situ measurements of those events, are desirable.

Chapter 6

Subvisible Cirrus at the West African Tropical Tropopause

6.1 Meteorological background

Cirrus clouds are known to play an important role in the Earth's radiation budget (Lynch, 1996). Their effects on infrared and visible radiation, and thus on the warming or cooling of the atmosphere, depends strongly on their microphysical properties (Gayet et al., 2006). One key property to describe the radiative properties of cirrus clouds is the optical thickness τ. Threshold values of τ for cirrus classification have been established (Sassen and Cho, 1992) and define cirrus clouds with $\tau < 0.03$ as subvisible, $0.03 < \tau < 0.3$ define thin cirrus, and $0.3 < \tau < 3$ opaque cirrus. This chapter focuses on the subvisible cirrus (SVC).

Horizontally extensive SVC layers have been observed in the tropics close to the tropopause. Several names for these cirrus clouds can be found in the literature (e.g. laminar cirrus, ultrathin tropical tropopause clouds (UTTC), high altitude cirrus (HAC)). Here, they will be referred to as tropical tropopause SVC, or simply SVC.

The infrared greenhouse effect of SVCs has been found to outweigh their solar albedo effect (e.g. Wang et al., 1996; Haladay and Stephens, 2009) and thus, the SVC have a net positive radiative effect on the top-of-atmosphere (TOA) energy budget. Values for the cloud radiative forcing range between $0.5\,\mathrm{W\,m^{-2}}$ and $1.7\,\mathrm{W\,m^{-2}}$ (Wang et al., 1996; McFarquhar et al., 2000; Haladay and Stephens, 2009). Davis et al. (2010) determined much smaller values of $0.001\,\mathrm{W\,m^{-2}}$ to $0.03\,\mathrm{W\,m^{-2}}$ from their measurements which they explained with the much smaller observed τ. Their calculated heating rates amount to $0.05\,\mathrm{K\,day^{-1}}$ to $0.1\,\mathrm{K\,day^{-1}}$. Other studies, in contrast, found higher heating rates of $1.66\,\mathrm{K\,day^{-1}}$ to $3.24\,\mathrm{K\,day^{-1}}$ (McFarquhar et al., 2000; Comstock et al., 2002; Bucholtz et al., 2010). However, most studies use satellite observations or ground-based remote sensing (radar and lidar), which are techniques that may fail in observing the thinnest SVC or may not detect small particles. This, in turn, can lead to deduction of larger cloud radiative forcings and heating rates, which has been stated by Davis et al. (2010).

Occurrence frequencies of SVC, i.e. the fraction of SVC observations within the total number of satellite overpasses, have been determined with the help of satellite observations. Wang et al. (1996) used the Stratospheric Aerosol and Gas Experiment (SAGE) II, a seven channel radiometer, aboard the Earth Radiation Budget Satellite

(ERBS). Based on over 6 years of observations they established a climatology of SVC that indicates that SVC concentrate generally near the tropopause. The highest SVC occurrence frequency of about $70\,\%$ can be found at $15.5\,\mathrm{km}$ altitude over Micronesia. The occurrence frequencies of SVCs at three different altitudes and their seasonal variations are shown in Figure 6.1. Similar global seasonal distributions of SVC were found by the Optical Spectrograph and InfraRed Imaging System (OSIRIS) aboard the Odin satellite (Bourassa et al., 2005). It is obvious that these clouds are present frequently in the tropics which makes a more detailed knowledge about their microphysical properties more important. On the one hand in order to learn about the interaction of the microphysical and radiative properties (c.f. the strong insolation in the tropics) but also to learn about the dehydration potential of SVC for air entering the stratosphere, as discussed in Section 6.1.2. A recent satellite study (Sassen et al., 2009) investigated a two-year data set of combined lidar and cloud radar measurements from the CALIPSO and CloudSat satellites. In addition, differences in the SVC occurrence frequency between day and night have been observed. Highest occurrence frequencies were found in the tropics during night, especially over the ocean. Land areas like eastern central Africa also have a strong nocturnal preference for these clouds. The Lidar In-space Technology Experiment (LITE) performed space shuttle borne observations of SVCs on board the Discovery in 1994 (Winker and Trepte, 1998). Thin sheets of SVCs have been detected close to the tropopause throughout the tropics with thicknesses generally between a few hundred metres and one kilometre while their horizontal extent reached up to $2700\,\mathrm{km}$. They point out that these clouds are unusually homogeneous in the horizontal and the cloud lifetimes can be in order of days.

Peter et al. (2003) supported these findings by investigating remote and in situ measurements from aircraft. Besides the small vertical and large horizontal extents and the location close to the cold point tropopause (a few hundred metres below), they found evidence for a high degree of homogeneity of the SVCs. Furthermore, they revealed that the SVC particles are of non-spherical shape and concluded that the particles consisted of water ice. In contradiction, Omar and Gardner (2001) stated that $31\,\%$ of the SVCs have optical similarities to type 1a PSCs. Due to the $90\,\%$ chance that these clouds form at temperatures of $185.0\,\mathrm{K} \pm 2.5\,\mathrm{K}$, particles of a size and composition similar to the type 1a PSCs must be considered as a possibility. The thermodynamical possibility of nitric acid clouds to form was brought forward by Hamill and Fiocco (1988) and evidence for such clouds was provided by Hervig and McHugh (2002) and by Voigt et al. (2008).

Only few in situ aircraft measurements of SVCs are reported: 1973 over the tropical West Pacific (Heymsfield, 1986; McFarquhar et al., 2000); 1999 over the Indian Ocean during APE-THESEO[15] (Thomas et al., 2002; Peter et al., 2003); 2006 over the tropical Eastern Pacific during CRAVE[16] (Lawson et al., 2008); and 2007 over the equatorial Eastern Pacific during TC4 (Davis et al., 2010). The findings about the microphysical properties of the SVCs sampled are summarised in Table 6.1. SVC coverage determined by aircraft observations were found to be $31\,\%$ over the western Indian Ocean (during APE-THESEO; Thomas et al., 2002), $29\,\%$ in the central Pa-

[15] Airborne Platform for Earth observation - (contribution to) the Third European Stratospheric Experiment on Ozone, Seychelles, February-March 1999; (Stefanutti et al., 2004)

[16] Costa Rica Aura Validation Experiment, Costa Rica, January-February 2006

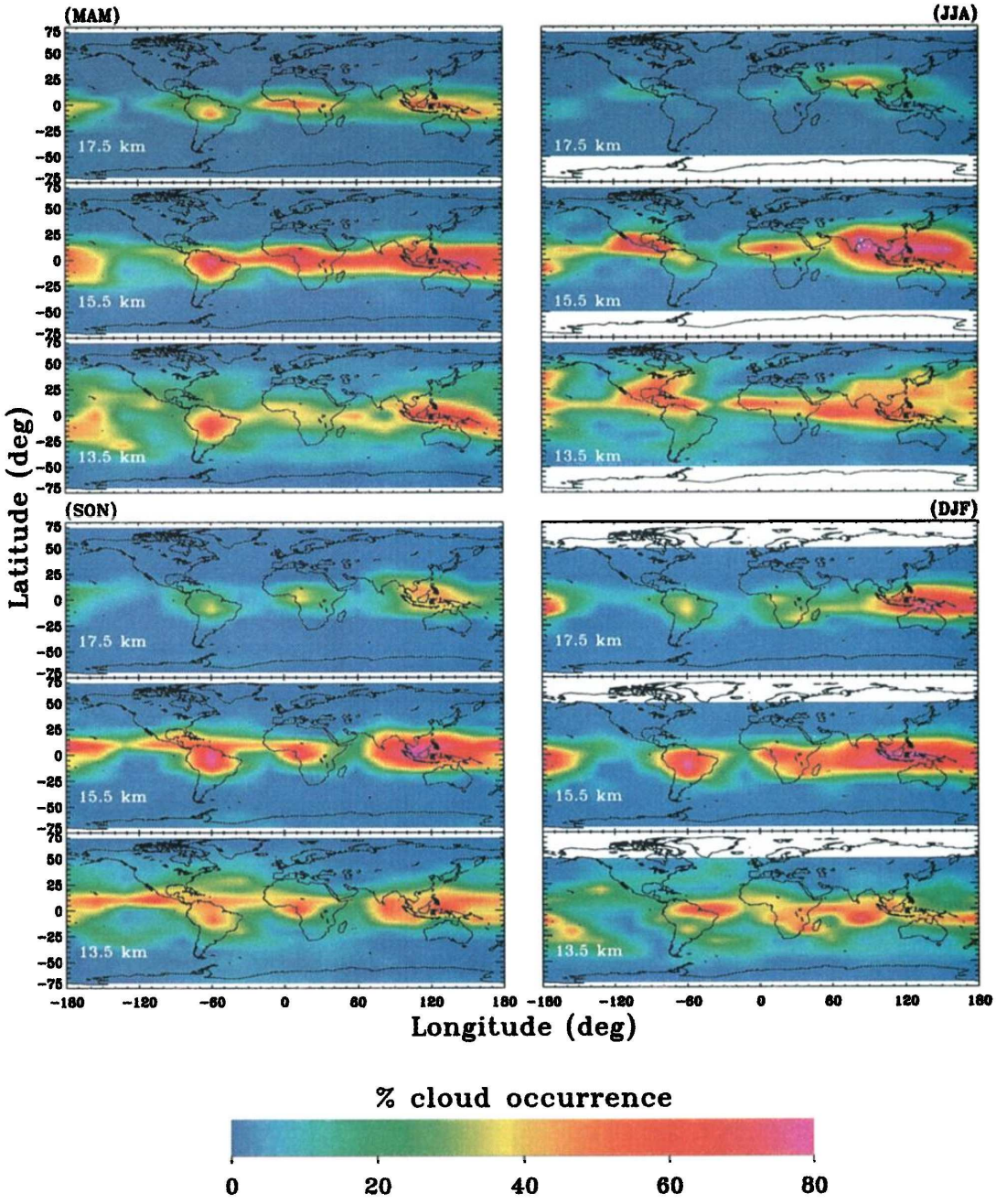

Figure 6.1: Latitude-longitude distributions of SVC occurrence frequency at different altitudes and differentiated by season, starting with MAM (i.e. March, April, May) in the upper left. Taken from Wang et al. (1996).

Table 6.1: Overview of microphysical properties of SVC measured in situ during former campaigns.

	IWC [$\mathrm{g\,m^{-3}}$]	N [$10^{-3}\,\mathrm{cm^{-3}}$]	r_{eff} [μm]	T [K]	RHi [%]
APE-THESEO*	3.2×10^{-6}	15		<190	<120
CRAVE	5.5×10^{-5}	66	8.8	<190	>160
TC4	5.6×10^{-6}	2	14.0	193 – 198	80 – 130
1973	$10^{-6} - 10^{-4}$	29 – 102	2.5 – 125	189 – 190	

*Note: These measurements have been performed with an FSSP-300 with lower and upper detection limits of $0.7\,\mu\mathrm{m}$ and $23\,\mu\mathrm{m}$, respectively. Therefore, values for the microphysical parameters might be higher in case larger particles were present but not detected.

cific Tropics (CEPEX[17]; McFarquhar et al., 2000), and even $65\,\%$ in the central Pacific region (lidar observations during TOTE/VOTE[18]; Pfister et al., 2001). The latter also described two basic types of SVC: a thin quasi-laminar layer and a thicker, more textured structure.
First direct measurements of SVC particle shapes were performed with a replicator (Heymsfield, 1986; McFarquhar et al., 2000) and showed columnar and trigonal particles. Further shapes of SVC ice particles were imaged with CPI instruments. Primarily quasi-spherical particles (Lawson et al., 2008; Davis et al., 2010) and some plate-like hexagonal particles (Lawson et al., 2008) were found.
The overview given above shows that in situ observations of SVC are rare and none of them was made over a continental area. This chapter thus presents unique in situ measurements of SVC microphysical properties over continental West Africa. Hence, these observations are an important contribution to the sparse SVC data set.

6.1.1 Formation of SVC

How SVCs form and how they can be maintained for such long time periods and with such a homogeneity still remains unclear. In general two ideas of formation mechanisms are discussed (e.g. Jensen et al., 1996; McFarquhar et al., 2000; Pfister et al., 2001):

- in situ formation due to cooling on both a synoptic scale and mesoscale or in situ formation from gravity waves and
- formation of SVC as remnants of anvils produced by recent (a few days) deep convection.

The distribution of tropical cirrus in relation to convection has been investigated by Massie et al. (2002) and McFarquhar et al. (2000), using Halogen Occultation Experiment (HALOE) aerosol extinction and Climate Diagnostics Center (CDC) outgoing longwave radiation (OLR) data for the years 1995 – 2000 and by considering SAGE II and International Satellite Cloud and Climatology Project (ISCCP) data, respectively. Massie et al. (2002) found that deep convection occupies only $7\,\%$ of the equatorial region, whereas $90\,\%$ of the cirrus clouds near the tropopause are located outside of

[17] Central Equatorial Pacific Experiment, Fiji, March-April 1993
[18] Tropical Ozone Transport Experiment/Vortex Ozone Transport Experiment, Hawaii, USA, December 1995 and February 1996

regions of deep convection. However, backtrajectories near the tropopause showed that half of the HALOE cirrus observations over the Maritime Continent are consistent with formation by convective blow-off, while the other half are consistent with in situ formation processes. When looking at the global distribution $27\,\%$ of the SVCs were found to occur in the vicinity of deep convection. Furthermore, $38.7\,\%$ of SVC occurred in areas where there had been some convective activity in the previous 12 hours (McFarquhar et al., 2000). In addition, a detailed cirrus cloud model showed that SVC can form as remnants of convective outflow (Jensen et al., 1996). The model predicts that within a few hours ice crystals with diameters larger than $20\,\mu\mathrm{m}$ to $40\,\mu\mathrm{m}$ will sediment out and leave behind a persistent cloud layer with relatively small particles. The optical depth of the residual cloud depends on the initial IWC and the vertical shear of the horizontal wind. To explain the in situ formation mechanism, the simulations by Jensen et al. (1996) included ice nucleation by homogeneous freezing of aerosols. The classical theory suggests that at prevailing conditions in the tropical UT large numbers ($\geq 0.4\,\mathrm{cm}^{-3}$) of small ice particles ($< 25\,\mu\mathrm{m}$) should be generated. In combination with slow updraughts persistent cirrus with low optical depth should thus be maintained. Kärcher (2002) described a model of SVC formation due to homogeneous freezing of supercooled aerosol particles. Ice particles form in a layer at the top of the cloud where supersaturation is reached due to adiabatic cooling. Longer-lived ($>10\,\mathrm{min}$) SVCs will only be generated at temperatures below $215\,\mathrm{K}$ and within a narrow range of updraught speeds below $1\,\mathrm{cm\,s}^{-1}$ to $2\,\mathrm{cm\,s}^{-1}$. Since the growing ice particles sediment out of the formation layer before the supersaturation is removed, these clouds will not reach an equilibrium state. Another approach to explain the non-convective SVC formation and persistence is to consider Kelvin or gravity waves. For example, Boehm and Verlinde (2000) used radiosonde data from the Atmospheric Radiation Measurement (ARM) program Nauru99 which was conducted during summer 1999 at Nauru. They identified eastward propagating Kelvin waves, whose characteristics indicated a generation by deep convection. Careful inspection revealed that SVC formation occurred exclusively in the cold phases of the waves. Thus, their study showed a close relationship between tropical waves and upper tropospheric cirrus occurrence. Gravity waves as source of SVC are also considered by several other studies (e.g. McFarquhar et al., 2000; Pfister et al., 2001; Massie et al., 2002).

Estimates of the the amount of equivalent water in the cirrus clouds yield that these only contain $1\,\%$–$5\,\%$ of the local gas phase water (Massie et al., 2002; Peter et al., 2003). Peter et al. (2003) claimed that to explain this small fraction and the small vertical thickness of the clouds a specific stabilisation mechanism is required. This stabilisation mechanism is formulated by Luo et al. (2003b). They suggest that the ice particles oscillate around the altitude where the supersaturation S_i equals one. Above the $S_i = 1$ level is a layer with moderate supersaturation while below a layer of subsaturation can be found. When the ice particles are lifted into the supersaturated region by large-scale upwelling air motions they will grow and increase in weight. At some point they will gain too much weight and sediment below the $S_i = 1$ level. In this region of subsaturation the particles sublimate, become lighter, and are then carried upwards again due to the rising air. However, in this modelling study a mean ice particle diameter of $10\,\mu\mathrm{m}$ to $12\,\mu\mathrm{m}$ was assumed based on the in situ data by Thomas et al. (2002) while more recent observations showed that SVCs may contain ice par-

ticles with sizes larger than $100\,\mu\mathrm{m}$. In order to allow the growth of large crystals with sizes of about $100\,\mu\mathrm{m}$ ice supersaturations must be surprisingly large ($RH_i > 190\,\%$; Jensen et al., 2008) if the ice crystals are not extremely thin plates. Therefore, the formation hypotheses by Jensen et al. (1996) and Luo et al. (2003b) need to be adjusted for larger particles.
In a further study, Jensen et al. (2010) argue that following past modelling studies, which assume that the dominant mechanism for production of ice crystals is the homogeneous freezing of aqueous aerosols, would lead to unrealistic microphysical properties of the clouds. Homogeneous freezing should produce much larger ice concentrations of only relatively small particles, narrower size distributions of the ice crystals, and much larger extinctions than measured during the recent campaigns. Heterogeneous nucleation in contrast, could potentially produce reasonably low number concentrations of ice particles that can grow to relatively large sizes. They also discuss the possibility that only a subset of aerosols act as effective IN and thereby limit the ice concentrations. Relying on measurements of IN performed during CRAVE and laboratory experiments, they suggest that ammonium sulfate particles are a possible candidate for such IN. This suggestion is supported by Froyd et al. (2010) who report on measurements of the composition of residual particles from evaporated SVC ice crystals. They state that the SVC were formed overwhelmingly from freezing of the dominant sulfate-organic aerosol type which was largely neutralised and probably in the form of ammonium sulfate. Therefore, they suggest heterogeneous nucleation involving either dry ammonium sulfate or glassy organic aerosols, which are found to act as heterogeneous nuclei that may explain low ice crystal numbers and high in-cloud humidity in the tropical tropopause layer (Murray et al., 2010), to be a plausible mechanism to initiate ice formation.

6.1.2 Dehydration potential

Several studies point out the potential of SVC in dehydrating tropospheric air before it enters the stratosphere (e.g. Wang et al., 1996; Winker and Trepte, 1998; Pfister et al., 2001; Luo et al., 2003a; Jensen et al., 2008; Davis et al., 2010, c.f. Section 5.1.2). A comparison of satellite observations of water vapour distributions at $19.5\,\mathrm{km}$ (lower stratosphere) and high SVC occurrences showed that the lowest water vapour mixing ratios were generally found at the same geographic locations as the clouds (Wang et al., 1996). This provides observational evidence of the connection between the stratospheric-tropospheric exchange, dehydration processes, and SVC occurrence. Likewise, Winker and Trepte (1998) state that in situ formed SVC may be taken as indicator for locations where air enters the lower stratosphere. The high altitude, low temperatures, and low number concentrations of the ice crystals make SVC well suited to act as drying agent during the last dehydration step before air enters the stratosphere (Peter et al., 2003). These conditions were studied by Luo et al. (2003a) who, with the help of a column model, roughly estimated the global mean dehydration induced by SVC. They obtained a lowering of water vapour of $0.35\,\mu\mathrm{mol/mol}$ in the air that is going to be exchanged from the troposphere to the stratosphere in the tropics. Jensen and Pfister (2004) used a Lagrangian, 1D cloud model to simulate ice cloud formation and dehydration along trajectories in the TTL. Their results show that air rising through the TTL is effectively dehydrated, irrespective of any wave activity. In

general, their model results suggest that the final water vapour mixing ratios are primarily controlled by the minimum temperatures encountered by the air parcels. For the simulated period the average final water mixing ratios were somewhat lower than the estimates of the stratospheric water vapour entry value derived from satellite and in situ measurements. Hence, they state that an additional source of water (such as injection by deep convection) may be required to explain the observed tropical tropopause humidity.
Even though model simulations all suggest dehydration of air entering the stratosphere, the measurements are not able to fully confirm these findings. During CRAVE no clear evidence of dehydration was found, even though the simulations suggest a significant dehydration (Jensen et al., 2008). Based on a 2D model Rosenfield et al. (1998) studied the influence of SVCs on the stratospheric water vapour taking into account also the heating rates of the clouds which amount to $0.1\,\mathrm{k\,day^{-1}}$ to $0.2\,\mathrm{k\,day^{-1}}$. Therewith, they found an increase in stratospheric water vapour of $1\,\mu\mathrm{mol/mol}$, while the dehydrating effect of sedimentation was found to be much smaller. Davis et al. (2010) observed similar heating rates during TC4 ($0.05\,\mathrm{k\,day^{-1}}$ to $0.1\,\mathrm{k\,day^{-1}}$). An upper bound estimate of the final dehydration was given by the IWC of the observed clouds which was at most $0.5\,\mu\mathrm{mol/mol}$. However, they state that their data are insufficient to estimate the net effect of the measured SVC on the stratospheric water budget, but on the other hand their data indicate that SVCs play a non-negligible role in determining the entry value of stratospheric water vapour.

In order to learn and answer the open questions about heating rates, the resulting dehydration potential, but also formation mechanisms or microphysical differences between SVCs at different locations, detailed measurements of the microphysical properties of these clouds are necessary.

6.2 Observations of SVC during SCOUT-AMMA

During the SCOUT-AMMA campaign four times SVCs close to the tropopause were observed. The encounters occurred on 7, 8, and 11 August 2006 and are indicated in the time series that can be found in Appendix C.1 (Figures C.6, C.7, and C.8). In the following the encounters are labelled *SVC1 – SVC4*. The duration of the cloud encounters (i.e. averaging time for the size distributions) ranged between $59\,\mathrm{s} - 143\,\mathrm{s}$ flight time. The SVCs were observed at altitudes between $15\,\mathrm{km}$ and $16.1\,\mathrm{km}$, which corresponds to potential temperatures between $361\,\mathrm{K}$ to $373\,\mathrm{K}$. The local cold point tropopause on these days was located at about $16.3\,\mathrm{km}$ altitude on 7 August 2006 and at $16.5\,\mathrm{km}$ altitude on the other two days. Thus, the SVCs were observed just a few hundred metres below the tropopause. It has to be noted that no shattering has been observed by the CIP during the SVC encounters, i.e. the interarrival times of the particles were always longer than the threshold time (c.f. Appendix Section A.1). The observed microphysical and meteorological parameters of all encounters are summarised in Table 6.2. The mean ice crystal number concentrations range from $1.6 \times 10^{-3}\,\mathrm{cm^{-3}}$ to $2.4 \times 10^{-2}\,\mathrm{cm^{-3}}$, the IWCs range from $2.6 \times 10^{-6}\,\mathrm{g\,m^{-3}}$ to $3.8 \times 10^{-4}\,\mathrm{g\,m^{-3}}$, and the effective radii vary between $2.3\,\mu\mathrm{m}$ and $21.3\,\mu\mathrm{m}$. *SVC1* comprises the lowest temperature with $192\,\mathrm{K}$ as well as

Table 6.2: Summary of meteorological and microphysical parameters of the subvisible cirrus cases, as observed during the SCOUT-AMMA campaign. Extent and extent+ refer to the horizontal dimension of the clouds. The last row provides estimates of the optical thickness τ which is a key parameter for the definition of SVCs.

	SVC1 7 August	SVC2 7 August	SVC3 8 August	SVC4 11 August
av. time [s]	127	65	59	143
extent [km]	22.2	11.1	9	23.2
extent+ [km]	33.7	15.2	33.2	27.9
$T_{ambient}$ [K]	192	195	197	195
θ [K]	368	364 – 367	361 – 363	363 – 373
Alt (range) [km]	16	15.3 – 15.8	15.0 – 15.3	15 – 16.1
RHi [%]	130	86	n.a.	94
$D_{p_{max}}$	42	84	130	43
N [$\mathrm{cm^{-3}}$]	$(1.6 \pm 0.7) \times 10^{-3}$	$(8.2 \pm 2.2) \times 10^{-3}$	$(24 \pm 6) \times 10^{-3}$	$(7 \pm 2) \times 10^{-3}$
IWC [$\mathrm{g\,m^{-3}}$]	0.3×10^{-5}	13.2×10^{-5}	37.7×10^{-5}	1.7×10^{-5}
r_{eff} [μm]	2.3	21.3	19.4	5.8
ABC [$\mathrm{m^{-1}\,sr^{-1}}$]	6.4×10^{-8}	9.6×10^{-8}	1.7×10^{-7}	8.8×10^{-8}
ADR [%]	28	44	21*	47
CI	0.57	0.29	0.89	−0.07
τ		0.006	0.01	0.005

*ADR was affected by noise on this flight, thus, the volume depolarisation ratio (DR) is given here.

the lowest number concentration and lowest IWC. On the other end, *SVC3* exhibits the warmest case with $197\,\mathrm{K}$ and has the largest number concentration and IWC. Although the difference between these temperatures is not large, the corresponding saturation vapour pressures with respect to ice differ by a factor of 2.7 which influences the capability of the clouds for freeze-drying the air ascending through them. The size distributions compiled from the four SVC events are displayed in Figure 6.2. All size distributions peak at around $14\,\mu\mathrm{m}$. Ice particles larger than $100\,\mu\mathrm{m}$ were observed during two events (*SVC2* and *SVC3*). Possibly due to the contribution of those large particles, the corresponding IWCs are more than an order of magnitude larger than the IWCs of the events *SVC1* and *SVC4*. All events show relatively small number concentrations that are of comparable magnitude to the former SVC observations (c.f. Tables 6.1 and 6.2). An ice particle concentration frequency distribution is shown in Figure 6.3, including all measured data points of the four SVC events observed during SCOUT-AMMA. The concentrations range from $0.38 \times 10^{-3}\,\mathrm{cm^{-3}}$ to $49 \times 10^{-3}\,\mathrm{cm^{-3}}$ while the median concentration amounts to about $8 \times 10^{-3}\,\mathrm{cm^{-3}}$, indicated by the grey dashed line. Unfortunately, no lidar was installed on board the M-55 Geophysica during the SCOUT-AMMA campaign. Thus, neither estimates about SVC occurrence frequency nor precise statements about the extension of the SVCs can be given. However, the covered flight distance within each SVC can be considered as an estimate of the horizontal extent. This extent is given in Table 6.2 and ranges between $9.0\,\mathrm{km}$ and $23.2\,\mathrm{km}$. One can speculate that the real horizontal extension was much larger. Indications for this are contributed by the MAS backscatter measurements which, due to its remote sensing range near the aircraft, indicate the presence of cloud particles partly before and/or after the averaging time

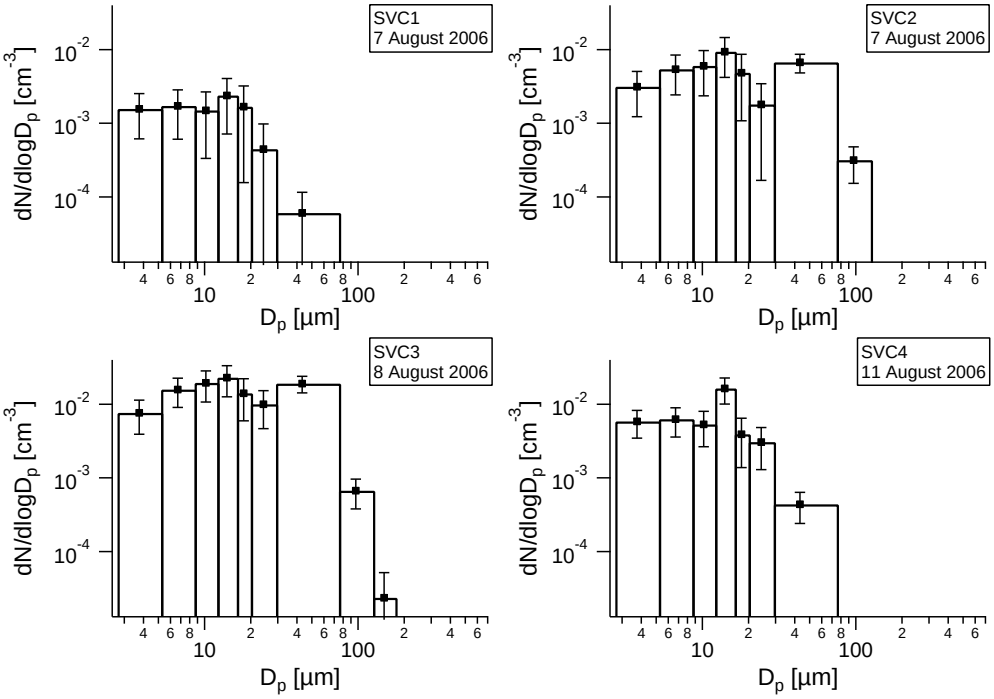

Figure 6.2: Combined FSSP-100 and CIP ice crystal size distributions of the SVC encounters on 7, 8, and 11 August 2006 with details summarised in Table 6.2. The local cold point tropopause height was located at about $16.3\,\mathrm{km}$ on 7 Aug and $16.5\,\mathrm{km}$ on the other days.

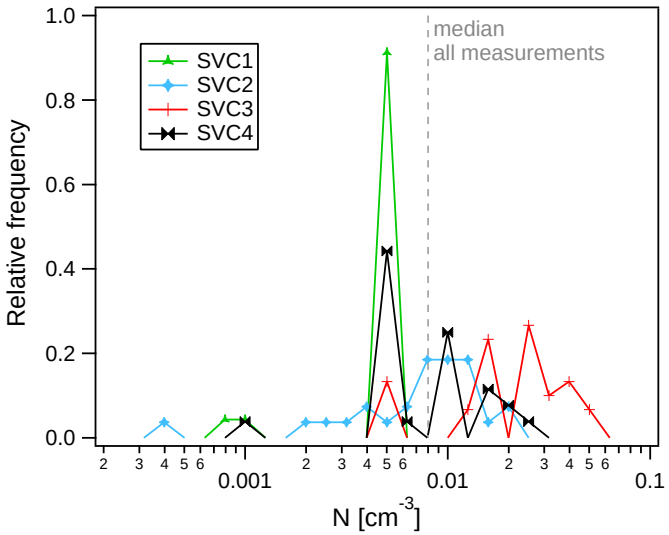

case	number of data points
SVC1	63
SVC2	32
SVC3	30
SVC4	71

Figure 6.3: Relative frequency of SVC ice particle number concentrations of the events measured during SCOUT-AMMA. The median number concentration of all events is indicated by the grey dashed line. The number of data points for each event is given at the right hand side.

period. In this regard it has to be noted that the SVC events occurred when the aircraft changed altitude or just after an altitude change in case of *SVC1*. Therefore, the SVC encounters might have stretched out further above or below the aircraft altitude. Additionally, few isolated cloud particles have been observed close to the SVC encounters. Taking into account the time periods that include the isolated cloud particles and MAS particle observations, a further estimate on the horizontal SVC extension is given, called extent+. The extent+ is found to range from $15.2\,\mathrm{km}$ to $33.7\,\mathrm{km}$. Still, the real horizontal extensions of the observed clouds are possibly much larger.
From the mean microphysical parameters and the vertical extent of the SVC cases *SVC2*, *SVC3*, and *SVC4* a rough estimate of τ can be obtained following Garrett et al. (2003)

$$\tau = \Delta z\, \beta_{ext} = \Delta z\, \frac{3\, CWC}{2\rho\, r_{eff}}, \tag{6.1}$$

with Δz the vertical cloud thickness, β_{ext} the extinction coefficient, CWC the condensed water content which is in the SVC cases equal to the IWC, and ρ the cloud particle density, here, the density of ice. Since *SVC1* has been probed on level flight, no estimate of the vertical cloud thickness can be made and thus no estimate about τ. For *SVC2*, *SVC3*, and *SVC4* τ results in 0.0061, 0.0095, and 0.0051, respectively. Furthermore, the satellite images of the respective flight sections show no presence of thick clouds.
Since the CIP images of the SVC particles contain only few shaded pixels due to the $25\,\mu\mathrm{m}$ resolution, it is not possible to identify specific ice particle shapes. The observed aerosol depolarisation ratios (ADR, see Table 6.2), however, range from $28\,\%$ to $47\,\%$, indicating that the particles contained depolarising structures and are thus not of spherical shape. The aerosol backscatter coefficient (ABC) varies according to the number concentrations, which indicates a good agreement between the cloud particle probes and the backscatter sonde (F. Cairo, personal communication, 2010). The increasing colour index (CI) reflects the increasing fraction of smallest particles.
Similar to Jensen et al. (2010) the measurements of the SCOUT-AMMA SVC events show broad size distributions which are indicative for heterogeneous ice nucleation. For illustration, Figure 6.4 shows the time series of the size distributions of the four SVC events. For every two-second time step on the x-axis, a size distribution is given with the particle diameter on the y-axis and the $dN/dlogD_p$ value in the colour code. Roughly $90\,\mathrm{cm}^3$ air is sampled by the FSSP-100 and around $1000\,\mathrm{cm}^3$ by the CIP (depending on particle size) during one second at the prevailing air speeds. Thus, about $2180\,\mathrm{cm}^3$ of air is sampled every time step by the probes. When assuming the median particle concentration of $8 \times 10^{-3}\,\mathrm{cm}^{-3}$ (the whole range of particle concentrations), the two probes would detect 17 (1 to 100) particles every time step distributed over the ten size bins in which particles have been observed in the SVC. This demonstration shows that it is not unlikely that a size bin remains empty and one needs a certain averaging time for achieving a reliable size distribution. Thus, these broad distributions are not an effect of averaging over the vertical and horizontal extents of the cloud.
Davis et al. (2010) comprised the average size distributions of the in situ measurements of SVCs from the literature in one figure (Davis et al., 2010, Figure 5). This figure is taken as basis for Figure 6.5 into which the individual SCOUT-AMMA measurements are inserted. In general, the African SVC events fit well into the previ-

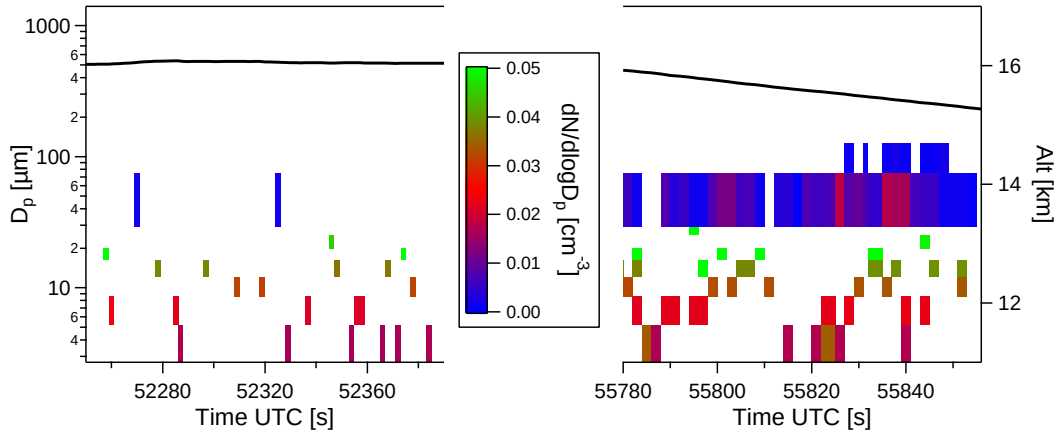

(a) *SVC1* (left) and *SVC2* (right)

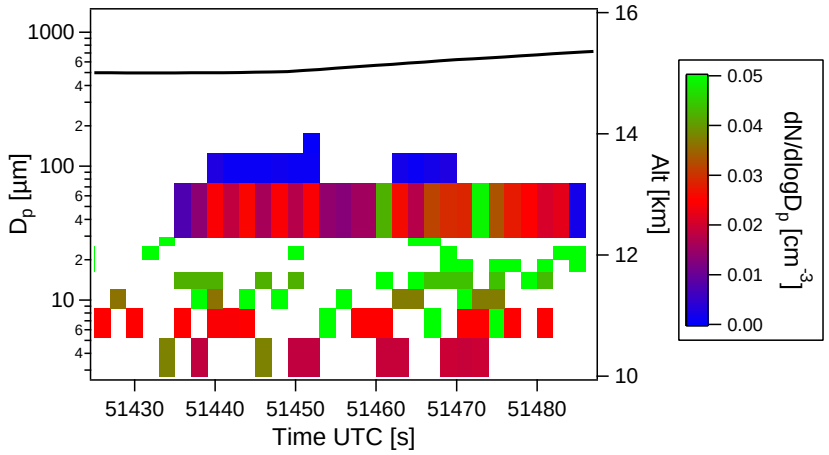

(b) *SVC3*

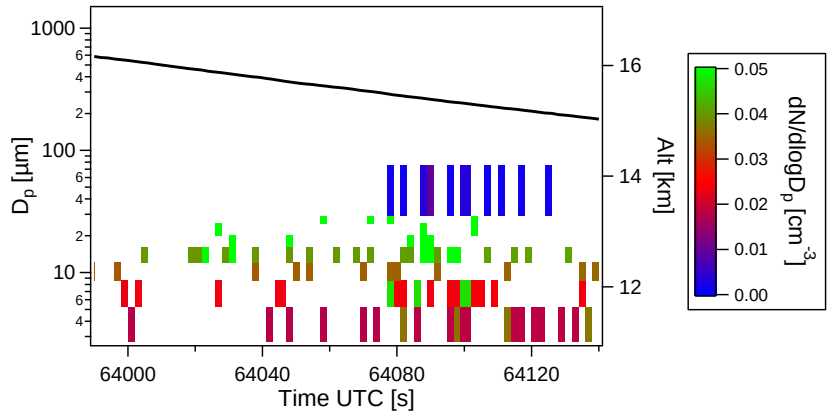

(c) *SVC4*

Figure 6.4: Time series of size distribution data of the SVC events. The colour coding indicates the $dN/dlogD_p$ value, the black line shows the aircraft altitude (for further explanation see text).

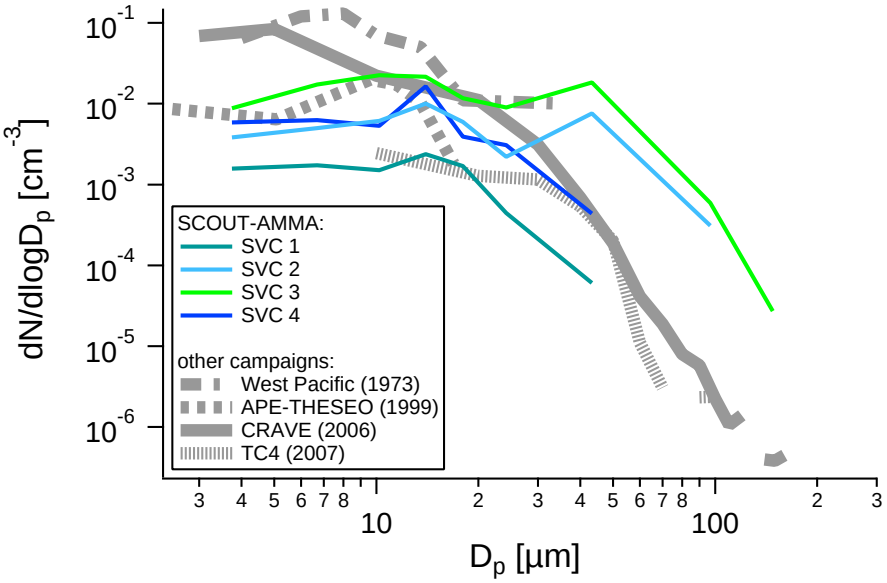

Figure 6.5: Summary of all previous in situ SVC size distribution measurements as shown in Davis et al. (2010) plus size distributions of the SVC events measured during SCOUT-AMMA. The particular measurements have been presented by Heymsfield (1986, tropical West Pacific), Thomas et al. (2002, APE-THESEO), Lawson et al. (2008, CRAVE), and Davis et al. (2010, TC4).

ous data, nevertheless, some differences are to be mentioned. So far the measurements show particles with sizes up to $165\,\mu\mathrm{m}$ (observed during CRAVE). However, the maximum measured size depends critically on the instruments used. During the APE-THESEO campaign and the measurements in 1973 the size ranges of the instruments had upper size limits of $25\,\mu\mathrm{m}$ and $50\,\mu\mathrm{m}$, respectively. Thus, there is no information about possibly present larger particles. It is noticeable that the concentrations in the size range of small particles (less than $30\,\mu\mathrm{m}$) differ by one order of magnitude or even more. The concentrations measured in 1973 constitute an upper and the TC4 observations together with *SVC1* a lower limit. Compared to the measurements obtained during CRAVE and over the West Pacific the current observations from SCOUT-AMMA show over an order of magnitude less particles with sizes below $10\,\mu\mathrm{m}$. The events *SVC2* and *SVC3* show much higher concentrations of particles larger than $50\,\mu\mathrm{m}$ compared to the measurements of CRAVE and TC4. These two events also have higher IWCs of $1.8 \times 10^{-4}\,\mathrm{g\,m^{-3}}$ and $4.2 \times 10^{-4}\,\mathrm{g\,m^{-3}}$ compared to $5.5 \times 10^{-5}\,\mathrm{g\,m^{-3}}$ (CRAVE) and $5.6 \times 10^{-6}\,\mathrm{g\,m^{-3}}$ (TC4). Particle number concentrations compare well with those reported in Table 6.1. Differences, however, might arise due to the different size ranges of the instruments used for the particular measurements. The lower size limit seems particularly important since more small than large particles are present.

6.2.1 Parameterisation of SVCs

In order to be able to calculate e.g. the radiative impact of the SVCs on a global scale (for example in climate models) a parameterisation for this cloud type is required. The representation of the clouds in models is the better the more accurate the parameterisation is. Therefore, fit functions are adjusted on the measurements on SVCs (as

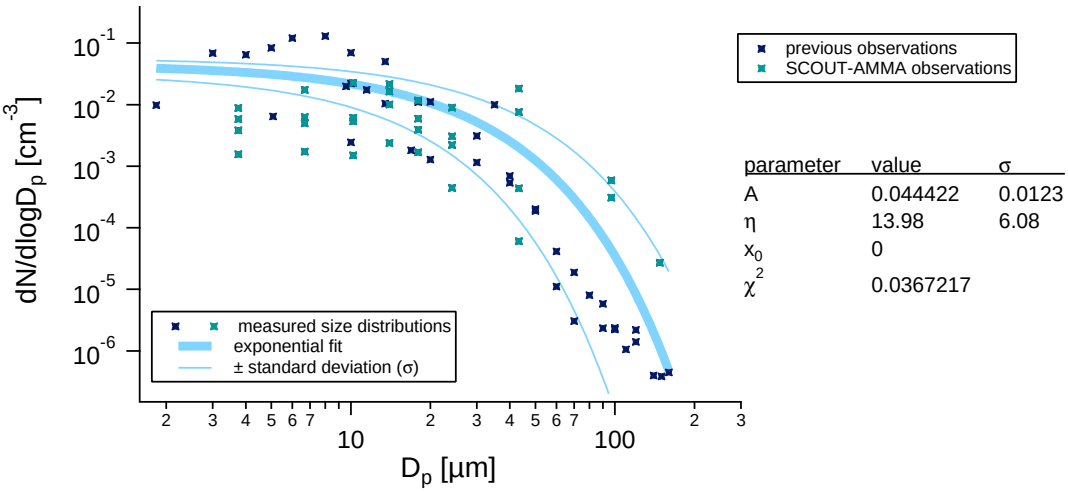

Figure 6.6: Exponential fit (thick blue line) following Eq. 6.2 on all so far reported in situ SVC measurements (blue markers) as shown in Figure 6.5. Thin lines show the standard deviation of the fitted function. The coefficients for the fit function are given in the table on the right hand side.

shown in Figure 6.5). Several fit functions have been tested (e.g. lognormal, exponential) and their representation of the measured size distributions is evaluated. A form of nonlinear, least-squares fitting, the Levenberg-Marquardt algorithm, is used to search for the coefficient values that minimise the chi-square, which is defined as:

$$\chi^2 = \sum_i (\frac{y - y_i}{\sigma_i})^2, \tag{6.2}$$

where y is a fitted value for a given point, y_i the measured data value for that point, and σ_i the standard deviation of y_i. The best fit was achieved using an exponential fit function:

$$f(x) = A \exp\left(-\frac{x - x_0}{\eta}\right), \tag{6.3}$$

with the constants A, x_0, and the decay constant η. This fit resulted in a χ^2 value of 0.0367 indicating a good quality of the fit. Since the significance test led to the unrealistically high confidence level of $100\,\%$ a linear regression on the $f(x)$ values is performed instead. This resulted in a Pearson correlation coefficient of $r = -0.89$ and the corresponding $r^2 = 0.79$. Both indicating a good correlation of the data points and validity of the exponential fit. Figure 6.6 shows the calculated exponential fit and its standard deviation on all the measured size distribution values that were shown in Figure 6.5. The values of the fit parameters and their standard deviations are given on the right hand side of the figure.

6.3 Discussion and summary

In the cloud diversity along the West African monsoon MCS tracks four events of subvisible cirrus have been observed close to the tropopause. The encounters occurred at altitudes between $15\,\mathrm{km}$ and $16.1\,\mathrm{km}$ which corresponds to a distance below the tropopause of $200\,\mathrm{m}$ to $1200\,\mathrm{m}$. Largest observed particles had sizes of up to $130\,\mu\mathrm{m}$.

The mean ice particle number concentration of the events was $10.3 \times 10^{-3}\,\mathrm{cm}^{-3}$, mean IWC $1.6 \times 10^{-4}\,\mathrm{g\,m}^{-3}$, and mean effective radius $12.4\,\mu\mathrm{m}$. Estimates of τ range from 0.005 to 0.01.

These measurements extend the sparse previous data set of SVCs in several aspects. They do not only contribute to the number of observations but are also the first reported measurements over West Africa and most notably, the first reported measurements above a continental area. The measured microphysical parameters and size distributions fit well into the picture drawn by former SVC measurements. Some differences can be seen but it is not clear whether these are statistically significant. The differences might arise due to different formation processes, locations (continental/maritime), meteorological conditions or altitude but also due to different instrumentation and the resulting different size ranges. However, the size distributions of SVC from the literature and the four events shown here are similar enough to establish a first mathematical description for this cloud type, which writes as:

$$\frac{dN}{d\log(D_p)} = 44.422 \times 10^{-3}\,cm^{-3} \exp\left(-\frac{D_p}{13.98\,\mu m}\right), \tag{6.4}$$

with the particle diameter D_p in $\mu\mathrm{m}$. This function is calculated based on observations performed in a temperature range of $188\,\mathrm{K}$ to $198\,\mathrm{K}$ and at relative humidities of $80\,\%$ to $160\,\%$ and is thus valid for these conditions. In order to define a parameterisation that is dependent on e.g. temperature or IWC, more measurements are needed to be able to give a statistically significant description. Moreover, the IWC calculated from the measurements here is particularly susceptible to uncertainty because of the missing shape information and low counting statistics. Therefore, it seems more reliable to use an absolute mathematical description rather than a varying parameterisation which is dependent on IWC.

The presence of relatively large particles ($> 100\,\mu\mathrm{m}$) shows that some explanations for the formation mechanisms of these clouds have to be revised (e.g. Jensen et al., 1996; Luo et al., 2003b) since such large particles would sediment out of the cloud. Thus, the SVCs could not be maintained. Considering the measured size distributions and number concentrations, one can conclude that the SVC measured over the West African continent have not been formed by homogeneous freezing since then they would have narrow size distributions and much larger particle concentrations, as shown by Jensen et al. (2010).

Wang et al. (1996) observed the zonal mean distributions of the occurrence frequency of SVC which reflect the characteristics of cloud activities with deep convection in the tropics, and general features consistent with the tropospheric mean circulation (Hadley and Ferrel cells) and corresponding seasonal variations. Since the West African Monsoon, during which the SVC events of the SCOUT-AMMA campaign have been observed, constitutes a highly convective environment, it appears plausible that also the SVC are originating from convective outflow. Therefore, the tracer measurements are analysed as in Section 4.2.2 in order to find convective signatures for the four SVC events. However, they do not show an indication for convective influence. Either the time past the originating convective event was long enough that after mixing with surrounding air tracer signatures had disappeared or the SVCs discussed here have formed in situ.

Furthermore, Wang et al. (1996) found evidence for the dehydrating effect of SVC

on the stratospheric water vapour. During SCOUT-AMMA and two other campaigns Schiller et al. (2009) found layers of enhanced water vapour in the lower stratosphere. These moist layers were a result of injection of moist tropospheric air by convective overshooting. However, the moistening over West Africa was only moderate. Thus, the dehydrating effect of the SCVs might have compensated the hydrating effect of the convective overshoots over West Africa (as described by Khaykin et al., 2009) to some extent and therefore the latter were found to be only moderate. However, in absence of a much more robust data basis such considerations remain speculative at this time.

Chapter 7

Comparison of general observations from West African and Australian tropical clouds

7.1 Background

In the foregoing chapters clouds of different types (MCS outflow clouds, clouds from convective overshoots, and SVCs) have been analysed and discussed. Those clouds have been observed at specific altitudes within the TTL. However, throughout the flights during SCOUT-O3 and SCOUT-AMMA clouds have been probed at lower altitudes as well. The entire data set includes measurements of clouds that have been observed during ascents, descents, and dives. With the help of these observations a complete picture of the vertical cloud structure in the UT/TTL can be drawn. This is one main aspect of this chapter. Furthermore, the cloud types will be compared and differences exposed.

7.1.1 Vertical cloud profiles

Several studies have shown that cloud microphysical parameters change with increasing altitude in the upper troposphere and correspondingly with increasing potential and decreasing ambient temperature (e.g. Griffith et al., 1980; Chen et al., 1997; Garrett et al., 2003; Schiller et al., 2008; Krämer et al., 2009; de Reus et al., 2009). For example, a decreasing effective radius has been explained by the preferential lifting of smaller ice crystals in the updraughts of large convective cells (de Reus et al., 2009). Garrett et al. (2003) suggest that at colder temperatures homogeneous ice nucleation favours the formation of smaller ice crystals due to the exponential dependence of saturation vapour pressure over ice on the ambient temperature (Kärcher and Lohmann, 2002). The nucleation prevails the effect of ageing of the clouds or gravitational settling of the ice crystals. Not only measurements but also model calculations of tropical cirrus clouds showed a decreasing effective radius with altitude (Chen et al., 1997). Krämer et al. (2009) report on frequencies of occurrence of ice particle mean radius and number concentrations which they derived from a combination of measurements performed in the Arctic, midlatitudes, and tropics. They found a decrease in radius with decreasing temperature as well as a decrease in number

concentration. In addition, several studies (e.g. McFarquhar and Heymsfield, 1997; Schiller et al., 2008) indicate a decreasing IWC with increasing altitude. Since smaller and fewer particles contribute less mass to the IWC, a decrease in IWC seems to be a consequence of a decrease in number concentrations and particle size. Schiller et al. (2008) provide a climatology of IWC derived from measurements in the Arctic, midlatitudinal, and tropical regions, over a temperature range of $183\,\mathrm{K}$ to $250\,\mathrm{K}$. They found a decrease of IWC with decreasing temperature over the whole temperature range. Outliers with enhanced IWC, which are related to recent impact of convection, were only found in the tropics.
The effect of decreasing ice particle size, IWC, and number concentration with increasing altitude is also evident in the size distributions. For example McFarquhar and Heymsfield (1996) showed the altitude dependence of size distributions measured in cirrus resulting from outflows of deep convection over the Fiji region during CEPEX. They observed increasingly more larger ice particles in the lower altitudes while the numbers of small particles did not vary appreciably. However, when performing measurements closer to the convective core they found higher number concentrations for all particle sizes than at comparable altitude further away from the convective core. Based on these measurements McFarquhar and Heymsfield (1997) established a parameterisation for size distributions. These are explicitly calculated as bimodal, with the smaller mode for particles smaller than $100\,\mu\mathrm{m}$ determined by a Gamma function, the larger mode by a lognormal function. Since the observations were obtained at ambient temperatures between $253\,\mathrm{K}$ and $203\,\mathrm{K}$ and IWCs ranging from $10^{-4}\,\mathrm{g\,m^{-3}}$ to $1\,\mathrm{g\,m^{-3}}$ have been measured, the parameterisation is valid for such conditions. Observations of size distributions obtained in tropical anvil clouds were also reported by de Reus et al. (2009). They, as well, observed a decrease in the number of larger particles when ascending to the tropopause. The size distributions which were observed in the stratosphere, however, exhibit larger particles comparable to those in the upper troposphere. For a better description of the size distributions they adjusted bi- or trimodal lognormal fits onto the size distributions in different altitude ranges. Based on observations by the Atmospheric Chemistry Experiment (ACE) Fouriertransform infrared (FTIR) instrument aboard the Canadian SciSat-1 satellite Eremenko et al. (2005) retrieved size distributions in cirrus clouds associated with a tropical convective system, shown in Figure 7.1. For altitudes above $15\,\mathrm{km}$ they found bimodal size distributions with mean mode diameters of about $6\,\mu\mathrm{m}$ for the smaller mode and between $20\,\mu\mathrm{m}$ to $40\,\mu\mathrm{m}$ for the larger mode. The distributions showed a decrease of the mean mode diameter to smaller sizes with increasing altitude. However, only particles with diameters $<60\,\mu\mathrm{m}$ could be retrieved and thus, a possible third mode could not be confirmed. Trimodal size distributions were shown by Chen et al. (1997) who modelled a precipitating anvil cloud. The three modes were found to peak at $10\,\mu\mathrm{m}$, $100\,\mu\mathrm{m}$, and $1\,\mathrm{mm}$. They state that these particles originated mainly from frozen interstitial haze drops (smallest mode), frozen cloud drops (medium mode), and from crystal aggregates and rimed ice (large mode). The particle size spectra which they found were typically broader and bimodal or unimodal in the lower part of the precipitating anvil. There, also significantly more large particles existed.

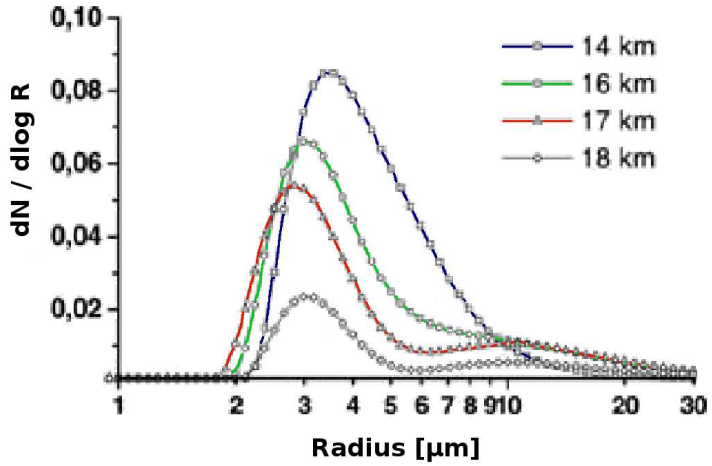

Figure 7.1: Number size distributions retrieved from satellite measurements at different altitudes in the UTLS at $17°$N/$162°$E made in February 2004. The observed cirrus cloud is associated with a tropical convection system. Adapted from Eremenko et al. (2005).

7.2 Observations of the vertical cloud structure

In the following the data of nine flights are examined (five flights from SCOUT-O3 and four from SCOUT-AMMA, cf. Table B.2 and B.3 in Appendix B). The cloud observations in the UTLS are analysed according to the different aspects mentioned above.

7.2.1 Microphysical parameters

In order to gain an overview about the vertical, microphysical structure of the tropical clouds, the effective radius, IWC, and number concentration obtained during the measurements are displayed as function of potential temperature as altitude equivalent in Figure 7.2. Figure 7.2(a) shows all particular measured data points (with two seconds accumulation time) while, for better comparison and overview, Figure 7.2(b) displays the medians for the microphysical parameters for each flight and supplementary a median for each campaign in the broad pale lines. First of all it can be seen that the clouds observed during the SCOUT-O3 campaign, indicated by the reddish colours, were observed at much higher altitudes as the clouds observed during SCOUT-AMMA, indicated by the bluish colours. Nevertheless, a decrease in the values of all cloud microphysical parameters in the upper troposphere (roughly between $345\,\mathrm{K}$ and $365\,\mathrm{K}$) is obvious. In the tropopause region (roughly between $365\,\mathrm{K}$ and $380\,\mathrm{K}$) the decrease flattens or the values of the microphysical parameters stay fairly constant. However, there is partly a broad variability of the values, particularly in the SCOUT-O3 measurements. Especially the medians of the IWC and effective radius measured during SCOUT-O3 and of the number concentrations measured during SCOUT-AMMA show a rather constant behaviour. No further decrease can be observed in the stratosphere but in contrast an increase of IWC, number concentration and effective radius. These stratospheric data comprise the observations of convective overshoots which are discussed in Chapter 5. Usually, no ice clouds would be expected at such altitudes. These cloud events have been identified as

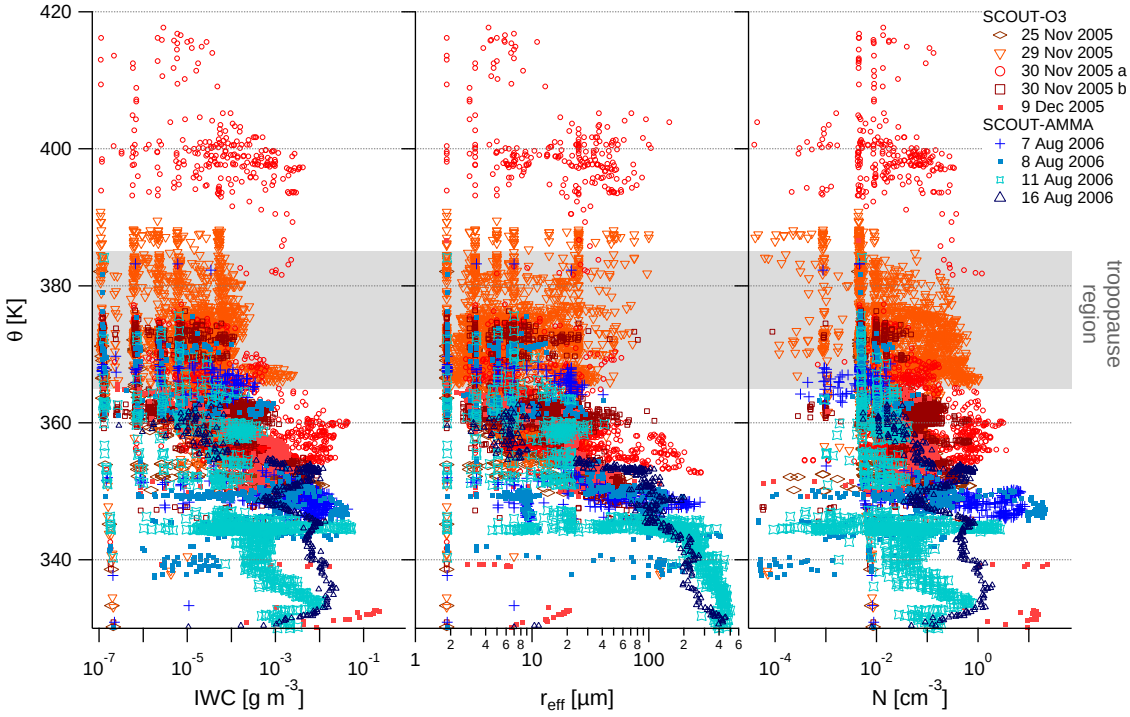

(a) All data points (two seconds accumulation time) of cloud measurements.

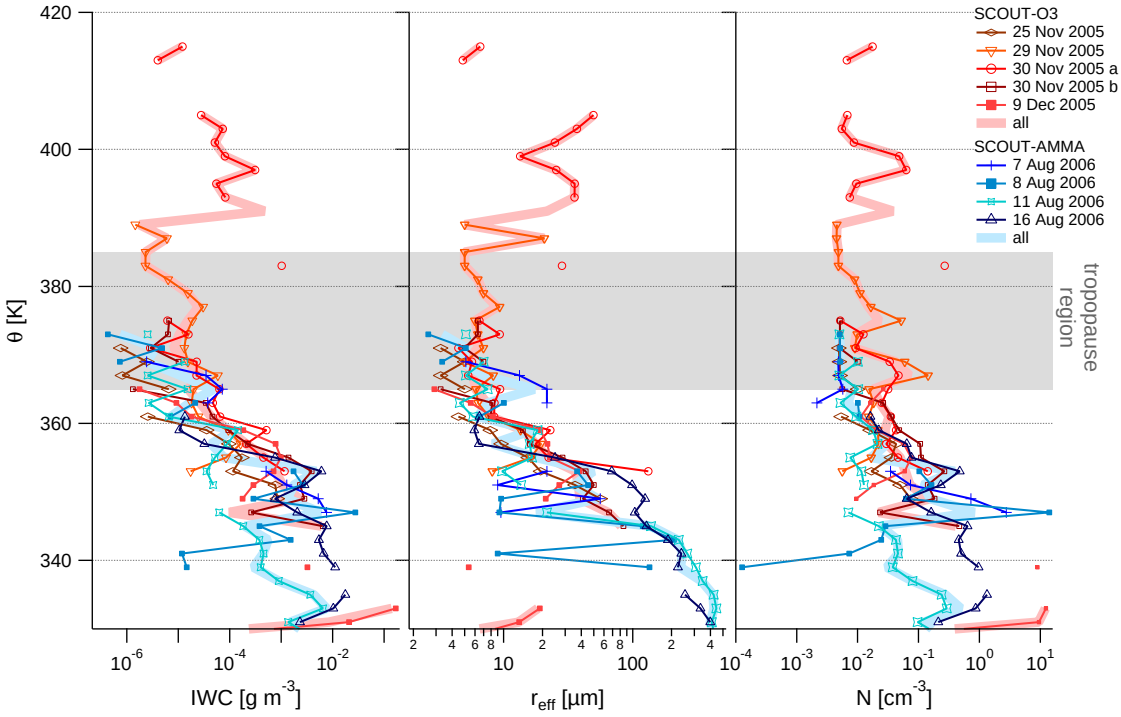

(b) Medians in $2\,\mathrm{K}$ θ-bins for each particular flight (thin lines with markers) and each campaign (broad pale lines).

Figure 7.2: Potential temperature profiles of IWC (left panel), effective radius (middle panel), and ice particle number concentration (right panel). Measurements obtained during SCOUT-O3 are indicated in reddish colours and SCOUT-AMMA in bluish colours.

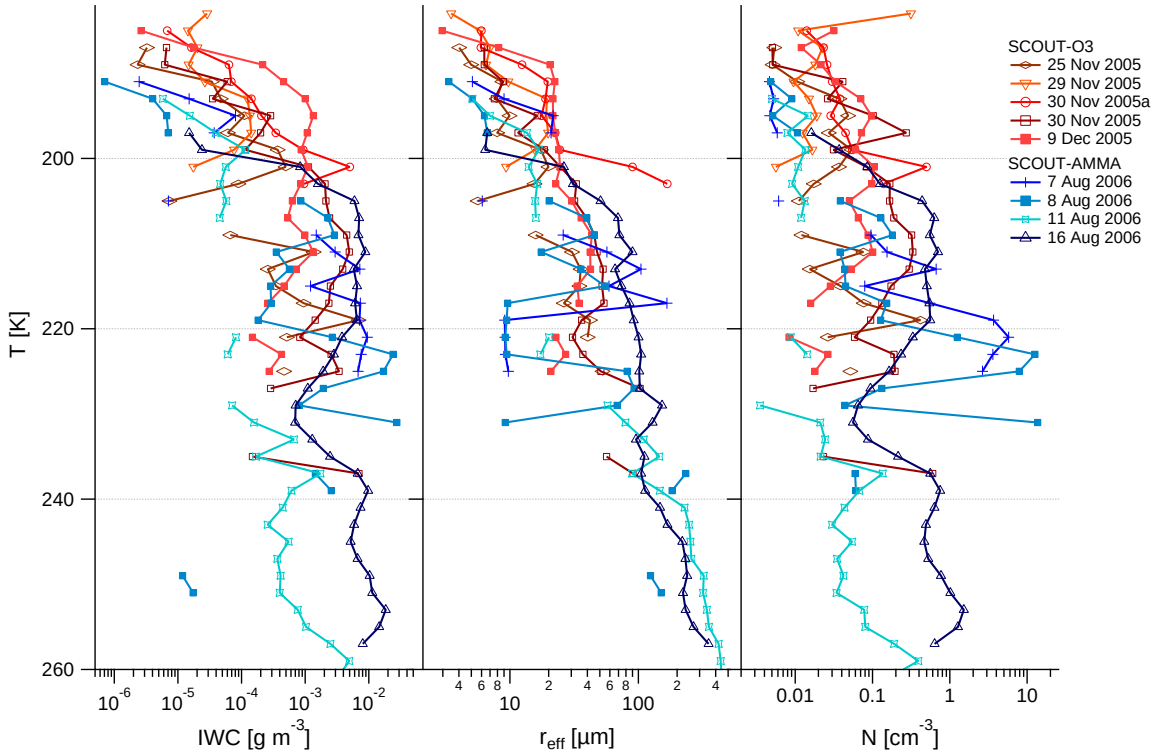

Figure 7.3: As Figure 7.2(b) but with ambient temperature as vertical coordinate. The medians are calculated in $2\,\mathrm{K}$ bins.

ice clouds in Section 5.2.3. The increase of the microphysical parameters can be seen as an effect of increasing temperature in the stratosphere. When looking at the ambient temperature profile instead of the potential temperature profile a continuous decrease in the values of the microphysical parameters with decreasing temperature can be found (see Figure 7.3). In this figure the stratospheric data points merge well with those from the troposphere at the respective temperatures.

7.2.2 Profiles of the radiative properties

Since the effective radius, which is a measure of the radiative property, changes with altitude it seems perspicuous that also the backscatter properties of the clouds change with altitude. In addition, the MAS data can give information about the ice particle morphology. Therefore, MAS data of aerosol depolarisation ratio (ADR), aerosol backscatter coefficient (ABC), and colour index (CI) are plotted versus potential temperature in Figure 7.4. The panels to the left show the observations and the medians of the respective parameters from SCOUT-AMMA campaign, the panels to the right those from SCOUT-O3 campaign, respectively. The bars denote the 33 and 67 percentiles. The West African measurements clearly show a decrease of ABC while ADR decreases slightly with altitude. Contrary, the CI increases in general. These observations indicate that the fraction of smallest ice particles increases when the aircraft is ascending which is in agreement with the cloud particle probes observations. The colour index increases with altitude in the SCOUT-O3 observations as well. Note, that for SCOUT-O3 the CI is given in arbitrary units due to problems with the absolute

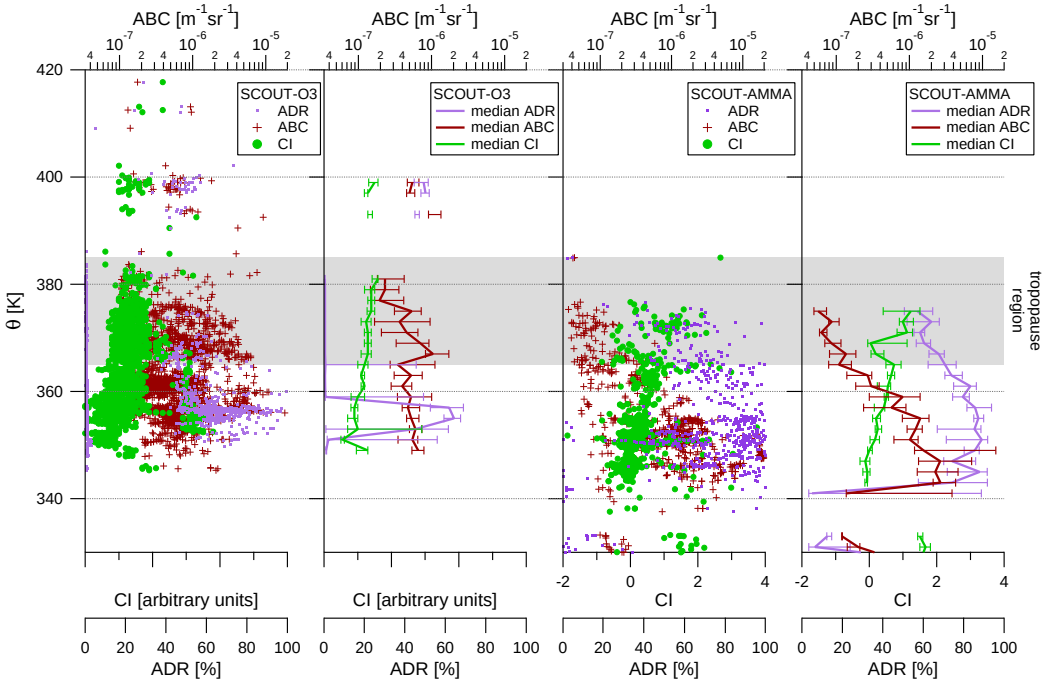

Figure 7.4: Vertical profiles of the MAS backscatter sonde data as observed during the flights of SCOUT-AMMA (left panel) and SCOUT-O3 (middle panel). The right panel displays the medians with the 33 and 67 percentiles in the error bars.

calibration. The behaviour of the CI (i.e. increase or decrease), however, is still dependable and significant. The ABC decreases slightly in the upper troposphere but shows higher values in the tropopause region. The ADR is rather variable and shows no clear trend. Similar values of all three backscatter parameters have been observed in the stratosphere compared to the values in the tropopause region. This is a further indication that these particles are of similar morphology in the tropopause region and in the stratosphere. Thus, due to the strong convective events during SCOUT-O3 the cloud particles were possibly transported upwards from lower altitudes. The ADR of the MCS outflow clouds and SVCs differ significantly with values around $90\,\%$ in the former and roughly $40\,\%$ in the latter cases. This variation indicates a change in the shape of the average scatterer, i.e. a change in the predominant particle shape.

7.2.3 Size distribution profiles

The vertical profile of size distributions obtained during the SCOUT-O3 campaign has been analysed and discussed by de Reus et al. (2009), showing a total of 90 size distributions. The same procedure has been applied to the SCOUT-AMMA cloud data as shown in the following. This resulted in a total of 117 size distributions. In the majority of the cases the size distributions have been compiled with an averaging time of $10\,\mathrm{s}$ to $20\,\mathrm{s}$. Some cases, however, for example the encounters of SVC (see Section 6), involved low number concentrations and therefore the averaging times have been adapted individually and ranged up to $200\,\mathrm{s}$. The specific treatment of size distributions is explained in the Appendix Sections A.3 and A.4.4. The size distributions are classified in $5\,\mathrm{K}$ to $10\,\mathrm{K}$ bins of potential temperature (similarly to Figure 2 in

de Reus et al., 2009, who applied $10\,\mathrm{K}$ to $20\,\mathrm{K}$ bins), normalised to a total $dN/d\log D_p$ value of 1, and are displayed in Figure 7.5. The thin black lines represent the single measurements while the blue lines display the median size distributions of each potential temperature bin for the SCOUT-AMMA data. It can be seen that the maximum particle sizes are decreasing when the aircraft is ascending to the tropopause region ($365\,\mathrm{K} < \theta < 385\,\mathrm{K}$). This agrees with the measurements obtained during the SCOUT-O3 campaign. The medians of these measurements are displayed in red. For completeness the size distributions of the stratospheric clouds ($\theta > 385\,\mathrm{K}$), measured during SCOUT-O3, are presented with the thin red lines in the uppermost panel. These clouds were a result of convective overshooting (c.f. Chapter 5, Figure 5.7).
Following the cirrus parameterisation deduced by McFarquhar and Heymsfield (1997) normalised ice crystal size distributions have been calculated. The average IWC and ambient temperature as observed within the potential temperature bins have been taken as input for the calculations. It has to be noted that the temperatures during the SCOUT-AMMA observations were lower, ranging from $195\,\mathrm{K}$ to $210\,\mathrm{K}$, compared to temperatures observed during CEPEX. The same is true for the SCOUT-O3 observations during which ambient temperatures reached down to $187\,\mathrm{K}$. The results of the calculations are shown in the broad pale blue lines for the SCOUT-AMMA observations and in the broad pale red lines for SCOUT-O3 observations. The size distributions resulting from the parameterisations show a similar decrease in maximum particle size with increasing potential temperature in the troposphere. However, they show a more pronounced mode at diameters of $100\,\mu\mathrm{m}$ to $300\,\mu\mathrm{m}$, which was not observed during either SCOUT campaign. The comparison of the calculated parameterisation size distributions with those measured during SCOUT-AMMA yields some clear differences: Especially in the two lowest potential temperature bins smaller particles and a smaller fraction of large particles have been observed during CEPEX. Measurements are fewer in the $355\,\mathrm{K}$ to $365\,\mathrm{K}$ bins but still particle sizes are larger than those calculated from the parameterisation. Particularly in the CIP size range, the shape of the size distributions indicates a higher fraction of large particles than observed during CEPEX. In the tropopause region the measurements and the parameterisation show a better agreement. Compared to the SCOUT-O3 observations the CEPEX measurements show clearly less large particles in the $345\,\mathrm{K}$ to $355\,\mathrm{K}$ bin and in the stratospheric θ-bin ($>385\,\mathrm{K}$).
A criticism of the CEPEX parameterisation is that it is sensitively dependent on the IWC, the derivation of which in turn is highly uncertain for complex ice particle shapes. Although the IWC comparison of the observations by CIP and FSSP-100 versus the hygrometer derived IWC during SCOUT-O3 (see Figure 4 of de Reus et al., 2009) yields a good agreement between these two very different measurement techniques, a representation independent of IWC is chosen here. In order to describe the size distributions, two to four modal lognormal size distributions were fitted to the median size distribution in each size bin. Each mode is calculated following

$$\left[\frac{dN}{d\log(D_p)}\right]_i = \frac{N_i}{\sqrt{2\pi}\log\sigma_g}\exp\left[-\frac{(\log\frac{D_p}{D_0}-\log\frac{\overline{D_{p_i}}}{D_0})^2}{2(\log\sigma_g)^2}\right], \tag{7.1}$$

with i the being the mode number, N number concentration in cm^{-3}, mean mode diameter $\overline{D_p}$ in $\mu\mathrm{m}$, and geometric standard deviation σ_g which is dimensionless (Hinds,

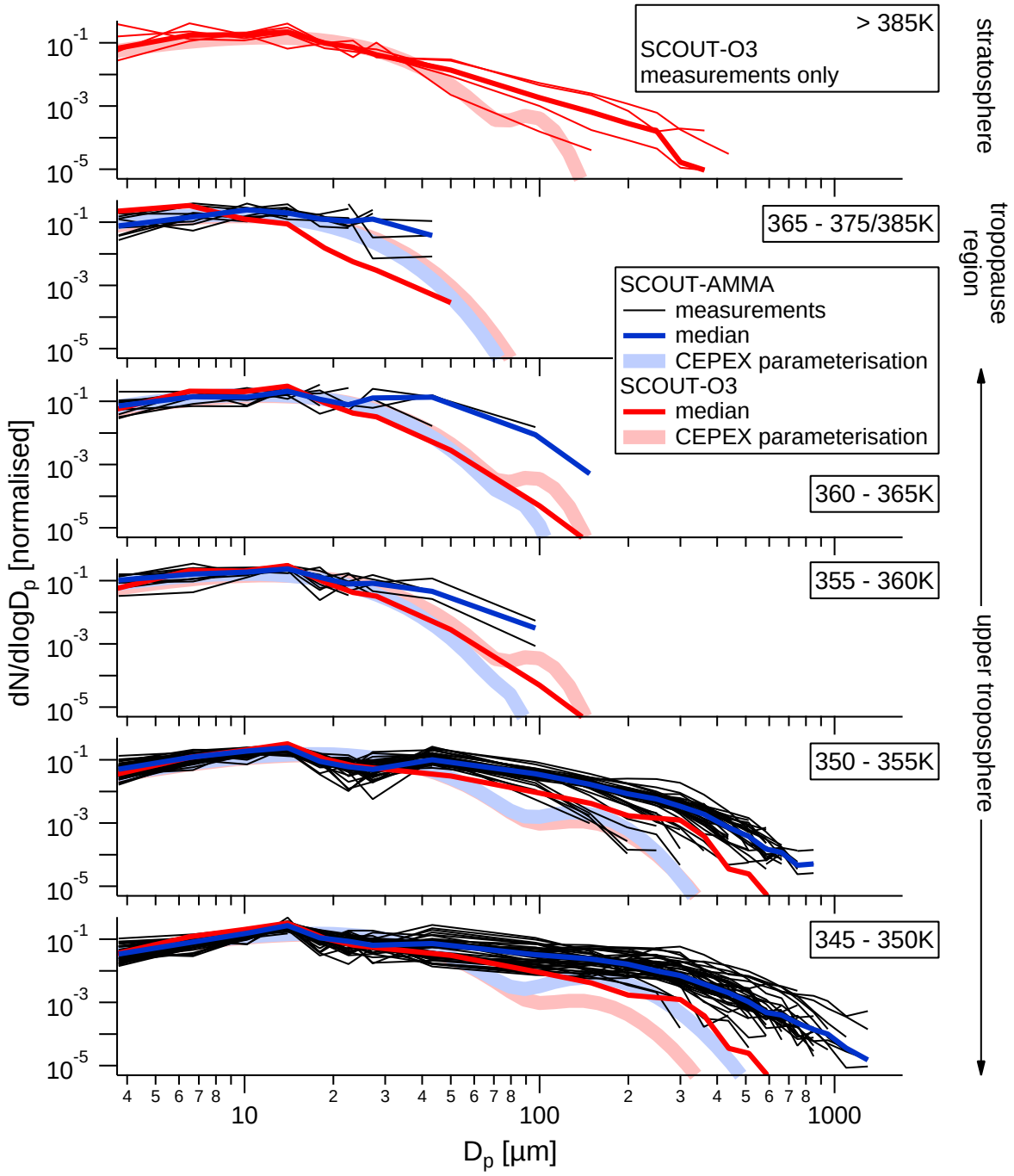

Figure 7.5: Normalised ice crystal size distributions of the cloud encounters during SCOUT-AMMA (black lines), divided into potential temperature bins. The median for each bin is displayed in bright blue. The broad pale blue curves show the size distribution as calculated following the CEPEX parameterisation. For comparison the measurements obtained during SCOUT-O3 campaign are displayed, medians in the bright red, CEPEX parameterisation in the broad pale red curves. Note: All SCOUT-AMMA measurements in the tropopause region θ-bin were observed below $375\,\mathrm{K}$.

Table 7.1: Parameters as defined in Eq. 7.1 for the two to four modal lognormal size distributions fitted to the median size distributions displayed in Figure 7.5. Furthermore, the fit parameters for the comparable fits obtained for the SCOUT-O3 campaign are presented (taken from de Reus et al., 2009).

	SCOUT-AMMA				SCOUT-O3		
θ [K]	N [cm^{-3}]	$\overline{D_p}$ [μm]	σ	θ [K]	N [cm^{-3}]	$\overline{D_p}$ [μm]	σ
				> 385	0.044	9	1.55
					0.008	25	1.55
					0.0004	65	1.75
365–375	0.0036	6.6	1.5	365–385	0.074	6	1.55
	0.0017	15.3	1.23		0.0009	18	1.55
360–365	0.012	9.5	1.7				
	0.0045	38	1.5	355–365	0.034	9	1.55
355–360	0.021	9.5	1.7		0.0009	25	1.55
	0.0025	40	1.4				
350–355	0.15	9.5	1.6				
	0.08	49	1.55				
	0.007	180	1.55	345–355	0.167	10	1.55
345–350	0.13	10	1.55		0.026	35	1.55
	0.025	40	1.55		0.004	90	1.75
	0.018	160	1.6				
	0.000 15	900	1.2				

1999). $D_0 = 1\mu m$ is needed to eliminate the unit. Thus, the total size distribution is the sum of the single modes:

$$\frac{dN}{d\log(D_p)} = \sum_i \left[\frac{dN}{d\log(D_p)}\right]_i . \tag{7.2}$$

The parameters of the fitted functions are given in Table 7.1. In general, the mean mode diameter and the number concentration decrease with increasing altitude. Similar calculations have been performed for the median size distribution obtained during the SCOUT-O3 experiment (as presented by de Reus et al., 2009). The resulting fit parameters are included in Table 7.1, as well. In the same manner they show a decrease in the mean mode diameter in the troposphere when ascending to the tropopause. Furthermore, three modes have been found for the size distribution in the $345\,\mathrm{K}$ to $355\,\mathrm{K}$ potential temperature bin, whereas the size distributions above (except the size distributions of the stratospheric clouds) show two modes as do the SCOUT-AMMA size distributions in the same altitudes. The size distribution fits are displayed in Figure 7.6 together with the CEPEX parameterisation. The decrease in mean mode diameters can clearly be seen. For size distributions that contain large particles the underestimation of particle size by the CEPEX parameterisation is evident. During SCOUT-AMMA fewer smaller sized particles have been observed compared to SCOUT-O3 and CEPEX but also more larger particles in the upper troposphere.

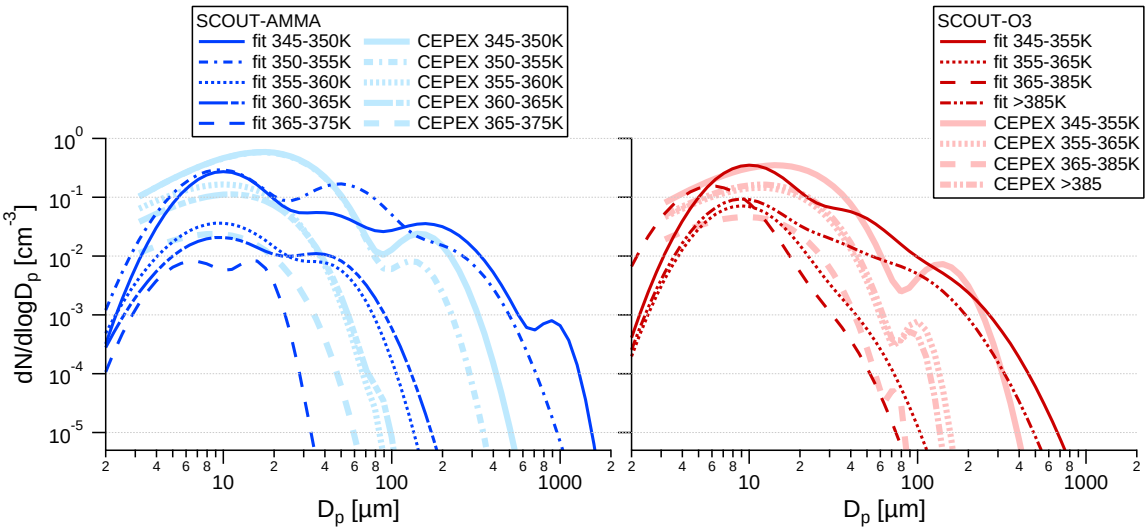

Figure 7.6: Lognormal fits of the size distributions and CEPEX parameterisations for SCOUT-AMMA (left panel) and SCOUT-O3 (right panel).

7.3 Activation of aerosol to cloud ice particles

If not frozen homogeneously any ice crystal requires an IN in order to freeze at typical atmospheric conditions. Since not all aerosol particles end up as cloud particle (some are more, some are less effective IN) an activation ratio can be determined, which is the ratio of activated aerosol particles that form a cloud particle (residual aerosol particles) to the interstitial aerosol particles. Several ground or mountain based studies have investigated the activation ratio (e.g. Verheggen et al., 2007; Drewnick et al., 2007; Kamphus et al., 2010). Due to the different size ranges of the instrumentation that was used to measure the interstitial and residual aerosol particles it is difficult to compare observed numbers. Nevertheless, a temperature dependence was found for ambient temperatures between $-27\,^{\circ}\mathrm{C}$ to $-5\,^{\circ}\mathrm{C}$ on the Jungfraujoch mountain station (Verheggen et al., 2007). The fraction of activated aerosol showed a decrease with decreasing temperature, and furthermore with increasing ice mass fraction (in mixed-phase clouds). Seifert et al. (2004) observed different correlations between interstitial and residual aerosol particles in cirrus clouds which were linked to the different stages of the cirrus life cycle during the two INCA[19] campaigns. The number concentrations of interstitial aerosol and ice crystal residuals were positively correlated during cloud formation, whereas the correlations were smaller or even negative in dissolving clouds. Measurements of cirrus over Southern Germany showed that small aerosol particles ($<0.5\,\mu\mathrm{m}$) play an important role in the nucleation of cirrus ice crystals at low temperatures ($-35\,^{\circ}\mathrm{C}$ to $-60\,^{\circ}\mathrm{C}$; Ström et al., 1997). The number concentration of ice crystal residues was found to be dominated by aerosol particles smaller than $0.3\,\mu\mathrm{m}$ in diameter.

[19] INterhemispheric differences in Cirrus properties from Anthropogenic emissions, Punta Arenas, Chile and Prestwick, Scotland, both in local autumn 2000

7.3.1 Concurrent observations of aerosol and cloud particles

During both, the SCOUT-O3 and SCOUT-AMMA campaign, concurrent cloud particle and aerosol measurements with the COPAS instrument have been performed. In order to give an estimate for the activation ratio of aerosol to cloud particles the number concentrations of aerosols larger than $15\,\mathrm{nm}$[20] and the number concentrations of cloud particles as measured by the FSSP-100 and CIP are compared. In this regard the aerosol number concentrations are considered as interstitial and the cloud particle number concentrations as residual number concentrations. It is important to note that this is just an estimate of the activation ratio. Many factors could affect this ratio, for example ice particles could have formed by homogeneous freezing (thus containing no IN) or by ice multiplication processes (which potentially happen in the thicker MCS clouds that contain high ice particle number concentrations). Both effects would lead to an overestimation of the residual particle number concentration. Interstitial aerosol particles could be removed by washout or coagulation, or their concentrations could be distorted due to mixing with entrained air which might carry a different aerosol load. Furthermore, some small ice particles might have entered the COPAS inlet system (upper size limit about $1\,\mu\mathrm{m}$) and thus, might have been counted as interstitial aerosol. Since the number of cloud particles is much smaller than the submicron aerosol number densities, the contribution of the cloud particles to the COPAS measurements can be considered as small or negligible. Despite the considerations above, the terms activation ratio and activation are used in the following even though the measured ratio of cloud to aerosol particle number concentrations may just roughly estimate the actual activation ratio.

For the SCOUT-O3 campaign it has been shown by de Reus et al. (2009) that the observed ratios of cloud to aerosol number densities ranged between $1/\,300$ and $1\,/30\,000$. A similar range has been found for the SCOUT-AMMA campaign. Furthermore, a decrease in aerosol and cloud particle number concentrations with decreasing ambient temperature was shown. On the basis of figure 10 by de Reus et al. (2009) Figure 7.7 displays the number concentrations of cloud particles versus aerosol particles. The original figure is extended with data points measured in the SVC and MCS outflow clouds during SCOUT-AMMA. The measurements of the Hector events during SCOUT-O3 are displayed in green squares, the overshooting convection events are highlighted in blue. The MCS outflow events of the SCOUT-AMMA campaign are depicted with blue triangles. For both deep convective cases (overshooting and outflow) tracer data (NO, NO_y, and CO_2) have been used to identify the convective events. Furthermore, the red triangles depict the data points of the SVC that were discussed in Chapter 6. The colouration exhibits two distinct features. The ratio of ice to aerosol particles of the deep convective events, after all in-cloud processes proceeded, are among the highest. About one aerosol particle out of 300 becomes activated, with a decrease in activation ratio for low concentrations (below $0.1\,\mathrm{cm}^{-3}$). The SVC on the other hand show the lowest activation ratios, just about one out of $30\,000$ aerosol particles becomes activated. These very low activation ratios indicate that deposition freezing might have formed the SVCs, whereas other processes (e.g., immersion freezing and homogeneous droplet freezing) may have

[20] In case that measurements of the COPAS $15\,\mathrm{nm}$ channel were not available, measurements of the $10\,\mathrm{nm}$ channel were taken instead.

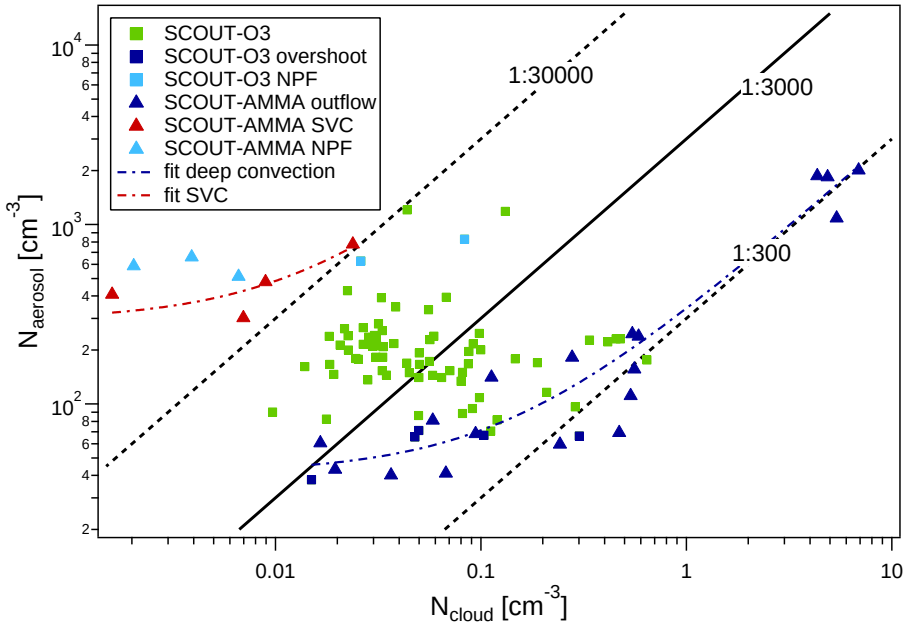

Figure 7.7: Interstitial aerosol (larger $15\,\mathrm{nm}$, or larger $10\,\mathrm{nm}$ in a few cases) versus cloud particle number concentration are displayed in order to give an estimate of the activation ratio of aerosols to cloud particles. Squares indicate data points measured during SCOUT-O3 while the other points are measured during SCOUT-AMMA. Dark blue colour signs deep convective events like convective overshooting tops (SCOUT-O3) or MCS outflow (SCOUT-AMMA). The red triangles indicate the measurements of the subvisible cirrus at the tropopause. Light blue coloured data points indicate in-cloud new particle formation (NPF) events.

Table 7.2: Fit function and parameters for the activation ratio of SVC and deep convective clouds, as in Figure 7.7.

fit equation	$N_{aerosol} = a + b \cdot N_{cloud}$	
	a	b
SVC	291.97	19 284
convective	41.33	300.41

been involved at varying intensities during the cloud lifetime in the formation of the deep convective clouds.
Additional to the SVC and deep convective activation ratios, some encounters of in-cloud new particle formation (NPF) events, i.e. nucleation events of aerosol particles, which are identified by high number concentrations of aerosol particles with sizes between $6\,\mathrm{nm}$ and $15\,\mathrm{nm}$, are included into Figure 7.7. These data points are coloured in light blue and show almost no trend with increasing ice particle number concentrations. Based on these few measured data points it can be speculated that NPF events preferably occur under circumstances where only a few cloud ice particles are present. When adjusting linear fits on the deep convective clouds and SVCs, respectively, fit values as given in Table 7.2 are found. These fits are also presented in Figure 7.7 as dash-dotted lines. Even though the activation ratios given here constitute just a rough estimate on the actual activation ratios, the linear fits provide data as boundaries for modelling purposes which may help to estimate the contributions of the different microphysical processes.

7.4 Discussion and summary

The data set of tropical clouds presented in this work comprises measurements of five flights during SCOUT-O3 and four flights during SCOUT-AMMA. From these data vertical profiles of the cloud microphysical parameters were presented. In the upper troposphere decreasing IWC, effective radius, and number concentration with increasing altitude have been observed during both tropical campaigns. These measurements are in agreement with former observations and modelling studies (e.g. Chen et al., 1997; Schiller et al., 2008; Krämer et al., 2009). In the tropopause region the decrease declined or even fairly constant values for the microphysical parameters have been found. Measurements of ice particles in the stratosphere showed increasing IWC, effective radius, and number concentration. Since those parameters decrease with decreasing ambient temperature, it is plausible that they increase with the increasing stratospheric temperatures. The variability of the microphysical parameters might be explained by the unequal distances of the observations to the convective core. As Schiller et al. (2008) and McFarquhar and Heymsfield (1996) state, enhanced IWC, particle size and numbers occur when measurements were obtained closer to convective cells.
Size distributions for these data were compiled, resulting in a total of 90 and 117 distributions for SCOUT-O3 and SCOUT-AMMA, respectively. The size distributions were binned with respect to potential temperature. The profiles of size distributions show that the ice particle numbers and sizes decrease when ascending to the tropopause. The size distributions in the tropopause region which were derived from SCOUT-O3 measurements, however, depict an increase of the numbers in small particle sizes (smaller than $11\,\mu\mathrm{m}$) but still a decrease in maximum particle size. The size distributions of the stratospheric clouds show an increase in particle size and, in turn, in the number concentrations of large particles.
For further comparison, size distributions according to the CEPEX parameterisation have been calculated for each potential temperature bin and campaign. While the calculated size distributions still show a decrease in particle sizes and the amount of the respective large particles, they clearly exhibit smaller sizes and a smaller large particle fraction when compared to the SCOUT-AMMA observations in the upper troposphere. This is also true for the lowest θ-bin and the stratospheric θ-bin of the SCOUT-O3 measurements. One reason for the disagreement could be caused by the ambient conditions. The CEPEX parameterisation was established based on data obtained at warmer ambient temperatures compared to the ambient temperatures for the SCOUT-O3 and SCOUT-AMMA observations. However, for the SCOUT-AMMA campaign it seems more likely that a main factor for the disagreement is due to the location. While CEPEX provides data obtained above a maritime area, SCOUT-AMMA comprises measurements from a continental area. Due to the overlaying SAL deep convection is inhibited in the region between ITZC and ITF (Hall and Peyrille, 2006). Therefore, only very energetic large scale deep convective systems, the MCS, break through this capping air layer, leading to stronger convection than in the CEPEX region. Similarly, Cetrone and Houze (2009) point out that the lower tropospheric temperature profile is nearly dry adiabatic over West Africa in contrast to the maritime profiles which are nearly moist adiabatic. Consequently, greater buoyancy can be achieved in the West African environment and as a result those continental MCS

tend to have deeper convective cores and produce larger hydrometeors. However, this argumentation does not reveal why the CEPEX parameterisation fails to reproduce the (maritime) measurements of SCOUT-O3. Since the Hector storm system is one of the most intense convective systems worldwide (Crook, 2001), it possibly contains stronger convective cores than the MCSs observed during CEPEX.
Two to four modal lognormal size distributions were fitted to the median size distributions in each potential temperature bin for both, SCOUT-O3 and SCOUT-AMMA. Several other studies have reported on bi- or trimodal size distributions, retrieved from satellite observations, modelling studies or in situ measurements (e.g. Eremenko et al., 2005; Chen et al., 1997; McFarquhar and Heymsfield, 1997; de Reus et al., 2009). Differences in the sizes of the cloud particles in the modelling and satellite studies possibly resulted from focusing on precipitating clouds containing larger hydrometeors or retrievals that enabled particles with sizes less than $60\,\mu\mathrm{m}$ only. When comparing e.g. the SVC measurements discussed in Chapter 6 or the size distributions from the $360\,\mathrm{K}$ to $365\,\mathrm{K}$-θ bin with the results retrieved from satellite measurements in Figure 7.1[21] (presented by Eremenko et al., 2005) one would find the peaks of the size distributions clearly shifted to larger sizes. This underscores the difficulty to retrieve cloud microphysical properties from satellite measurements. However, in agreement with the adjusted fits here, several studies using different techniques show bi- or trimodal size distributions with decreasing mean mode diameters. In the stratosphere, however, the mean mode diameters increase again, and the size distributions look similar to those of the upper troposphere. This might be a result of the increasing ambient temperatures in the stratosphere.
The comparison of cloud ice to interstitial aerosol particle number densities has shown that the activation ratios of aerosol to cloud particles differ quite significantly depending on cloud type. While clouds that originate from deep convection, such as MCS outflow clouds and clouds in overshooting convection, have a very high activation ratio of $1/\,300$, the SVC have a very low activation ratio of $1\,/30\,000$. The latter is in agreement to Jensen et al. (2010) who state that only few aerosol particles will act as very efficient IN in the formation of SVC. Furthermore, the different activation ratios may be indicative of different formation mechanisms. While only few, effective, aerosol particles act as IN for the deposition of water vapour in the SVCs (where it is too cold for involvement of supercooled water in the ice particle formation), more aerosol particles become activated in the deep convective clouds. In the updraughts here, the aerosol particles are more subject to become immersed into or to collide with supercooled water droplets, thus causing immersion or contact freezing. Additionally, riming plays a important role in the updraughts when supercooled droplets collide with existing ice particles. An additional hint of different ice particle formation history is given by the ice particle morphology as observed by the backscattersonde. The MAS data show a higher colour index and lower aerosol depolarisation ratio in the SVC compared to the MCS outflow clouds, indicating different structures in the ice particle shapes. From the CIP images shapes are not determinable for the SVCs. However, in the MCS outflow clouds on 7 and 16 August the CIP images showed mostly heavily rimed ice crystals or rimed aggregates, and aggregates and columns in the stratospheric clouds. Following the difference in the MAS observations between

[21] Note that a direct comparison is not possible since the unit for the $dN/d\log R$ axis has been omitted by Eremenko et al. (2005).

the deep convective clouds and the SVCs the latter do most probably not contain aggregates or rimed ice crystals but ice particles of other crystal structures.
In this entire discussion of clouds within the tropical UTLS it should be kept in mind that it is extremely challenging and difficult to provide direct in situ measurements of the type presented here from these clouds.

Chapter 8

Overall summary and conclusions

8.1 Instrumental implementation

In situ cloud particle instruments have been used widely since several decades. Experience with the measurements, further developments of the instruments, and particularly the development of better and faster electronics have led to a significant improvement of these instruments. One of the latest developments is the Cloud Imaging Probe (CIP). The instrument images the shadow of cloud particles as they pass the instruments laser beam. The CIP has been deployed during two tropical field campaigns in Southern Australia (SCOUT-O3) and West Africa (SCOUT-AMMA). SCOUT-O3 was the first field experiment of the Mainz CIP. Furthermore, it was the first campaign during which a CIP has been deployed in the altitudes of the tropical UTLS, i.e. reaching up to $19\,\mathrm{km}$. Even under the challenging environmental conditions of the tropics (e.g. very warm temperatures at ground and during take off, very low temperatures in the UTLS) the CIP has performed very well.
Before the data measured by the CIP can be analysed the single images have to be checked and corrected for faulty images. The underlying mechanisms for the corrections are summarised and described in detail in Section 2.4. These methods have been adapted and partly developed within this thesis. The specific selection of the mechanisms is chosen individually for each flight to best fit the measurement conditions.

8.2 Observations of TTL clouds

During the tropical campaigns SCOUT-O3 (Darwin, Australia, 2005) and SCOUT-AMMA (Ouagadougou, Burkina Faso, 2006) the CIP has been deployed in a total of 12 flights side by side with the FSSP-100. Measurements in UTLS clouds were obtained during nine flights, five during SCOUT-O3 (four local and one transfer flight) and four during SCOUT-AMMA (three local and one transfer flight). Different types of clouds have been probed. The data of the particular cloud types are presented and discussed in the chapters of Part II (Chapters 4 through 7) of this thesis: clouds in MCS outflows (Section 4.3), overshooting convection (Section 5.3), SVC (Section 6.3), and also the vertical profiles of all observed UTLS clouds (Section 7.4).
From the complete data set vertical profiles of the clouds in an altitude range of about

$10\,\mathrm{km}$ to $19\,\mathrm{km}$ have been obtained. These profiles show decreasing number concentration, IWC, and effective radius with decreasing temperature. Furthermore, a decrease of these parameters with increasing altitude up to the tropopause has been found. These observations are in agreement with former measurements and modelling studies (e.g. Chen et al., 1997; Schiller et al., 2008; Krämer et al., 2009). In the tropopause region, however, the decrease of the microphysical parameters declined or stayed fairly constant and the few stratospheric measurements showed increasing values, consistent with increasing temperatures just above the tropopause.
Size distributions for the clouds were compiled and classified in bins of potential temperature. The size distributions exhibit a decrease in particle number concentrations and sizes when ascending to the tropopause, while the size distributions of the stratospheric clouds show an increase in ice particle size. Such an altitude dependence has also been observed by McFarquhar and Heymsfield (1996) during the CEPEX campaign. The size distributions obtained during the SCOUT-AMMA campaign show the presence of larger particles and a higher fraction of large particles compared to SCOUT-O3 size distributions. Further comparisons clearly showed that the CEPEX parameterisation (McFarquhar and Heymsfield, 1997) exhibits smaller ice particle sizes and a smaller fraction of large particles in the upper troposphere during SCOUT-AMMA and in the stratosphere during SCOUT-O3. The failure of representing the observed size distributions from SCOUT-AMMA is possibly an effect of the geographical location. Deep convection above continental areas (as West Africa) can achieve greater buoyancies which leads to stronger convective cores. Therefore, larger hydrometeors can be produced in deep convection over continental areas compared to maritime areas (Hall and Peyrille, 2006; Cetrone and Houze, 2009). In order to give a description of the continental West African clouds for modelling purposes, two to four modal lognormal size distributions have been fitted to the size distributions in each potential temperature bin.
Measurements within Mesoscale Convective System (MCS) outflows have been performed during the SCOUT-AMMA campaign. With the help of tracer data, i.e. NO, NO_y, CO, CO_2, and O_3, satellite images, and trajectory analysis the outflows have been identified and their ages estimated. The ages ranged from young (less than three hours), over recent (about five hours) to aged (about ten hours). Additionally, one precursory state has been observed. The observations showed that with increasing age of the outflow ice particle number concentrations and IWCs decreased as well as the effective radius and maximum particle size. Since the outflows were located at increasing distance to the convective cores, the decreasing microphysical properties are consistent with the observations of McFarquhar and Heymsfield (1996) and Schiller et al. (2009) who state that an enhancement in the values of the microphysical properties have been observed closer to the convective core. The outflows were located at increasing altitude with increasing age, between $11.0\,\mathrm{km}$ and $14.3\,\mathrm{km}$. These findings have been summarised in Figures 4.19 and 4.20 and in Table 4.7. In order to provide a better comparison between the different TTL cloud types the meteorological and mean cloud microphysical parameters of all TTL cloud observations are summarised in Table 8.1.
High reaching overshooting convection has been observed over the Tiwi Islands during the SCOUT-O3 campaign even injecting ice particles into the stratosphere. Most of the stratospheric cloud events were encountered on the “Golden Hector Day” and

Table 8.1: Summary of the meteorological and mean microphysical parameters for the different TTL cloud types.

Cloud	Alt [km]	θ [K]	$T_{ambient}$ [K]	N [cm^{-3}]	IWC [$\mathrm{g\,m}^{-3}$]	r_{eff} [μm]
MCS_{young}	$11.0-12.5$	$346-350$	$220-225$	3.3	31.9×10^{-3}	133.1
MCS_{recent}	$11.5-13.7$	$350-354$	$205-224$	0.37	4.9×10^{-3}	83.2
MCS_{aged}	$13.7-14.3$	$352-356$	$200-208$	0.01	5.2×10^{-5}	11.0
overshoot	$18.0-18.7$	$386-414$	$186-192$	0.07	3.4×10^{-4}	19.8
SVC	$15.0-16.4$	$363-373$	$192-198$	0.01	1.6×10^{-4}	12.4

reached up to $1.4\,\mathrm{km}$ above the cold point tropopause. Unexpectedly large ice particles with diameters up to about $500\,\mu\mathrm{m}$ have been observed and imaged by the CIP. The values for number concentration, IWC, effective radius and maximum particle size ranged between those of the recent and aged outflow. The ice particles have been found to originate from the troposphere. Calculations of stratospheric residence times and evaporation times of these particles showed that a large part of the ice particles will evaporate in the stratosphere. Thus, these overshoots provide a moisture source for the dry stratospheric air. These measurements give a further indication on the importance of high reaching overshooting convection on the hydration of the stratosphere and on the troposphere to stratosphere transport.

Besides the deep convective clouds a third cloud type has been observed in the TTL above West Africa, the subvisible cirrus (SVC). Four encounters occurred at altitudes between $15.0\,\mathrm{km}$ and $16.1\,\mathrm{km}$, i.e. a few hundred metres below the cold point tropopause. Comparable values for the microphysical parameters have been found as for former SVC measurements and they are similar to those of the aged outflow. The data of all (previous and recent) SVC measurements were taken as input for the calculation of an exponential fit on the SVC size distributions which can be used as a rough parameterisation. The presence of relatively large particles (up to $130\,\mu\mathrm{m}$ during SCOUT-AMMA) showed that some hypotheses for the formation mechanisms and for the maintenance of these clouds need to be revised. The broad size distributions are furthermore an indication for heterogeneous ice nucleation (as suggested by Jensen et al., 2010). The observed moistening of convective overshooting events during SCOUT-AMMA (Khaykin et al., 2009; Schiller et al., 2009) was only moderate compared to measurements at other locations. This might be a further hint for the dehydrating effect of SVCs which might have compensated a part of the moistening due to convective overshoots.

The estimated activation ratio of aerosol to cloud particles for SVC was found to be the lowest of all clouds. This observation consolidates the suggestion that only a subset of aerosols act as very effective IN for deposition freezing, thereby limiting the ice concentrations (Jensen et al., 2010). The estimated activation ratios of the MCS outflow and convective overshoot clouds, i.e. the deep convective clouds, differ significantly from those of the SVC. The observations showed that the estimated activation ratios of deep convective clouds were found among the highest activation ratios. This gives an indication for different ice particle formation processes which is further confirmed by the depolarisation measurements. The latter show that the ice particles in SVC and MCS outflow have different ice crystal structures.

In order to provide a final overview, size distributions and particle images from the dif-

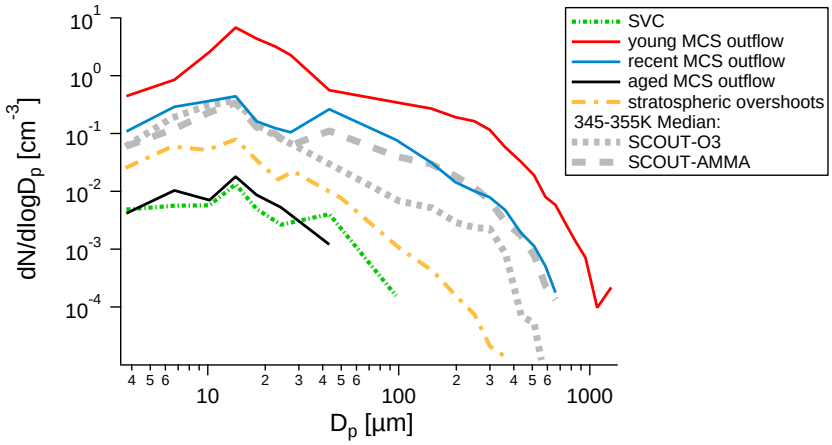

(a) Median size distributions as obtained from the measurements within the different cloud types.

Figure 8.1: Comparison of the different cloud types as observed in the TTL during SCOUT-O3 and SCOUT-AMMA.

ferent cloud types are summarised and compared in Figure 8.1. The median size distributions from the different cloud types are depicted in Figure 8.1(a) and additionally the median size distributions of the $345\,\mathrm{K} < \theta < 355\,\mathrm{K}$ bin are displayed. Furthermore, the sketch of TTL clouds (Figure 1.6) is revisited and expanded with representative CIP image stripes for all observed cloud types. Additionally, a cloud profile of CIP images from the ascent of 16 August 2006 is shown on the left hand side of Figure 8.1(b). The figures show that the ice particle sizes and numbers decrease within the outflows with increasing age and with increasing altitude, respectively. Ascending further up through the tropopause region into the stratosphere the particle sizes increase again (c.f. size distribution of SVCs) and the stratospheric size distributions show additionally higher number concentrations. One could conclude that the SVC have not formed as remnants of convective outflow since the particles are larger than in the aged outflow which would be a precursor of the SVC. In general, smaller particles and lower number concentrations of particles larger $\sim 30\,\mu\mathrm{m}$ have been observed during SCOUT-O3. The young MCS outflow exhibits much larger number concentrations than the size distribution at the comparable potential temperature altitude. Furthermore, the maximum particle sizes in the outflow events are larger than in other clouds at comparable altitudes.

The results presented in Chapter 5 (overshooting convection and stratospheric ice particles during SCOUT-O3) made a significant contribution to the publication by de Reus et al. (2009). Furthermore, the MCS outflow and SVC observations during SCOUT-AMMA, i.e. the results of Chapter 4 and 6, are presented in a recent publication by Frey et al. (2011) which additionally includes some of the results of Chapter 7. Contributions to further publications that are partly linked to this thesis are listed in the List of Publications (page 183, followed by a list of conference contributions). Summarising, this thesis presents an important set of in situ data extending the sparse data set of clouds in the tropical UTLS, exhibiting first MCS outflow measurements over West Africa and first SVC measurements over a continental area,

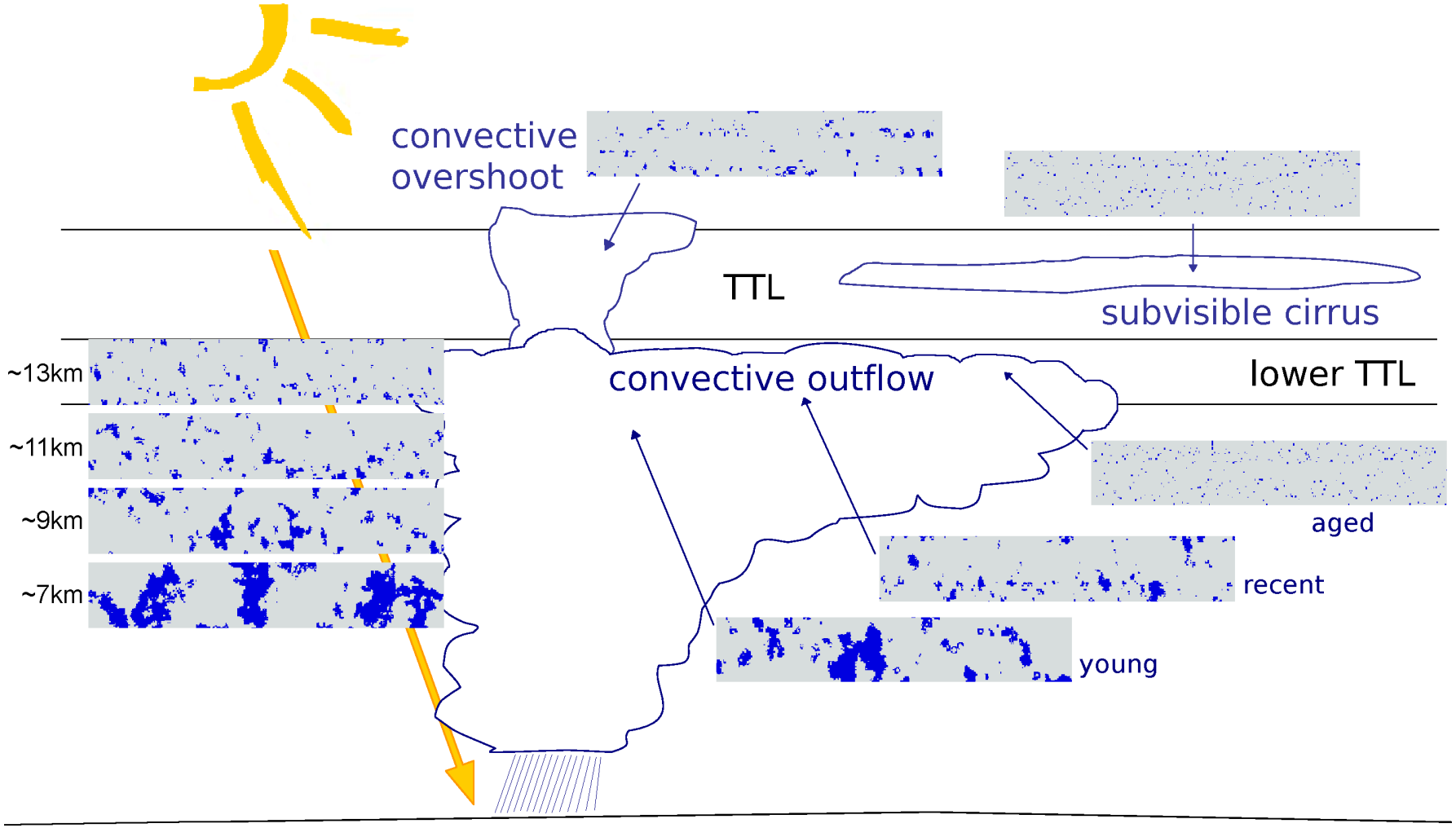

(b) Sketch of TTL clouds (adapted from Figure 1.6) including stripes of consecutive CIP images representative for the different clouds. The images on the left hand side were obtained during ascent on 16 Aug 2006.

Figure 8.1: *continued*

and finally giving unprecedented evidence of ice particles in the stratosphere resulting from overshooting convection.

8.3 Future work

One crucial issue for the in situ cloud particle measurements is to find a solution for the shattering problem. Desirably, such a solution would be applicable to revise former measurements, especially those of the FSSP type instruments since no recording of interarrival times is possible with those instruments. If data are not corrected for shattering, the presence and amount of smaller ice particles remains highly uncertain in clouds that show a high probability of shattering (as the deep convective clouds). Recently, alternative probe tips which shall reduce shattering were used in a study by Korolev et al. (2011). So far, however, no methods are available that are able to quantify the shattering. Thus, under shattering conditions only those instruments can obtain reliable measurements that can identify shattered particles. As soon as mechanisms for the quantification of shattering and for data reduction of former FSSP measurements are available, the older data should be revised. Newer FSSP type instruments have fast enough electronics to be able to report interarrival times. Thus, the interarrival time method for rejection of shattering artefacts can then be applied, too.
Further developments of the CIP are made. Newer CIP versions use diode arrays with a resolution of $15\,\mu\mathrm{m}$ instead of $25\,\mu\mathrm{m}$ and thus more diminutive ice particle structures can be imaged. Greyscale versions shall improve the sizing characteristics and shall image more shape details. However, no data reduction scheme using all three shadow intensities has been reported until now. This will be one of the next tasks for the use of greyscale CIP data. Furthermore, for any OAP type instrument, an out-of-focus correction for non spherical particles should be established since some ice crystal shape appearances alter significantly when imaged out-of-focus. Newer and faster electronics eliminate some of the issues for data correction and are thus advantageous for the instruments. For example, the first slice is now recorded by the electronics and also the response time is reduced, diminishing or even eliminating the related problems.
The discussion has shown that in situ measurements of tropical UTLS clouds are still sparse and do not suffice to achieve a statistically significant parameterisation. Most abundant measurements in this regard were performed within MCS anvils. However, most of those observation were performed over maritime regions and those studies mostly do not separate between outflow and detrained air masses, e.g. by means of tracer measurements as performed in this thesis. In order to compare and corroborate the observations presented here, more measurements are needed. A combination of in situ measurements of microphysical parameters, backscattering, depolarisation, humidity, trace gases, interstitial aerosol, and updraught speeds (e.g. for clarifying SVC maintenance) as well as remote (lidar/radar) measurements to identify the vertical and horizontal extend of the clouds would be desirable. Furthermore, continuous remote measurements could give indications about the clouds lifetimes. Some of the many open questions regarding tropical deep convective clouds and SVC are:

- Which mechanisms stand behind the formation and maintenance of SVCs?
- How large is their horizontal extent, does this extent vary over continental and maritime regions?
- Do microphysical properties of SVCs vary over continental and maritime regions (as they seem to do in MCS anvil clouds)?
- Do MCSs over West Africa have particular properties due to the large desert area, i.e. are there differences to MCSs over other continental areas (as India)?
- Are there differences in the microphysical properties of the MCS anvils and outflow clouds due to different island/ocean distribution over the maritime regions?
- What is the effect of overshooting convection on the heat and moisture balance of the TTL?
- What is the chemical composition of the aerosols and clouds in the TTL and what controls this?
- How do the climate change and increasing greenhouse gases affect the clouds in the tropical UTLS and what effect does a change have on the troposphere to stratosphere transport?

One has to keep in mind that for observations, as presented here, aiming at answering those questions specialised high altitude research aircraft are necessary but only three of them are available worldwide.

Part III

Appendix

Particle Gallery

In this particle gallery CIP images are displayed that were observed during several campaigns. Besides the images (all $1600\,\mu\mathrm{m}$ in width) the ambient temperature and altitude of the observation is given, as well as the relative humidity with respect to ice, if available. The uppercase latter indicates during which campaign the images has been recorded:

A	SCOUT-AMMA	2006	Burkina Faso
O	OMAC	2007	Germany
C	CONCERT[1]	2008	Germany
R	RECONCILE[2]	2010	Sweden

needle rosettes

	236.0 K	10.0 km		A		236.6 K	9.9 km		A
	217.5 K	12.0 km	80 %	A		217.4 K	12.0 km	74 %	A
	235.7 K	10.0 km		A		257.5 K	5.0 km	91 %	C
	256.3 K	5.2 km	86 %	C		239.1 K	7.5 km	108 %	C
	235.4 K	8.0 km		C		235.0 K	6.8 km		R
	258.0 K	5.0 km	91 %	C		254.8 K	5.4 km	88 %	C
	258.6 K	1.7 km		R		234.6 K 232.3 K	8.1 km 8.4 km		C C

bullet rosettes

	206.7 K	13.5 km		A		250.9 K	8.1 km		A
	267.7 K	5.6 km		A		269.8 K	5.2 km		A

[1] CONtrail and Cirrus ExpeRimenT, October/November 2008, Germany (Voigt et al., 2010)
[2] Reconciliation of essential process parameters for an enhanced predictability of arctic stratospheric ozone loss and its climate interactions, January-March 2010, Sweden

columns and capped columns

	259.6 K	7.0 km	A		269.9 K	5.2 km	A
	223.1 K	11.5 km	A		237.1 K	6.6 km	R
	256.4 K	1.3 km	R		255.8 K	1.2 km	R

plates

	269.9 K	5.3 km	A	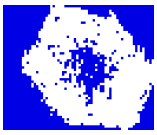	267.7 K	5.6 km	A
	261.3 K	6.7 km	A		259.6 K	7.0 km	A
	255.1 K	at ground	R		267.2 K	5.7 km	A
	255.1 K	at ground	R		256.6 K	3.4 km	R
	257.2 K	1.0 km	R		256.1 K	1.2 km	R
	255.1 K	at ground	R		257.2 K	1.0 km	R

stellar plates

	256.0 K	1.3 km	R		256.7 K	2.1 km	R
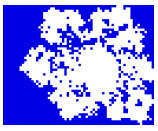	256.7 K	2.1 km	R		257.1 K	1.4 km	R
	256.0 K	1.3 km	R		256.5 K	1.1 km	R
	257.7 K	1.0 km	R		258.8 K	0.5 km	R

aggregates

	259.5 K	7.0 km		A		217.6 K	12.0 km	122 %	A
	255.0 K	7.4 km		A		257.2 K	7.3 km		A
	268.1 K	5.5 km		A		255.1 K	at ground		R
	254.7 K	5.4 km	90 %	C		274.8 K	3.3 km	80 %	O
	255.3 K	2.5 km		R		255.5 K	2.4 km		R
	256.2 K	1.3 km		R	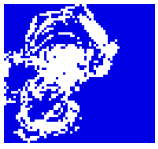	256.7 K	1.0 km		R

chain aggregates

	219.8 K	11.9 km	84 %	A	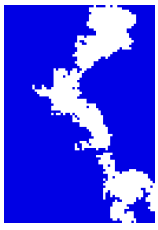	219.6 K	11.9 km	70 %	A
	213.3 K	12.5 km	76 %	A		235.8 K	8.0 km		C

triangular ice particles

	243.0 K	7.0 km	106 %	C		244.7 K	6.8 km	101 %	C
	239.2 K	7.5 km	108 %	C					

graupel and rimed crystals

	272.1 K	3.5 km	92 %	O		272.1	3.4	93	O
	274.8 K	3.3 km	83 %	O		272.1	3.6	86	O
	274.3 K	3.4 km	84 %	O		274.6	3.3	78	O
	272.0 K	3.6 km	86 %	O		273.5	3.5	82	O
	274.8 K	3.3 km	84 %	O		274.7	3.3	79	O

List of abbreviations

1D	one-dimensional
1DC	one-dimensional cloud probe
2D	two-dimensional
2DC	two-dimensional cloud probe
2D-S	two-dimensional stereo probe
3D	three-dimensional
ACE	Atmospheric Chemistry Experiment
AEW	African Easterly Waves
AEJ	African Easterly Jet
AIDA	Aerosol Interactions and Dynamics in the Atmosphere
AIIE	Airborne Icing Instrumentation Evaluation
AIRTOSS	AIRcraft TOwed Sensor Shuttle
ALTO	Airborne Laser Tunable Observer
AMA	Asian Monsoon Anticyclone
AMMA	African Monsoon Multidisciplinary Analysis
APE	Airborne Polar Experiment
APE-THESEO	Airborne Platform for Earth observation - (contribution to) the Third European Stratospheric Experiment on Ozone
ARM	Atmospheric Radiation Measurement
CALIPSO	Cloud-Aerosol Lidar and Infrared Pathfinder Satellite Observations
CAS	Cloud and Aerosol Spectrometer
CCD	charge-coupled device
CCM	chemistry-climate model
CCL	convective condensation level
CDC	Climate Diagnostics Center
CDP	Cloud Droplet Probe
CEPEX	Central Equatorial Pacific Experiment
CFC	chlorofluorocarbon
CIP	Cloud Imaging Probe
CLACE	Cloud and Aerosol Characterisation Experiment
CN	condensation nucleus
CNES	Centre National d'Études Spatiales (French space agency)
COLD	Cryogenically Operated Laser Diode
COPAS	COndensation PArticle counting System
CPC	Condensation Particle Counters
CPI	Cloud Particle Imager
CRAVE	Costa Rica Aura Validation Experiment

CRISTA-NF	Cryogenic Infrared Spectrometers and Telescopes for the Atmosphere - New Frontiers
CRM	Cloud Resolving Model
CT	convective temperature
CWC	condensed water content
DMT	Droplet Measurement Technologies
DOF	Depth Of Field
ECMWF	European Centre of Medium Range Weather Forecast
EEIG	European Economic Interest Grouping
EL	equilibrium level
ENVISAT	Environmental Satellite
ERBS	Earth Radiation Budget Satellite
ESA	European Space Agency
EUFAR	European Facility For Airborne Research
EUMETSAT	European Organisation for the Exploitation of Meteorological Satellites
FISH	Fast In situ Stratospheric Hygrometer
FLASH	FLuorescent Airborne Stratospheric Hygrometer
FOZAN	Fast OZone ANalyser
fps	frames per second
FSSP	Forward Scattering Spectrometer Probe
FTIR	Fourier Transform infrared
FTS	Fourier Transform Spectrometer
GCM	global climate model
HAC	high altitude cirrus
HAGAR	High Altitude Gas AnalyseR
HALO	High Altitude and LOngrange research aircraft
HALOE	Halogen Occultation Experiment
HALOX	HALogen OXide monitor
HOLODEC	Holographic Detector for Clouds
IDL	Interactive Data Language
IN	ice nucleus
INCA	INterhemispheric differences in Cirrus properties from Anthropogenic emissions
IPCC	Intergovernmental Panel on Climate Change
IR	infrared
ISCCP	International Satellite Cloud and Climatology Project
ITCZ	intertropical convergence zone
ITD	intertropical discontinuity
ITF	intertropical front
IWC	Ice Water Content
LCL	lifting condensation level
LITE	Lidar In-space Technology Experiment
LMO	Level of Maximum Overshoot
LNB	level of neutral buoyancy
LWC	Liquid Water Content
LZRH	level of zero radiative heating

MAL	Miniature Aerosol Lidar
MARSHALS	Michelson Interferometer for Passive Atmospheric Sounding
MAS	Multiwavelength Aerosol Scatterometer
MCC	Mesoscale Convective Complex
MCS	Mesoscale Convective System
MDB	Myasishchev Design Bureau
MIPAS	Michelson Interferometer for Passive Atmospheric Sounding
MSG	Meteosat Second Generation
NASA	National Aeronautics and Space Administration
NCAR	National Center for Atmospheric Research
NWP	numerical weather prediction
OAP	Optical Array Probe
OLR	outgoing longwave radiation
OMAC	Observation Methodologies of the first indirect Aerosol effect in water Clouds
OSIRIS	Optical Spectrograph and InfraRed Imaging System
PADS	Particle Analysis and Display System
pbp	particle by particle
PhD	Doctor of Philosophy
PR	precipitation radar
PSC	polar stratospheric cloud
SAGE	Stratospheric Aerosol and Gas Experiment
SAL	Saharan Air Layer
SCOUT-O3	Stratospheric-Climate Links with Emphasis on the Upper Troposphere and Lower Stratosphere
SID	Small Ice Detector
SIOUX	StratospherIc Observation Unit for nitrogen oXides
SOP	Special Observing Periods
SPP	Signal Processing Package
SVC	subvisible cirrus
TAS	true airspeed
TC4	Tropical Composition, Clouds and Climate Coupling
TDC	Thermo Dynamic Complex
TEJ	Tropical Easterly Jet
TOA	top-of-atmosphere
TOGA COARE	Tropical Ocean Global Atmosphere Coupled Ocean-Atmosphere Response Experiment
TOTE/VOTE	Tropical Ozone Transport Experiment/Vortex Ozone Transport Experiment
TRMM	Tropical Rainfall Measuring Mission
TROCCINOX	TROpical Convection, CIrrus, and Nitrogen OXides experiment
TST	troposphere to stratosphere transport
TTL	Tropical Tropopause Layer
UAV	Unmanned Aerial Vehicles
UCAR	the University Corporation for Atmospheric Research
UCSE	Unified Communications for System Engineer
UT	upper troposphere

UTC	Coordinated Universal Time
UTLS	upper troposphere/lower stratosphere
UTTC	ultrathin tropical tropopause cloud
UV	ultraviolet
WAM	West African Monsoon
WAS	Whole Air Sampler
WMO	World Meteorological Organisation

List of chemical species

CH_4	methane
$CFC-11$	trichlorofluoromethane
$CFC-12$	dichlorodifluoromethane
CO	carbon monoxide
CO_2	carbon dioxide
H_2	molecular hydrogen
H_2O	molecular water
H_2O(ice)	molecular water ice
$Halon-1211$	bromochlorodifluoromethane
HNO_3	nitric acid
LNO_x	lightning NOx
N_2O	nitrous oxide
NO	nitric oxide
NO_2	nitrogen dioxide
NO_x	NO + NO_2
NO_y	the sum of all oxidised nitrogen compounds including NO_x
O_3	ozone
PAN	peroxyacyl nitrate
SF_6	sulfur hexafluoride

List of symbols

Symbol	Physical parameter	Unit
ar	area ratio	
A	particle surface area	$\mu\mathrm{m}^2$
A_{proj}	projected area (by a particle)	$\mu\mathrm{m}^2$
ABC	aerosol backscatter ratio	$\mathrm{m}^{-1}\,\mathrm{sr}^{-1}$
ADR	aerosol depolarisation ratio	$\%$
Alt	altitude	km
CI	colour index	
CWC	condensed water content	$\mathrm{g}\,\mathrm{m}^{-3}$
D_0	actual particle diameter	$\mu\mathrm{m}$
D_{edge}	outer diameter of particle image	$\mu\mathrm{m}$
D_{spot}	diameter of Poisson spot	$\mu\mathrm{m}$
D_p	particle diameter	$\mu\mathrm{m}$
D_{pmax}	maximum particle diameter	$\mu\mathrm{m}$
$\overline{D_{pM}}$	mass weighted mean diameter	$\mu\mathrm{m}$
$\overline{D_{pN}}$	number weighted mean diameter	$\mu\mathrm{m}$
DOF	depth of field	cm
DR	depolarisation ratio	$\%$
f	sampling frequency	Hz
G	geometric cross-sectional area of water drops per unit volume	$\mathrm{m}^2\,\mathrm{m}^{-3}$
IWC	ice water content	$\mathrm{g}\,\mathrm{m}^{-3}$
J_{ev}	evaporation rate	$\mathrm{cm}^{-2}\,\mathrm{s}^{-1}$
LWC	liquid water content	$\mathrm{g}\,\mathrm{m}^{-3}$
m	particle mass	$\mu\mathrm{g}$
Ma	Mach number	
num	number of diodes	
N	number concentration	cm^{-3}
$N_{aerosol}$	aerosol particle number concentration	cm^{-3}
N_{cloud}	cloud particle number concentration	cm^{-3}
p	pressure	hPa
r_a	radius of a sphere of equivalent cross-sectional area	$\mu\mathrm{m}$
r_{eff}	effective radius	$\mu\mathrm{m}$
r_p	particle radius	$\mu\mathrm{m}$
res	diode resolution	$\mu\mathrm{m}$
Re	Reynolds number	

RH	relative humidity	$\%$
RHi	relative humidity with respect to ice	$\%$
SA	sample area	mm^2
S_i	supersaturation with respect to ice	
S_w	supersaturation with respect to water	
SV	sample volume	cm^3
t_{ev}	evaporation time	s
t_s	sample time	s
T	temperature	K
T_a	ambient temperature	K
T_f	freezing temperature	K
TAS	true airspeed	$\mathrm{m\,s}^{-1}$
v	particle velocity	$\mathrm{m\,s}^{-1}$
V	particle volume	$\mu\mathrm{m}^3$
V_t	terminal velocity	$\mathrm{m\,s}^{-1}$
w_{eff}	effective array width	$\mu\mathrm{m}$
$w_{eff}^{'}$	effective array width (reconstructed particles)	$\mu\mathrm{m}$
Z	particle distance from object plane	m
Z_d	dimensionless distance	
β_{ext}	extinction coefficient	km^{-1}
Γ	temperature lapse rate	$\mathrm{K\,kg}^{-1}$
Δz	vertical thickness	km
η	decay constant	
θ	potential temperature	K
λ	wavelength	$\mu\mathrm{m}$
ν	kinematic viscosity	$\mathrm{m}^2\,\mathrm{s}^{-1}$
ρ	particle density (ice or water)	$\mathrm{g\,m}^{-3}$
σ_g	geometric standard deviation	
τ	optical thickness	
χ^2	chi-square (fit quality parameter)	

List of constants

Symbol	Physical constant	Value and Unit
c_p	specific heat capacity for dry air at constant pressure	$1005.6\,\mathrm{J\,kg^{-1}K^{-1}}$
c_v	specific heat capacity for dry air at constant volume	$716.49\,\mathrm{J\,kg^{-1}K^{-1}}$
M	molar mass of water	$18\,\mathrm{g\,mol^{-1}}$
N_A	Avogadro constant	$6.022 \times 10^{23}\,\mathrm{mol^{-1}}$
R	gas constant for dry air	$287.058\,\mathrm{J\,kg^{-1}\,K^{-1}}$
γ	ratio of specific heats in dry air	1.4
ρ_i	density of ice	$0.917 \times 10^6\,\mathrm{g\,m^{-3}}$
ρ_w	density of water	$0.9998 \times 10^6\,\mathrm{g\,m^{-3}}$

Appendix A

Cloud particle data quality assessment

A.1 Applied corrections

Table A.1: Summary of applied correction and rejection mechanisms (c.f. Section 2.4) on CIP images. For all flights the maximum dimension has been used for particle sizing.

	SCOUT-O3 (overshooting convection)	SCOUT-AMMA (MCS outflow, SVC)
reconstruction first slice	yes	yes
missizing y-direction	yes	yes
area ratio	0.1 (ice clouds)	0.1 (ice clouds)
out-of-focus[i]	yes	yes
reconstruction empty images	yes	yes
reconstruction partial images[ii]	no	yes
shattering[iii]	yes	yes
double particles	no (did not occur)	yes

[i] The observed ice particles during SCOUT-O3 and SCOUT-AMMA were mostly of spherical or quasi-spherical shape (e.g. graupel). Therefore, the out-of-focus correction is applicable without adding large sizing errors as would have been the case when mostly needles are measured.

[ii] For the SCOUT-O3 campaign partial images have been rejected, since the focus was placed on stratospheric ice particles which were mainly smaller. Thus, a rejection of partial images does not result in a high loss of particle images. The cloud measurements of the SCOUT-AMMA campaign focused on MCS outflow clouds which consist of fairly large particles. Therefore, the partial images have been reconstructed. However, when the reconstruction resulted in particle diameters larger than two times the diode array length, these particles have been rejected. This did not lead to a high loss of particle images (a maximum of a few hundred per flight). However, for the size distributions the upper size limit of the particles is set to $1400\,\mu\mathrm{m}$ for two reasons. Irregularly shaped ice crystals have a high chance of being reconstructed erroneously (applies to SCOUT-AMMA measurements), while the rejected partial images during SCOUT-O3 may lead to an undercount of the largest ice particles.

[iii] The interarrival time threshold has been adapted for each flight separately. During the encounters of SVCs and of the aged outflows no shattering has been observed according to the interarrival time method.

A.2 Statistics of CIP image corrections

Table A.2: Statistics of investigated CIP particle images that were detected during the measurements performed in UTLS clouds at potential temperatures $>345\,\mathrm{K}$ during SCOUT-O3 (2005) and SCOUT-AMMA (2006). The numbers (#) and percentages of particle images for which the respective corrections/rejections have been performed are displayed for area ratio (ar), out-of-focus (oof) images, empty images, partial images, and shattering. One image can be counted in more than one category, e.g. a partial image can have such a short interarrival time that it is also counted in the shattering category.

		ar		oof		empty		partial		shattering	
date	$\#_{total}$	#	%	#	%	#	%	#	%	#	%
25 Nov 2005	9608	23	0.2	23	0.2	473	4.9	753	7.8	724	7.5
29 Nov 2005	3060	1	0.0	1	0.0	279	9.1	32	1.0	21	0.7
30[a] Nov 2005	104 834	493	0.5	1601	1.5	6377	6.1	12 768	12.2	6292	6.0
30[b] Nov 2005	47 358	96	0.2	512	1.1	2886	6.1	3753	7.9	2328	4.9
9 Dec 2005	5141	1	0.0	4	0.0	353	6.7	415	8.1	86	1.7
$\sum$	170 001	10 982	6.5	2141	1.3	10 368	6.1	17 721	10.4	9451	5.6
7 Aug 2006	119 978	928	0.8	12 729	10.6	2605	2.2	22 395	18.7	5762	4.8
8 Aug 2006	34 033	88	0.3	2126	6.4	810	2.4	4538	13.3	1059	3.1
11 Aug 2006	7101	23	0.3	958	13.5	193	2.7	1273	17.9	264	3.7
16 Aug 2006	88 173	358	0.4	1922	2.2	5300	6.0	14 641	16.6	5459	6.2
$\sum$	249 296	10 305	4.1	17 735	7.1	8908	3.6	42 847	17.2	12 544	5.0

Remark on Double Particles
On 7 August 2006 the Double Particles problem occurred frequently within a time window of about $200\,\mathrm{s}$ during the descent. However, there were several breaks of a few seconds in between the Double Particles and thus not the whole time period needed to be rejected from data analysis. On the flights of 8 and 11 August 2006 the Double Particles did occur within time windows of roughly $60\,\mathrm{s}$ and $20\,\mathrm{s}$, respectively. However, the occurrences of Double Particles on these two days were at altitudes below $\theta = 345K$ and thus not in the area of the main focus of the analysis. Neither the flight on 16 August 2006 nor any flight during the SCOUT-O3 campaign were affected by the Double Particles.

A.3 Combined size distributions of FSSP-100 and CIP

In order to cover the full observed size range of cloud particles, the size distributions shown in this thesis are combined from the measurements of the FSSP-100 and the CIP. Therefore, the FSSP-100 size distributions are simply overlaid onto the CIP size distributions. The first CIP size bin actually extends down to sizes of $25\,\mu\mathrm{m}$ but is only displayed down to $29.2\,\mu\mathrm{m}$ which is the upper size limit of the FSSP-100 size distribution. No smoothing or averages have been applied to the size distribution data and the unaltered measurement results are shown. Figure A.1 (the case of overshooting convection on 29 November 2005, as displayed in Figure 5.7) gives an example for such a combined size distribution. The FSSP-100 size distribution is displayed in red, CIP in green. The overlapping part is indicated by the greyish colour. The error bars are derived from counting statistics and sample volume uncertainty. This is an example for conditions with low counting statistics. In such cases with low

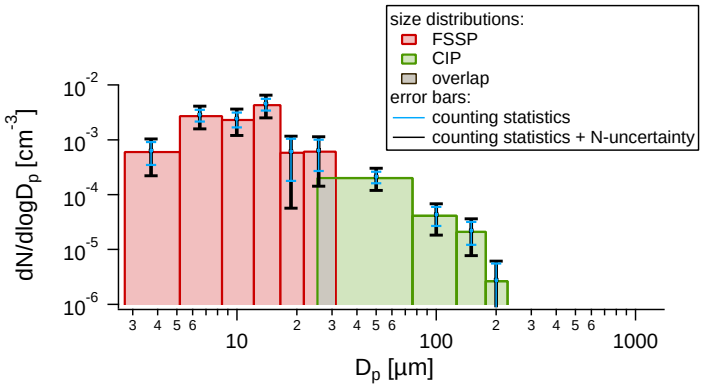

Figure A.1: Combined size distribution of CIP and FSSP-100 measurements displayed in green and red shaded bars, respectively. The blue error bars show the counting statistics uncertainty and the red error bars display the combined uncertainty resulting from counting statistics and sample volume.

number concentrations the sixth and seventh size bin of the FSSP are combined into one size bin (as in this figure). It has to be reminded that the CIP data are corrected for shattering while the FSSP-100 data are not. The FSSP-100 size distributions are considered as contaminated by shattering in all bins in case the two highest bins (or the combined highest bin in conditions with low counting statistics) do not well overlap with the lowest CIP bin. Size distributions with poor overlap were discarded from further analysis, however, this was rarely the case (see Section A.4.4).

A.4 Instrument performance and the removal of shattering artefacts

For the measurements presented in this thesis (and any other measurements performed with in situ cloud particle probes) there are two main issues: the instrument performance and the question how to ensure that shattering does not affect the measurements significantly. Therefore, this sections presents the general arguments related to those two issues and specifies how data have been treated in order to avoid shattering biased results from the combined FSSP-100 and CIP measurements.

A.4.1 General arguments

Experiments dedicated to shattering

Korolev et al. (2011) performed wind tunnel studies as well as an airborne experiment with modified probe tips which were developed to reduce shattering. Those experiments were conducted under vastly different conditions when compared with the measurements which are reported in this thesis (SCOUT-O3 and SCOUT-AMMA). The latter were performed at much lower temperatures (i.e. below $-40\,^{\circ}\mathrm{C}$ and down to $-80\,^{\circ}\mathrm{C}$) and at much lower humidities and number concentrations than (1.) the wind tunnel measurements and (2.) the measurements in mostly mixed phase clouds of the Airborne Icing Instrumentation Evaluation (AIIE) campaign. Thus, an extrapolation of the factor 100 to 1000 enhancements due to shattering from the reported con-

ditions of the AIIE to the low temperature, low humidity, low concentration conditions during SCOUT-O3 and SCOUT-AMMA is not justified until solid evidence for this is provided for example by dedicated wind tunnel experiments or more airborne instrument intercomparisons (like e.g. Jensen et al., 2009) at such UTLS conditions. This is also suggested by the study of Lawson (2011), who performed measurements in anvil cirrus at temperatures from $-30\,^{\circ}\mathrm{C}$ to $-63\,^{\circ}\mathrm{C}$ and concluded that the post processing interarrival time analysis is well suited for rejection of suspected shattered particles and that this analysis might even carry more weight than the application of modified tips. For example, the ice particles measured in the UTLS have no quasi liquid layers and may even consist of a glassy physical structure (Murray et al., 2010) and thus their break up and bounce behaviour will differ from the behaviour of the much warmer hydrometeors. For these reasons, it is by far premature to conclude that all FSSP-100 data are obsolete because of the shattering influence, especially when other data from partly overlapping instruments -like the CIP- are available. One should still be able to provide useful data after careful analyses of the individual size distributions. What "careful analysis" implies, which ultimately led to the rejection of data not included in this thesis, is described below in Section A.4.4. Of course, shattering influence cannot be excluded completely, but the presented data can be limited to cases where shattering influence is believed to be low, and the possibly contaminated data can be highlighted to the reader.

CIP and FSSP performance

Jensen et al. (2009) state: "The agreement between size distributions derived from the CIP and 2D-S imaging instruments is excellent throughout their overlapping size range ($>50\,\mu\mathrm{m}$)." The authors refer to tropical measurements in Costa Rica at $11.4\,\mathrm{km}$ to $12\,\mathrm{km}$ altitude and probably these are similar to the young outflow conditions of 7 August 2006 (c.f. Section 4.2.3). Since the 2D-S is believed to reliably measure even smaller particles ($>100\,\mu\mathrm{m}$) at high airspeeds (up to $230\,\mathrm{m\,s^{-1}}$ Jensen et al., 2009) this statement indicates a good performance of the CIP.
Concerning the FSSP performance, Cairo et al. (2011) state in their conclusions: "A comparison of optical properties for tropical high altitude cirrus clouds, directly measured and inferred from particle size distribution observations, has been carried out. Results suggest that the fraction of the size spectrum available from FSSP particle counter observation, i.e. particles with diameters from $2.7\,\mu\mathrm{m}$ to $31\,\mu\mathrm{m}$, is effective in reproducing cirrus optical properties in the visible part of the spectrum. This result keeps validity for backscattering cross sections spanning over 5 orders of magnitude. Optical particle counters observations are thus a valid tool to assess the cloud particle density and to provide size distributions for modelling cloud microphysical processes and radiative effects in the visible region of the spectrum." To arrive at this result Cairo et al. (2011) used a careful selection of the SCOUT-O3, SCOUT-AMMA, and TROCCINOX data. They applied the MAS backscatter sonde on the M55 Geophysica to measure directly backscatter and depolarisation in the vicinity of the aircraft within the tropical high altitude cirrus clouds and compared this data with the backscatter ratios derived from the in situ measured particle size distributions from the FSSPs. The optical backscatter for the most part depends on the small particle concentrations reported by the FSSP and much less on the larger sizes from the CIP. If shattering

had enhanced the corresponding small particle number densities by factors of 100 to 1000, then this intercomparison would have severely failed. Of course, this only holds for the used data sets and may not be extrapolated to cirrus in general.

Lyman-α hygrometer derived IWC vs. CIP and FSSP

In the study by de Reus et al. (2009), the IWCs derived from Lyman-α hygrometer H_2O measurements are directly compared with the concurrently measured particle IWCs, as calculated by using the Baker and Lawson (2006) scheme, for the observations during the SCOUT-O3 campaign. They showed that the IWCs independently derived from these measurements did agree remarkably well within the measurement uncertainties. Measured IWCs ranged between $10^{-5}\,\mathrm{g\,m^{-3}}$ and $10^{-2}\,\mathrm{g\,m^{-3}}$. If shattering had significantly influenced the FSSP-100 results then discrepancies between the IWCs derived from the gas phase and the particle measurements could have been expected. Thus, shattering is believed to not significantly alter the IWCs and the FSSP-100 size distributions during the SCOUT-O3 measurements. For IWCs larger than roughly $0.001\,\mathrm{g\,m^{-3}}$ the underlying volumes are mostly influenced by the large particles. For the smaller IWCs the FSSP-100 size range contributes more than $50\,\%$ of the IWC. At least here one can assume that additionally detected particles from shattering would enhance the IWC artificially for the CIP and FSSP-100. However, in Figure 4 of de Reus et al. (2009) the IWCs from the particle instruments are even too low when compared with the gas phase instruments. The IWCs of the encountered outflow events during SCOUT-AMMA range from $2 \times 10^{-5}\,\mathrm{g\,m^{-3}}$ to $6 \times 10^{-2}\,\mathrm{g\,m^{-3}}$ with many values below $0.001\,\mathrm{g\,m^{-3}}$. For the data presented from the subvisible cirrus and uppermost UT cirrus the IWCs were much lower than $0.001\,\mathrm{g\,m^{-3}}$. (Note for clarity: A similar plot unfortunately cannot be prepared for the SCOUT-AMMA flights, because the four involved instruments were not often enough operational concurrently at the same time and while inside the clouds.) At least for these cases it is unlikely that shattering influence of factors between 100 and 1000 would have gone by unnoticed.

Comparison AMMA/SCOUT data with CEPEX

In Figure 7.5 a summary of the SCOUT-O3 data from Darwin and the SCOUT-AMMA data from West Africa is presented together with the parameterisation which McFarquhar and Heymsfield (1998) extracted from their CEPEX measurements. In the lowest potential temperature bin of the figure IWCs larger than $0.001\,\mathrm{g\,m^{-3}}$ were found such that the argument from Section A.4.1 is not applicable here. However, the measurements agree quite well with the CEPEX parameterisation particularly for the particle sizes below roughly $20\,\mu\mathrm{m}$. The major differences between CEPEX and SCOUT-AMMA occur at the very large sizes. During CEPEX the particles were measured with a VIPS and a 2-DC probe. The VIPS has an entirely different inlet-geometry and measurement principle w.r.t. the FSSP and shattering -presumably- is not an issue. If shattering had introduced artefacts to the particle number concentrations during SCOUT-AMMA on the factor 100 to 1000 levels like indicated by Korolev et al. (2011), then this intercomparison would have turned out very differently. This point is better visible in Figure 7.6. Again the lognormal fits of the measurements compare well with the CEPEX parameterisation, especially for the small sizes in the lowest potential

temperature bin. (For the higher potential temperatures the results lie well below the CEPEX data, except for the SCOUT-O3 tropopause region size distributions, and/or particles were too small for significant shattering.) Here, the ordinate displays absolute concentrations and not normalised as in Figure 7.5.

Based on these general arguments Frey et al. (2011) believe that careful inspection and selection of the data does allow the investigator to retain the CIP data and some of the FSSP measurements.

A.4.2 CIP performance and shattering artefacts

Small particle detection

It has been questioned whether the CIP has problems with the detection of particles with diameters less than $150\,\mu\mathrm{m}$. The Mainz CIP has newer electronics with faster response times compared to the first CIP instruments and the 2DC probe. Baumgardner et al. (2001) described this improvement and determined that there is no more dependency of the depth of field on the aircraft's velocity (which was described by Baumgardner and Korolev, 1997). Furthermore, Lawson (2011) stated, based on recent measurements, that the CIP reliably measures droplets of $50\,\mu\mathrm{m}$ at speeds below $150\,\mathrm{m\,s^{-1}}$. During the SCOUT-AMMA measurements the aircraft velocities were $135\,\mathrm{m\,s^{-1}}$ (young outflow case), $140\,\mathrm{m\,s^{-1}}$ (recent outflow case), and between $145\,\mathrm{m\,s^{-1}}$ and $157\,\mathrm{m\,s^{-1}}$ in the aged outflow. Thus, it can be assumed that the CIP has reliably reported the particles over its entire detection range, keeping also in mind the statement from Jensen et al. (2009, see Section A.4.1 above).

Percentage of shattering in te CIP data derived from adaption of the interarrival time criterion

In the analyses of the SCOUT-O3 and SCOUT-AMMA data the interarrival time rejection has always been applied to the whole data set of each flight including the subvisible cirrus cases. The shortest interarrival time encountered by the CIP measurements during the four SVC cases was $180\,\mu\mathrm{s}$ which is much larger than the interarrival time thresholds of $2.6\,\mu\mathrm{s}$ to $5\,\mu\mathrm{s}$ which were adopted for the respective data sets. A test to determine the number of erroneously removed particles due to the interarrival time criterion as suggested by Baumgardner (2011) was not possible since no particles were erroneously removed from the SVC cases. The shortest interarrival time encountered during the aged outflow events from 11 August was $1300\,\mu\mathrm{s}$ and thus, no particles have been rejected during these events.
In order to gain a feeling how many CIP images are rejected due to shattering, the fraction of shattered particles is calculated as percentage of the total number of particles detected by the CIP. The percentage itself does not give information about the particle sizes of the shattered artefacts. For the SCOUT-AMMA data over $85\,\%$ of the shattered particles are found in the smallest three size bins (i.e. particles smaller $175\,\mu\mathrm{m}$). Nevertheless, in cases with higher shattering there is no striking difference between the CIP size distributions that still contain the shattered particles compared to the ones with removed shattering, as Figure A.2 indicates. A period of measure-

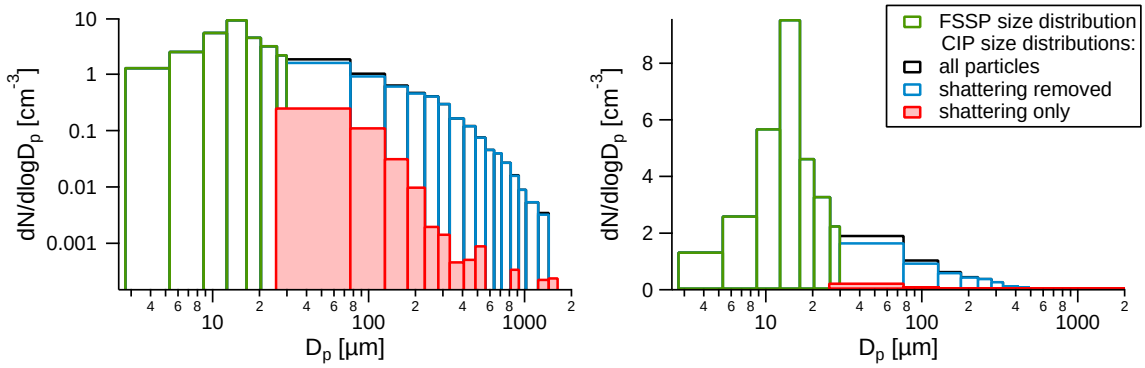

Figure A.2: Combined size distribution of CIP and FSSP-100 obtained during a period with high shattering on a flight through a convective anvil outflow on 7 August 2006. The black bars show the size distribution that is not corrected for shattering. The blue one is shattering corrected. The red bars show the size distribution of solely shattered particles, as identified by the CIP using the interarrival time technique.

ments in a dense convective anvil outflow cloud has been chosen that contained high number concentrations of particles. For this case, the size distribution of purely shattered particles is displayed (red) in order to show the contribution of shattering to the measurements. The black size distribution is obtained using the particle data including shattering artefacts and the blue curve shows the size distribution for the data with removed shattering. The difference between the black and blue size distribution (i.e. $0.26\,\mathrm{cm}^{-3}$ in the first CIP size bin) is almost not visible, no matter if displayed on a logarithmic (left panel) or linear scale (right panel). This shows that even at times with a high amount of shattering the size distributions are not affected significantly. For the most part the difference probably is within the limits of uncertainty due to counting statistics and the sample volume. The overlap of FSSP-100 and CIP is good even though about $10\,\%$ of the detected particles by the CIP result from shattering. In case that more than $10\,\%$ shattering is observed by the CIP, the FSSP part of the combined size distributions is indicated as probably affected by shattering by a shading.

A.4.3 General treatment of FSSP-100 data: Application of the T-matrix method

In principle the size bins from the T-matrix model of the FSSP (models 300 and 100) scattering geometries after Borrmann et al. (2000a) can be used. However, the adopted T-matrix code does not converge anymore for particles with sizes above $16\,\mu\mathrm{m}$ diameter. The FSSP-100 data used in this thesis extend from $2.7\,\mu\mathrm{m}$ to $29.2\,\mu\mathrm{m}$. Based on the T-matrix method this range could be subdivided into 15 bins including three bins from $16\,\mu\mathrm{m}$ to $29.2\,\mu\mathrm{m}$. It needs to be assumed that the T-matrix results can be extrapolated to these last three bins. In practice, the size range from $2.7\,\mu\mathrm{m}$ to $29.2\,\mu\mathrm{m}$ covered by the FSSP-100 here is subdivided only into 7 bins. This artificial reduction of the size resolution was done by carefully inspecting the corresponding scattering cross sections from the Mie- and the T-matrix curves and defining the bin limits manually. The reason is, that in fact it is difficult to apply the FSSP-100 for ice particles and that the T-matrix method only can serve to demonstrate -within narrow limits- that it is not impossible to measure inside cirrus. (This was the original

intent of the Borrmann et al., 2000a, publication.) To be conservative and reduce potential crossensitivity, where particles are counted into bins they do not belong to, the size resolution was decreased from 15 to 7 bins. For the subvisible cirrus data the counting statistics mostly is not good, such that a further reduction of the size resolution to only six bins is justified even more. In summary, the T-matrix scattering cross section curves are used but the size resolution was decreased to one half of the theoretically possible number of bins.

A.4.4 Removal of shattering artefacts

The Mainz CIP probe tips have been designed to minimise shattering (sharp edges). However, this design is not as sophisticated as the designs described by Korolev et al. (2011). In contrast, the FSSP-100 probe tips have a different design which certainly leads to a higher shattering probability. Unfortunately, the FSSP-100 does not provide single particle information (as arrival times). Thus, an interarrival time threshold for removing shattering artefacts (as for the CIP, c.f. Section 2.4.7) can not be applied. However, with the interarrival time technique time periods can be identified from the CIP data for which measurements are affected by shattering. In case that there is very little or no shattering evident in the CIP data, shattering is assumed to be within the instrument uncertainty (i.e. $20\,\%$) for FSSP-100 data. In these cases the size distributions of both instruments show a good agreement for the size range in which both instruments overlap. Such a good agreement, however, was not always obtained. Especially during certain flight manoeuvres (e.g. high climb rates or acute turns) of the aircraft the overlap range of the two instruments was found to disagree.

Rejection of data based on poor overlap between FSSP-100 and CIP size distribution

Such cases of poor overlap always exhibit much higher FSSP-100 concentrations in the last two bins than the CIP in its first bin. The CIP is considered as reporting the correct concentrations (after application of the state-of-the-art corrections), because unlike for the FSSP-100 there are tools like interarrival time analyses available for identification of shattering events. If both instruments exhibit overlap within their error bars, the FSSP data are considered not to be significantly influenced by shattering.
Nevertheless, the volume of data that had to be rejected based on poor overlap is rather small. All relevant measurements for this study were obtained at potential temperatures above $345\,\mathrm{K}$ and poor overlaps were mostly found below this level. Data from below roughly $10\,\mathrm{km}$ are not shown in this thesis except for the time series of 16 August and the corresponding size distributions (Section 4.2.4, Figures 4.11 and 4.12). From the measurements above $345\,\mathrm{K}$, only three size distributions needed to be discarded. Specifically, on the flight on 8 August one and on the flight on 11 August only two size distributions (accumulated from time periods of 10 and 20 seconds, respectively) were removed at potential temperatures between $345\,\mathrm{K}$ and $346\,\mathrm{K}$. Thus, only the lowest potential temperature bin in Figure 7.5 (lowest panel) is affected from such rejection. Data obtained in the outflow regions on 7 August and 16 August and in the subvisible cirrus cases are not affected by data rejection due to poor overlap.

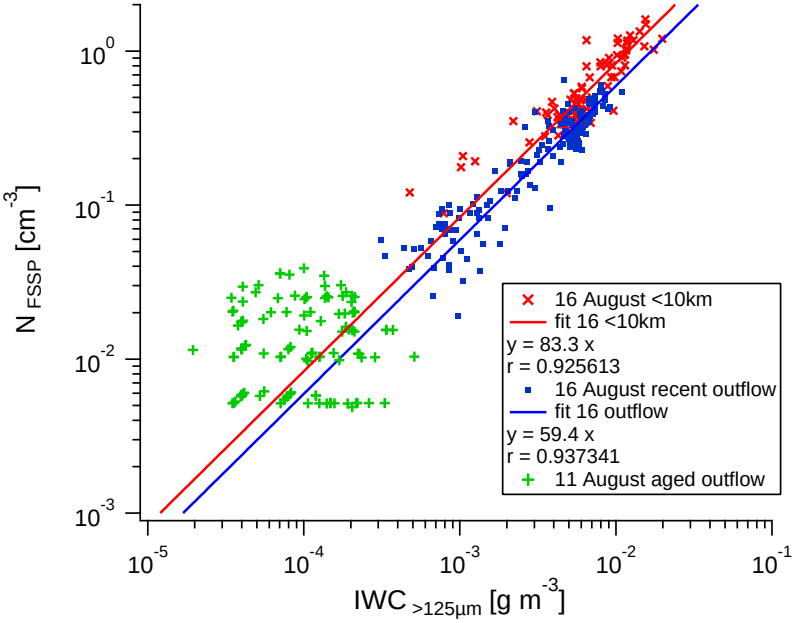

Figure A.3: Correlation analysis of small particle number concentrations (N_{FSSP}) and large particle (D_p <125 μm) IWC following Jensen et al. (2009). Displayed are cloud events from the SCOUT-AMMA flights on 11 and 16 August 2006. See text for further explanations.

Furthermore, due to the Double Particles problem some data shortly before and during the MCS outflow crossing on 7 August was lost (c.f. Remark on Double Particles in Table A.2). This lost data should also have been measured at the lowest considered potential temperatures ($345\,\mathrm{K}$–$350\,\mathrm{K}$). The measurements obtained in the outflow regions on 16 August and 11 August, in the subvisible cirrus cases, and during the SCOUT-O3 campaign are not affected by this problem.
“Poor overlap conditions” seem to occur preferably when the Geophysica performs particular manoeuvres like narrow turns. It has to be borne in mind that good overlaps between aircraft borne aerosol instruments of such different nature are all but common occurrence. For example the agreement in the overlapping size ranges of the FCAS and FSSP-300 instruments deployed on the ER-2 in conditions, which are simple by comparison, namely within the stratospheric Pinatubo aerosol, was much worse (Wilson et al., 1993; Jonsson et al., 1995).

Small crystal concentration - large crystal mass correlations

In order to identify measurements potentially affected by shattering Jensen et al. (2009) suggest to perform an analysis using correlations between large particle IWC and small particle number concentrations. Figure A.3 shows the concentration of FSSP particles vs. IWC from the CIP particles larger $125\,\mu\mathrm{m}$ for the flights from 11 and 16 August 2006. The data from 11 August (green crosses) are from inside and the vicinity of aged outflow events, and show no correlation. This follows the expectation of Jensen et al. (2009) for aged clouds in case shattering is not significant. By contrast, Jensen et al. (2009) do expect a correlation for young ice clouds based on microphysical arguments. Furthermore, they anticipate such a correlation in case shattering introduces significant amounts of artefacts. Indeed, the measurements

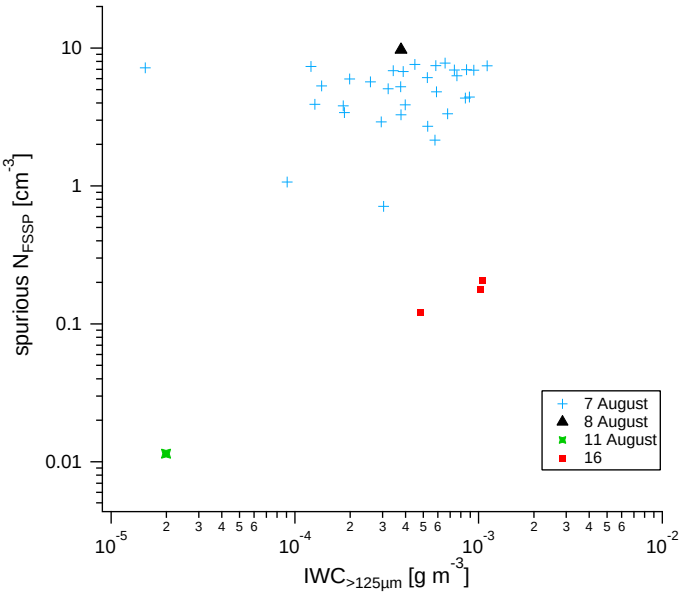

Figure A.4: Correlation analysis of spurious small particle number concentrations (spurious N_{FSSP}) and large particle (D_p $<125\,\mu\mathrm{m}$) IWC. Displayed are data from the SCOUT-AMMA flights. See text for further explanations.

from 16 August in young clouds and recent outflow (blue dots) also exhibit such a correlation. More shattering has been detected by the CIP for the cloud measurements below $10\,\mathrm{km}$ (red x), and the red data points (plus line) indicate a stronger slope of the correlation compared to the recent outflow case in blue data points and line (note the log scales and the absolute difference in the coefficients for the slopes). The young cloud data of 7 August show a similar figure as those from the 16 August but exhibit a somewhat worse correlation. Thus, the analysis confirms the expectations of Jensen et al. (2009).
In order to quantify possible shattering Jensen et al. (2009) suggested a further step for analysis. They applied five different filter criteria to their CAS data to find enhanced, spurious concentrations due to shattering. As can be seen in Figure A.4 there are only very few measurements left in the data after this filtering is applied. For 7 August, only, enough data points (light blue) remain after the filtering to perform a correlation analysis. However, only a poor correlation results with a Pearson coefficient of 0.05, which indicates that the few spurious particles do not depend on IWC, i.e. the presence of the largest particles. Thus, shattering seems to have not impacted the measurements to a significant amount. In summary the data confirm the assumption of Jensen et al. (2009), according to which (1.) in young outflow scenarios a correlation between the IWC from particles with sizes above $125\,\mu\mathrm{m}$ and the number densities of small particles is present, (2.) no correlation in SVC and aged outflows can be found, and (3.) not as much alarming data points survive the filtering as was the case for the CAS.

In summary, a careful analysis of the data was conducted for this thesis in order to remove contamination of shattering artefacts. This led to the removal of some measurements from the data base and cases of doubt are properly marked in the figures.

Appendix B

Experimental setup

Table B.1: Instrumentation of the M55 Geophysica during SCOUT-O3 and SCOUT-AMMA campaign.

Instrument	Measured parameter	Technique	Reference
in situ chemistry			
ALTO	CH_4	laser spectrometry	D'Amato et al. (2002)
COLD	CO	laser spectrometry	Viciani et al. (2008)
FISH	H_2O (total)	Lyman-α fluorescence hygrometer	Zöger et al. (1999)
FLASH	H_2O (gas phase)	Lyman-α fluorescence hygrometer	Sitnikov et al. (2007)
FOZAN	O_3	chemiluminescence	Yushkov et al. (1999)
HAGAR	N_2O, H_2, CH_4, SF_6, CFC-11, CFC-12, Halon-1211	gas chromatography	Volk et al. (2000)
HAGAR-CO_2	CO_2	IR absorption	Volk et al. (2000)
HALOX	ClO, BrO, $ClONO_2$	chemical conversion resonance fluorescence,	von Hobe et al. (2005)
SIOUX	NO, NO_y	chemiluminescence	Voigt et al. (2005)
WAS	long- and short-lived source gases, trace gas isotopes	whole air sampler	Franz and Röckmann (2005)
remote sensors			
CHRISTA-NF	O_3, H_2O, CO, HNO_3, N_2O	mid-IR spectrometry	Spang et al. (2008)
MARSHALS	O_3, H_2O, CO, HNO_3, N_2O	FTS limb-sounding millimetre spectrometer	
MIPAS	limb-scan profiles of T, H_2O, O_3, CFCs and nitrogen species	mid-IR spectroscopy (passive)	Fischer et al. (2008)

Table B.1: *continued*

Instrument	Measured parameter	Technique	Reference
cloud/aerosol particles			
CIP	cloud particles	Particle shadow cast	de Reus et al. (2009)
COPAS	condensation nuclei	CPC	Weigel et al. (2009)
FSSP	cloud particles	Mie scattering	Dye and Baumgardner (1984)
MAL	remote particle backscatter and depolarisation profile ($2\,\mathrm{km}$ from aircraft altitude)	microjoule-lidar	Mitev et al. (2002)
MAS	particle backscatter and depolarisation	backscattersonde	Buontempo et al. (2006)
meteorology			
MTP	temperature and pressure profiles	passive microwave radiometer	Denning et al. (1989)
TDC	ambient temperature, pressure, and wind	PT500, 5-hole probe	Shur et al. (2007)

B.1 Campaign flight overview

Table B.2: Flight objectives and CIP data status during SCOUT-O3.

Date	Flight objective	Data status
12 Nov 2005	Transfer	no data
16 Nov 2005	Hector, upwind survey, anvil	no data
19 Nov 2005	cirrus, Hector	no data
23 Nov 2005	TTL survey	no data
25 Nov 2005	cirrus, late Hector	
28 Nov 2005	M55 aborted, outflow of Hector	highest flight altitude $11.3\,\mathrm{km}$
29 Nov 2005	Mesoscale Convective System	clouds during ascent and descent
30 Nov 2005a	Hector	convective overshoot, stratospheric ice particles
30 Nov 2005b	post Hector, cirrus	
5 Dec 2005	TTL survey, remote sensing	no data
9 Dec 2005	Transfer	

Table B.3: Flight objectives and CIP data status during SCOUT-AMMA.

Date	Flight objective	Data status
31 Jul 2006	Transfer Verona-Marrakesh	not on board
1 Aug 2006	Transfer Marrakesh-Ouagadougou	not on board
4 Aug 2006	Long range transport	not on board
7 Aug 2006	MCS close up	MCS young outflow, in situ cirrus
8 Aug 2006	CALIPSO validation	MCS outflow, in situ cirrus
11 Aug 2006	MCS aged outflow	MCS aged outflow
13 Aug 2006	Long range transport	low clouds
16 Aug 2006	Transfer Ouagadougou-Marrakech	MCS young outflow
17 Aug 2006	Transfer Marrakech-Verona	no clouds

Appendix C

Database

In the following the additional figures are displayed, representing the data base of the analysed flights for reference purpose. Thus, vertical profiles including the SCOUT-AMMA MCS outflow measurements as well as the complete time series for the MCS outflow, SVC, and convective overshoot probings are presented.

C.1 MCS outflow

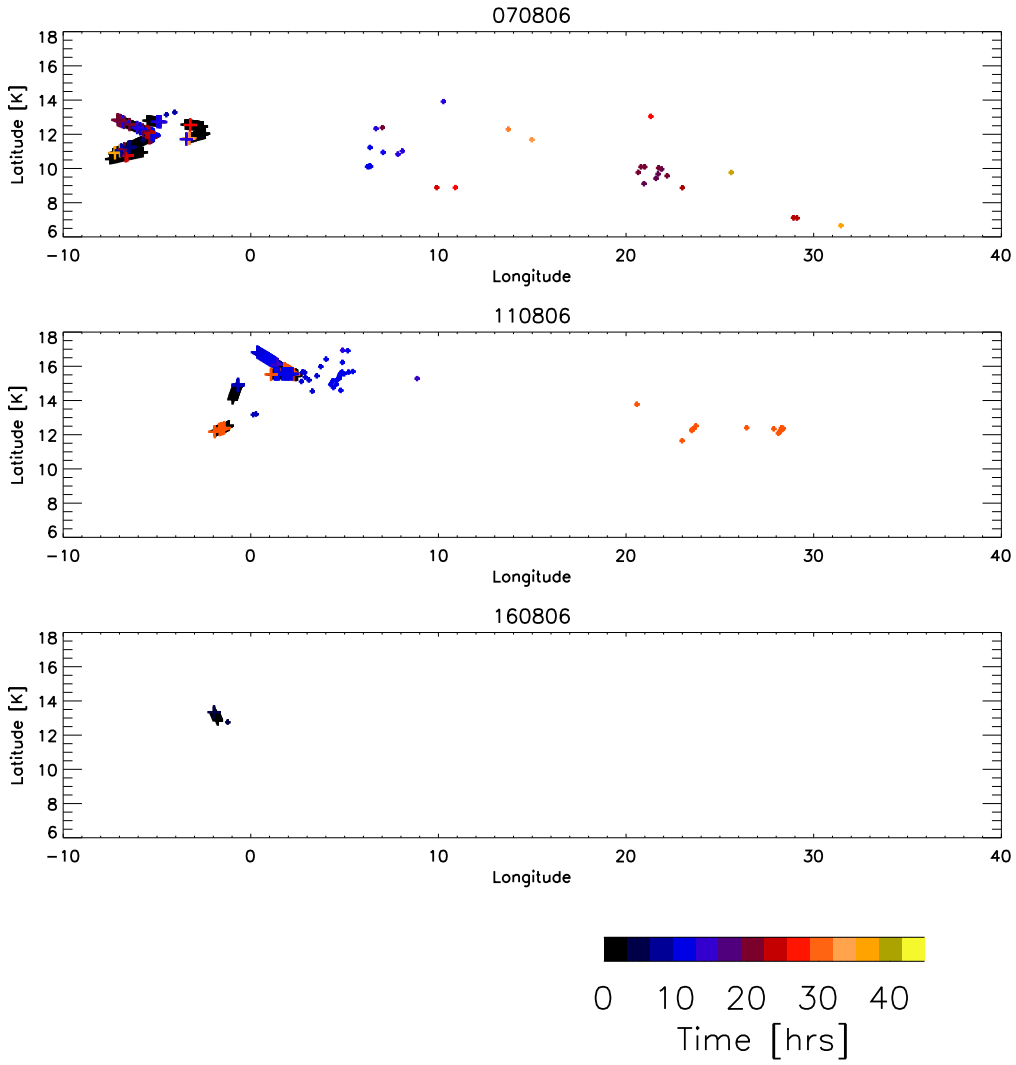

Figure C.1: MSG observations and ECMWF trajectories for the 7, 11, and 16 Aug 2006. MSG observations of deep convective clouds are shown as light crosses, the colour indicates the time before flight. The points where trajectories intersecting MCS in the past are highlighted on the flight path. (Courtesy of F. Fierli)

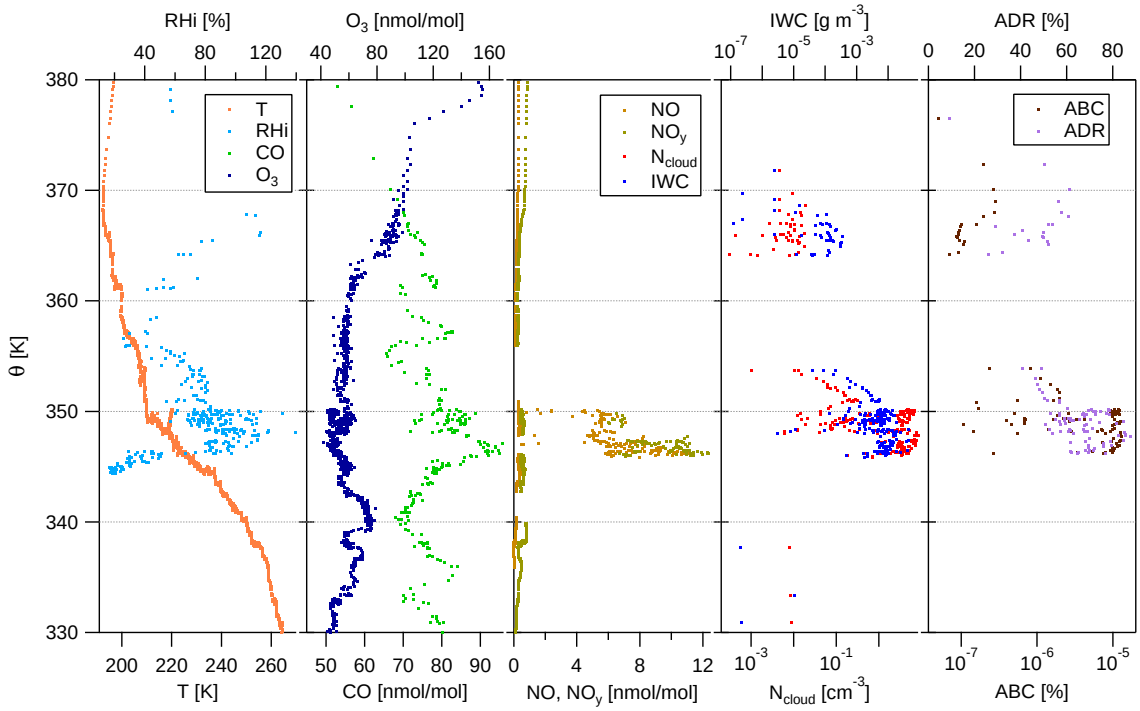

Figure C.2: Vertical profiles obtained during the descent of the measurement flight on 7 Aug 2006.

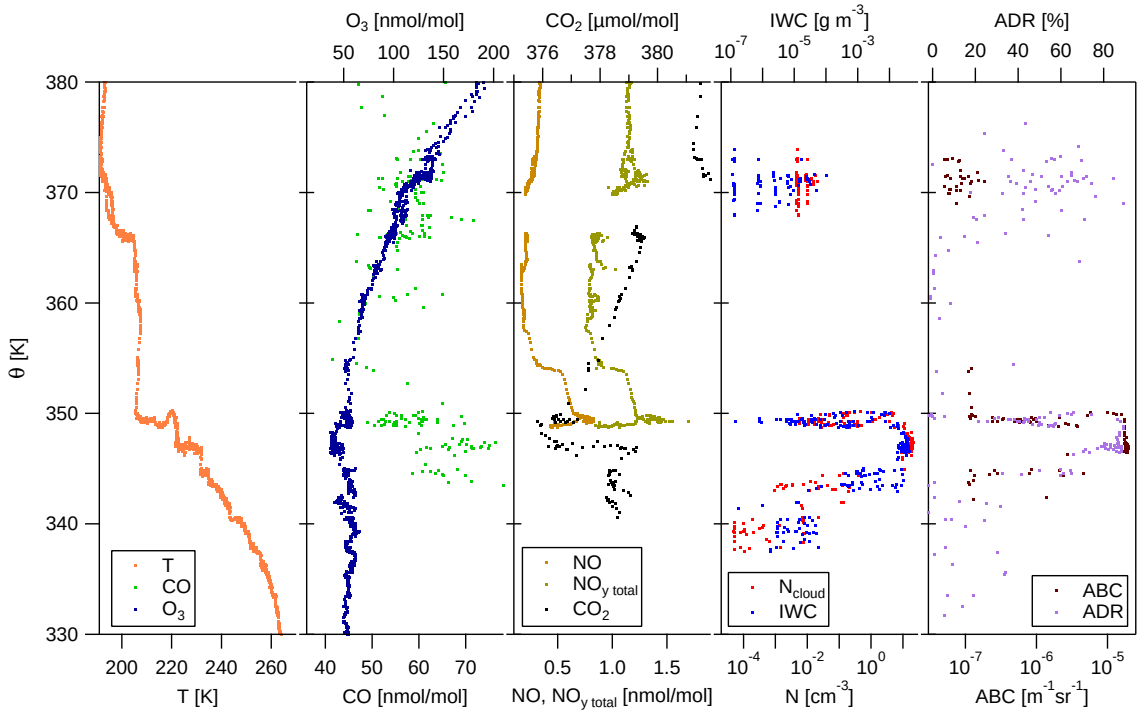

Figure C.3: Vertical profiles obtained during the ascent of the measurement flight on 8 Aug 2006.

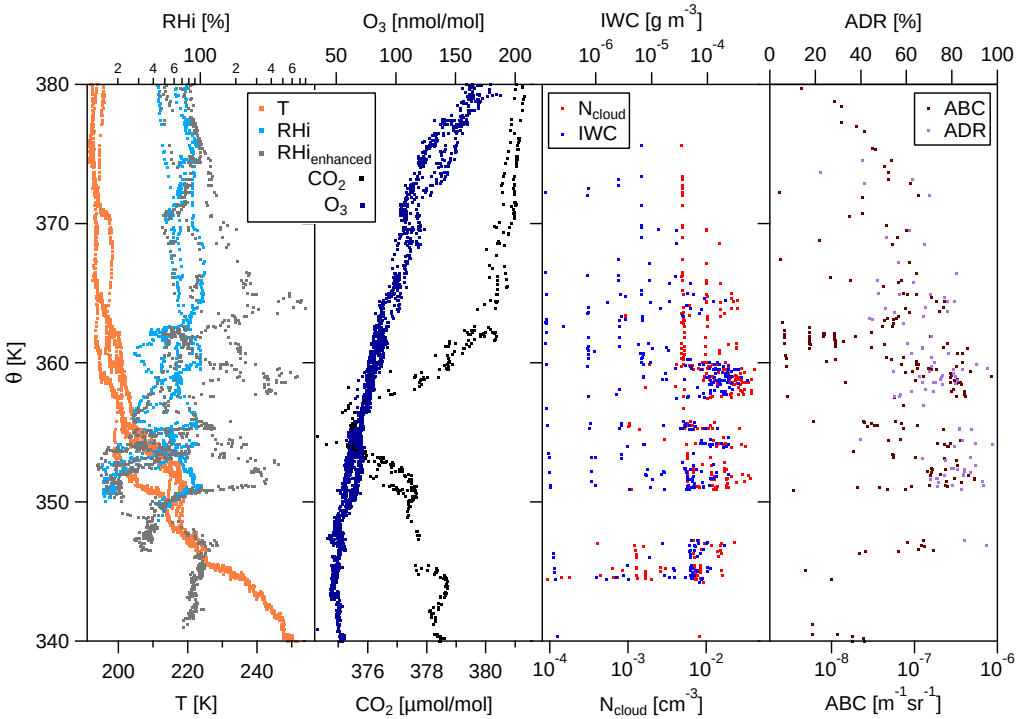

Figure C.4: Vertical profiles obtained during the outflow phases of the measurement flight on 11 Aug 2006.

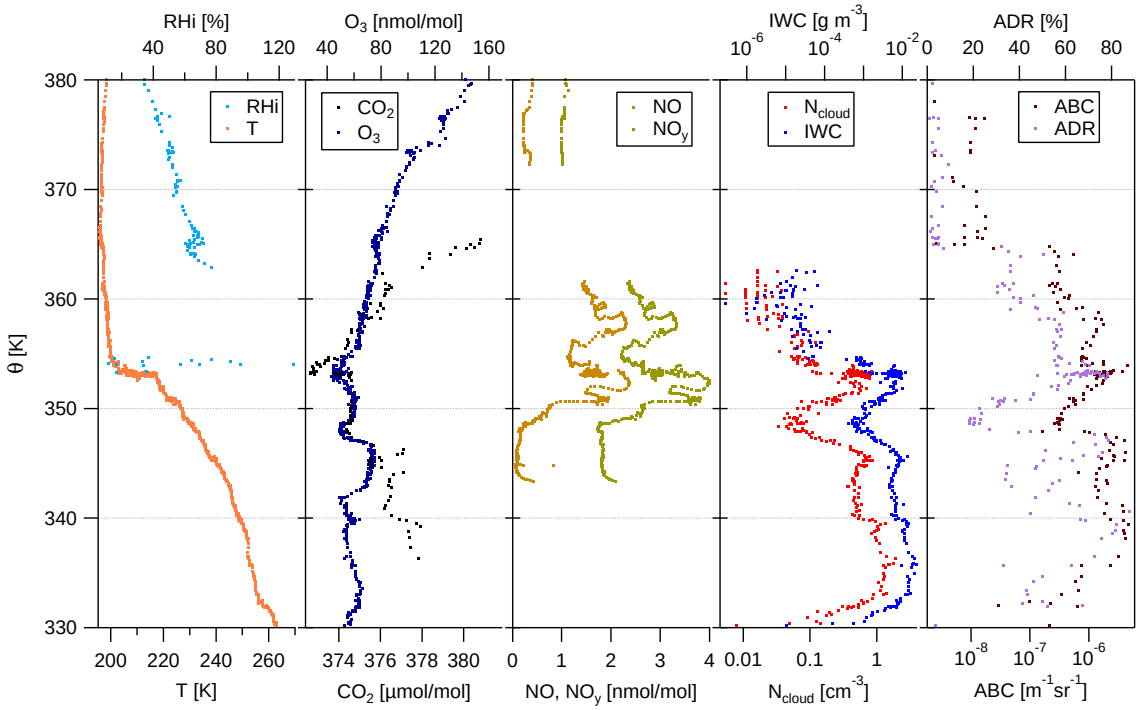

Figure C.5: Vertical profiles obtained during the ascent of the measurement flight on 16 Aug 2006.

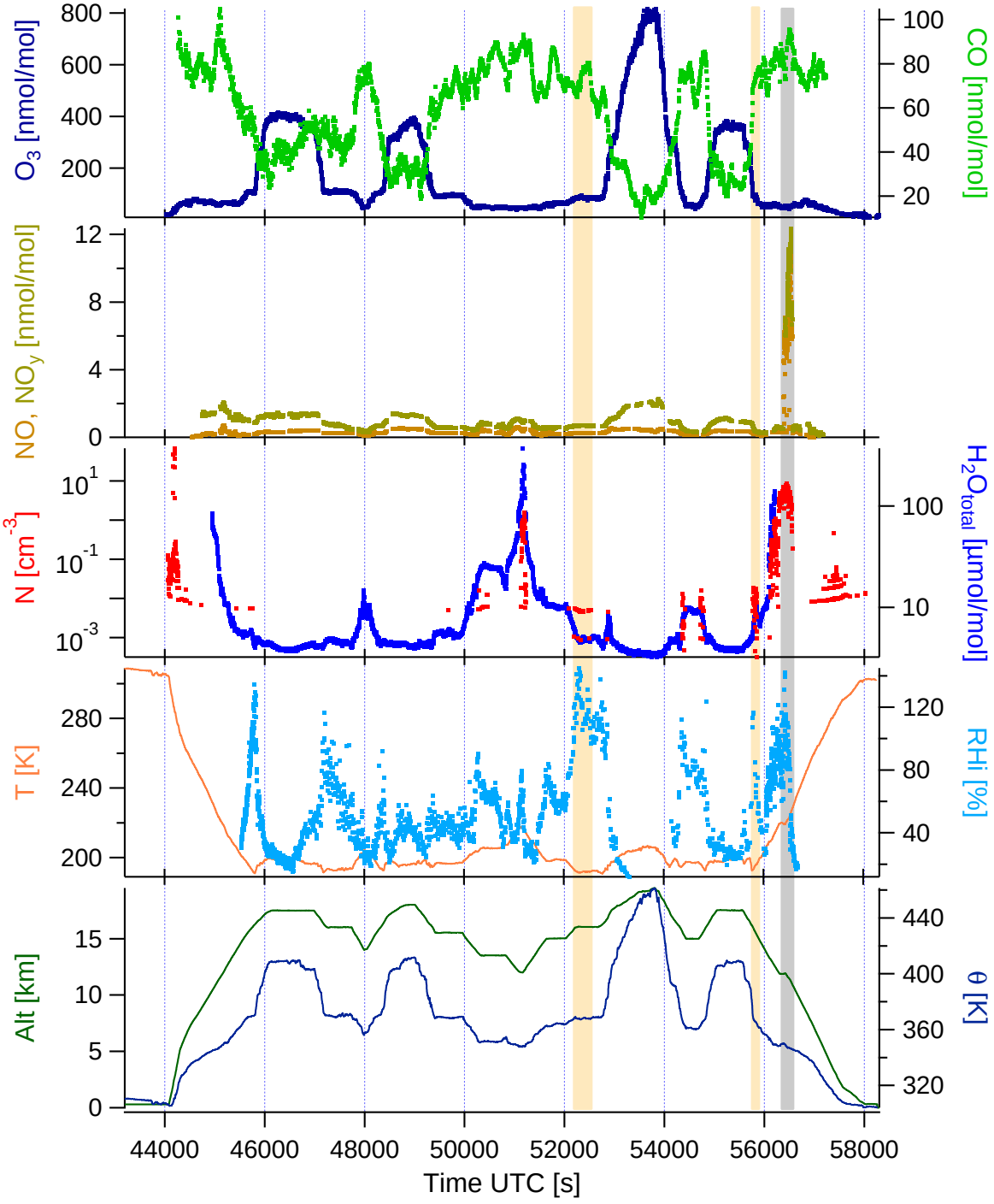

Figure C.6: Time series of the measurement flight on 7 Aug 2006.

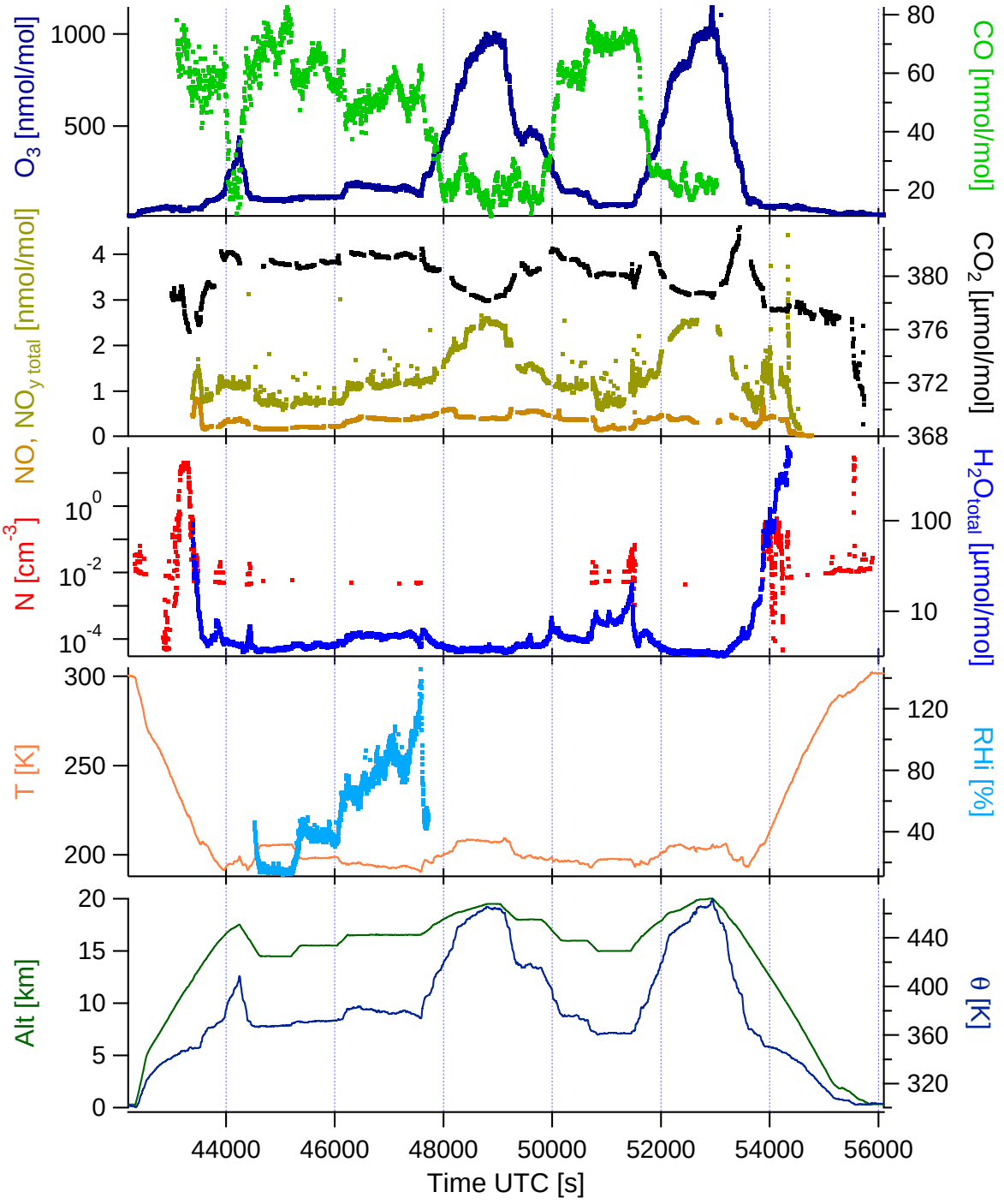

Figure C.7: Time series of the measurement flight on 8 Aug 2006.

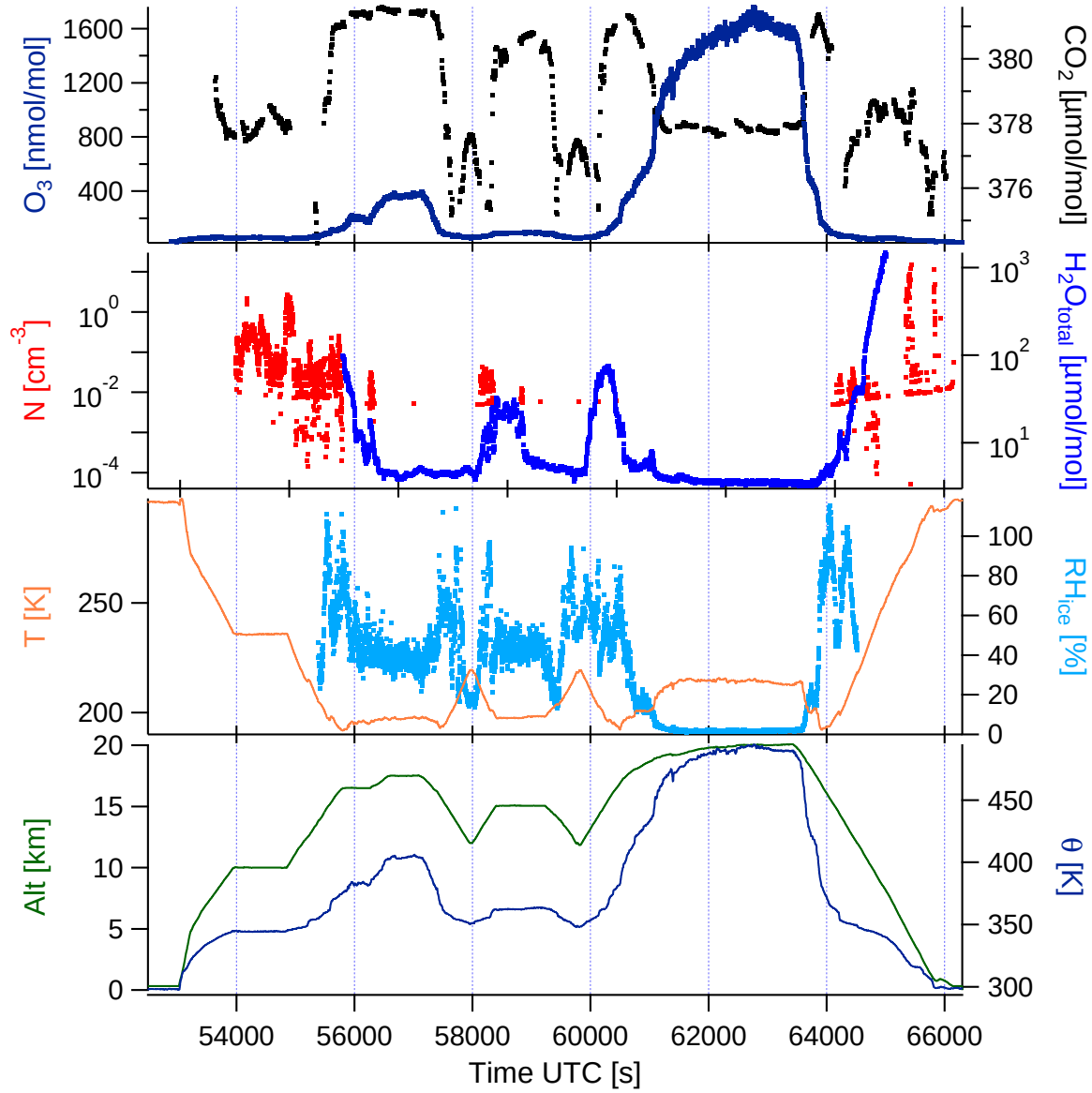

Figure C.8: Time series of the measurement flight on 11 Aug 2006.

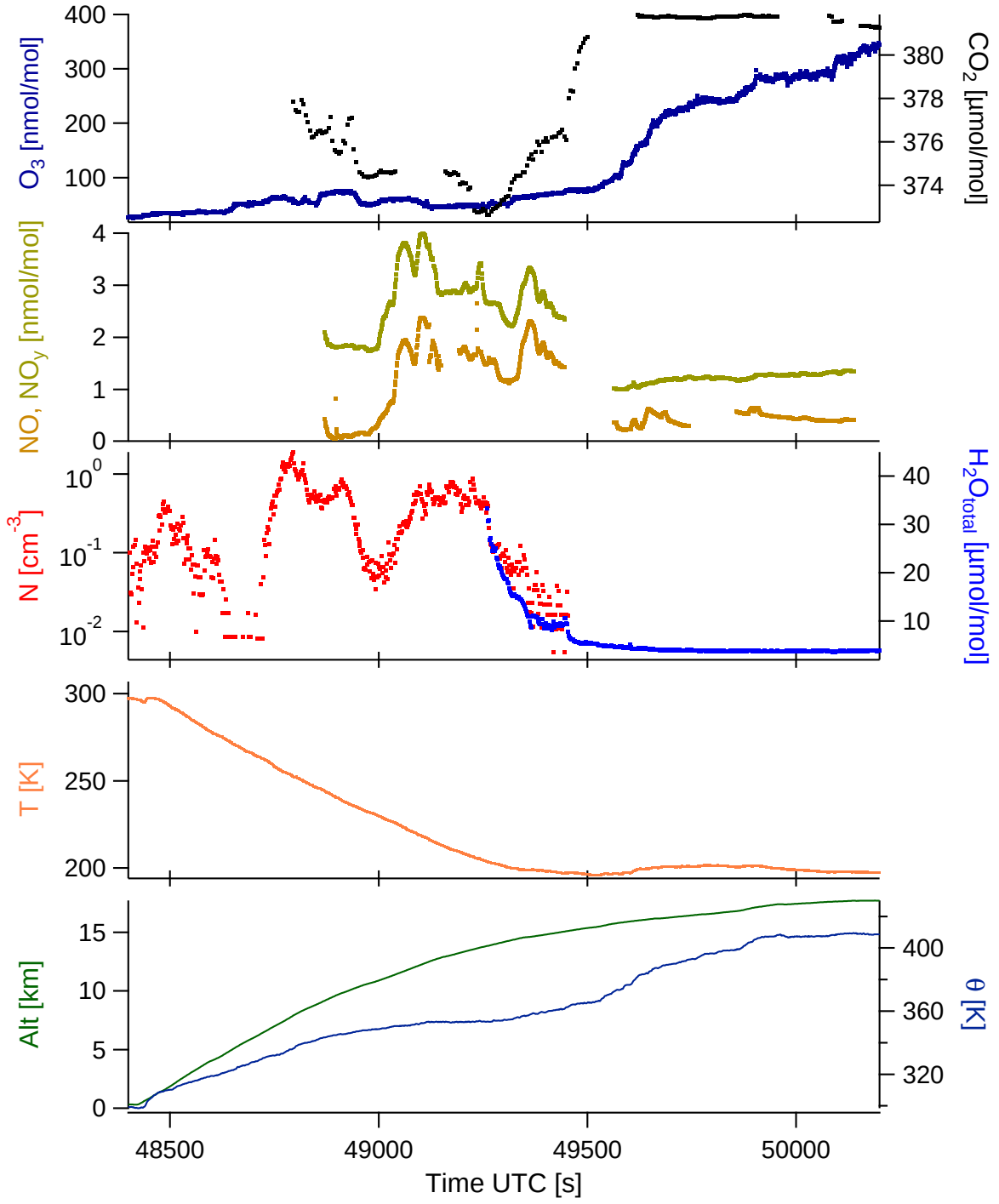

Figure C.9: Time series of the measurement flight on 16 Aug 2006.

C.2 Convective overshoots

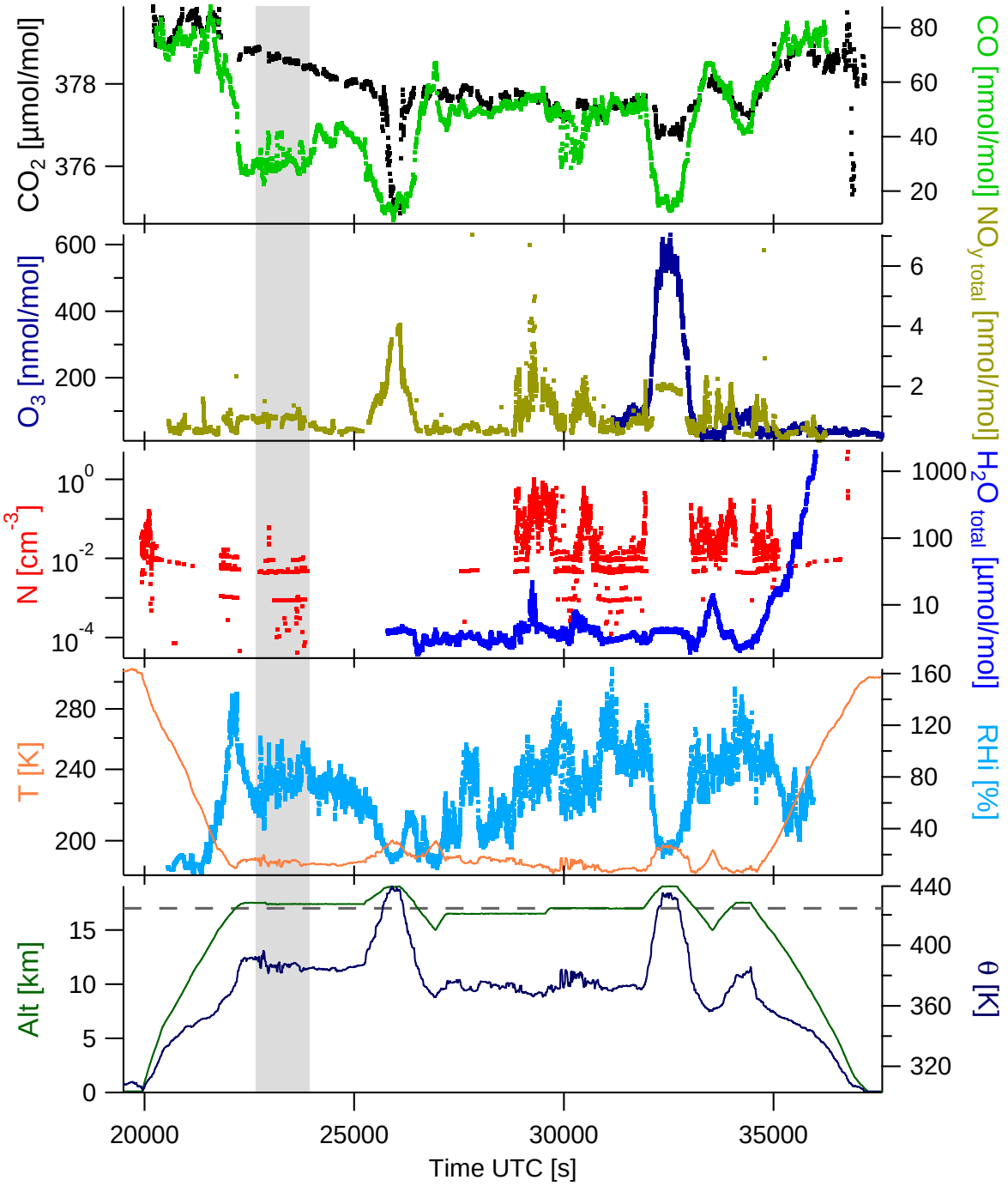

Figure C.10: Time series of measurement flight on 29 Nov 2005. The grey dashed line indicates the cold point tropopause height, the grey shading indicates the time period during which ice particles have been observed in the stratosphere.

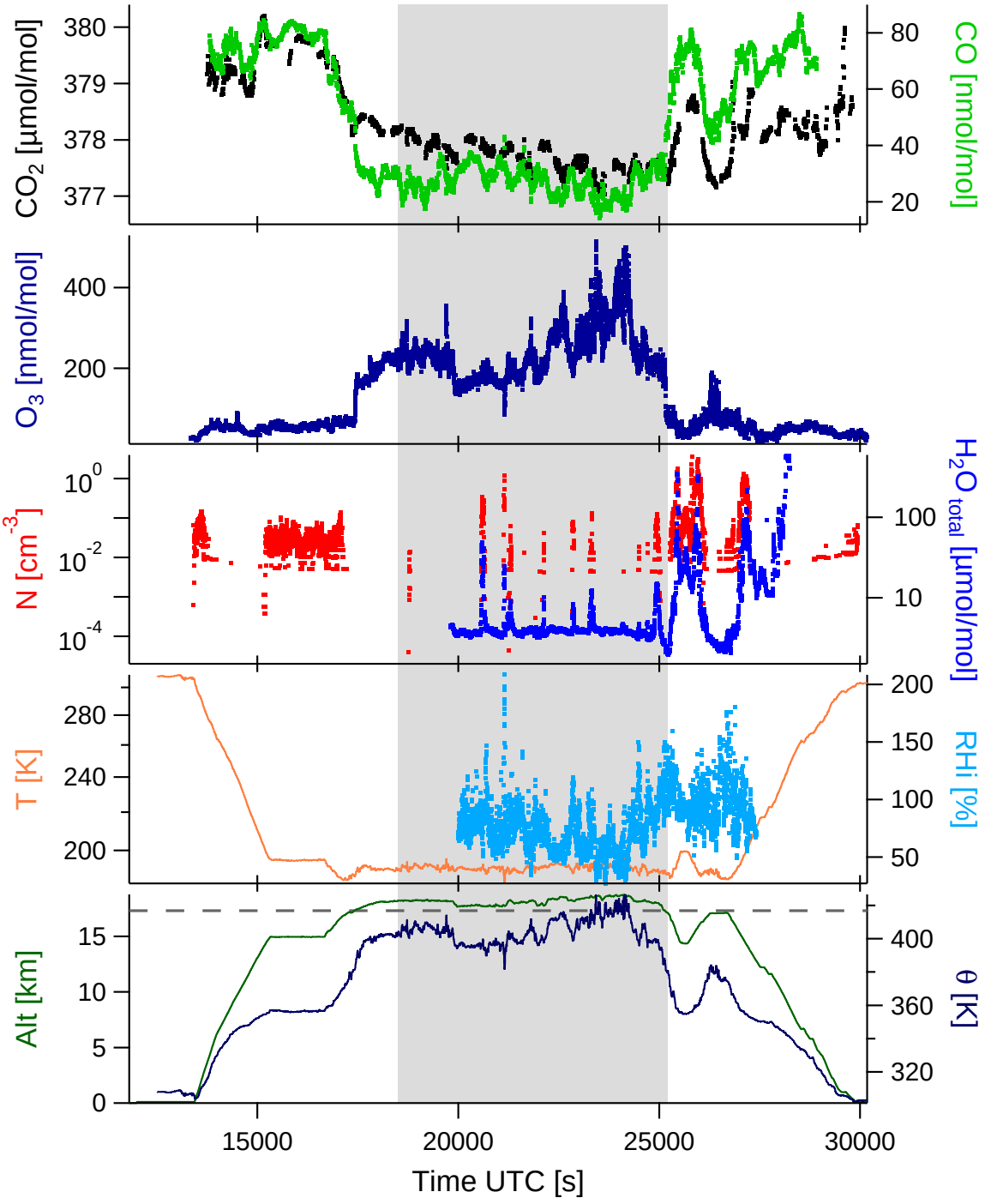

Figure C.11: Time series of meteorological parameters for the first flight on 30 Nov 2005. The grey dashed line indicates the cold point tropopause height, the grey shading indicates the time period shown in Figure 5.6.

List of Publications

The following publications have appeared in or were submitted to peer reviewed journals during the time of my doctorate and reflect to a large part results or applied methods from this thesis.

Cairo, F., Di Donfrancesco, G., Snels, M., Fierli, F., Viterbini, M., Borrmann, S., and **Frey, W.**: A comparison of light backscattering and particle size distribution measurements in tropical cirrus clouds, Atmos. Meas. Tech., 4, 557–570, doi:10.5194/amt-4-557-2011, 2011.

Davis, S., Hlavka, D., Jensen, E., Rosenlof, K., Yang, Q., Schmidt, S., Borrmann, S., **Frey, W.**, Lawson, P., Voemel, H., and Bui, T. P.: In situ and lidar observations of tropopause subvisible cirrus clouds during TC4, J. Geophys. Res., 115, D00J17, doi:10.1029/2009JD013093, 2010.

de Reus, M., Borrmann, S., Bansemer, A., Heymsfield, A. J., Weigel, R., Schiller, C., Mitev, V., **Frey, W.**, Kunkel, D., Kürten, A., Curtius, J., Sitnikov, N. M., Ulanovsky, A., and Ravegnani, F.: Evidence for ice particles in the tropical stratosphere from in-situ measurements, Atmos. Chem. Phys., 9, 6775–6792, doi:10.5194/acp-9-6775-2009, 2009.

Drüe, C., **Frey, W.**, Hoff, A., and Hauf, T.: Aircraft type-specific errors in AMDAR weather reports from commercial aircraft, Q. J. Roy. Meteor. Soc., 134, 229–239, doi:10.1002/qj.205, 2008.

Frey, W., Eichler, H., de Reus, M., Maser, R., Wendisch, M., and Borrmann, S.: A new airborne tandem platform for collocated measurements of microphysical cloud and radiation properties, Atmos. Meas. Tech., 2, 147–158, doi:10.5194/amt-2-147-2009, 2009.

Frey, W., Borrmann, S., Kunkel, D., Weigel, R., de Reus, M., Schlager, H., Roiger, A., Voigt, C., Hoor, P., Curtius, J., Krämer, M., Schiller, C., Volk, C. M., Homan, C. D., Fierli, F., Di Donfrancesco, G., Ulanovsky, A., Ravegnani, F., Sitnikov, N. M., Viciani, S., D'Amato, F., Shur, G. N., Belyaev, G. V., Law, K. S., and Cairo, F.: In-situ measurements of tropical cloud properties in the West African monsoon: upper tropospheric ice clouds, mesoscale convective system outflow, and subvisual cirrus, Atmos. Chem. Phys. Discuss., 11, 745–812, doi:10.5194/acpd-11-745-2011, 2011.

Voigt, C., Schumann, U., Jurkat, T., Schäuble, D., Schlager, H., Petzold, A., Gayet, J.-F., Krämer, M., Schneider, J., Borrmann, S., Schmale, J., Jessberger, P., Hamburger, T., Lichtenstern, M., Scheibe, M., Gourbeyre, C., Meyer, J., Kübbeler,

M., **Frey, W.**, Kalesse, H., Butler, T., Lawrence, M. G., Holzäpfel, F., Arnold, F., Wendisch, M., Döpelheuer, A., Gottschaldt, K., Baumann, R., Zöger, M., Sölch, I., Rautenhaus, M., and Dörnbrack, A.: In-situ observations of young contrails – overview and selected results from the CONCERT campaign, Atmos. Chem. Phys., 10, 9039–9056, doi:10.5194/acp-10-9039-2010, 2010.

von Hobe, M., Grooß, J.-U., Günther, G., Konopka, P., Gensch, I., Krämer, M., Spelten, N., Afchine, A., Schiller, C., Ulanovsky, A., Sitnikov, N., Shur, G., Yushkov, V., Ravegnani, F., Cairo, F., Roiger, A., Voigt, C., Schlager, H., Weigel, R., **Frey, W.**, Borrmann, S., Müller, R., and Stroh, F.: Evidence for heterogeneous chlorine activation in the tropical UTLS, Atmos. Chem. Phys., 11, 241–256, doi:10.5194/acp-11-241-2011, 2011.

Weigel, R., Borrmann, S., Kazil, J., Minikin, A., Stohl, A., Wilson, J. C., Reeves, J. M., Kunkel, D., de Reus, M., **Frey, W.**, Lovejoy, E. R., Volk, C. M., Viciani, S., D'Amato, F., Cairo, F., Schlager, H., Law, K. S., Shur, G. N., Belyaev, G. V., and Curtius, J.: In situ observations of new particle formation in the tropical upper troposphere: the role of clouds and the nucleation mechanism, Atmos. Chem. Phys. Discuss., 11, 9249–9312, doi:10.5194/acpd-11-9249-2011, 2011.

Conference contributions

Talks

Borrmann, S., Weigel, R., Kazil, J., Minikin, A., Stohl, A., Wilson, J. C., Kunkel, D., de Reus, M., **Frey, W.**, Lovejoy, E. R., Volk, C. M., Viciani, S., Cairo, F., Law, K. S., Curtius, J. and Team: The role of clouds and of neutral as well as ion induced pathway for the new particle formation in the tropical upper troposphere: In-situ measurements from continental South America and West Africa, *EGU General Assembly*, Vienna, Austria, 3 - 8 Apr 2011

Weigel, R., Ebert, M., Molleker, S., **Frey, W.**, Gunter, G., Volk, C. M., Schlager, H., Cairo, F., Di Donfrancesco, G., Borrmann, S.: The abundance, shape and chemical composition of non-volatile particles in the Arctic winter Stratosphere and their potential activation by Polar Stratospheric Cloud elements, *EGU General Assembly*, Vienna, Austria, 3 - 8 Apr 2011

Borrmann, S. and **Frey, W.** and the SCOUT-AMMA science Team: In-situ measurements of tropical cloud properties in the West African Monsoon: Upper tropospheric ice clouds, Mesoscale Convective System outflow, and subvisual cirrus, *EGU General Assembly*, Vienna, Austria, 3 - 8 Apr 2011

Frey, W., Borrmann, S., Kunkel, D., Weigel, R., Schlager, H., Ulanovsky, A., Schiller, C., Sitnikov, N. M., Ravegnani, F., Volk, C. M., Shur, G. N., Belyaev, G. V., Vicani, S., Voigt, C., Law, K. S., Cairo, F.: In-situ ice particle measurements in the UT/LS and in mesoscale convective system outflows during the West-African Monsoon, *13th AMS Conference on Cloud Physics*, Portland, Oregon, USA, 28 Jun - 2 Jul 2010.

von Hobe, M. and the **RECONCILE Science Team**: Project Overview RECONCILE and first Results, *EGU General Assembly*, Vienna, Austria, 2 - 7 May 2010

Frey, W., de Reus, M., Eichler, H., Maser, R., Wendisch, M. and Borrmann, S.: A new airborne tandem measurement platform for cloud-radiation interaction studies: The AIRcraft Towed Sensor Shuttle (AIRTOSS), *EMS Annual Meeting 2009, & European Conference on Applications of Meteorology (ECAM)*, Toulouse, France, 28 Sep - 2 Oct 2009.

Borrmann, S., Kunkel, D., **Frey, W.**, Law, K. S., Cairo, F., Some, L.: AMMA-SCOUT M55 data team, Aerosols and clouds in the tropical tropopause layer: In-situ measurements of microphysics and chemistry over West Africa, *Third AMMA International Conference*, Ouagadougou, Burkina Faso, 20 - 24 Jul 2009.

Posters

Poole, L. R., Pitts, M. C., **Frey, W.**, Molleker, S., Weigel, R. and Borrmann, S.: Comparison off PSC Measurements from CALIIPSO and the M–55 Geophysica During the 2010 RECONCIILE Field Campaign, *EGU General Assembly*, Vienna, Austria, 3 - 8 Apr 2011

Frey, W., de Reus, M., Borrmann, S., Schiller, C., Sitnikov, N. M., Ulanovsky, A., Ravegnani, F., Mahoney, M. J.: Measurements of ice particles in the UTLS during SCOUT and AMMA, *EGU General Assembly*, Vienna, Austria, 19 - 24 Apr 2009

Frey, W., de Reus, M., Eichler, H., Maser, R., Mey, B., Wendisch, M. and Borrmann, S.: AIRTOSS (AIRcraft Towed Sensor Shuttle): a tandem measurement platform for cloud-radiation studies, Poster, *15th International Conference On Cloud Physics and Precipitation*, Cancun, Mexico, 7 - 11 Jul 2008.

de Reus, M., Bansemer, A., **Frey, W.**, Vössing, H., Raupach, S., Schiller, C., Sitnikov, N., Heymsfield, A. and Borrmann, S.: In-situ measurements of ice crystals in the tropical stratosphere, *15th International Conference on Cloud Physics and Precipitation*, Cancun, Mexico, 7 - 11 Jul 2008.

Further oral presentations

Frey, W. and the M55 Geophysica data team: Wolkenpartikelmessungen auf dem Höhenforschungsflugzeug Geophysica, *Meteorological Colloquium*, Institute of Meteorology and Climatology, Leibniz University Hannover, Germany, 29 Apr 2010

Frey, W., Borrmann, S., Weigel, R., Molleker, S., Schneider, W., Böttger, T. and von Glahn, C.: FSSP observations of polar stratospheric clouds during RECONCILE, *RECONCILE Science Meeting*, Kiruna, Sweden, 8 - 9 Mar 2010

Frey, W., de Reus, M. and Borrmann, S.: Flugzeugmessungen in den Wolken, *Annual Symposium of the Excellence Cluster Geocycles*, Mainz, Germany, 17 Jun 2008

Frey, W., de Reus, M., Borrmann, S. and Bansemer, A.: Cloud microphysical measurements with the Cloud Imaging Probe (CIP), *IMPRS evaluation*, Mainz, Germany, 14 Mar 2008

Bibliography

Adler, R. F. and Mack, R. A.: Thunderstorm Cloud Top Dynamics as Inferred from Satellite Observations and a Cloud Top Parcel Model, J. Atmos. Sci., 43, 1945–1960, doi:10.1175/1520-0469(1986)043⟨1945:TCTDAI⟩2.0.CO;2, 1986.

Adriani, A., Cairo, F., Viterbini, M., Mandolini, S., Pulvirenti, L., and Di Donfrancesco, G.: Multiwavelength aerosol scatterometer for airborne experiments to study the optical properties of stratospheric aerosol, J. Atmos. Ocean. Tech., 16, 1329–1336, doi:10.1175/1520-0426(1999)016⟨1329:MASFAE⟩2.0.CO;2, 1999.

Alcala, C. M. and Dessler, A. E.: Observations of deep convection in the tropics using the Tropical Rainfall Measuring Mission (TRMM) precipitation radar, J. Geophys. Res. - Atmos., 107, 4792, doi:10.1029/2002JD002457, 2002.

Archer, D.: Fate of fossil fuel CO_2 in geologic time, J. Geophys. Res. - Oceans, 110, C09S05, doi:10.1029/2004JC002625, 2005.

Avery, M., Twohy, C., McCabe, D., Joiner, J., Severance, K., Atlas, E., Blake, D., Bui, T. P., Crounse, J., Dibb, J., Diskin, G., Lawson, P., McGill, M., Rogers, D., Sachse, G., Scheuer, E., Thompson, A. M., Trepte, C., Wennberg, P., and Ziemke, J.: Convective distribution of tropospheric ozone and tracers in the Central American ITCZ region: Evidence from observations during TC4, J. Geophys. Res., 115, D00J21, doi:10.1029/2009JD013450, 2010.

Bailey, M. P. and Hallett, J.: Growth Rates and Habits of Ice Crystals between $-20\,^{\circ}\mathrm{C}$ and $-70\,^{\circ}\mathrm{C}$, J. Atmos. Sci., 61, 514–544, doi:10.1175/1520-0469(2004)061⟨0514:GRAHOI⟩2.0.CO;2, 2004.

Bailey, M. P. and Hallett, J.: A Comprehensive Habit Diagram for Atmospheric Ice Crystals: Confirmation from the Laboratory, AIRS II, and Other Field Studies, J. Atmos. Sci., 66, 2888–2899, doi:10.1175/2009JAS2883.1, 2009.

Baker, B. and Lawson, R. P.: Improvement in Determination of Ice Water Content from Two-Dimensional Particle Imagery: Part I: Image-to-Mass Relationships, J. Appl. Meteorol. Clim., 45, 1282–1290, doi:10.1175/JAM2399.1, 2006.

Baran, A. J.: A review of the light scattering properties of cirrus, J. Quant. Spectrosc. Ra., 110, 1239–1260, doi:10.1016/j.jqsrt.2009.02.026, 2009.

Barnes, G.: Severe Convective Storms, vol. 28 of *AMS Meteorological Monograph Series*, chap. 10: Severe local storms in the tropics, pp. 358–432, AMS, 2001.

Barret, B., Ricaud, P., Mari, C., Attié, J.-L., Bousserez, N., Josse, B., Le Flochmoën, E., Livesey, N. J., Massart, S., Peuch, V.-H., Piacentini, A., Sauvage, B., Thouret, V., and Cammas, J.-P.: Transport pathways of CO in the African upper troposphere during the monsoon season: a study based upon the assimilation of spaceborne observations, Atmos. Chem. Phys., 8, 3231–3246, doi:10.5194/acp-8-3231-2008, 2008.

Barret, B., Williams, J. E., Bouarar, I., Yang, X., Josse, B., Law, K., Pham, M., Le Flochmoën, E., Liousse, C., Peuch, V. H., Carver, G. D., Pyle, J. A., Sauvage, B., van Velthoven, P., Schlager, H., Mari, C., and Cammas, J.-P.: Impact of West African Monsoon convective transport and lightning NO_x production upon the upper tropospheric composition: a multi-model study, Atmos. Chem. Phys., 10, 5719–5738, doi:10.5194/acp-10-5719-2010, 2010.

Baumgardner, D.: Interactive comment on Atmos. Chem. Phys. Discuss., 11, 745, 2011, 2011.

Baumgardner, D. and Korolev, A.: Airspeed Corrections for Optical Array Probe Sample Volumes, J. Atmos. Ocean. Tech., 14, 1224–1229, doi:10.1175/1520-0426(1997)014⟨1224%3AACFOAP⟩2.0.CO%3B2, 1997.

Baumgardner, D., Strapp, W., and Dye, J. E.: Evaluation of the Forward Scattering Spectrometer Probe. Part II: Corrections for Coincidence and Dead-Time Losses, J. Atmos. Ocean. Tech., 2, 626–632, doi:10.1175/1520-0426(1985)002⟨0626:EOTFSS⟩2.0.CO;2, 1985.

Baumgardner, D., Jonsson, H., Dawson, W., O'Connor, D., and Newton, R.: The cloud, aerosol and precipitation spectrometer: a new instrument for cloud investigations, Atmos. Res., 59, 251–264, doi:10.1016/S0169-8095(01)00119-3, 2001.

Bechara, J., Borbon, A., Jambert, C., Colomb, A., and Perros, P. E.: Evidence of the impact of deep convection on reactive Volatile Organic Compounds in the upper tropical troposphere during the AMMA experiment in West Africa, Atmos. Chem. Phys., 10, 10 321–10 334, doi:10.5194/acp-10-10321-2010, 2010.

Bergeron, T.: On the physics of cloud and precipitation, in: Proceedings 5th Assembly U.G.G.I., pp. 156–178, U.G.G.I., 1935.

Beringer, J., Tapper, N. J., and Keenan, T. D.: Evolution of maritime continent thunderstorms under varying meteorological conditions over the Tiwi Islands, Int. J. Climatol., 21, 1021–1036, doi:10.1002/joc.622, 2001.

Bertram, T. H., Perring, A. E., Wooldridge, P. J., Crounse, J. D., Kwan, A. J., Wennberg, P. O., Scheuer, E., Dibb, J., Avery, M., Sachse, G., Vay, S. A., Crawford, J. H., McNaughton, C. S., Clarke, A., Pickering, K. E., Fuelberg, H., Huey, G., Blake, D. R., Singh, H. B., Hall, S. R., Shetter, R. E., Fried, A., Heikes, B. G., and Cohen, R. C.: Direct measurements of the convective recycling of the upper troposphere, Science, 315, 816–820, doi:10.1126/science.1134548, 2007.

Boehm, M. T. and Verlinde, J.: Stratospheric influence on upper tropospheric tropical cirrus, Geophys. Res. Lett., 27, 3209–3212, doi:10.1029/2000GL011678, 2000.

Bohren, C. F. and Huffman, D.: Absorption and scattering of light by small particles, Wiley science paperback series, Wiley, 1983.

Borrmann, S. and Jaenicke, R.: Application of Microholography For Ground-based In-situ Measurements In Stratus Cloud Layers - A Case-study, J. Atmos. Ocean. Tech., 10, 277–293, doi:10.1175/1520-0426(1993)010⟨0277:AOMFGB⟩2.0.CO;2, 1993.

Borrmann, S., Solomon, S., Dye, J. E., and Luo, B. P.: The potential of cirrus clouds for heterogeneous chlorine activation, Geophys. Res. Lett., 23, 2133–2136, doi:10.1029/96GL01957, 1996.

Borrmann, S., Luo, B. P., and Mishchenko, M.: Application of the T-matrix method to the measurement of aspherical (ellipsoidal) particles with forward scattering optical particle counters, J. Aerosol Sci., 31, 789–799, doi:10.1016/S0021-8502(99)00563-7, 2000a.

Borrmann, S., Thomas, A., Rudakov, V., Yushkov, V., Lepuchov, B., Deshler, T., Vinnichenko, N., Khattatov, V., and Stefanutti, L.: Stratospheric aerosol measurements in the Arctic winter of 1996/1997 with the M-55 Geophysika high-altitude research aircraft, Tellus B, 52, 1088–1103, doi:10.1034/j.1600-0889.2000.00100.x, 2000b.

Bouniol, D., Delanoë, J., Duroure, C., Protat, A., Giraud, V., and Penide, G.: Microphysical characterisation of West African MCS anvils, Q. J. Roy. Meteor. Soc., 136, 323–344, doi:10.1002/qj.557, 2010.

Bourassa, A., Degenstein, D., and Llewellyn, E.: Climatology of the subvisual cirrus clouds as seen by OSIRIS on Odin, Adv. Space Res., 36, 807–812, doi:10.1016/j.asr.2005.05.045, 2005.

Brenguier, J. L., Bourrianne, T., Coelho, A. D., Isbert, J., Peytavi, R., Trevarin, D., and Weschler, P.: Improvements of droplet size distribution measurements with the Fast-FSSP (Forward Scattering Spectrometer Probe), J. Atmos. Ocean. Tech., 15, 1077–1090, doi:10.1175/1520-0426(1998)015⟨1077:IODSDM⟩2.0.CO;2, 1998.

Brock, C. A., Hamill, P., Wilson, J. C., Jonsson, H. H., and Chan, K. R.: Particle Formation in the Upper Tropical Troposphere: A Source of Nuclei for the Stratospheric Aerosol, Science, 270, 1650–1653, doi:10.1126/science.270.5242.1650, 1995.

Brown, P. R. A.: Use of Holography for Airborne Cloud Physics Measurements, J. Atmos. Ocean. Tech., 6, 293–306, doi:10.1175/1520-0426(1989)006⟨0293:UOHFAC⟩2.0.CO;2, 1989.

Brown, P. R. A. and Francis, P. N.: Improved Measurements Of The Ice Water-Content In Cirrus Using A Total-Water Probe, J. Atmos. Ocean. Tech., 12, 410–414, doi:10.1175/1520-0426(1995)012⟨0410:IMOTIW⟩2.0.CO;2, 1995.

Brunner, D., Siegmund, P., May, P. T., Chappel, L., Schiller, C., Müller, R., Peter, T., Fueglistaler, S., MacKenzie, A. R., Fix, A., Schlager, H., Allen, G., Fjæraa, A. M., Streibel, M., and Harris, N. R. P.: The SCOUT-O3 Darwin Aircraft Campaign: rationale and meteorology, Atmos. Chem. Phys., 9, 93–117, doi:10.5194/acp-9-93-2009, 2009.

Bucholtz, A., Hlavka, D. L., McGill, M. J., Schmidt, K. S., Pilewskie, P., Davis, S. M., Reid, E. A., and Walker, A. L.: Directly measured heating rates of a tropical subvisible cirrus cloud, J. Geophys. Res., 115, D00J09, doi:10.1029/2009JD013128, 2010.

Buontempo, C., Cairo, F., Di Donfrancesco, G., Morbidini, R., Viterbini, M., and Adriani, A.: Optical measurements of atmospheric particles from airborne platforms: in situ and remote sensing instruments for balloons and aircrafts, Ann. Geophys., 49, 57–64, doi:10.4401/ag-3149, 2006.

Burpee, R. W.: Origin and Structure of Easterly Waves In Lower Troposphere of North Africa, J. Atmos. Sci., 29, 77–90, doi:10.1175/1520-0469(1972)029⟨0077:TOASOE⟩2.0.CO;2, 1972.

Burpee, R. W.: Characteristics of North African Easterly Waves During Summers of 1968 and 1969, J. Atmos. Sci., 31, 1556–1570, doi:10.1175/1520-0469(1974)031⟨1556:CONAEW⟩2.0.CO;2, 1974.

Cairo, F., Adriani, A., Viterbini, M., Di Donfrancesco, G., Mitev, V., Matthey, R., Bastiano, M., Redaelli, G., Dragani, R., Ferretti, R., Rizi, V., Paolucci, T., Bernardini, L., Cacciani, M., Pace, G., and Fiocco, G.: Polar stratospheric clouds observed during the Airborne Polar Experiment-Geophysica Aircraft in Antarctica (APE-GAIA) campaign, J. Geophys. Res., 109, D07 204, doi:10.1029/2003JD003930, 2004.

Cairo, F., Pommereau, J. P., Law, K. S., Schlager, H., Garnier, A., Fierli, F., Ern, M., Streibel, M., Arabas, S., Borrmann, S., Berthelier, J. J., Blom, C., Christensen, T., D'Amato, F., Di Donfrancesco, G., Deshler, T., Diedhiou, A., Durry, G., Engelsen, O., Goutail, F., Harris, N. R. P., Kerstel, E. R. T., Khaykin, S., Konopka, P., Kylling, A., Larsen, N., Lebel, T., Liu, X., MacKenzie, A. R., Nielsen, J., Oulanowski, A., Parker, D. J., Pelon, J., Polcher, J., Pyle, J. A., Ravegnani, F., Rivière, E. D., Robinson, A. D., Röckmann, T., Schiller, C., Simoes, F., Stefanutti, L., Stroh, F., Some, L., Siegmund, P., Sitnikov, N., Vernier, J. P., Volk, C. M., Voigt, C., von Hobe, M., Viciani, S., and Yushkov, V.: An introduction to the SCOUT-AMMA stratospheric aircraft, balloons and sondes campaign in West Africa, August 2006: rationale and roadmap, Atmos. Chem. Phys., 10, 2237–2256, doi:10.5194/acp-10-2237-2010, 2010.

Cairo, F., Di Donfrancesco, G., Snels, M., Fierli, F., Viterbini, M., Borrmann, S., and Frey, W.: A comparison of light backscattering and particle size distribution measurements in tropical cirrus clouds, Atmos. Meas. Tech., 4, 557–570, doi:10.5194/amt-4-557-2011, 2011.

Carbone, R. E., Wilson, J. W., Keenan, T. D., and Hacker, J. M.: Tropical island convection in the absence of significant topography: Part I: Life cycle of diurnally forced convection, Mon. Weather Rev., 128, 3459–3480, doi:10.1175/1520-0493(2000)128⟨3459:TICITA⟩2.0.CO%3B2, 2000.

Cecil, D. J., Goodman, S. J., Boccippio, D. J., Zipser, E. J., and Nesbitt, S. W.: Three years of TRMM precipitation features. Part I: Radar, radiometric, and lightning characteristics, Mon. Weather Rev., 133, 543–566, doi:10.1175/MWR-2876.1, 2005.

Cetrone, J. and Houze, R. A.: Anvil clouds of tropical mesoscale convective systems in monsoon regions, Q. J. Roy. Meteor. Soc., 135, 305–317, doi:10.1002/qj.389, 2009.

Chaboureau, J.-P., Cammas, J.-P., Duron, J., Mascart, P. J., Sitnikov, N. M., and Vössing, H.-J.: A numerical study of tropical cross-tropopause transport by convective overshoots, Atmos. Chem. Phys., 7, 1731–1740, doi:10.5194/acp-7-1731-2007, 2007.

Chen, J.-P., McFarquhar, G. M., Heymsfield, A. J., and Ramanathan, V.: A modeling and observational study of the detailed microphysical structure of tropical cirrus anvils, J. Geophys. Res., 102, 6637–6653, doi:10.1029/96JD03513, 1997.

Chen, S. S. and Houze, R. A.: Diurnal variation and life-cycle of deep convective systems over the tropical pacific warm pool, Q. J. Roy. Meteor. Soc., 123, 357–388, doi:10.1002/qj.49712353806, 1997.

Comstock, J. M., Ackerman, T. P., and Mace, G. G.: Ground-based lidar and radar remote sensing of tropical cirrus clouds at Nauru Island: Cloud statistics and radiative impacts, J. Geophys. Res., 107, 4714–4728, doi:10.1029/2002JD002203, 2002.

Connolly, P. J., Saunders, C. P. R., Gallagher, M. W., Bower, K. N., Flynn, M. J., Choularton, T. W., Whiteway, J., and Lawson, R. P.: Aircraft observations of the influence of electric fields on the aggregation of ice crystals, Q. J. Roy. Meteor. Soc., 131, 1695–1712, doi:10.1256/qj.03.217, 2005.

Connolly, P. J., Choularton, T. W., Gallagher, M. W., Bower, K. N., Flynn, M. J., and Whiteway, J. A.: Cloud-resolving simulations of intense tropical Hector thunderstorms: Implications for aerosol-cloud interactions, Q. J. Roy. Meteor. Soc., 132, 3079–3106, doi:10.1256/qj.05.86, 2006.

Conway, B. J., Caughey, S. J., Bentley, A. N., and Turton, J. D.: Ground-based and Airborne Holography of Ice and Water Clouds, Atmos. Environ., 16, 1193–1207, doi:10.1016/0004-6981(82)90208-6, 1982.

Cook, K. H.: Generation of the African easterly jet and its role in determining West African precipitation, J. Climate, 12, 1165–1184, doi:10.1175/1520-0442(1999)012⟨1165:GOTAEJ⟩2.0.CO;2, 1999.

Corti, T., Luo, B. P., de Reus, M., Brunner, D., Cairo, F., Mahoney, M. J., Martucci, G., Matthey, R., Mitev, V., dos Santos, F. H., Schiller, C., Shur, G., Sitnikov, N. M., Spelten, N., Vössing, H. J., Borrmann, S., and Peter, T.: Unprecedented evidence for deep convection hydrating the tropical stratosphere, Geophys. Res. Lett., 35, L10 810, doi:10.1029/2008GL033641, 2008.

Cotton, R., Osborne, S., Ulanowski, Z., Hirst, E., Kaye, P. H., and Greenaway, R. S.: The Ability of the Small Ice Detector (SID-2) to Characterize Cloud Particle and Aerosol Morphologies Obtained during Flights of the FAAM BAe-146 Research Aircraft, J. Atmos. Ocean. Tech., 27, 290–303, doi:10.1175/2009JTECHA1282.1, 2010.

Crook, N. A.: Understanding Hector: The dynamics of island thunderstorms, Mon. Weather Rev., 129, 1550–1563, doi:10.1175/1520-0493(2001)129⟨1550:UHTDOI⟩2.0.CO;2, 2001.

Curry, M. J. and Schemenauer, R. S.: The Small-Particle Response Of An Optical Array Precipitation Probe, J. Appl. Meteorol., 18, 816–821, doi:10.1175/1520-0450(1979)018⟨0816:TSPROA⟩2.0.CO;2, 1979.

D'Amato, F., Mazzinghi, P., and Castagnoli, F.: Methane analyzer based on TDL's for measurements in the lower stratosphere: design and laboratory tests, Appl. Phys. B-Lasers O, 75, 195–202, doi:10.1007/s00340-002-0981-x, 2002.

Danielsen, E. F.: A Dehydration Mechanism For the Stratosphere, Geophys. Res. Lett., 9, 605–608, doi:10.1029/GL009i006p00605, 1982.

Danielsen, E. F.: Insitu Evidence of Rapid, Vertical, Irreversible Transport of Lower Tropospheric Air Into the Lower Tropical Stratosphere By Convective Cloud Turrets and By Larger-scale Upwelling In Tropical Cyclones, J. Geophys. Res. - Atmos., 98, 8665–8681, doi:10.1029/92JD02954, 1993.

Davis, S., Hlavka, D., Jensen, E., Rosenlof, K., Yang, Q., Schmidt, S., Borrmann, S., Frey, W., Lawson, P., Vömel, H., and Bui, T. P.: In situ and lidar observations of tropopause subvisible cirrus clouds during TC4, J. Geophys. Res. - Atmos., 115, D00J17, doi:10.1029/2009JD013093, 2010.

de Reus, M., Borrmann, S., Bansemer, A., Heymsfield, A. J., Weigel, R., Schiller, C., Mitev, V., Frey, W., Kunkel, D., Kürten, A., Curtius, J., Sitnikov, N. M., Ulanovsky, A., and Ravegnani, F.: Evidence for ice particles in the tropical stratosphere from in-situ measurements, Atmos. Chem. Phys., 9, 6775–6792, doi:10.5194/acp-9-6775-2009, 2009.

Denning, R. F., Guidero, S. L., Parks, G. S., and Gary, B. L.: Instrument Description of the Airborne Microwave Temperature Profiler, J. Geophys. Res. - Atmos., 94, 16 757–16 765, doi:10.1029/JD094iD14p16757, 1989.

Dessler, A. E.: A reexamination of the "stratospheric fountain" hypothesis, Geophys. Res. Lett., 25, 4165–4168, doi:10.1029/1998GL900120, 1998.

Dessler, A. E., Palm, S. P., and Spinhirne, J. D.: Tropical cloud-top height distributions revealed by the Ice, Cloud, and Land Elevation Satellite (ICESat)/Geoscience Laser Altimeter System (GLAS), J. Geophys. Res. - Atmos., 111, D12 215, doi:10.1029/2005JD006705, 2006.

Drewnick, F., Schneider, J., Hings, S. S., Hock, N., Noone, K., Targino, A., Weimer, S., and Borrmann, S.: Measurement of ambient, interstitial, and residual aerosol particles on a mountaintop site in central Sweden using an aerosol mass spectrometer and a CVI, J. Atmos. Chem., 56, 1–20, doi:10.1007/s10874-006-9036-8, 2007.

Dye, J. E. and Baumgardner, D.: Evaluation of the Forward Scattering Spectrometer Probe. Part I: Electronic and Optical Studies, J. Atmos. Ocean. Tech., 1, 329–344, doi:10.1175/1520-0426(1984)001⟨0329:EOTFSS⟩2.0.CO;2, 1984.

Edwards, J., Havemann, S., Thelen, J.-C., and Baran, A.: A new parametrization for the radiative properties of ice crystals: Comparison with existing schemes and impact in a GCM, Atmos. Res., 83, 19–35, doi:10.1016/j.atmosres.2006.03.002, 2007.

Emery, E. F., Miller, D. R., Plaskon, S. R., Strapp, W., and Lillie, L.: Ice Particle Impact on Cloud Water Content Instrumentation, Tech. rep., NASA, 2004.

Eremenko, M. N., Zasetsky, A. Y., Boone, C. D., and Sloan, J. J.: Properties of high-altitude tropical cirrus clouds determined from ACE FTS observations, Geophys. Res. Lett., 32, L15S07, doi:10.1029/2005GL022428, 2005.

Field, P. R., Heymsfield, A. J., and Bansemer, A.: Shattering and Particle Interarrival Times Measured by Optical Array Probes in Ice Clouds, J. Atmos. Ocean. Tech., 23, 1357–1371, doi:10.1175/JTECH1922.1, 2006.

Fierli, F., Orlandi, E., Law, K. S., Cagnazzo, C., Cairo, F., Schiller, C., Borrmann, S., Di Donfrancesco, G., Ravegnani, F., and Volk, C. M.: Impact of deep convection in the tropical tropopause layer in West Africa: in-situ observations and mesoscale modelling, Atmos. Chem. Phys., 11, 201–214, doi:10.5194/acp-11-201-2011, 2011.

Findeisen, W.: Kolloidmeteorologische Vorgänge bei Neiderschlagsbildung, Meteorol. Z., 55, 121–133, 1938.

Fink, A. H.: Das westafrikanische Monsunsystem, Promet, 32, 114–122, 2006.

Fink, A. H. and Reiner, A.: Spatiotemporal variability of the relation between African Easterly Waves and West African Squall Lines in 1998 and 1999, J. Geophys. Res. - Atmos., 108, 4332–4349, doi:10.1029/2002JD002816, 2003.

Fischer, H., Birk, M., Blom, C., Carli, B., Carlotti, M., von Clarmann, T., Delbouille, L., Dudhia, A., Ehhalt, D., Endemann, M., Flaud, J. M., Gessner, R., Kleinert, A., Koopman, R., Langen, J., López-Puertas, M., Mosner, P., Nett, H., Oelhaf, H., Perron, G., Remedios, J., Ridolfi, M., Stiller, G., and Zander, R.: MIPAS: an instrument for atmospheric and climate research, Atmos. Chem. Phys., 8, 2151–2188, doi:10.5194/acp-8-2151-2008, 2008.

Folkins, I.: Origin of lapse rate changes in the upper tropical troposphere, J. Atmos. Sci., 59, 992–1005, doi:10.1175/1520-0469(2002)059⟨0992:OOLRCI⟩2.0.CO;2, 2002.

Folkins, I., Loewenstein, M., Podolske, J., Oltmans, S. J., and Proffitt, M.: A barrier to vertical mixing at $14\,\mathrm{km}$ in the tropics: Evidence from ozonesondes and aircraft measurements, J. Geophys. Res. - Atmos., 104, 22 095–22 102, doi:10.1029/1999JD900404, 1999.

Forster, P., Ramaswamy, V., Artaxo, P., Berntsen, T., Betts, R., Fahey, D., Haywood, J., Lean, J., Lowe, D., Myhre, G., Nganga, J., Prinn, R., Raga, G., Schulz, M., and Van Dorland, R.: Climate Change 2007: The Physical Science Basis. Contribution of Working Group I to the Fourth Assessment Report of the Intergovernmental Panel on Climate Change, chap. Changes in Atmospheric Constituents and in Radiative Forcing, Cambridge University Press, Cambridge, United Kingdom and New York, NY, USA., 2007.

Franz, P. and Röckmann, T.: High-precision isotope measurements of $H_2^{16}O$, $H_2^{17}O$, $H_2^{18}O$, and the $\Delta^{17}O$-anomaly of water vapor in the southern lowermost stratosphere, Atmos. Chem. Phys., 5, 2949–2959, doi:10.5194/acp-5-2949-2005, 2005.

Frey, W., Eichler, H., de Reus, M., Maser, R., Wendisch, M., and Borrmann, S.: A new airborne tandem platform for collocated measurements of microphysical cloud and radiation properties, Atmos. Meas. Tech., 2, 147–158, doi:10.5194/amt-2-147-2009, 2009.

Frey, W., Borrmann, S., Kunkel, D., Weigel, R., de Reus, M., Schlager, H., Roiger, A., Voigt, C., Hoor, P., Curtius, J., Krämer, M., Schiller, C., Volk, C. M., Homan, C. D., Fierli, F., Di Donfrancesco, G., Ulanovsky, A., Ravegnani, F., Sitnikov, N. M., Viciani, S., D'Amato, F., Shur, G. N., Belyaev, G. V., Law, K. S., and Cairo, F.: In-situ measurements of tropical cloud properties in the West African monsoon: upper tropospheric ice clouds, mesoscale convective system outflow, and subvisual cirrus, Atmos. Chem. Phys. Discuss., 11, 745–812, doi:10.5194/acpd-11-745-2011, 2011.

Froyd, K. D., Murphy, D. M., Lawson, P., Baumgardner, D., and Herman, R. L.: Aerosols that form subvisible cirrus at the tropical tropopause, Atmos. Chem. Phys., 10, 209–218, doi:10.5194/acp-10-209-2010, 2010.

Fueglistaler, S., Dessler, A. E., Dunkerton, T. J., Folkins, I., Fu, Q., and Mote, P. W.: Tropical tropopause layer, Rev. Geophys., 47, RG1004, doi:10.1029/2008RG000267, 2009.

Fugal, J. P. and Shaw, R. A.: Cloud particle size distributions measured with an airborne digital in-line holographic instrument, Atmos. Meas. Tech., 2, 259–271, doi:10.5194/amt-2-259-2009, 2009.

Garrett, T. J., Gerber, H., Baumgardner, D. G., Twohy, C. H., and Weinstock, E. M.: Small, highly reflective ice crystals in low-latitude cirrus, Geophys. Res. Lett., 30, 2132, doi:10.1029/2003GL018153, 2003.

Garrett, T. J., Dean-Day, J., Liu, C., Barnett, B., Mace, G., Baumgardner, D., Webster, C., Bui, T., Read, W., and Minnis, P.: Convective formation of pileus cloud near the tropopause, Atmos. Chem. Phys., 6, 1185–1200, doi:10.5194/acp-6-1185-2006, 2006.

Gayet, J. F., Auriol, F., Oshchepkov, S., Schroder, F., Duroure, C., Febvre, G., Fournol, J. F., Crepel, O., Personne, P., and Daugereon, D.: In situ measurements of the scattering phase function of stratocumulus, contrails and cirrus, Geophys. Res. Lett., 25, 971–974, doi:10.1029/98GL00541, 1998.

Gayet, J. F., Shcherbakov, V., Mannstein, H., Minikin, A., Schumann, U., Ström, J., Petzold, A., Ovarlez, J., and Immler, F.: Microphysical and optical properties of midlatitude cirrus clouds observed in the southern hemisphere during INCA, Q. J. Roy. Meteor. Soc., 132, 2719–2748, doi:10.1256/qj.05.162, 2006.

Gayet, J. F., Treffeisen, R., Helbig, A., Bareiss, J., Matsuki, A., Herber, A., and Schwarzenboeck, A.: On the onset of the ice phase in boundary layer Arctic clouds, J. Geophys. Res. - Atmos., 114, D19 201, doi:10.1029/2008JD011348, 2009.

Giles, J.: Meteorologists pour into west Africa, Nature, 442, 496–496, doi:10.1038/442496a, 2006.

Gordon, G. L. and Marwitz, J. D.: An Airborne Comparison of Three PMS Probes, J. Atmos. Ocean. Tech., 1, 22–27, doi:10.1175/1520-0426(1984)001⟨0022:AACOTP⟩2.0.CO;2, 1984.

Grewe, V.: Impact of Lightning on Air Chemistry and Climate, in: Lightning: Principles, Instruments and Applications, edited by Betz, H. D., Schumann, U., and Laroche, P., pp. 537–549, Springer Netherlands, doi:10.1007/978-1-4020-9079-0_25, 2009.

Griffith, K. T., Cox, S. K., and Knollenberg, R. G.: Infrared Radiative Properties Of Tropical Cirrus Clouds Inferred From Aircraft Measurements, J. Atmos. Sci., 37, 1077–1087, doi:10.1175/1520-0469(1980)037⟨1077:IRPOTC⟩2.0.CO;2, 1980.

Grosvenor, D. P., Choularton, T. W., Coe, H., and Held, G.: A study of the effect of overshooting deep convection on the water content of the TTL and lower stratosphere from Cloud Resolving Model simulations, Atmos. Chem. Phys., 7, 4977–5002, doi:10.5194/acp-7-4977-2007, 2007.

Gu, G. J. and Adler, R. F.: Seasonal evolution and variability associated with the West African monsoon system, J. Climate, 17, 3364–3377, doi:10.1175/1520-0442(2004)017⟨3364%3ASEAVAW⟩2.0.CO%3B2, 2004.

Haladay, T. and Stephens, G.: Characteristics of tropical thin cirrus clouds deduced from joint CloudSat and CALIPSO observations, J. Geophys. Res. - Atmos., 114, D00A25, doi:10.1029/2008JD010675, 2009.

Hall, N. M. J. and Peyrille, P.: Dynamics of the west African monsoon, J. Phys. IV, 139, 81–99, doi:10.1051/jp4:2006139007, 2006.

Hallett, J. and Mossop, S. C.: Production of Secondary Ice Particles During Riming Process, Nature, 249, 26–28, doi:10.1038/249026a0, 1974.

Hamburger, T.: Einfluss von mesoskaligen konvektiven Systemen auf das troposphärische Aerosol im westafrikanischen Monsunsystem, Master's thesis, LMU München, 2007.

Hamill, P. and Fiocco, G.: Nitric acid aerosols at the tropical tropopause, Geophys. Res. Lett., 15, 1189–1192, doi:10.1029/GL015i011p01189, 1988.

Hartmann, D.: Radiative Effects of Clouds on Earth's Climate, in: Aerosol-Cloud-Climate Interactions, edited by Hobbs, P. V., vol. 54 of *International Geophysics*, chap. Chapter 6, pp. 151 – 173, Academic Press, doi:10.1016/S0074-6142(08)60215-6, 1993.

Hastenrath, S.: Climate dynamics of the tropics, Atmospheric sciences library, Kluwer Academic Publishers, 1991a.

Hastenrath, S.: Climate dynamics of the tropics, chap. 7, pp. 210–252, Atmospheric sciences library, Springer, 1991b.

Hervig, M. and McHugh, M.: Tropical nitric acid clouds, Geophys. Res. Lett., 29, 1125–1128, doi:10.1029/2001GL014271, 2002.

Heymsfield, A. J.: Ice Particles Observed In A Cirriform Cloud At $-83\,^{\circ}\mathrm{C}$ and Implications For Polar Stratospheric Clouds, J. Atmos. Sci., 43, 851–855, doi:10.1175/1520-0469(1986)043⟨0851:IPOIAC⟩2.0.CO;2, 1986.

Heymsfield, A. J.: On measurements of small ice particles in clouds, Geophys. Res. Lett., 34, L23 812, doi:10.1029/2007GL030951, 2007.

Heymsfield, A. J. and Parrish, J. L.: A Computational Technique for Increasing the Effective Sampling Volume of the PMS Two-Dimensional Particle Size Spectrometer, J. Appl. Meteorol., 17, 1566–1572, doi:10.1175/1520-0450(1978)017⟨1566:ACTFIT⟩2.0.CO;2, 1978.

Heymsfield, A. J., Lewis, S., Bansemer, A., Iaquinta, J., Miloshevich, L. M., Kajikawa, M., Twohy, C., and Poellot, M. R.: A General Approach for Deriving the Properties of Cirrus and Stratiform Ice Cloud Particles, J. Atmos. Sci., 59, 3–29, doi:10.1175/1520-0469(2002)059⟨0003:AGAFDT⟩2.0.CO;2, 2002.

Heymsfield, A. J., Schmitt, C., Bansemer, A., van Zadelhoff, G.-J., McGill, M. J., Twohy, C., and Baumgardner, D.: Effective Radius of Ice Cloud Particle Populations Derived from Aircraft Probes, J. Atmos. Ocean. Tech., 23, 361–380, doi:10.1175/JTECH1857.1, 2006.

Highwood, E. J. and Hoskins, B. J.: The tropical tropopause, Q. J. Roy. Meteor. Soc., 124, 1579–1604, doi:10.1002/qj.49712454911, 1998.

Hinds, W.: Aerosol technology: properties, behavior, and measurement of airborne particles, Wiley-Interscience, Wiley, 1999.

Hirst, E., Kaye, P. H., Greenaway, R. S., Field, P., and Johnson, D. W.: Discrimination of micrometre-sized ice and super-cooled droplets in mixed-phase cloud, Atmos. Environ., 35, 33–47, doi:10.1016/S1352-2310(00)00377-0, 2001.

Hobbs, P. V. and Rangno, A. L.: Ice Particle Concentrations In Clouds, J. Atmos. Sci., 42, 2523–2549, doi:10.1175/1520-0469(1985)042⟨2523:IPCIC⟩2.0.CO;2, 1985.

Höller, H., Betz, H.-D., Schmidt, K., Calheiros, R. V., May, P., Houngninou, E., and Scialom, G.: Lightning characteristics observed by a VLF/LF lightning detection network (LINET) in Brazil, Australia, Africa, and Germany, Atmos. Chem. Phys., 9, 7795–7824, doi:10.5194/acp-9-7795-2009, 2009.

Holton, J. R. and Gettelman, A.: Horizontal transport and the dehydration of the stratosphere, Geophys. Res. Lett., 28, 2799–2802, doi:10.1029/2001GL013148, 2001.

Homan, C. D., Volk, C. M., Kuhn, A. C., Werner, A., Baehr, J., Viciani, S., Ulanovski, A., and Ravegnani, F.: Tracer measurements in the tropical tropopause layer during the AMMA/SCOUT-O3 aircraft campaign, Atmos. Chem. Phys., 10, 3615–3627, doi:10.5194/acp-10-3615-2010, 2010.

Houze, R. A.: Observed Structure of Mesoscale Convective Systems and Implications For Large-scale Heating, Q. J. Roy. Meteor. Soc., 115, 425–461, doi:10.1002/qj.49711548702, 1989.

Houze, R. A.: International Geophysics Series, vol. 53 of *International Geophysics Series*, Academic Press, doi:10.1016/S0074-6142(08)62858-2, 1993a.

Houze, R. A.: Chapter 9 Mesoscale Convective Systems, in: Cloud Dynamics, edited by Houze, Robert A., J., vol. 53 of *International Geophysics*, pp. 334 – 404, Academic Press, doi:10.1016/S0074-6142(08)62853-3, 1993b.

Houze, R. A.: Mesoscale convective systems, Rev. Geophys., 42, RG4003, doi:10.1029/2004RG000150, 2004.

Hovenac, E. A. and Hirleman, E. D.: Use Of Rotating Pinholes And Reticles For Calibration Of Cloud Droplet Instrumentation, J. Atmos. Ocean. Tech., 8, 166–171, doi:10.1175/1520-0426(1991)008⟨0166:UORPAR⟩2.0.CO;2, 1991.

Huntrieser, H., Schlager, H., Roiger, A., Lichtenstern, M., Schumann, U., Kurz, C., Brunner, D., Schwierz, C., Richter, A., and Stohl, A.: Lightning-produced NO_x over Brazil during TROCCINOX: airborne measurements in tropical and subtropical thunderstorms and the importance of mesoscale convective systems, Atmos. Chem. Phys., 7, 2987–3013, doi:10.5194/acp-7-2987-2007, 2007.

Huntrieser, H., Schlager, H., Lichtenstern, M., Roiger, A., Stock, P., Minikin, A., Höller, H., Schmidt, K., Betz, H.-D., Allen, G., Viciani, S., Ulanovsky, A., Ravegnani, F., and Brunner, D.: NO_x production by lightning in Hector: first airborne measurements during SCOUT-O3/ACTIVE, Atmos. Chem. Phys., 9, 8377–8412, doi:10.5194/acp-9-8377-2009, 2009.

Jaegle, L., Jacob, D. J., Wang, Y., Weinheimer, A. J., Ridley, B. A., Campos, T. L., Sachse, G. W., and Hagen, D. E.: Sources and chemistry of NO_x in the upper troposphere over the United States, Geophys. Res. Lett., 25, 1705–1708, doi:10.1029/97GL03591, 1998.

Janicot, S., Thorncroft, C. D., Ali, A., Asencio, N., Berry, G., Bock, O., Bourles, B., Caniaux, G., Chauvin, F., Deme, A., Kergoat, L., Lafore, J. P., Lavaysse, C., Lebel, T., Marticorena, B., Mounier, F., Nedelec, P., Redelsperger, J. L., Ravegnani, F., Reeves, C. E., Roca, R., de Rosnay, P., Schlager, H., Sultan, B., Tomasini, M., and Ulanovsky, A.: Large-scale overview of the summer monsoon over West Africa during the AMMA field experiment in 2006, Ann. Geophys., 26, 2569–2595, doi:10.5194/angeo-26-2569-2008, 2008.

Jensen, E. J. and Pfister, L.: Transport and freeze-drying in the tropical tropopause layer, J. Geophys. Res. - Atmos., 109, D02 207, doi:10.1029/2003JD004022, 2004.

Jensen, E. J., Toon, O. B., Selkirk, H. B., Spinhirne, J. D., and Schoeberl, M. R.: On the formation and persistence of subvisible cirrus clouds near the tropical tropopause, J. Geophys. Res., 101, 21 361–21 375, doi:10.1029/95JD03575, 1996.

Jensen, E. J., Pfister, L., Bui, T. V., Lawson, P., Baker, B., Mo, Q., Baumgardner, D., Weinstock, E. M., Smith, J. B., Moyer, E. J., Hanisco, T. F., Sayres, D. S., Clair, J. M. S., Alexander, M. J., Toon, O. B., and Smith, J. A.: Formation of large ($\simeq 100\,\mu$m) ice crystals near the tropical tropopause, Atmos. Chem. Phys., 8, 1621–1633, doi: 10.5194/acp-8-1621-2008, 2008.

Jensen, E. J., Lawson, P., Baker, B., Pilson, B., Mo, Q., Heymsfield, A. J., Bansemer, A., Bui, T. P., McGill, M., Hlavka, D., Heymsfield, G., Platnick, S., Arnold, G. T., and Tanelli, S.: On the importance of small ice crystals in tropical anvil cirrus, Atmos. Chem. Phys., 9, 5519–5537, doi:10.5194/acp-9-5519-2009, 2009.

Jensen, E. J., Pfister, L., Bui, T.-P., Lawson, P., and Baumgardner, D.: Ice nucleation and cloud microphysical properties in tropical tropopause layer cirrus, Atmos. Chem. Phys., 10, 1369–1384, doi:10.5194/acp-10-1369-2010, 2010.

Joe, P. and List, R.: Testing and Performance of Two-Dimensional Optical Array Spectrometers with Greyscale, J. Atmos. Ocean. Tech., 4, 139–150, doi: 10.1175/1520-0426(1987)004⟨0139:TAPOTD⟩2.0.CO;2, 1987.

Johnson, D. A. and Hallett, J.: Freezing and shattering of supercooled water drops, Q. J. Roy. Meteor. Soc., 94, 468–482, doi:10.1002/qj.49709440204, 1968.

Jonsson, H. H., Wilson, J. C., Brock, C. A., Knollenberg, R. G., Newton, R., Dye, J. E., Baumgardner, D., Borrmann, S., Ferry, G. V., Pueschel, R., Woods, D. C., and Pitts, M. C.: Performance of A Focused Cavity Aerosol Spectrometer For Measurements In the Stratosphere of Particle-size In the $0.06\,\mu$m–$2.0\,\mu$m-diameter Range, J. Atmos. Ocean. Tech., 12, 115–129, doi:10.1175/1520-0426(1995)012⟨0115:POAFCA⟩2.0.CO;2, 1995.

Kalesse, H.: Influence of Ice Crystal Habit and Cirrus Spatial Inhomogeneities on the Retrieval of Cirrus Optical Thickness and Effective Radius, Ph.D. thesis, Johannes Gutenberg-Universität Mainz, Fachbereich 08 für Physik, Mathematik und Informatik, 2009.

Kamphus, M., Ettner-Mahl, M., Klimach, T., Drewnick, F., Keller, L., Cziczo, D. J., Mertes, S., Borrmann, S., and Curtius, J.: Chemical composition of ambient aerosol, ice residues and cloud droplet residues in mixed-phase clouds: single particle analysis during the Cloud and Aerosol Characterization Experiment (CLACE 6), Atmos. Chem. Phys., 10, 8077–8095, doi:10.5194/acp-10-8077-2010, 2010.

Kärcher, B.: Properties of subvisible cirrus clouds formed by homogeneous freezing, Atmos. Chem. Phys., 2, 161–170, doi:10.5194/acp-2-161-2002, 2002.

Kärcher, B. and Lohmann, U.: A parameterization of cirrus cloud formation: Homogeneous freezing of supercooled aerosols, J. Geophys. Res., 107, D23, doi: 10.1029/2001JD001429, 2002.

Keenan, T. D., Ferrier, B., and Simpson, J.: Development and Structure of A Maritime Continent Thunderstorm, Meteorol. Atmos. Phys., 53, 185–222, doi:10.1007/BF01029612, 1994.

Khaykin, S., Pommereau, J.-P., Korshunov, L., Yushkov, V., Nielsen, J., Larsen, N., Christensen, T., Garnier, A., Lukyanov, A., and Williams, E.: Hydration of the lower stratosphere by ice crystal geysers over land convective systems, Atmos. Chem. Phys., 9, 2275–2287, doi:10.5194/acp-9-2275-2009, 2009.

Kiehl, J. T. and Trenberth, K. E.: Earth's annual global mean energy budget, B. Am. Meteorol. Soc., 78, 197–208, doi:10.1175/1520-0477(1997)078⟨0197:EAGMEB⟩2.0.CO;2, 1997.

Kiladis, G. N., Thorncroft, C. D., and Hall, N. M. J.: Three-dimensional structure and dynamics of African easterly waves: Part I: Observations, J. Atmos. Sci., 63, 2212–2230, doi:10.1175/JAS3741.1, 2006.

Kinne, S. and Liou, K.-N.: The effects of the nonsphericity and size distribution of ice crystals on the radiative propertues of cirrus clouds, Atmos. Res., 24, 273–284, doi:10.1016/0169-8095(89)90049-5, 1989.

Kley, D., Schmeltekopf, A. L., Kelly, K., Winkler, R. H., Thompson, T. L., and McFarland, M.: Transport of water through the tropical tropopause, Geophys. Res. Lett., 9, 617–620, doi:10.1029/GL009i006p00617, 1982.

Knollenberg, R. G.: The Optical Array: An Alternative to Scattering or Extinction for Airborne Particle Size Determination, J. Appl. Meteorol., 9, 86–103, doi:10.1175/1520-0450(1970)009⟨0086:TOAAAT⟩2.0.CO;2, 1970.

Knollenberg, R. G., Dascher, A. J., and Huffman, D.: Measurements Of The Aerosol And Ice Crystal Populations In Tropical Stratospheric Cumulonimbus Anvils, Geophys. Res. Lett., 9, 613–616, doi:10.1029/GL009i006p00613, 1982.

Korolev, A.: Reconstruction of the sizes of spherical particles from their shadow images: Part I: Theoretical considerations, J. Atmos. Ocean. Tech., 24, 376–389, doi:10.1175/JTECH1980.1, 2007.

Korolev, A. and Isaac, G. A.: Shattering during sampling by OAPs and HVPS. Part I: Snow particles, J. Atmos. Ocean. Tech., 22, 528–542, doi:10.1175/JTECH1720.1, 2005.

Korolev, A., Kuznetsov, S., Makarov, Y. E., and Novikov, V.: Evaluation of Measurements of Particle Size and Sample Area from Optical Array Probes, J. Atmos. Ocean. Tech., 8, 514–522, doi:10.1175/1520-0426(1991)008⟨0514:EOMOPS⟩2.0.CO;2, 1991.

Korolev, A. V., Strapp, J. W., and Isaac, G. A.: Evaluation of the Accuracy of PMS Optical Array Probes, J. Atmos. Ocean. Tech., 15, 708–720, doi:10.1175/1520-0426(1998)015⟨0708:EOTAOP⟩2.0.CO;2, 1998.

Korolev, A. V., Emery, E. F., Strapp, J. W., Cober, S. G., Isaac, G. A., Wasey, M., and Marcotte, D.: Small ice particles in tropospheric clouds: fact or artifact? Airborne Icing Instrumentation Evaluation Experiment, B. Am. Meteorol. Soc., 0, e–View, doi:10.1175/2010BAMS3141.1, in press, 2011.

Koteswaram, P.: The Easterly Jet Stream in the Tropics, Tellus, 10, 43–57, doi:10.1111/j.2153-3490.1958.tb01984.x, 1958.

Krämer, M., Schiller, C., Afchine, A., Bauer, R., Gensch, I., Mangold, A., Schlicht, S., Spelten, N., Sitnikov, N., Borrmann, S., de Reus, M., and Spichtinger, P.: Ice supersaturations and cirrus cloud crystal numbers, Atmos. Chem. Phys., 9, 3505–3522, doi:10.5194/acp-9-3505-2009, 2009.

Krüger, K., Tegtmeier, S., and Rex, M.: Variability of residence time in the Tropical Tropopause Layer during Northern Hemisphere winter, Atmos. Chem. Phys., 9, 6717–6725, doi:10.5194/acp-9-6717-2009, 2009.

Law, K. S., Fierli, F., Cairo, F., Schlager, H., Borrmann, S., Streibel, M., Real, E., Kunkel, D., Schiller, C., Ravegnani, F., Ulanovsky, A., D'Amato, F., Viciani, S., and Volk, C. M.: Air mass origins influencing TTL chemical composition over West Africa during 2006 summer monsoon, Atmos. Chem. Phys., 10, 10 753–10 770, doi:10.5194/acp-10-10753-2010, 2010.

Lawson, R. P.: Effects of ice particles shattering on optical cloud particle probes, Atmos. Meas. Tech. Discuss., 4, 939–968, doi:10.5194/amtd-4-939-2011, 2011.

Lawson, R. P. and Baker, B. A.: Improvement in Determination of Ice Water Content from Two-Dimensional Particle Imagery. Part II: Applications to Collected Data, J. Appl. Meteorol. Clim., 45, 1291–1303, doi:10.1175/JAM2399.1, 2006.

Lawson, R. P. and Cormack, R. H.: Theoretical Design And Preliminary Tests Of Two New Particle Spectrometers For Cloud Microphysics Research, Atmos. Res., 35, 315–348, doi:10.1016/0169-8095(94)00026-A, 1995.

Lawson, R. P., Baker, B. A., Schmitt, C. G., and Jensen, T. L.: An overview of microphysical properties of Arctic clouds observed in May and July 1998 during FIRE ACE, J. Geophys. Res. - Atmos., 106, 14 989–15 014, doi:10.1029/2000JD900789, 2001.

Lawson, R. P., O'Connor, D., Zmarzly, P., Weaver, K., Baker, B., Mo, Q. X., and Jonsson, H.: The 2D-S (Stereo) probe: Design and preliminary tests of a new airborne, high-speed, high-resolution particle Imaging probe, J. Atmos. Ocean. Tech., 23, 1462–1477, doi:10.1175/JTECH1927.1, 2006.

Lawson, R. P., Pilson, B., Baker, B., Mo, Q., Jensen, E., Pfister, L., and Bui, P.: Aircraft measurements of microphysical properties of subvisible cirrus in the tropical tropopause layer, Atmos. Chem. Phys., 8, 1609–1620, doi:10.5194/acp-8-1609-2008, 2008.

Lawson, R. P., Jensen, E., Mitchell, D. L., Baker, B., Mo, Q., and Pilson, B.: Microphysical and radiative properties of tropical clouds investigated in TC4 and NAMMA, J. Geophys. Res., 115, D00J08, doi:10.1029/2009JD013017, 2010.

Lelieveld, J., Brühl, C., Jöckel, P., Steil, B., Crutzen, P. J., Fischer, H., Giorgetta, M. A., Hoor, P., Lawrence, M. G., Sausen, R., and Tost, H.: Stratospheric dryness: model simulations and satellite observations, Atmos. Chem. Phys., 7, 1313–1332, doi:10.5194/acp-7-1313-2007, 2007.

Leroux, S. and Hall, N. M. J.: On the Relationship between African Easterly Waves and the African Easterly Jet, J. Atmos. Sci., 66, 2303–2316, doi:10.1175/2009JAS2988.1, 2009.

Levine, J. S., Augustsson, T. R., Anderson, I. C., Hoell, J. M., and Brewer, D. A.: Tropospheric Sources of NO_x - Lightning and Biology, Atmos. Environ., 18, 1797–1804, doi:10.1016/0004-6981(84)90355-X, 1984.

Liu, C. T. and Zipser, E. J.: Global distribution of convection penetrating the tropical tropopause, J. Geophys. Res. - Atmos., 110, D23 104, doi:10.1029/2005JD006063, 2005.

Liu, L. and Mishchenko, M. I.: Constraints on PSC particle microphysics derived from lidar observations, J. Quant. Spectrosc. Ra., 70, 817–831, doi:10.1016/S0022-4073(01)00048-6, 2001.

Lowe, D. and MacKenzie, A. R.: Polar stratospheric cloud microphysics and chemistry, J. Atmos. Sol.-Terr. Phy., 70, 13–40, doi:10.1016/j.jastp.2007.09.011, 2008.

Luo, B. P., Peter, T., Fueglistaler, S., Wernli, H., Wirth, M., Kiemle, C., Flentje, H., Yushkov, V. A., Khattatov, V., Rudakov, V., Thomas, A., Borrmann, S., Toci, G., Mazzinghi, P., Beuermann, J., Schiller, C., Cairo, F., Di Donfrancesco, G., Adriani, A., Volk, C. M., Strom, J., Noone, K., Mitev, V., MacKenzie, R. A., Carslaw, K. S., Trautmann, T., Santacesaria, V., and Stefanutti, L.: Dehydration potential of ultrathin clouds at the tropical tropopause, Geophys. Res. Lett., 30, 1557, doi:10.1029/2002GL016737, 2003a.

Luo, B. P., Peter, T., Wernli, H., Fueglistaler, S., Wirth, M., Kiemle, C., Flentje, H., Yushkov, V. A., Khattatov, V., Rudakov, V., Thomas, A., Borrmann, S., Toci, G., Mazzinghi, P., Beuermann, J., Schiller, C., Cairo, F., Di Don-Francesco, G., Adriani, A., Volk, C. M., Ström, J., Noone, K., Mitev, V., MacKenzie, R. A., Carslaw, K. S., Trautmann, T., Santacesaria, V., and Stefanutti, L.: Ultrathin Tropical Tropopause Clouds (UTTCs): II. Stabilization mechanisms, Atmos. Chem. Phys., 3, 1093–1100, doi:10.5194/acp-3-1093-2003, 2003b.

Lynch, D. K.: Cirrus clouds: Their role in climate and global change, Acta Astronaut., 38, 859 – 863, doi:10.1016/S0094-5765(96)00098-7, 1996.

Lynch, D. K.: Cirrus, Oxford University Press, Oxford; Cambridge; New York, 2002.

Mace, G. G., Deng, M., Soden, B., and Zipser, E.: Association of tropical cirrus in the $10\,\mathrm{km}$–$15\,\mathrm{km}$ layer with deep convective sources: An observational study combining millimeter radar data and satellite-derived trajectories, J. Atmos. Sci., 63, 480–503, doi:10.1175/JAS3627.1, 2006.

Macke, A. and Francis, P. N.: The role of ice particle shapes and size distributions in the single scattering properties of cirrus clouds, J. Atmos. Sci., 55, 2874–2883, doi:10.1175/1520-0469(1998)055⟨2874%3ATROIPS⟩2.0.CO%3B2, 1998.

Maddox, R. A.: Mesoscale Convective Complexes, B. Am. Meteorol. Soc., 61, 1374–1387, doi:10.1175/1520-0477(1980)061⟨1374:MCC⟩2.0.CO;2, 1980.

Marcy, T. P., Popp, P. J., Gao, R. S., Fahey, D. W., Ray, E. A., Richard, E. C., Thompson, T. L., Atlas, E. L., Loewenstein, M., Wofsy, S. C., Park, S., Weinstock, E. M., Swartz, W. H., and Mahoney, M. J.: Measurements of trace gases in the tropical tropopause layer, Atmos. Environ., 41, 7253–7261, doi:10.1016/j.atmosenv.2007.05.032, 2007.

Massie, S., Gettelman, A., Randel, W., and Baumgardner, D.: Distribution of tropical cirrus in relation to convection, J. Geophys. Res. - Atmos., 107, 4591, doi:10.1029/2001JD001293, 2002.

McCormick, M. P., Chiou, E. W., McMaster, L. R., Chu, W. P., Larsen, J. C., Rind, D., and Oltmans, S.: Annual Variations of Water-vapor In the Stratosphere and Upper Troposphere Observed By the Stratospheric Aerosol and Gas Experiment-II, J. Geophys. Res. - Atmos., 98, 4867–4874, doi:10.1029/92JD02218, 1993.

McFarquhar, G. M. and Heymsfield, A. J.: Microphysical Characteristics of Three Anvils Sampled during the Central Equatorial Pacific Experiment, J. Atmos. Sci., 53, 2401–2423, doi:10.1175/1520-0469(1996)053⟨2401:MCOTAS⟩2.0.CO;2, 1996.

McFarquhar, G. M. and Heymsfield, A. J.: Parameterization of Tropical Cirrus Ice Crystal Size Distributions and Implications for Radiative Transfer: Results from CEPEX, J. Atmos. Sci., 54, 2187–2200, doi:10.1175/1520-0469(1997)054⟨2187:POTCIC⟩2.0.CO;2, 1997.

McFarquhar, G. M. and Heymsfield, A. J.: The Definition and Significance of an Effective Radius for Ice Clouds, J. Atmos. Sci., 55, 2039–2052, doi:10.1175/1520-0469(1998)055⟨2039:TDASOA⟩2.0.CO;2, 1998.

McFarquhar, G. M., Heymsfield, A. J., Spinhirne, J., and Hart, B.: Thin and subvisual tropopause tropical cirrus: Observations and radiative impacts, J. Atmos. Sci., 57, 1841–1853, doi:10.1175/1520-0469(2000)057⟨1841:TASTTC⟩2.0.CO;2, 2000.

McFarquhar, G. M., Um, J., Freer, M., Baumgardner, D., Kok, G. L., and Mace, G.: Importance of small ice crystals to cirrus properties: Observations from the Tropical Warm Pool International Cloud Experiment (TWP-ICE), Geophys. Res. Lett., 34, L13 803, doi:10.1029/2007GL029865, 2007.

Mekonnen, A., Thorncroft, C. D., and Aiyyer, A. R.: Analysis of convection and its association with African easterly waves, J. Climate, 19, 5405–5421, doi:10.1175/JCLI3920.1, 2006.

Mitchell, D. L. and Heymsfield, A. J.: Refinements in the treatment of ice particle terminal velocities, highlighting aggregates, J. Atmos. Sci., 62, 1637–1644, doi:10.1175/JAS3413.1, 2005.

Mitchell, D. L., Zhang, R., and Pitter, R. L.: Mass-Dimensional Relationships for Ice Particles and the Influence of Riming on Snowfall Rates, J. Appl. Meteorol., 29, 153–163, doi:10.1175/1520-0450(1990)029⟨0153:MDRFIP⟩2.0.CO;2, 1990.

Mitev, V., Matthey, R., , and Makanov, V.: Miniature backscatter lidar for cloud and aerosol observation from high altitude aircraft, Rec. Res. Dev. Geophys, 4, 207–223, doi:10.1127/0941-2948/2005/0046, 2002.

Möhler, O., Stetzer, O., Schaefers, S., Linke, C., Schnaiter, M., Tiede, R., Saathoff, H., Krämer, M., Mangold, A., Budz, P., Zink, P., Schreiner, J., Mauersberger, K., Haag, W., Kärcher, B., and Schurath, U.: Experimental investigation of homogeneous freezing of sulphuric acid particles in the aerosol chamber AIDA, Atmos. Chem. Phys., 3, 211–223, doi:10.5194/acp-3-211-2003, 2003.

Monks, P. S., Granier, C., Fuzzi, S., Stohl, A., Williams, M. L., Akimoto, H., Amann, M., Baklanov, A., Baltensperger, U., Bey, I., Blake, N., Blake, R. S., Carslaw, K., Cooper, O. R., Dentener, F., Fowler, D., Fragkou, E., Frost, G. J., Generoso, S., Ginoux, P., Grewe, V., Guenther, A., Hansson, H. C., Henne, S., Hjorth, J., Hofzumahaus, A., Huntrieser, H., Isaksen, I. S. A., Jenkin, M. E., Kaiser, J., Kanakidou, M., Klimont, Z., Kulmala, M., Laj, P., Lawrence, M. G., Lee, J. D., Liousse, C., Maione, M., McFiggans, G., Metzger, A., Mieville, A., Moussiopoulos, N., Orlando, J. J., O'Dowd, C. D., Palmer, P. I., Parrish, D. D., Petzold, A., Platt, U., Pöschl, U., Prevot, A. S. H., Reeves, C. E., Reimann, S., Rudich, Y., Sellegri, K., Steinbrecher, R., Simpson, D., ten Brink, H., Theloke, J., van der Werf, G. R., Vautard, R., Vestreng, V., Vlachokostas, C., and von Glasow, R.: Atmospheric composition change - global and regional air quality, Atmos. Environ., 43, 5268–5350, doi:10.1016/j.atmosenv.2009.08.021, 2009.

Mossop, S. C.: The Origin and Concentration of Ice Crystals In Clouds, B. Am. Meteorol. Soc., 66, 264–273, doi:10.1175/1520-0477(1985)066⟨0264:TOACOI⟩2.0.CO;2, 1985.

Murphy, D. M., Fahey, D. W., Proffitt, M. H., Liu, S. C., Chan, K. R., Eubank, C. S., Kawa, S. R., and Kelly, K. K.: Reactive Nitrogen and Its Correlation With Ozone in the Lower Stratosphere and Upper Troposphere, J. Geophys. Res., 98, 8751–8773, doi:10.1029/92JD00681, 1993.

Murray, B. J., Wilson, T. W., Dobbie, S., Cui, Z., Al-Jumur, S. M. R. K., Möhler, O., Schnaiter, M., Wagner, R., Benz, S., Niemand, M., Saathoff, H., Ebert, V., Wagner, S., and Kärcher, B.: Heterogeneous nucleation of ice particles on glassy aerosols under cirrus conditions, Nature Geosci., 3, 233–237, doi:10.1038/NGEO817, 2010.

Newell, R. E. and Gould-Stewart, S.: A Stratospheric Fountain, J. Atmos. Sci., 38, 2789–2796, doi:10.1175/1520-0469(1981)038⟨2789:ASF⟩2.0.CO;2, 1981.

Nielsen, J. K., Larsen, N., Cairo, F., Di Donfrancesco, G., Rosen, J. M., Durry, G., Held, G., and Pommereau, J. P.: Solid particles in the tropical lowest stratosphere, Atmos. Chem. Phys., 7, 685–695, doi:10.5194/acp-7-685-2007, 2007.

Omar, A. H. and Gardner, C. S.: Observations by the Lidar In-Space Technology Experiment (LITE) of high-altitude cirrus clouds over the equator in regions exhibiting extremely cold temperatures, J. Geophys. Res., 106, 1227–1236, doi: 10.1029/2000JD900489, 2001.

Park, S., Jimenez, R., Daube, B. C., Pfister, L., Conway, T. J., Gottlieb, E. W., Chow, V. Y., Curran, D. J., Matross, D. M., Bright, A., Atlas, E. L., Bui, T. P., Gao, R. S., Twohy, C. H., and Wofsy, S. C.: The CO_2 tracer clock for the Tropical Tropopause Layer, Atmos. Chem. Phys., 7, 3989–4000, doi:10.5194/acp-7-3989-2007, 2007.

Parker, D. J., Thorncroft, C. D., Burton, R. R., and Diongue-Niang, A.: Analysis of the African easterly jet, using aircraft observations from the JET2000 experiment, Q. J. Roy. Meteor. Soc., 131, 1461–1482, doi:10.1256/qj.03.189, 2005.

Peter, T.: Microphysics and heterogeneous chemistry of polar stratospheric clouds, Annu. Rev. Phys. Chem., 48, 785–822, doi:10.1146/annurev.physchem.48.1.785, 1997.

Peter, T., Luo, B. P., Wirth, M., Kiemle, C., Flentje, H., Yushkov, V. A., Khattatov, V., Rudakov, V., Thomas, A., Borrmann, S., Toci, G., Mazzinghi, P., Beuermann, J., Schiller, C., Cairo, F., Di Donfrancesco, G., Adriani, A., Volk, C. M., Ström, J., Noone, K., Mitev, V., MacKenzie, R. A., Carslaw, K. S., Trautmann, T., Santacesaria, V., and Stefanutti, L.: Ultrathin Tropical Tropopause Clouds (UTTCs): I. Cloud morphology and occurrence, Atmos. Chem. Phys., 3, 1083–1091, doi: 10.5194/acp-3-1083-2003, 2003.

Pfister, L., Selkirk, H. B., Jensen, E. J., Schoeberl, M. R., Toon, O. B., Browell, E. V., Grant, W. B., Gary, B., Mahoney, M. J., Bui, T. V., and Hintsa, E.: Aircraft observations of thin cirrus clouds near the tropical tropopause, J. Geophys. Res. - Atmos., 106, 9765–9786, doi:10.1029/2000JD900648, 2001.

Pitter, R. L. and Pruppacher, H. R.: A wind tunnel investigation of freezing of small water drops falling at terminal velocity in air, Q. J. Roy. Meteor. Soc., 99, 540–550, doi:10.1002/qj.49709942111, 1973.

Ploeger, F., Konopka, P., Günther, G., Grooß, J. U., and Müller, R.: Impact of the vertical velocity scheme on modeling transport in the tropical tropopause layer, J. Geophys. Res. - Atmos., 115, D03 301, doi:10.1029/2009JD012023, 2010.

Pommereau, J. P.: Troposphere-to-stratosphere transport in the tropics, CR Geosci., 342, 331–338, doi:10.1016/j.crte.2009.10.015, 2010.

Pommereau, J.-P., Garnier, A., Held, G., Gomes, A. M., Goutail, F., Durry, G., Borchi, F., Hauchecorne, A., Montoux, N., Cocquerez, P., Letrenne, G., Vial, F., Hertzog, A., Legras, B., Pisso, I., Pyle, J. A., Harris, N. R. P., Jones, R. L., Robinson, A. D., Hansford, G., Eden, L., Gardiner, T., Swann, N., Knudsen, B., Larsen, N., Nielsen, J. K., Christensen, T., Cairo, F., Fierli, F., Pirre, M., Marécal, V., Huret, N., Rivière, E. D., Coe, H., Grosvenor, D., Edvarsen, K., Di Donfrancesco, G., Ricaud, P., Berthelier, J.-J., Godefroy, M., Seran, E., Longo, K., and Freitas, S.: An overview of the HIBISCUS campaign, Atmos. Chem. Phys., 11, 2309–2339, doi: 10.5194/acp-11-2309-2011, 2011.

Pratte, P., van den Bergh, H., and Rossi, M. J.: The kinetics of H_2O vapor condensation and evaporation on different types of ice in the range $130\,\mathrm{K}$–$210\,\mathrm{K}$, J. Phys. Chem. A, 110, 3042–3058, doi:10.1021/jp053974s, 2006.

Pruppacher, H. R. and Klett, J. D.: Microphysics of Clouds and Precipitation, vol. 18 of *Atmospheric and Oceanographic Sciences Library*, Springer Netherlands, 2 edn., doi:10.1007/978-0-306-48100-0, 2010.

Quante, M.: The role of clouds in the climate system, J. Phys. IV, 121, 61–86, doi:10.1051/jp4:2004121003, 2004.

Quante, M. and Matthias, V.: Water in the Earth's atmosphere, J. Phys. IV, 139, 37–61, doi:10.1051/jp4:2006139005, 2006.

Randall, D., Khairoutdinov, M., Arakawa, A., and Grabowski, W.: Breaking the Cloud Parameterization Deadlock, B. Am. Meteorol. Soc., 84, 1547–1564, doi:10.1175/BAMS-84-11-1547, 2003.

Rangno, A. L. and Hobbs, P. V.: Ice particles in stratiform clouds in the Arctic and possible mechanisms for the production of high ice concentrations, J. Geophys. Res., 106, 15 065–15 075, doi:10.1029/2000JD900286, 2001.

Real, E., Law, K. S., Schlager, H., Roiger, A., Huntrieser, H., Methven, J., Cain, M., Holloway, J., Neuman, J. A., Ryerson, T., Flocke, F., de Gouw, J., Atlas, E., Donnelly, S., and Parrish, D.: Lagrangian analysis of low altitude anthropogenic plume processing across the North Atlantic, Atmos. Chem. Phys., 8, 7737–7754, doi:10.5194/acp-8-7737-2008, 2008.

Real, E., Orlandi, E., Law, K. S., Fierli, F., Josset, D., Cairo, F., Schlager, H., Borrmann, S., Kunkel, D., Volk, C. M., McQuaid, J. B., Stewart, D. J., Lee, J., Lewis, A. C., Hopkins, J. R., Ravegnani, F., Ulanovski, A., and Liousse, C.: Cross-hemispheric transport of central African biomass burning pollutants: implications for downwind ozone production, Atmos. Chem. Phys., 10, 3027–3046, doi:10.5194/acp-10-3027-2010, 2010.

Redelsperger, J.-L., Thorncroft, C. D., Diedhiou, A., Lebel, T., Parker, D. J., and Polcher, J.: African Monsoon Multidisciplinary Analysis: An International Research Project and Field Campaign, B. Am. Meteorol. Soc., 87, 1739–1746, doi:10.1175/BAMS-87-12-1739, 2006.

Reed, R. J., Norquist, D. C., and Recker, E. E.: Structure and Properties of African Wave Disturbances As Observed During Phase III of Gate, Mon. Weather Rev., 105, 317–333, doi:10.1175/1520-0493(1977)105⟨0317:TSAPOA⟩2.0.CO;2, 1977.

Reuter, A. and Bakan, S.: Improvements of Cloud Particle Sizing with a 2D-Grey Probe, J. Atmos. Ocean. Tech., 15, 1196–1203, doi:10.1175/1520-0426(1998)015⟨1196:IOCPSW⟩2.0.CO;2, 1998.

Riediger, O.: Entwicklung und Einsatz eines flugzeuggetragenen Instrumentes zur in-situ-Messung langlebiger Spurengase in der Stratosphäre, Ph.D. thesis, Johann Wolfgang Goethe-Universität, Frankfurt am Main, 2000.

Rogers, R. R. and Yau, M. K.: A Short Course in Cloud Physics, vol. 113 of *Natural Philosophy*, Butterworth-Heinemann (Elsevier Science), 3rd edn., 1989.

Romps, D. M. and Kuang, Z.: Overshooting convection in tropical cyclones, Geophys. Res. Lett., 36, L09 804, doi:10.1029/2009GL037396, 2009.

Rosenfield, J. E., Considine, D. B., Schoeberl, M. R., and Browell, E. V.: The impact of subvisible cirrus clouds near the tropical tropopause on stratospheric water vapor, Geophys. Res. Lett., 25, 1883–1886, doi:10.1029/98GL01294, 1998.

Rosinski, J. and Morgan, G.: Cloud condensation nuclei as a source of ice-forming nuclei in clouds, J. Aerosol Sci., 22, 123 – 133, doi:10.1016/0021-8502(91)90022-A, 1991.

Rossow, W. B. and Pearl, C.: 22-Year survey of tropical convection penetrating into the lower stratosphere, Geophys. Res. Lett., 34, L04 803–, doi:10.1029/2006GL028635, 2007.

Sassen, K. and Cho, B. S.: Subvisual Thin Cirrus Lidar Dataset For Satellite Verification And Climatological Research, J. Appl. Meteorol., 31, 1275–1285, doi:10.1175/1520-0450(1992)031⟨1275:STCLDF⟩2.0.CO;2, 1992.

Sassen, K., Wang, Z., and Liu, D.: Cirrus clouds and deep convection in the tropics: Insights from CALIPSO and CloudSat, J. Geophys. Res., 114, D00H06, doi::10.1029/2009JD011916, 2009.

Schiller, C., Krämer, M., Afchine, A., Spelten, N., and Sitnikov, N.: Ice water content of Arctic, midlatitude, and tropical cirrus, J. Geophys. Res., 113, D24 208, doi:10.1029/2008JD010342, 2008.

Schiller, C., Grooß, J.-U., Konopka, P., Plöger, F., Silva dos Santos, F. H., and Spelten, N.: Hydration and dehydration at the tropical tropopause, Atmos. Chem. Phys., 9, 9647–9660, doi:10.5194/acp-9-9647-2009, 2009.

Schmidt, S., Lehmann, K., and Wendisch, M.: Minimizing Instrumental Broadening of the Drop Size Distribution with the M-Fast-FSSP, J. Atmos. Ocean. Tech., 21, 1855–1867, doi:10.1175/JTECH-1673.1, 2004.

Schreiner, J., Voigt, C., Weisser, C., Kohlmann, A., Mauersberger, K., Deshler, T., Kröger, C., Rosen, J., Kjome, N., Larsen, N., Adriani, A., Cairo, F., Di Donfrancesco, G., Ovarlez, J., Ovarlez, H., and Dörnbrack, A.: Chemical, microphysical, and optical properties of polar stratospheric clouds, J. Geophys. Res., 107, 8313, doi:10.1029/2001JD000825, 2003.

Schumann, U. and Huntrieser, H.: The global lightning-induced nitrogen oxides source, Atmos. Chem. Phys., 7, 3823–3907, doi:10.5194/acp-7-3823-2007, 2007.

Seifert, M., Ström, J., Krejci, R., Minikin, A., Petzold, A., Gayet, J.-F., Schlager, H., Ziereis, H., Schumann, U., and Ovarlez, J.: Aerosol-cirrus interactions: a number based phenomenon at all?, Atmos. Chem. Phys., 4, 293–305, doi:10.5194/acp-4-293-2004, 2004.

Shaik, H. A. and Cleland, S. J.: The tropical circulation in the Australian/Asian region - November 2005 to April 2006, Aust. Meteorol. Mag., 55, 219–230, 2006.

Shcherbakov, V., Gayet, J. F., Baker, B., and Lawson, P.: Light scattering by single natural ice crystals, J. Atmos. Sci., 63, 1513–1525, 2006.

Sherwood, S. C. and Dessler, A. E.: On the control of stratospheric humidity, Geophys. Res. Lett., 27, 2513–2516, doi:10.1029/2000GL011438, 2000.

Sherwood, S. C. and Dessler, A. E.: A Model for Transport across the Tropical Tropopause, J. Atmos. Sci., 58, 765–779, doi:10.1175/1520-0469(2001)058⟨0765:AMFTAT⟩2.0.CO;2, 2001.

Shur, G., Sitnikov, N., and Drynkov, A.: A mesoscale structure of meteorological fields in the tropopause layer and in the lower stratosphere over the southern tropics (Brazil), Russ. Meteorol. Hydrol., 32, 487–494, doi:10.3103/S106837390708002X, 2007.

Simpson, J., Keenan, T. D., Ferrier, B., Simpson, R. H., and Holland, G. J.: Cumulus Mergers In the Maritime Continent Region, Meteorol. Atmos. Phys., 51, 73–99, doi:10.1007/BF01080881, 1993.

Sitnikov, N. M., Yushkov, V. A., Afchine, A. A., Korshunov, L. I., Astakhov, V. I., Ulanovskii, A. E., Krämer, M., Mangold, A., Schiller, C., and Ravegnani, F.: The FLASH instrument for water vapor measurements on board the high-altitude airplane, Instrum. Exp. Tech., 50, 113–121, doi:10.1134/S0020441207010174, 2007.

Smedley, A. R. D., Saunders, C. P. R., and Webb, A. R.: Small-particle size determination by optical array probe oversampling, J. Atmos. Ocean. Tech., 20, 1568–1575, doi:10.1175/1520-0426(2003)020⟨1568:SSDBOA⟩2.0.CO;2, 2003.

Sokolov, L. and Lepuchov, B.: Protocol of interaction between Unit for Connection with Scientific Equipment (UCSE) and on-board scientific equipment of Geophysica aircraft (Second edition), Myasishchev Design Bureau (MDB), 1998.

Solomon, S., Borrmann, S., Garcia, R. R., Portmann, R., Thomason, L., Poole, L. R., Winker, D., and McCormick, M. P.: Heterogeneous chlorine chemistry in the tropopause region, J. Geophys. Res. - Atmos., 102, 21 411–21 429, doi:10.1029/97JD01525, 1997.

Spang, R., Hoffmann, L., Kullmann, A., Olschewski, F., Preusse, P., Knieling, P., Schroeder, S., Stroh, F., Weigel, K., and Riese, M.: High resolution limb observations of clouds by the CRISTA-NF experiment during the SCOUT-O3 tropical aircraft campaign, Adv. Space Res., 42, 1765–1775, doi:10.1016/j.asr.2007.09.036, 2008.

Stefanutti, L., Sokolov, L., Balestri, S., MacKenzie, A. R., and Khattatov, V.: The M-55 Geophysica as a platform for the airborne polar experiment, J. Atmos. Ocean. Tech., 16, 1303–1312, doi:10.1175/1520-0426(1999)016⟨1303:TMGAAP⟩2.0.CO;2, 1999.

Stefanutti, L., MacKenzie, A. R., Santacesaria, V., Adriani, A., Balestri, S., Borrmann, S., Khattatov, V., Mazzinghi, P., Mitev, V., Rudakov, V., Schiller, C., Toci, G., Volk, C. M., Yushkov, V., Flentje, H., Kiemle, C., Redaelli, G., Carslaw, K. S., Noone, K., and Peter, T.: The APE-THESEO tropical campaign: An overview, J. Atmos. Chem., 48, 1–33, doi:10.1023/B:JOCH.0000034509.11746.b8, 2004.

Stewart, D. J., Taylor, C. M., Reeves, C. E., and McQuaid, J. B.: Biogenic nitrogen oxide emissions from soils: Impact on NO_x and ozone over west Africa during AMMA (African Monsoon Multidisciplinary Analysis): Observational study, Atmos. Chem. Phys., 8, 2285–2297, doi:10.5194/acp-8-2285-2008, 2008.

Strapp, J. W., Albers, F., Reuter, A., Korolev, A. V., Maixner, U., Rashke, E., and Vukovic, Z.: Laboratory Measurements of the Response of a PMS OAP-2DC, J. Atmos. Ocean. Tech., 18, 1150–1170, doi:10.1175/1520-0426(2001)018⟨1150:LMOTRO⟩2.0.CO;2, 2001.

Ström, J., Strauss, B., Anderson, T., Schröder, F., Heintzenberg, J., and Wendling, P.: In situ observations of the microphysical properties of young cirrus clouds, J. Atmos. Sci., 54, 2542–2553, doi:10.1175/1520-0469(1997)054⟨2542:ISOOTM⟩2.0.CO;2, 1997.

Stubenrauch, C. J., Chedin, A., Radel, G., Scott, N. A., and Serrar, S.: Cloud properties and their seasonal and diurnal variability from TOVS path-B, J. Climate, 19, 5531–5553, 2006.

Sultan, B. and Janicot, S.: The West African monsoon dynamics. Part II: The ”preonset” and ”onset” of the summer monsoon, J. Climate, 16, 3407–3427, 2003.

Sussmann, R., Borsdorff, T., Rettinger, M., Camy-Peyret, C., Demoulin, P., Duchatelet, P., Mahieu, E., and Servais, C.: Technical Note: Harmonized retrieval of column-integrated atmospheric water vapor from the FTIR network – first examples for long-term records and station trends, Atmos. Chem. Phys., 9, 8987–8999, doi:10.5194/acp-9-8987-2009, 2009.

Takano, Y. and Liou, K. N.: Solar Radiative-transfer In Cirrus Clouds. Part I: Single-scattering and Optical-properties of Hexagonal Ice Crystals, J. Atmos. Sci., 46, 3–19, doi:10.1175/1520-0469(1989)046⟨0003:SRTICC⟩2.0.CO;2, 1989.

Thomas, A., Borrmann, S., Kiemle, C., Cairo, F., Volk, M., Beuermann, J., Lepuchov, B., Santacesaria, V., Matthey, R., Rudakov, V., Yushkov, V., MacKenzie, A. R., and Stefanutti, L.: In situ measurements of background aerosol and subvisible cirrus in the tropical tropopause region, J. Geophys. Res., 107, 4763, doi:10.1029/2001JD001385, 2002.

Thompson, A. M., Tao, W. K., Pickering, K. E., Scala, J. R., and Simpson, J.: Tropical deep convection and ozone formation, B. Am. Meteorol. Soc., 78, 1043–1054, doi:10.1175/1520-0477(1997)078⟨1043:TDCAOF⟩2.0.CO;2, 1997.

Thompson, A. M., Doddridge, B. G., Witte, J. C., Hudson, R. D., Luke, W. T., Johnston, J. E., Johnston, B. J., Oltmans, S. J., and Weller, R.: A tropical Atlantic paradox: Shipboard and satellite views of a tropospheric ozone maximum and

wave-one in January-February 1999., Geophys. Res. Lett., 27, 3317–3320, doi:10.1029/1999GL011273, 2000.

Thorncroft, C. D. and Blackburn, M.: Maintenance of the African easterly jet, Q. J. Roy. Meteor. Soc., 125, 763–786, doi:10.1002/qj.49712555502, 1999.

Tompkins, A. M., Diongue-Niang, A., Parker, D. J., and Thorncroft, C. D.: The African easterly jet in the ECMWF Integrated Forecast System: 4D-Var analysis, Q. J. Roy. Meteor. Soc., 131, 2861–2885, doi:10.1256/qj.04.136, 2005.

Toon, O. B., Starr, D. O., Jensen, E. J., Newman, P. A., Platnick, S., Schoeberl, M. R., Wennberg, P. O., Wofsy, S. C., Kurylo, M. J., Maring, H., Jucks, K. W., Craig, M. S., Vasques, M. F., Pfister, L., Rosenlof, K. H., Selkirk, H. B., Colarco, P. R., Kawa, S. R., Mace, G. G., Minnis, P., and Pickering, K. E.: Planning, implementation, and first results of the Tropical Composition, Cloud and Climate Coupling Experiment (TC4), J. Geophys. Res., 115, D00J04, doi:10.1029/2009JD013073, 2010.

Trenberth, K. E., Fasullo, J., and Smith, L.: Trends and variability in column-integrated atmospheric water vapor, Clim. Dynam., 24, 741–758, doi:10.1007/s00382-005-0017-4, 2005.

Trenberth, K. E., Fasullo, J. T., and Kiehl, J.: Earth's Global Energy Budget, B. Am. Meteorol. Soc., 90, 311–323, doi:10.1175/2008BAMS2634.1, 2009.

Tuck, A.: Production of nitrogen-oxides by lightning discharges, Q. J. Roy. Meteor. Soc., 102, 749–755, doi:10.1002/qj.49710243404, 1976.

Ulanovsky, A. E., Yushkov, V. A., Sitnikov, N. M., and Ravegnani, F.: The FOZAN-II fast-response chemiluminescent airborne ozone analyzer, Instrum. Exp. Tech., 44, 249–256, doi:10.1023/A:1017535608026, 2001.

Vardiman, L.: The Generation of Secondary Ice Particles in Clouds by Crystal-Crystal Collision, J. Atmos. Sci., 35, 2168–2180, doi:10.1175/1520-0469(1978)035⟨2168:TGOSIP⟩2.0.CO;2, 1978.

Vaughan, G., Schiller, C., MacKenzie, A. R., Bower, K., Peter, T., Schlager, H., Harris, N. R. P., and May, P. T.: SCOUT-03/ACTIVE - High-altitude aircraft measurements around deep tropical convection, B. Am. Meteorol. Soc., 89, 647–662, doi:10.1175/BAMS-89-5-647, 2008.

Verheggen, B., Cozic, J., Weingartner, E., Bower, K., Mertes, S., Connolly, P., Gallagher, M., Flynn, M., Choularton, T., and Baltensperger, U.: Aerosol partitioning between the interstitial and the condensed phase in mixed-phase clouds, J. Geophys. Res. - Atmos., 112, D23 202, doi:10.1029/2007JD008714, 2007.

Viciani, S., D'Amato, F., Mazzinghi, P., Castagnoli, F., Toci, G., and Werle, P.: A cryogenically operated laser diode spectrometer for airborne measurement of stratospheric trace gases, Appl. Phys. B-Lasers O, 90, 581–592, doi:10.1007/s00340-007-2885-2, 2008.

Voigt, C., Schlager, H., Luo, B. P., Dörnbrack, A., Roiger, A., Stock, P., Curtius, J., Vössing, H., Borrmann, S., Davies, S., Konopka, P., Schiller, C., Shur, G., and Peter, T.: Nitric Acid Trihydrate (NAT) formation at low NAT supersaturation in Polar Stratospheric Clouds (PSCs), Atmos. Chem. Phys., 5, 1371–1380, doi:10.5194/acp-5-1371-2005, 2005.

Voigt, C., Schlager, H., Roiger, A., Stenke, A., de Reus, M., Borrmann, S., Jensen, E., Schiller, C., Konopka, P., and Sitnikov, N.: Detection of reactive nitrogen containing particles in the tropopause region - evidence for a tropical nitric acid trihydrate (NAT) belt, Atmos. Chem. Phys., 8, 7421–7430, doi:10.5194/acp-8-7421-2008, 2008.

Voigt, C., Schumann, U., Jurkat, T., Schäuble, D., Schlager, H., Petzold, A., Gayet, J.-F., Krämer, M., Schneider, J., Borrmann, S., Schmale, J., Jessberger, P., Hamburger, T., Lichtenstern, M., Scheibe, M., Gourbeyre, C., Meyer, J., Kübbeler, M., Frey, W., Kalesse, H., Butler, T., Lawrence, M. G., Holzäpfel, F., Arnold, F., Wendisch, M., Döpelheuer, A., Gottschaldt, K., Baumann, R., Zöger, M., Sölch, I., Rautenhaus, M., and Dörnbrack, A.: In-situ observations of young contrails – overview and selected results from the CONCERT campaign, Atmos. Chem. Phys., 10, 9039–9056, doi:10.5194/acp-10-9039-2010, 2010.

Volk, C. M., Riediger, O., Strunk, M., Schmidt, U., Ravegnani, F., Ulanovsky, A., and Rudakov, V.: In situ tracer measurements in the tropical tropopause region during APE-THESEO, in: Stratospheric Ozone 1999, Proc. 5th European Workshop on Stratospheric Ozone, edited by Harris, N. R. P., Guirlet, M., and Amanatidis, G. T., no. 73 in EUR19340, pp. 661–664, St. Jean de Luz, 2000.

von Blohn, N., Mitra, S. K., Diehl, K., and Borrmann, S.: The ice nucleating ability of pollen: Part III: New laboratory studies in immersion and contact freezing modes including more pollen types, Atmos. Res., 78, 182–189, doi:DOI: 10.1016/j.atmosres.2005.03.008, 2005.

von Hobe, M., Grooß, J.-U., Müller, R., Hrechanyy, S., Winkler, U., and Stroh, F.: A re-evaluation of the ClO/Cl_2O_2 equilibrium constant based on stratospheric in-situ observations, Atmos. Chem. Phys., 5, 693–702, doi:10.5194/acp-5-693-2005, 2005.

von Hobe, M., Grooß, J.-U., Günther, G., Konopka, P., Gensch, I., Krämer, M., Spelten, N., Afchine, A., Schiller, C., Ulanovsky, A., Sitnikov, N., Shur, G., Yushkov, V., Ravegnani, F., Cairo, F., Roiger, A., Voigt, C., Schlager, H., Weigel, R., Frey, W., Borrmann, S., Müller, R., and Stroh, F.: Evidence for heterogeneous chlorine activation in the tropical UTLS, Atmos. Chem. Phys., 11, 241–256, doi:10.5194/acp-11-241-2011, 2011.

Wallace, J. and Hobbs, P.: Atmospheric science: an introductory survey, International geophysics series, Elsevier Academic Press, 2006.

Wang, P. H., Minnis, P., McCormick, M. P., Kent, G. S., and Skeens, K. M.: A 6-year climatology of cloud occurrence frequency from stratospheric aerosol and gas experiment II observations (1985-1990), J. Geophys. Res. - Atmos., 101, 29 407–29 429, doi:10.1029/96JD01780, 1996.

Webster, P. J. and Lukas, R.: TOGA COARE: The Coupled Ocean–Atmosphere Response Experiment, B. Am. Meteorol. Soc., 73, 1377–1416, doi:10.1175/1520-0477(1992)073⟨1377:TCTCOR⟩2.0.CO;2, 1992.

Wegener, A.: Thermodynamik der Atmosphäre, J. A. Barth, 1911.

Weigel, R., Hermann, M., Curtius, J., Voigt, C., Walter, S., Böttger, T., Lepukhov, B., Belyaev, G., and Borrmann, S.: Experimental characterization of the COndensation PArticle counting System for high altitude aircraft-borne application, Atmos. Meas. Tech., 2, 243–258, doi:10.5194/amt-2-243-2009, 2009.

Weigel, R., Borrmann, S., Kazil, J., Minikin, A., Stohl, A., Wilson, J. C., Reeves, J. M., Kunkel, D., de Reus, M., Frey, W., Lovejoy, E. R., Volk, C. M., Viciani, S., D'Amato, F., Cairo, F., Schlager, H., Law, K. S., Shur, G. N., Belyaev, G. V., and Curtius, J.: In situ observations of new particle formation in the tropical upper troposphere: the role of clouds and the nucleation mechanism, Atmos. Chem. Phys. Discuss., 11, 9249–9312, doi:10.5194/acpd-11-9249-2011, 2011.

Wendisch, M., Yang, P., and Pilewskie, P.: Effects of ice crystal habit on thermal infrared radiative properties and forcing of cirrus, J. Geophys. Res. - Atmos., 112, D08 201, doi:10.1029/2006JD007899, 2007.

Wilson, J. C., Jonsson, H. H., Brock, C. A., Toohey, D. W., Avallone, L. M., Baumgardner, D., Dye, J. E., Poole, L. R., Woods, D. C., Decoursey, R. J., Osborn, M., Pitts, M. C., Kelly, K. K., Chan, K. R., Ferry, G. V., Loewenstein, M., Podolske, J. R., and Weaver, A.: In-situ Observations of Aerosol and Chlorine Monoxide After the 1991 Eruption of Mount-pinatubo - Effect of Reactions On Sulfate Aerosol, Science, 261, 1140–1143, doi:10.1126/science.261.5125.1140, 1993.

Winker, D. M. and Trepte, C. R.: Laminar cirrus observed near the tropical tropopause by LITE, Geophys. Res. Lett., 25, 3351–3354, doi:0.1029/98GL01292, 1998.

Winterhalter, R., Kippenberger, M., Williams, J., Fries, E., Sieg, K., and Moortgat, G. K.: Concentrations of higher dicarboxylic acids C_5–C_{13} in fresh snow samples collected at the High Alpine Research Station Jungfraujoch during CLACE 5 and 6, Atmos. Chem. Phys., 9, 2097–2112, doi:10.5194/acp-9-2097-2009, 2009.

World Meteorological Organization: International cloud atlas, vol. 1- Manual on the observation of clouds and other meteors of *International Cloud Atlas*, Secretariat of the World Meteorological Organization, revised edition 1975 edn., 1975.

Yano, J.-I. and Phillips, V. T. J.: Ice-Ice Collisions: An Ice Multiplication Process in Atmospheric Clouds, J. Atmos. Sci., 68, 322–333, doi:10.1175/2010JAS3607.1, 2011.

Yushkov, V., Oulanovsky, A., Lechenuk, N., Roudakov, I., Arshinov, K., Tikhonov, F., Stefanutti, L., Ravegnani, F., Bonafe, U., and Georgiadis, T.: A Chemiluminescent Analyzer for Stratospheric Measurements of the Ozone Concentration (FOZAN), J. Atmos. Ocean. Tech., 16, 1345–1350, doi:10.1175/1520-0426(1999)016⟨1345:ACAFSM⟩2.0.CO;2, 1999.

Yuter, S. E., Houze, R. A., Brodzik, S. R., Smull, B. F., Daugherty, J. R., and Marks, F. D.: TOGA COARE Aircraft Mission Summary Images: An Electronic Atlas, B. Am. Meteorol. Soc., 76, 319–328, doi:$10.1175/1520\text{-}0477(1995)076\langle 0319:\mathrm{TCAMSI}\rangle 2.0.\mathrm{CO};2$, 1995.

Ziereis, H., Schlager, H., Schulte, P., van Velthoven, P. F. J., and Slemr, F.: Distributions of NO, NO_x, and NO_y in the upper troposphere and lower stratosphere between $28°$ and $61°$N during POLINAT 2, J. Geophys. Res. - Atmos., 105, 3653–3664, doi:$10.1029/1999\mathrm{JD}900870$, 2000.

Zöger, M., Afchine, A., Eicke, N., Gerhards, M.-T., Klein, E., McKenna, D. S., Mörschel, U., Schmidt, U., Tan, V., Tuitjer, F., Woyke, T., and Schiller, C.: Fast in situ stratospheric hygrometers: A new family of balloon-borne and airborne Lyman-α photofragment fluorescence hygrometers, J. Geophys. Res., 104, 1807–1816, doi:$10.1029/1998\mathrm{JD}100025$, 1999.

Acknowledgements

I would like to thank everyone who supported and contributed in any way to this thesis. I try to list all below and I apologise sincerely to all of them who I forget to mention.

First of all, I like to thank [redacted] for giving me the opportunity to work on this interesting subject, participate in the one or other field campaign, presenting my results on conferences, and for a lot of helpful discussion and support.

[redacted] introduced me to the institute, the instruments, the subsequent data analysis, and anything else related to my work. . . Thanks a lot for all your help and support!

[redacted] and [redacted] (the other two in the NOVA group when I started my PhD) made my start in Mainz much easier, thanks! Furthermore, the other members of the [redacted] group and the particle chemistry department were always open for questions, thanks for your help!

[redacted] took over the head of the NOVA group and was also always there for questions and support, thanks!

For helpful discussions about the SCOUT-AMMA data I like to acknowledge [redacted]. Also [redacted] gave a lot of helpful comments, particularly in his function as reviewer of the AIRTOSS and SCOUT-AMMA publications.

To keep the instruments running and doing their job, the people in the workshops are the ones to acknowledge. Without you, campaigns would hardly be possible!

For the CIP data analysis I used and refined the software code written by [redacted] from NCAR. Thank you for letting me use the code and for helping me with all the questions I had!

Never refusing explaining MAS data and never complaining over never ending questions. . . Thanks [redacted] (my favourite italian)!

The pilots, ground crews, organisators of all the campaigns I analysed data of or participated in, i.e. SCOUT-O3, SCOUT-AMMA, OMAC, AIRTOSS, CONCERT, RECONCILE.

I have used a lot of campaign data from other groups, namely from the instruments: FISH, FLASH, MAS, MAL, COLD, FOZAN, SIOUX, TDC, UCSE, and also satellite images and trajectory analysis. I'd really like to thank all of you who have been involved in the instrument preparation and maintenance, data acquisition and analysis, and thanks for letting me use the data!

What would an institute's life would be like without any colleagues that share with you a lot of your time? Thanks to all of you from IPA and MPI! Especially thanks for the coffee breaks!

Not to forget those who really tried hard to find any misspelling, bugs, or any nonsense I wrote, dear proof-readers ([redacted], [redacted], [redacted], [redacted], [redacted]): Great job!

Thanks to all the people who helped me with LaTeX and IGOR Pro.

To the IPA and MPI secretaries: I don't need to mention that you are very important persons! Thanks for all you have done for me!

And really, I thank everybody who made it reading the whole thesis! Whao, I am impressed, I hope, I haven't bored you too much!